2022

A Decoupled Engineering Methodology for Accurate Prediction of Ablative Surface Boundary Conditions in Thermal Protection Systems

Justin Cooper
University of Kentucky, justin.m.cooper@nasa.gov
Digital Object Identifier: https://doi.org/10.13023/etd.2022.131

STUDENT AGREEMENT:

I represent that my thesis or dissertation and abstract are my original work. Proper attribution has been given to all outside sources. I understand that I am solely responsible for obtaining any needed copyright permissions. I have obtained needed written permission statement(s) from the owner(s) of each third-party copyrighted matter to be included in my work, allowing electronic distribution (if such use is not permitted by the fair use doctrine) which will be submitted to UKnowledge as Additional File.

I hereby grant to The University of Kentucky and its agents the irrevocable, non-exclusive, and royalty-free license to archive and make accessible my work in whole or in part in all forms of media, now or hereafter known. I agree that the document mentioned above may be made available immediately for worldwide access unless an embargo applies.

I retain all other ownership rights to the copyright of my work. I also retain the right to use in future works (such as articles or books) all or part of my work. I understand that I am free to register the copyright to my work.

REVIEW, APPROVAL AND ACCEPTANCE

The document mentioned above has been reviewed and accepted by the student's advisor, on behalf of the advisory committee, and by the Director of Graduate Studies (DGS), on behalf of the program; we verify that this is the final, approved version of the student's thesis including all changes required by the advisory committee. The undersigned agree to abide by the statements above.

Justin Cooper, Student

Dr. Alexandre Martin, Major Professor

Dr. Jesse Hoagg, Director of Graduate Studies

A Decoupled Engineering Methodology for Accurate Prediction of Ablative Surface Boundary Conditions in Thermal Protection Systems

---

DISSERTATION

A dissertation submitted in partial
fulfillment of the requirements for
the degree of Doctor of Philosophy
in the College of Engineering at the
University of Kentucky

By
Justin Martyn Cooper
Lexington, Kentucky

Director: Dr. Alexandre Martin, Professor of Mechanical Engineering
Lexington, Kentucky 2022

ABSTRACT OF DISSERTATION

A Decoupled Engineering Methodology for Accurate Prediction of Ablative Surface Boundary Conditions in Thermal Protection Systems

The main objective of the present work is to demonstrate a method for prediction of aerothermal environments in the engineering design of hypersonic vehicles as an alternative to the current heritage method. Flat plate and stagnation point boundary layer theory require multiple assumptions to establish the current engineering paradigm. Chief among these assumptions is the similarity between mass and heat transfer. Origins of these assumptions are demonstrated and their relationship to conservative engineering design is analyzed, as well as conditions where they possibly break down. An alternative approach for assessing aerothermal environments from the fluid domain is presented, which permits removal of these assumptions but maintains the integrity of the engineering process. Two demonstration cases are presented, one a simplified graphite ablator and the other a mock engineering process for an Apollo test capsule.

KEYWORDS: Aerothermodynamics, Atmospheric Entry, Computational Fluid Dynamics, Material Response, Convective Heat Transfer, Boundary Layer Theory

Justin Martyn Cooper

May 3, 2022

A Decoupled Engineering Methodology for Accurate Prediction of Ablative Surface Boundary Conditions in Thermal Protection Systems

By
Justin Martyn Cooper

Alexandre Martin
Director of Dissertation

Jesse Hoagg
Director of Graduate Studies

May 3, 2022
Date

Dedicated to my daughter, Maggie Rose Cooper, the rose of the winds.

ACKNOWLEDGMENTS

When I left home at the age of 18 to join the military, I would remain lost for many years after my service. When I met Liz, I finally came back home. My wife is the love of my life, plain and simple. She completes me in every sense of the word, completion. Without her encouragement to return to school, our life would have been much different. She listened to me rant and rave with a white board through every semester of school. I credit a majority of my success to her empathic insight and support.

My two *big* kids, Ethan and Aislinn, never once helped me study. In fact, quite the contrary. But through their innocence and the love they gave me, I was driven to succeed. As they become older human beings, they should know this is for them, to inspire and instill the idea that anything is possible (even if it isn't probable). Then there's my Maggie Rose, whose exuberant presence cannot be understated. She is my compass rose, a true north indicator, for whom I cannot fail. She came at a time of deep sorrow in our family and illuminated us all with her simple and pure being.

I must also acknowledge my sister, Willow, and my mother, Willow. Both of whom helped support my family and me throughout the roughest part of raising a family and trying to get through graduate school and find a job.

Professionally I must first acknowledge Dr. Alexandre Martin, Ph. D., P.E. He is a different type of professor. He demonstrates a genuine interest in his students, and proved this on multiple occassions by working with my demanding, out of the ordinary, circumstances. Never once did he fail me, no matter the situation. His prodiguous knowledge was often far ahead of mine, taking me days to weeks to reach the same conclusion that he would scribble on a piece of paper. The opportunities he afforded me are still resonating throughout my life to this day.

Under Dr. Martin I met Dr. Haoyue (how-you-eh) Weng, a doctoral student. He was the first to teach me to code and answer what I see now as a prolific assault of annoying questions. I still enjoy a great, but (physically) distant relationship with him and acknowledge him as my first true mentor.

My sincerest acknowledgement goes to Adam Amar and his strange affinity for cats. His breadth of knowledge in aerothermal engineering is (in my mind) completely unmatched. The manner and speed which he arrives at conclusions concerning complex topics is astonishing. Like Dr. Martin, he stood beside me through every circumstance I encountered. Even as he professionally ascends the ladder at NASA, he is always available as an insightful engineer and valuable colleague (despite his incessant sarcasm).

On the other side of the same coin is Brandon Oliver. Possibly the antitheses of Adam Amar, they share the near same mountain of aerothermodynamic experience, varying only in demeanor. Brandon is a reserved and profound man who doesn't like to waste words and recognizes himself when he has gone down into the weeds. He has taken a particular keen interest in my dissertation and provided a myriad of insightful conversations about chemical equilibrium, engineering assumptions, and the like. We share an invisible bond as men who enjoy knowledge (perhaps painfully), both completing doctorates actively working as engineers. To him I express my most grateful thanks.

Gio Salazar was my first mentor upon arrival at Johnson Space Center. It is impossible to enumerate the number of conversations we have had on all types of different levels concerning the path and direction of my studies and all things aerothermodynamics. Even as his path took him to a different sector of the industry, we still remain in touch and frequently discuss the topics at hand, including our never-ending journey to model thermocouple wires in complex geometries. To him I credit a large portion of my training as a young engineer and a sustained relationship which frequently

offers insight unattainable elsewhere.

Of course, I must also acknowledge Ben and Lindsay Kirk. Ben, as the branch chief, saw my vision for this dissertation and actually helped to fund it as part of NASA's mission for pursuing excellence and state of the art. But more than that, I appreciate Ben not only being an amazing supervisor, but also a friend who let me live with him while I was trying to buy a home for my family. His knowledge of all things NASA is incredible and as of today, he has begun the journey to a new destination. I wish him all the best. Lindsay also had to endure my residency, but also is a frequent colleague to whom a necessary discussion about film coefficients and chemical equilibrium is also endured.

There is an almost innumerable list of friends and colleagues I have made on the way. All the lab guys and gals; Chris, Ali, Olivia, Raghava, Rick, Zack, Ting-ting, Umran. Even more NASA folks; Justin, Peter J., Peter McC., Kyle (NSTRF guy), Walter, Logan, Jon, Jerry, and the list goes on and on and continues to grow. To all of you who fill my life with meaning, I am always grateful.

TABLE OF CONTENTS

LIST OF FIGURES

LIST OF TABLES

Chapter 1 Introduction and Problem Statement

> And don't tell me that man doesn't belong out there. Man belongs wherever he wants to go - and he'll do plenty well when he gets there.
>
> Wernher von Braun, *Time 17*

Before civilization existed, mankind most likely spent a lot of time looking to the heavens. In the unpolluted preindustrial world, a ball of fire may have streaked across the sky, sparking the imagination of pre-modern man. This heavenly spectacle may have seemed magical, perhaps even divine, but in fact it was space-faring debri entering the Earth atmosphere. This debri, most likely carbonaceous or silicate-based, entered at high velocity generating an enormous amount of heat as it vaporized into nothingness. A portion of that heat was converted into visible radiation, providing the wondrous illumination that we associate with meteors. Little would the past man have known that in the 20^{th} century modern man would begin to approach speeds of the same magnitude. At these speeds, it is up to the aerothermodynamicist to understand the hypersonic physics associated with flight through a fluid medium and the engineering challenges that it presents.

1.1 Origin of hypersonic development

In the late 1930's, a team lead by German scientist Wernher von Braun began development of weaponized rockets in Nazi Germany, building on the work that Robert Goddard (15, 16) had produced on rocket engines. The development of the V2 rocket culminated in its use against the city of London in 1944. This first family of cruise

missiles flew above Mach 5, well above the supersonic limit fighter pilots were reaching at the time. It would not be until 1946 that Tsien coined the term *hypersonic*, commonly defined as speeds at or in excess of Mach 5(17). For the practicing aerothermodynamicist, the more precise definition may be applied; *a region of flight occuring at any velocity such that the physics of the flow are dominated by aerodynamic heating*(18). The study of this region of flight became critically important in the post-war United States 1950's as the military pressed for what would eventually be coined the intercontinental ballistic missile or ICBM.

On the road to the first ICBM, the most dramatic surge in hypersonic advancement came on 14 May 1955 under the Atlas program after repeated successful tests of the Castle series hydrogen bombs(19). While Wernher von Braun had been extricated from Germany to work for the U.S. Army on now shorter range rockets, the Air Force had been tasked with the unthinkable challenge of delivering payloads thousands of nautical miles away with the desired accuracies of +1,500 ft. General Thomas White, the Air Force Vice Chief of Staff at the time, lobbied for the development of the program and was given **the maximum effort possible with no limitations on funding**(19). This demonstrates the urgency of the development of hypersonic science during a time when Russia and China were seen as threats to the Allied Powers. In a move to bolster U.S. confidence after the Russian (Soviet) Sputnik satellites were placed in orbit, President Eisenhower revealed to the public a Jupiter re-entry vehicle on national television, stating: "It has been hundreds of miles into outer space and back(18)." Multiple newspapers lead with Ike standing next to the iconic vehicle, seen in Fig. 1.1.

One of the cornerstone cruxes of adapting V-2 German era rockets to long range thermonuclear missiles was design of a nose cone which could accommodate conversion of the kinetic energy of a rocket powered vehicle into heat. In order for the President to make such a bold proclamation, scientists and engineers had to deter-

Figure 1.1: President Eisenhower (Ike) standing next to Jupiter-C nose cone (1)

mine a method for a vehicle weighing several hundreds of thousands of pounds and traveling at hypersonic speeds up to Mach 20 to survive this awesome level of heat. The research involved with this capability is the cornerstone of modern hypersonic and ablation theory.

1.2 Outlook

Presently, the moon has become the focal point of many of the world's space programs. Table 1.1 shows a recent flurry of activity between the world's spacefaring nations, with China being the most prolific. These missions have all mostly been intelligence gathering missions, except for Chang'e 5. After a string of successful rover landings, the Chinese National Space Agency (CNSA) has decided to perform a lunar sample return. Unlike the orbiting satellites and the wandering rovers, this mission demands a return to planet Earth. The implication is that an atmospheric entry at high

velocity will be performed and subsequently an ablative heatshield will be required for that journey.

Mission	Space Agency	Objective	Launch Date
Kaguya (Selene)	JAXA	Lunar Orbit	09.2007
Chang'e 1	CNSA	Lunar Orbit	10.2007
Chandrayaan-1	ISRO	Lunar Orbit/Impact	10.2008
LCROSS	NASA	Lunar Orbit/Impact	06.2009
LRO	NASA	Lunar Orbit	06.2009
Artemis P1/P2	NASA	L1 and L2	02.2007
Chang'e 2	CNSA	Lunar Orbit and L2	10.2010
Grail	NASA	Lunar Orbit	09.2011
LADEE	NASA	Lunar Orbit/Impact	09.2013
Chang'e 3	CNSA	Lunar Lander	12.2013
Chang'e 4	CNSA	Lunar Lander	12.2018
Beresheet	ISA	Lunar Landing	02.2019
Chandrayaan-2	ISRO	Lunar Orbiter/Lander	06.2019
Chang'e 5	CNSA	Lunar Sample Return	11.2020

Table 1.1: Recent lunar missions by various space agencies

The National Aeronautics and Space Administration (NASA) has announced a deep space exploration program whose fundamental premise is to establish a permanent (sustainable) presence in space, outside of low Earth orbit. One of the core concepts of this architecture is the Lunar Gateway, Fig. 1.2. Similar to the International Space Station, this structure will orbit the Moon and allow the transition of personnel and payload between surface and orbit. With this clear, long term commitment to a trans-lunar presence, an established supply chain will be essential for maintaining operations. Every return mission bringing personnel, research, and payload back to Earth will be conducted at lunar entry velocities and require an ablative heatshield.

A peripheral focus of the major space organizations has been the Red Planet, Mars. Only the most sophisticated countries in the world have attempted landings on Mars, earning it the ominous title of *spacecraft graveyard*. Figure 1.3 shows the

Figure 1.2: NASA Gateway, Artist Concept (2)

lattitude and longitude of various landings. The mission dates highlighted with a yellow dashed line are landing failures, which constitute a significant portion of the attempted landings over the past 50 years. Each colored marker represents a different major space organization. The figure shows that the three Russian attempts, Mars 2, 3, and 6 did not survive their landing. Mars 3 landed but survived only 20 seconds of transmission before going radio silent. In fact, as recently as 2016, ESA's Schiaparelli EDM lander did not survive entry, descent, and landing. This provides evidence that even with our technology advanced 50 years into the future, the atmospheric entry barrier to Mars is still a formidable challenge. The first successful landing was NASA's Viking 1 lander on July 20, 1976. The iconic *foot* of the spacecraft is seen in Fig. 1.4, the first image beamed back to Earth. As recently as 2021, the emergence of the Chinese space program has seen the CNSA landing the rover Zhurong on Mars, just months after the successful landing of NASA's Perseverance. Figure 1.5 shows the historic picture of the second nation to successfully make a Mars landing. The proximity of the two rovers' landing sites may be seen in Fig. 1.3, between the red and

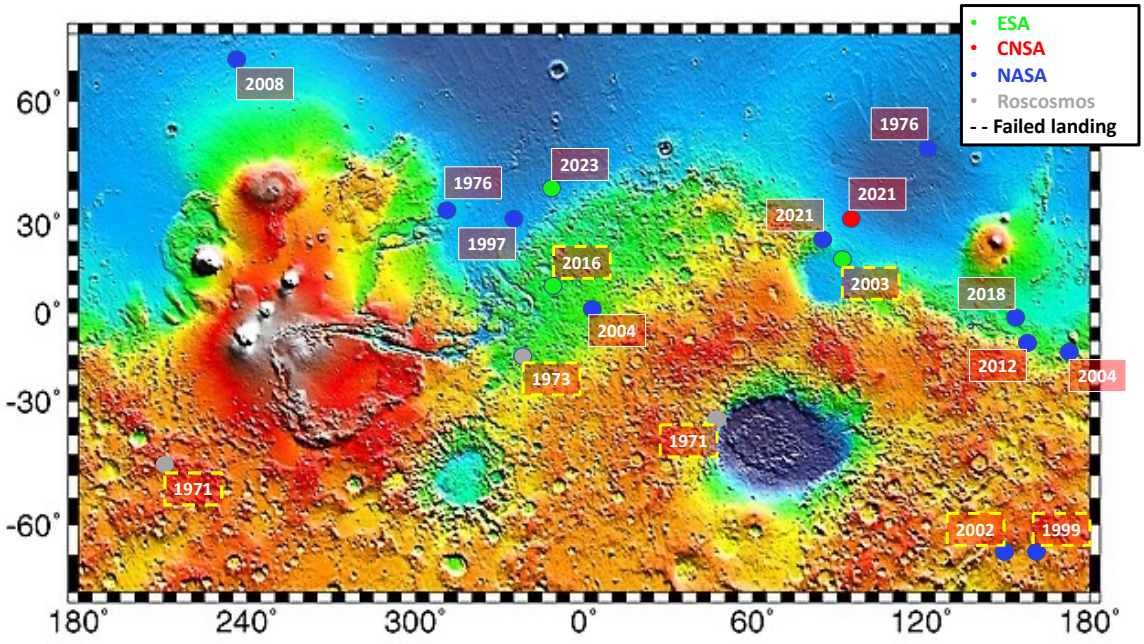

Figure 1.3: Mars landing sites for robotic exploration of the red planet (3)

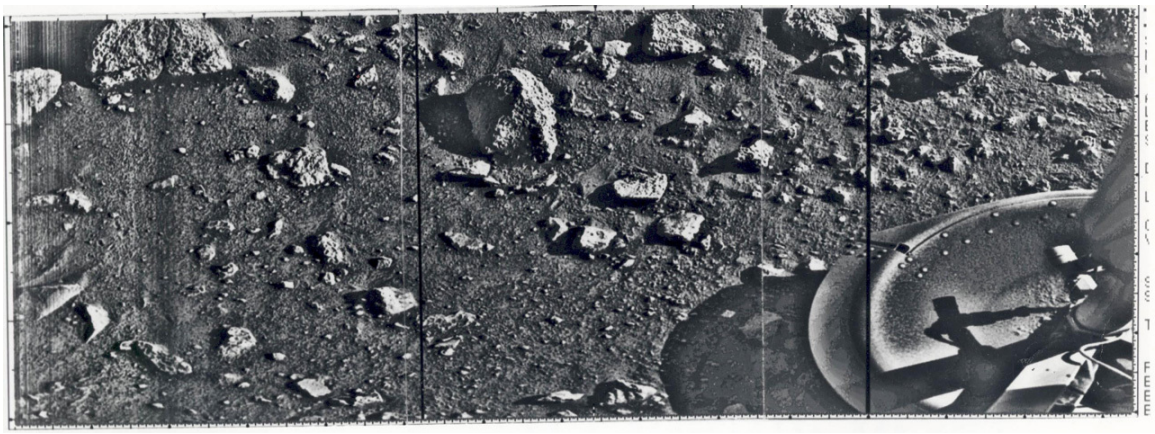

Figure 1.4: Viking 1 Lander, first picture from Mars, July 20, 1976 (4)

blue 2021 markers. This proximity is a beautiful analogy for the rising competitive nature of space exploration between the CNSA and NASA.

The contemporary outlook for space exploration is centered around establishing a human presence beyond low Earth orbit. Every step beyond LEO will require an ablative heatshield to get us back. Every atmosphere entered will require an ablative heatshield to survive. With a healthy competition now emerging in space exploration, it is imperative that aerothermodynamicists understand how these materials behave

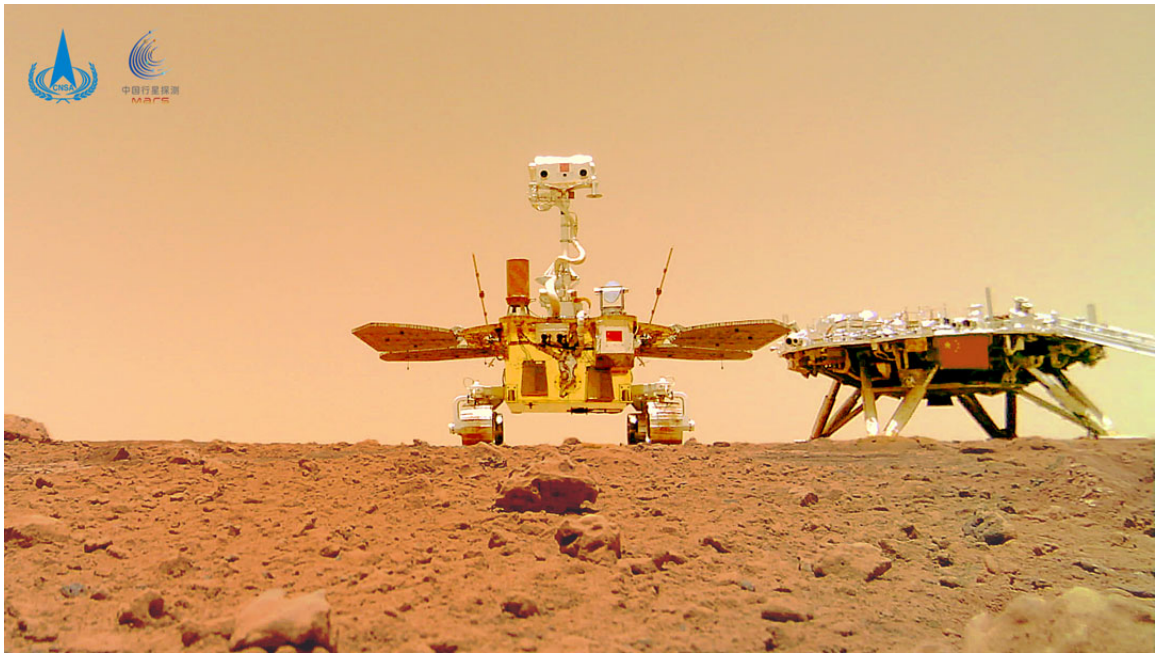

Figure 1.5: Zhurong rover after landing on Mars (5)

in a complex, multi-physics setting to ensure the safety of those daring enough to step into the darkness and to preserve the human spirit of exploration.

1.3 The hypersonic heating problem

> ...re-entry... is perhaps one of the most difficult problems one can imagine.
>
> Theodore von Kármán

The *gedanken* (thought) experiment of a vehicle flying at thousands of miles per hour is a difficult conceptual challenge, since these physical scenarios are not naturally encountered in every day life. However, by looking at the initial state of a vehicle, one can begin to establish an intuition for how much energy is involved in an atmospheric entry. Looking to Fig. 1.6, massive plumes of flame three times larger than the closest building rage beneath a Delta-4 heavy launch. The tiny triangular shape perched atop the massive three booster system is the Orion spacecraft. The kinetic

Figure 1.6: Delta-4 Heavy launch of Exploratory Flight Test-1 (6)

energy transferred to the vehicle from the rocket engines will need to be dissipated for the vehicle to safely land.

After the ascent (which involves a certain level of aerodynamic heating), the vehicle encounters an exo-atmospheric environment with very few fluid particle interactions. However, a return to a planetary body will see the density of the atmospheric particles increasing as the vehicle approaches the surface. This rapidly increases the frequency of particle collisions between the vehicle's surface and the surrounding fluid medium. The resulting collisions have the primary effect of converting kinetic energy into thermal energy. As will be shown, if the entirety of the energy is absorbed by the spacecraft, then the structural material comprising it will rapidly vaporize, resulting in a loss of the vehicle and payload. This, is the so-called *hypersonic heating problem.*

To explain the hypersonic heating problem, the vehicle is assumed a point body mass, and it may be imagined as any object moving through a fluid medium at hypersonic velocity ($M > 5$). The free-body diagram is a simple balance of forces

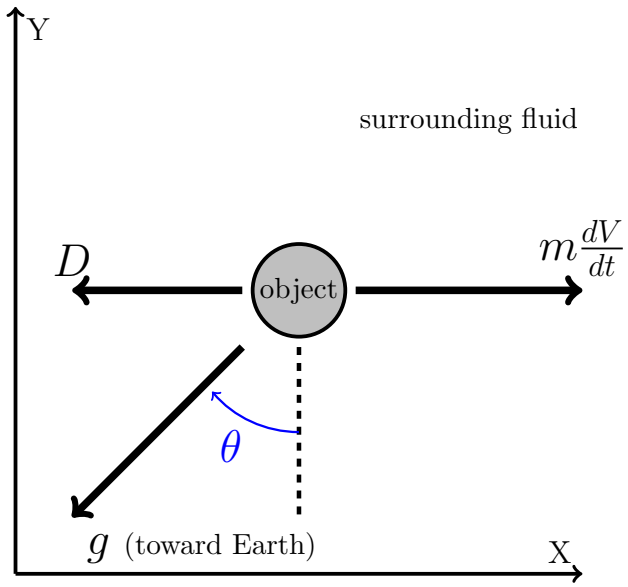

Figure 1.7: Free-body diagram of an accelerating object in a fluid medium

(Fig. 1.7). With properly aligned coordinates in the direction of the accelerating object, Newton's first law yields

$$m\frac{dV}{dt} - mg\sin\theta = -D. \tag{1.1}$$

Here m is the mass of the object, $\frac{dV}{dt}$ is the rate of the change of the velocity of the object with respect to time, g is the gravitational force exerted on the object by the Earth, and D is the total drag force exerted on the object by the atmosphere. Let

$$D = \mathrm{C_D}\rho A V^2/2 \tag{1.2}$$

where D is the drag force due to normal and tangential/shear stresses. As well, $\mathrm{C_D}$ is the drag coefficient, ρ the density of the working fluid, A the projected surface area, and V the velocity of the object.

Mass is assumed to be constant, or in the case of an ablator the mass change at the surface is considered neglible to the entire mass of the vehicle. Next, assume the gravitational force on the object to be neglible compared to the drag force exerted on the object. This gives

$$m\frac{dV}{dt} = -D. \tag{1.3}$$

Let the definition of the Stanton number (derived in Chapter 2.3) be

$$\mathrm{C_H} = \frac{\dot{q}}{\rho V A \left(h_o - h_w\right)} \tag{1.4}$$

where $\dot{q}$ is the rate of heat transferred to the object ($\frac{dQ}{dt}$), h_o is the stagnation (or total) enthalpy of the working fluid which is a conserved property, and h_w is the enthalpy of the working fluid at the surface temperature of the object. Recall the definitions

$$h_o = \int_0^{T_\infty} c_p dT + \frac{V^2}{2} \tag{1.5}$$

and

$$h_w = \int_0^{T_w} c_p dT. \tag{1.6}$$

where c_p is the specific heat at constant pressure of the working fluid and T_∞ is the freestream temperature. The w subscript denotes the enthalpy at the wall of the vehicle, incidating there is no kinetic term, as any velocity there is zero (no-slip boundary condition). Now assuming the specific heat of the gas mixture is constant, and T_∞ and T_w are of the same order of magnitude, then it follows that

$$\begin{aligned} \Delta h &= c_p \left(T_\infty - T_w\right) + \frac{V^2}{2} \\ \Delta h &\approx \frac{V^2}{2}. \end{aligned} \tag{1.7}$$

This is already an important distinction. Equation 1.7 implies that the kinetic energy is responsible for the energy potential across the boundary layer. Rearranging the definition of the Stanton number gives

$$\dot{q} = \frac{dQ}{dt} = \rho V \mathrm{C_H} A \left(h_o - h_w\right). \tag{1.8}$$

Inserting the approximation from Eq. 1.7 gives:

$$\frac{dQ}{dt} = \rho V \mathrm{C_H} A \frac{V^2}{2} \tag{1.9}$$

$$dQ = \rho V \mathrm{C_H} A \frac{V^2}{2} dt \tag{1.10}$$

$$dt = dQ \left[\frac{1}{\rho V \mathrm{C_H} A \frac{V^2}{2}} \right] \tag{1.11}$$

Substituting into the balance of forces on the vehicle now yields

$$m\frac{dV}{dt} = -D \tag{1.12}$$

$$mdV = -Ddt \tag{1.13}$$

$$mdV = -DdQ \left[\frac{1}{\rho V \mathrm{C_H} A \frac{V^2}{2}} \right]. \tag{1.14}$$

Substituting the definition of the drag force (Eq. 1.2) gives

$$mdV = -\left(\mathrm{C_D}\rho A V^2/2\right) dQ \left[\frac{1}{\rho V \mathrm{C_H} A \frac{V^2}{2}} \right] \tag{1.15}$$

$$mdV = -\mathrm{C_D} dQ \left[\frac{1}{V \mathrm{C_H}} \right] \tag{1.16}$$

Or upon simplifying

$$dQ = -\frac{\mathrm{C_H}}{\mathrm{C_D}} \left(mVdV\right). \tag{1.17}$$

The final step is integrating from initial to final values of heat transferred to the object and the velocity of the object. Permitting the assumption of a constant coefficient (which in reality it is far from), gives

$$\begin{aligned} \int_i^f dQ &= -\frac{\mathrm{C_H}}{\mathrm{C_D}} m \left(\int_i^f V dV \right) \\ Q_f - Q_i &= -\frac{\mathrm{C_H}}{\mathrm{C_D}} m \frac{1}{2} \left(V_f^2 - V_i^2 \right) \\ Q_f &= \frac{\mathrm{C_H}}{\mathrm{C_D}} \frac{1}{2} m V_i^2 \end{aligned} \tag{1.18}$$

or

$$Q_f = \frac{\mathrm{C_H}}{\mathrm{C_D}} \left(KE\right)_i \tag{1.19}$$

where Q_f is the final heat transferred to the object and V_i is the initial velocity of the object during entry into the fluid. Q_i and V_f are assumed to be zero for this analysis to encompass the maximum allowable transfer of energy.

Equation 1.19 is a very crude approximation of the heating endured by the object traveling through the fluid. From this simplified model it is possible to ascertain key features of the hypersonic heating problem. The initial kinetic energy has appeared as a key parameter resulting from the velocity integration. Minimizing this term will result in a smaller integrated heat load. Likewise, minimizing the mass of the object will result in a smaller amount of energy transferred. Not only is the heat transfer governed by the components of the object's initial kinetic energy, but also the dimensionless leading coefficient term. By the conservation of energy, the non-dimensional coefficient is the ratio of energy transferred to the object versus the energy transferred to the surrounding medium. If the coefficient is driven to zero, then all of the object's energy will be dissipated into the surrounding medium. If the coefficient is unity, then all of the object's kinetic energy will be absorbed as thermal energy.

Both the Stanton number and the drag coefficient are determined by aerodynamic variables, medium properties, object geometry, and even object composition. Objects with low drag coefficients will thus absorb consequently high amounts of energy. With an ever increasing drag coefficient, portions of the thermal energy will be dissipated into the medium. Conversely, as the Stanton number increases so does the heating to the vehicle. Hypersonic design is predicated on minimizing the heat transfer through this leading coefficient term. The idea of a *leading coefficient term* will be revisited multiple times in the succeeding text.

Return to the gedanken experiment of a spacecraft entering Earth's atmosphere. In Fig. 1.8, the entry velocity along the x-axis is a typical range of velocities for space craft returning from low earth orbit, lunar trajectories, or a distant comet. The y-axis

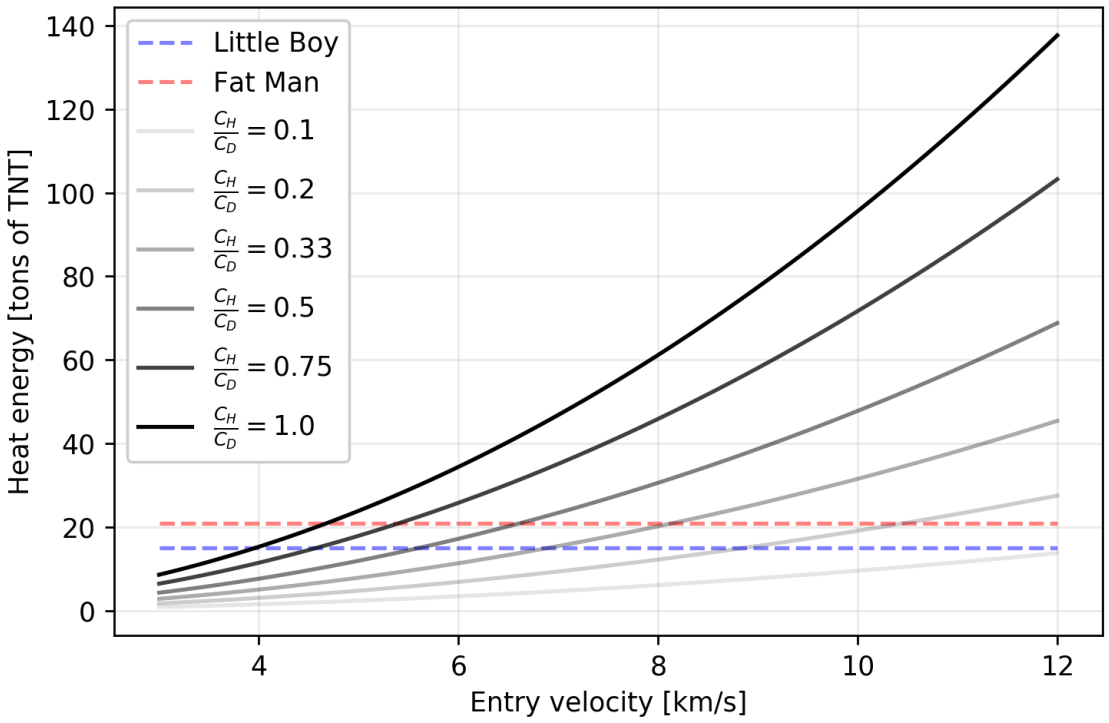

Figure 1.8: Estimated heat transfer to an arbitrary object of 8000 kg mass

represents the total amount of heat transferred to said vehicle (measured in tons of kilograms of TNT) based on the computation of Eq. 1.19. Each line represents a different leading heat transfer coefficient term.

A vehicle traveling at 12 km/s upon entry would have a total kinetic energy of approximately $140,000$ kg of TNT being detonated. To comprehend this enormous amount of energy, the detonation yields of the Hiroshima and Nagasaki atomic bombs are co-plotted in Fig. 1.8. Little Boy (Hiroshima) yielded a 15 ± 3 kiloton explosion (20), whereas Fat Man yielded a 21 ± 2.1 kilotons. Even with an aptly designed spacecraft and minimized coefficient ratio, the vehicle will endure the energy equivalent of tens of tons of TNT detonating. It should be evident, that without engineering design to ensure minimization of this leading coefficient, the usual materials for aerodynamic structural construction (such as aluminum) will fail.

1.4 The vehicle heating problem

The analysis presented in Section 1.3 relied upon two well-known dimensionless quantities and a few key assumptions. From these assumptions the heat flux from the fluid to the vehicle wall was approximated, and further integrated to give the heat load. However, to understand if a vehicle will survive atmospheric entry, the desired temperature distribution of the thermal protection system must be computed. This computation is known as Material Response (MR) and involves the careful solution of the first law of thermodynamics.

$$dU = Q - W \tag{1.20}$$

The first law of thermodynamics states that the change in internal energy (U) within a system is equal to the net heat transfer *into* the system minus the net work *done* by the system. When applied correctly, and noting that work is not performed by the heat shield system, the first law yields the heat equation

$$\rho c_p \frac{\partial T}{\partial t} = q_{in} - q_{out} + S, \tag{1.21}$$

where the first term on the left is the energy storage term comprised of the material density (ρ), the material specific heat (c_p), the material temperature (T), and the time (t). The quantities q_{in} and q_{out} are fluxes which constitute methods of energy transfer at the boundary of the system. The S term here is a source/sink term that constitutes the conversion to or from energy, typically in the form of chemical reactions.

To simplify this analysis, assume that the source term is also negligible, the heat-shield domain is 1-dimensional, and that only a conduction flux exists through the material. By inserting Fourier's Law into Eq. 1.21 the simple form of the heat equation becomes

$$\rho c_p \frac{\partial T}{\partial t} = \frac{\partial}{\partial \eta}\left(k \frac{\partial T}{\partial \eta}\right) \tag{1.22}$$

where the partial derivative with respect to η denotes the surface normal vector. The problem is fully defined by the boundary conditions and the initial state of the heat shield, such that

$$k \left.\frac{dT}{d\eta}\right|_{w} = \dot{q}'' \tag{1.23}$$

$$k \left.\frac{dT}{d\eta}\right|_{sub} = 0 \tag{1.24}$$

$$T(\eta, t=0) = T_i \tag{1.25}$$

where the w subscript refers to the vehicle wall, the *sub* subscript refers to the substructure interface between heatshield and vehicle, and T_i is the initial temperature of the heatshield domain. The first boundary condition is of the Neumann type and constitutes the heat flux entering the heatshield material wall, while the second boundary condition is adiabatic (zero heat flux) which makes the assumption that no heat transfer takes place between the heatshield and the substructure of the vehicle. In practice, this analysis is complicated by numerous factors, one of which is that the substructure and all materials between it and the heatshield must be included in the analysis. The analytical solution (21) to Eqs. 1.22 and 1.25 is given by

$$T(\eta, t) = T_i + \Phi(\alpha, \eta, D, t)\, \dot{q}'' \tag{1.26}$$

where D is the depth of the entire domain being analyzed, $\alpha = k/(\rho C_p)$ is the thermal diffusivity, and Φ is given by

$$\Phi = \frac{D}{k}\left[\frac{\alpha t}{D^2} + \frac{1}{3} - \frac{\eta}{D} + \frac{1}{2}\left(\frac{\eta}{D}\right)^2 - \frac{2}{\pi^2}\phi\right] \tag{1.27}$$

where

$$\phi = \sum_{n=1}^{\infty} \frac{1}{n^2} \exp\left(-n^2\pi^2 \frac{\alpha t}{D^2}\right) \cos\left(n\pi \frac{\eta}{D}\right). \tag{1.28}$$

Inserting Eq. 1.7 and Eq. 1.8 into Eq. 1.26 and noting that $\dot{q}'' = \dot{q}/A$ gives

$$T(\eta, t) = T_i + \Phi \rho V^3 \mathrm{C_H}, \tag{1.29}$$

a crude approximation for the transient temperature history at any select location η in the heatshield material of the vehicle. A few comments are warranted according to Eq. 1.29.

First, the most obvious observation is that the velocity of the vehicle is the dominant factor controlling the heating. If the velocity can be managed actively through guidance or minimized by varying entry parameters then the vehicle heating can be reduced. Further, the atmospheric density contributes to the heating proportionally. Therefore, if the vehicle can decelerate in the upper atmosphere where there are less particles, the heating may be reduced. Again, the Stanton number appears as a proportionality constant. The Stanton number implies that if the ratio of the heat conducted into the vehicle versus the available energy in the boundary layer is decreased, then the vehicle heating will be decreased. Finally, the Φ term must be assessed. For any given body point, this term is linear with respect to time. The further into the body (or the deeper the body point), Φ will be decreased. However, if the total depth D or the material properties represented by the thermal diffusivity α are varied, then the slope of the Φ term will be changed. Physically, this makes sense, as an increased depth requires a longer amount of time to conduct energy. As well, a lower thermal diffusivity decreases the rate at which the energy will be conducted.

However, in its current form, Eq. 1.29 assumes that $\dot{q}''$ is a constant across all time, when in fact it is known from the previous analysis that this is not the case. In fact, each of the variables comprising the heat flux value given by Eq. 1.8 will change with respect to time. While it is possible to take the maximum velocity as constant and produce a conservative estimate, for this analysis some published data will allow a refinement of the heat flux values.

Consider the trajectory flown by the AS-202 Apollo test capsule (8), seen in Fig. 1.9. The altitude data may be used in conjunction with the Standard Atmosphere model (22) to compute the density of the air around the vehicle. With this data, the

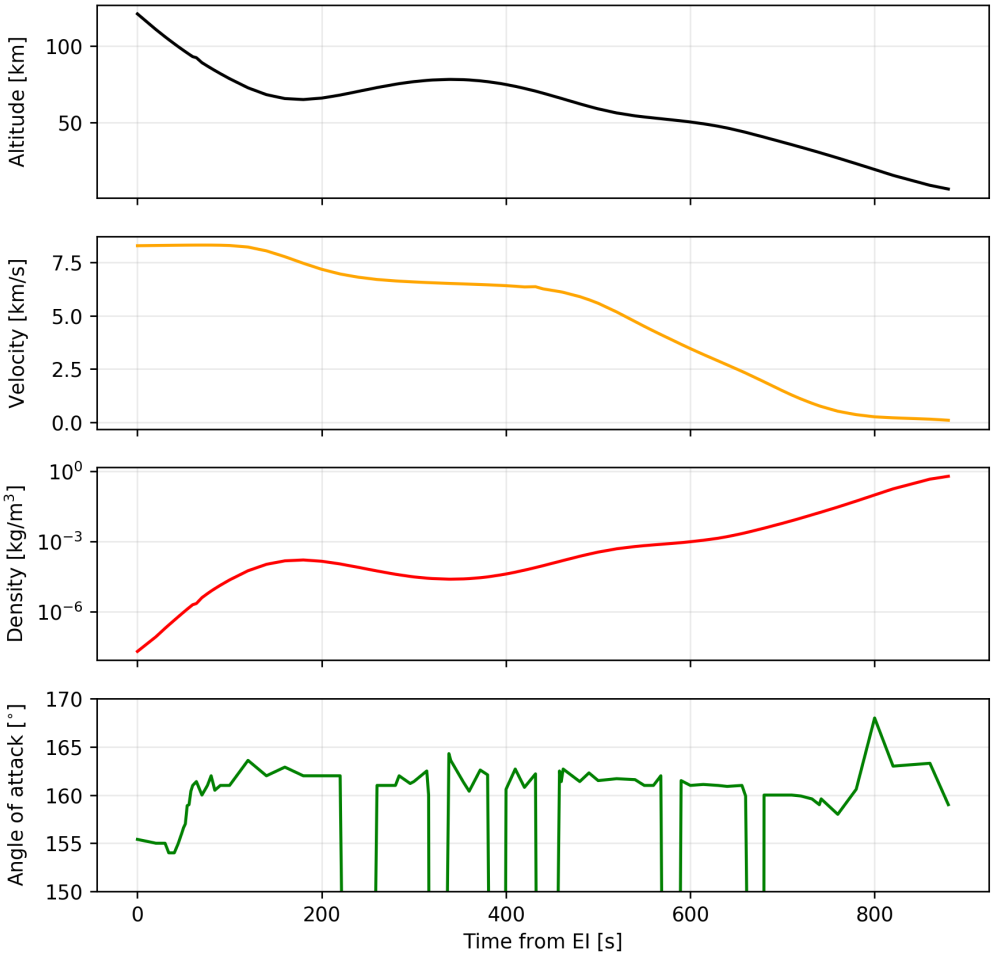

Figure 1.9: Trajectory properties of the AS-202 Apollo test capsule

only further assumption now required is a constant Stanton number to govern the percentage of heat transfer to the vehicle.

By designating all independent variables, Eq. 1.29 may be computed over the course of the trajectory which results in transient temperature signals for any given body point through the domain. Figure 1.10 shows the result of these computations according to the parameters listed in Table 1.2. The abscissa is the 0-fixed time based on the first trajectory point and the ordinate is the measured temperature at the η

Parameter	Value	Units
Initial Temperature [T_i]	300	K
Solid Thermal Conductivity [k]	0.56	W/m/K
Solid Density [ρ]	250	kg/m^3
Solid Specific Heat [C_p]	1800	J/kg/K
Heatshield Depth [D]	0.0381	m
Stanton Number [C_H]	0.001	Dimensionless

Table 1.2: Material response parameters for AS-202 analysis

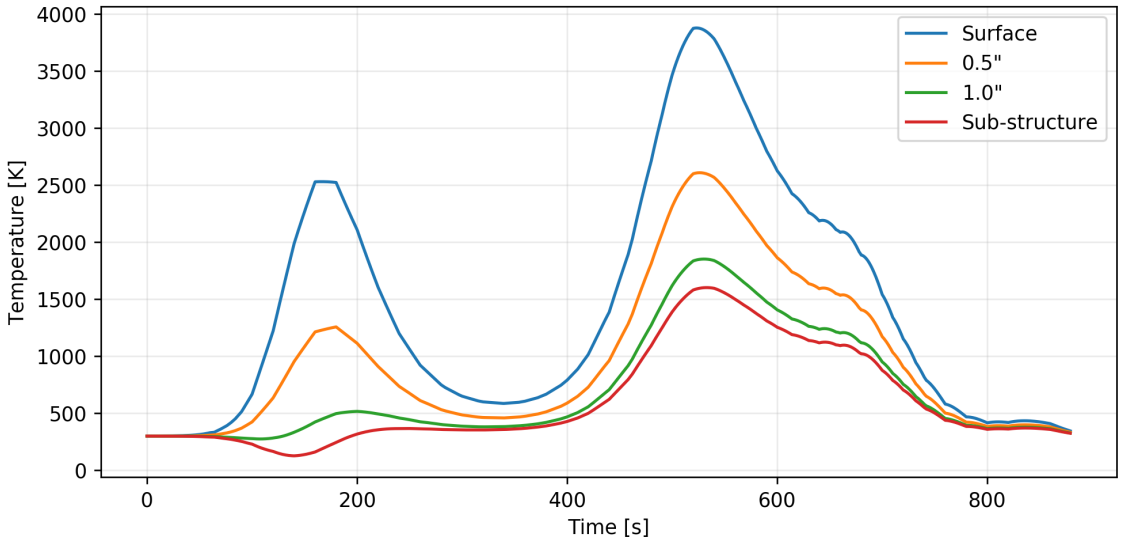

Figure 1.10: Thermocouple signals at varying heatshield depths across AS-202 trajectory using Eq. 1.29

location. The thermal properties are constant approximated properties of low-density carbon based ablators and the heat shield depth is estimated to be 1.5 inches. The initial temperature for each body point is 300 K. The Stanton number which relates the amount of energy conducted into the vehicle to the flow field energy state, is quite low. Essentially, the physical assumption implied by this value is that only $1/1000^{th}$ of the energy available from the flow field is entering the vehicle through conduction. Even with these assumptions, it may be seen that the surface temperature on the AS-202 heatshield would reach almost 4000 K, an intolerably high temperature which would rapidly vaporize a carbon based heatshield. Similarly, inside the material at

depths of 0.5, 1, and 1.5 inches the same trend is seen. Alarmingly high temperatures exist at the second heat pulse. The back, adiabatic wall (typically called the *bondline* since it represents where the TPS is attached to the vehicle) comes in at approximately 1500 K. This is enough energy to considerably weaken the structural integrity of the spacecraft.

It is important to emphasize that this is a first order engineering assessment of a hypersonic entry. The heat flux boundary condition comes from the definition of the Stanton number and the assumption that the wall and far-field temperatures are roughly equivalent, which results in a third order velocity term. Further, the heat equation is for a homogeneous material with constant thermal properties. It contains no in-depth decomposition, which results in no pyrolysis gas generation. At the boundary, only the heat flux is applied without regard for complex ablating physics.

Clearly, a refinement in both acquiring $\dot{q}''$ and in computing the heat equation is required. However, the fundamental building blocks of the engineering methodology for the design of hypersonic vehicles have been illustrated. Given the known inputs about the vehicle, the design process for atmospheric entry may be summarized by these steps:

1. Use models to assess the vehicle state along a family of trajectories.

2. Use models to assess the surface state of the vehicle along the given trajectories.

3. Use models to assess the surface and in-depth properties of the vehicle.

The term *model* refers to an equation or set of equations that can describe a physical process at some level of fidelity. Packaged with it are specific assumptions made about the vehicle or the flow field in which the vehicle travels. In the previous example, the Stanton number relationship (which for example assumes only conduction at the wall and a specific enthalpy difference) and the analytical heat equation solution (which assumes a semi-infinite 1-dimensional domain) were the models used.

In the work that follows, the trajectory data or the output from step 1 will be considered perfect. In reality, the trajectory a vehicle flies will be some variation of a family of trajectories called a monte carlo dispersion. This is a compounded uncertainty in the entire design process, but for simplicity it will not be addressed. The next step in the design process will further be referred to as the *flow field* process or simply the Computational Fluid Dynamics (CFD). The output of this step is the boundary condition information to be transferred to step 3. This process will be further referred to as the Material Response (MR). To improve upon the crude methodology, the full set of governing equations may be employed (see Appendix A).

1.5 Engineering design

The design process outlined in Chapters 1.3 and 1.4 consisted of two equations and produced a conservative estimate of the heat flux to the AS-202 Apollo test capsule. It took approximately 15 minutes to produce a computer code that calculated the temperature history for any in-depth point on the vehicle in under 5 seconds. The only problem is that it is likely too conservative, resulting in an unreasonable amount of heat flux to be managed. This is typically the trade off between engineering approximations and high fidelity solutions. **The cost of accuracy is time.**

Going from Eqs. 1.8 and 1.26 to the complete governing equation set (see Appendix A) requires a significant amount of time and effort. Terms in the conservation equations must be modeled with various assumptions, each of which adds a level of uncertainty to the resulting solutions. Not only can various interpretations or models affect the solution, but the methods to solve the equations and the framework in which to cast them (such as finite volume vs. finite element) can present problems. For example, finite volume frameworks guarantee conservation but often make it difficult to define boundary conditions.

Perhaps the most complex part of solving the governing equations are the bound-

ary conditions (see Appendix C) at the vehicle wall, for both the fluid and material domains. Ideally, the boundary conditions for both equation sets should be the same, since it is the same vehicle wall and fluxes should balance at the boundary. The reasons for why both equation sets cannot be solved simultaneously can be understood by taking a more detailed look at the *process* involved in designing a spacecraft.

Recall that chapters 1.3 and 1.4 demonstrated one possible engineering level approach. The importance of the velocity of the vehicle was a crucial role in understanding the amount of heat transfer occurring. In addition, the role of mitigating the heat transfer via leading coefficient terms such as the Stanton number and the drag coefficient was highlighted. Perhaps if the Stanton number were decreased by a further 10% the predicted temperatures on the AS-202 spacecraft would meet certain requirements. Perhaps if the heat flux estimate had been computed through full-scale 3-dimensional CFD solutions the heat transfer would have been reduced to reasonable levels. The goal is always the same: Understand the levels of heating the vehicle will endure such that it may be designed to safely re-enter and deliver its payload (astronauts, munitions, science, etc). The process of iteratively performing aerothermodynamic analysis to meet certain safety requirements is an engineering design methodology.

Decoupled engineering design

One possible high fidelity engineering design methodology is summarized in Fig. 1.11. In a sense, this is an expanded form of the crude 3-step process outlined earlier. Previously, only the CFD and MR domains were considered. This figure shows the decision making process that encompasses the design methodology. Starting from the vehicle geometry itself, the volume surrounding the vehicle is generated as a computational domain. The governing conservation equations are solved for each point (or cell center) across this domain, subject to certain aerothermodynamic assumptions. These

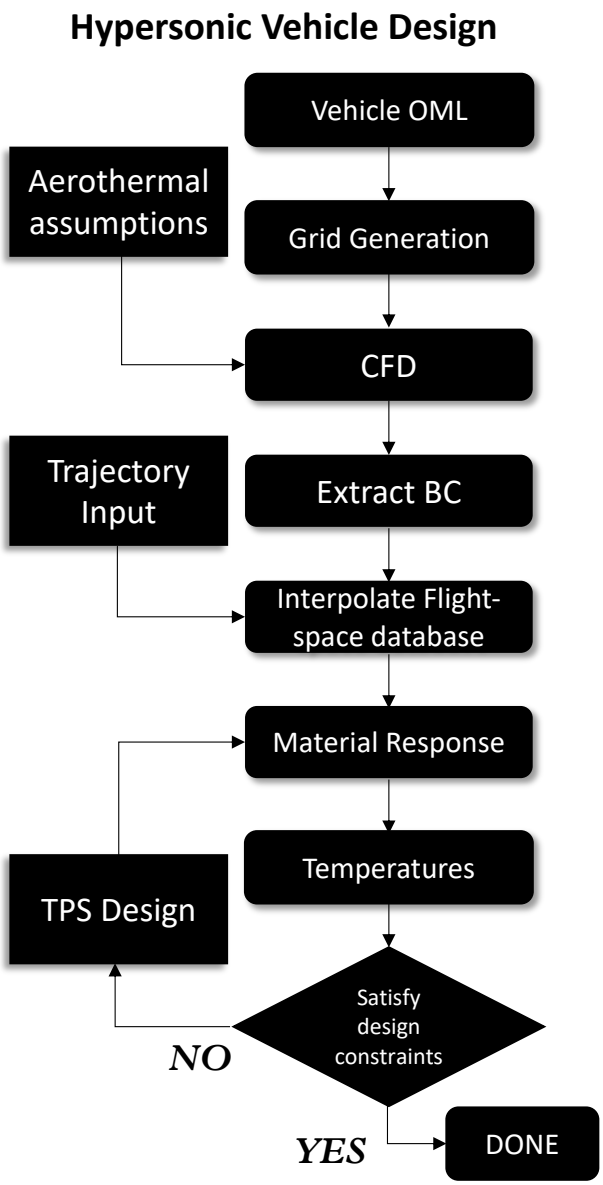

Figure 1.11: Decoupled engineering design methodology

assumptions are built into the models and they exist within nearly each term of the governing equations and their boundary conditions.

The CFD performed will depend on the desired approach. For this text, the database approach is analyzed. Based upon the expected flight corridor, CFD is computed throughout flight space to cover the range of possible trajectories to be encountered. The boundary condition information is extracted from the CFD so-

lutions as a post-processing step and stored separately. The vehicle is then *flown* through the database. This means that given an input vehicle trajectory, the boundary condition information is interpolated between known solution locations within the database. This results in a time dependent boundary condition which may be applied to solving the MR computation.

It should be noted that possible approaches exist other than the database approach and are used throughout industry. For example, one such approach may use the worst possible trajectories for the highest conservative estimates on heat flux (steep entry angle, short flight time) and heat load (shallow entry angle, long flight time). In this approach, only the trajectory points along the known trajectory are computed, removing the need for flight space interpolation and possibly reducing the overall cost of CFD.

The boundary condition information resulting from flight-space database interpolation is subsequently used in the MR caclulation. Again, just as with the CFD, there are assumptions built into the MR calculation which must be considered. The solution to this calculation yields the temperature distribution of the TPS. This information ultimately determines if the design constraints have been met. The so-called TPS design process involves modifying the aerothermodynamic assumptions such that when the MR computation is performed the design constraints are met. If this can be accomplished, then the design process is finalized.

However, if a design constraint cannot be met by changes in the TPS design process, then a change must occur in one of the processes upstream of the material response. This creates a feedback loop where thermal relief may be desired in the MR calculation and must be accomplished by altering the modeling assumptions in the CFD used to construct the boundary condition. Similarly, variables in the vehicle OML itself (such as the height of a given protrusion on the vehicle surface) or the trajectory input may be subject to changes to accomplish the goal of lowering thermal

environments for the MR calculations to meet design constraints.

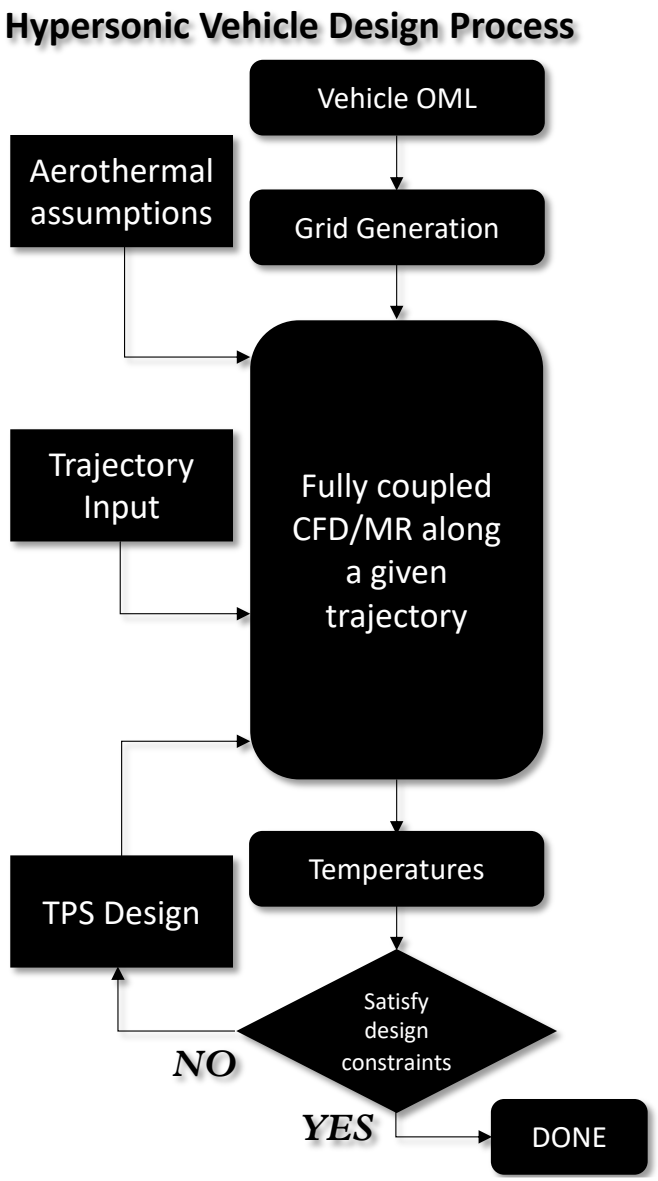

Figure 1.12: Fully coupled design engineering methodology

Fully coupled engineering design

When considering the analysis of a hypersonic vehicle with an ablative TPS, the physics which exist at the surface are coupled between the vehicle material and the surrounding flow field. In other words, they create a feedback loop where one system

affects the other continuosly. Therefore, the highest fidelity answer involves coupling the two computational domains. This approach is known as *fully coupled* and has been demonstrated in the literature (23, 24).

Figure 1.12 shows how the proposed engineering methodology would change under a shift to the fully coupled approach. The most significant change is that the CFD, the generation of boundary conditions, the database interpolation, and the MR have all been replaced by a single box which symbolizes a single combined fully coupled CFD and MR calculation on a single trajectory. All of the various controllable factors which allow iteration of the vehicle design to meet the constraints now flow into this single box. At a minimum, this requires that each desired trajectory (for some n trajectories) must be re-computed whenever a design change is made. In other words, the changes may not be segregated to singular elements, as in the decoupled approach. The increased computational time due to simulating both domains, coupled with this process flaw make the fully coupled approach prohibitively expensive when practicing real world design problems which undergo multiple changes through the design life cycle.

However, this is not to say that the fully coupled approach is without merit. In fact, this very high level of fidelity can serve as an anchoring point to establish levels of confidence in the models that are chosen for the decoupled design process. In the instance of this text, it is not further considered.

1.6 The contemporary approach

The contemporary approach for aerothermodynamic vehicle design will often use the flow of work associated with Fig. 1.11. The critical step in this process is the extraction of the boundary condition information from the CFD. The further treatment of that information as it is applied to the boundary condition of the MR solver is also significantly important in the overall evaluation of environments. To accomplish this

in an efficient manner, it is common practice in industry to use transfer coefficients.

Transfer coefficients are tools developed from boundary layer theory that allow information to be *transferred* from one domain to another rapidly. The primary advantage, and the original intent for their creation, was computational speed. Additionally, the treatment of mass transfer, such as in the case of the oxidation of a carbon heatshield, can be quickly and flexibly modeled using the transfer coefficient paradigm. Prolific use of this methodology has made it an immutable component of aerothermodynamic vehicle design.

The transfer coefficient methodology is not without its disadvantages. By examining the underlying theory, it becomes clear that the critical assumptions used in the construction of transfer coefficients are not applicable through all phases of flight. Chief among them is the heat and mass transfer analogy, which at a fundamental level suggests that the concentration boundary layers of all species will be similar to the energy boundary layer. This assumption itself, requires that the Lewis number of the flow field be unity ($\mathrm{Le} = 1$) and that the species diffusion coefficients be equal. Both of these can be considered questionable, depending on the species present in the flow field. Furthermore, the mass transfer inherently assumes that the interface between the flow field and the wall be in chemical equilibrium. In essence, this is the assumption that chemical reactions will have an infinite amount of time to take place. The advective effect due to mass transfer is replaced with a blowing model derived from a simple form of the energy equation. Other, more nuanced details emerge as the transfer coefficient methodology is further investigated. However, the use of this methodology persists, with these assumptions as inherent and noted uncertainties in the evaluation of environments. For the remainder of this text, the transfer coefficient methodology will be denoted *film coefficient methodology* based on the context of its derivation.

In contrast to these heritage assumptions, a large motivation toward creating

a new engineering paradigm comes from a renewed interest in understanding the chemical reaction mechanisms of ablative systems. Kinetic surface reaction models have been developed (see the literature review) which incorporate a large deal of physics that not only include the state variables such as temperature and pressure, but also topological variables such as site density. These advances in modeling demand a framework in which they may be incorporated into the overall aerothermodynamic vehicle design process.

1.7 Problem statement

At this point, enough general information has been given to clearly define the problem statement.

> *Provide a novel aerothermodynamic engineering methodology, subject to vehicle design constraints, that permits future optimization of thermal protection system boundary conditions by eliminating engineering assumptions known to be poor in specific flight regimes, and replaces them with models that incorporate additional physics, such as chemical reactions and diffusive flow processes.*

To do so, the current method of transmitting information between respective domains must be exhaustively investigated. Through this examination, the assumptions required to construct the models which comprise the CFD and MR boundary conditions will be analyzed and their validity assessed. An alternative method of constructing boundary conditions for both domains will be presented, which allows the continued use of the decoupled design approach while at the same time eliminating unnecessary assumptions.

Chapter 2 Fundamental Concepts

> Primary causes are unknown to us; but are subject to simple and constant laws, which may be discovered by observation...
>
> Joseph Fourier, 1955
>
> *Analytical Theory of Heat*

In this chapter, the *primary causes* (the underlying theory) which give rise to the film coefficient methodology are detailed. The derivation of Spalding's general formulation for transfer conductances is first outlined. Much as the boundary layer equations (Appendix B) are a reduced form of the governing equations (Appendix A), the transfer conductances are the result of a reduced form of the boundary layer equations. Next, the film theory is introduced, itself a further reduced form of the Spalding general formulation. The transfer coefficients and associated blowing parameters are shown to arise simply from taking the quotient of the various diffusive fluxes and integrating across the *thin film*. The relationship between the conserved variables then reveals the precedent for the heat and mass transfer analogy. The blowing correction model is derived (itself an analogous procedure to that of Mickley) to tie together the blowing parameters with the transfer coefficient. The last two sections introduce engineering models which account for high velocity and large temperature gradients in the boundary layer.

2.1 Spalding's General Formulation and Mass Transfer Conductances

In 1959 Spadling set forth a general formulation for mass transfer problems. He reached this form of the conserved equations in the broadest sense possible and with-

out specifically targetting hypersonic problems that involve ablators, although he does make note of its applicability to the problem in his paper. In that which follows, the high velocity, chemically reacting boundary layer equations from Appendix B are reduced to Spalding's general form with a theoretical contribution from Lees. The assumptions starting at this point in the analysis underpin modern ablation theory.

To reach the Spalding form, it is important to understand how the diffusive fluxes are modeled. For the boundary layer theory circa 1960, they are modeled by

$$j_i = -\rho D_i \frac{\partial Y_i}{\partial y} \qquad \text{mass} \tag{2.1}$$

$$\tau_{xy} = \mu \frac{\partial u}{\partial y} \qquad \text{momentum} \tag{2.2}$$

$$\dot{q}'' = k \frac{\partial T}{\partial y} \qquad \text{energy} \tag{2.3}$$

which shows that each physical phenomena is governed by a surface normal gradient and a transport coefficient. The mass diffusion model is due to Fick's Law (25), the viscous shear stress component is due to the Navier-Stokes momentum equation, and the conduction term is due to Fourier's Law (26). Spalding's idea is to reduce the boundary layer equations so that only the advection and diffusion terms exist.

Equations B.7, B.9, and B.10 express the boundary layer energy equation as

$$\rho_g u h + u P_e + \rho_g v h + \tau \mathbf{u} - \dot{\mathbf{q}}'' - \sum_i^{ngs} \mathbf{J_i} h_i = 0 \tag{2.4}$$

where ρ_g is the fluid mixture density, h is the total enthalpy, u is the x-momentum velocity component, v is the y-momentum velocity, τ is the stress tensor, $\mathbf{u}$ is the velocity vector, $\dot{\mathbf{q}}''$ is the conduction heat flux, and $\sum_i^{ngs} \mathbf{J_i} h_i$ is the energy carried by mass diffusion. To reduce the equation set, assume that the contribution by viscous forces is a neglible contributor to the energy, such that

$$\tau \mathbf{u} = 0. \tag{2.5}$$

Similarly, consider the pressure term negligible such that

$$uP_e = 0. \tag{2.6}$$

Next, consider that Fourier's Law of Conduction was derived under laboratory conditions where the thermal properties of fluids do not vary strongly. Under hypersonic flight conditions, the temperatures in a flow can increase significantly, causing large changes in the values of the thermal properties. Therefore, it is no longer reasonable to model the conduction term with respect to temperature. In this case, consider the expansion

$$\dot{\mathbf{q}}'' = k\frac{\partial T}{\partial y} = \frac{k}{\mu\bar{c}_p}\mu\bar{c}_p\frac{\partial T}{\partial y} \tag{2.7}$$

where $\bar{c}_p$ is the frozen specic heat which is summed over all species but neglects chemical reactions. Following Bromberg (27), employ the identity

$$\begin{aligned}\frac{\partial h}{\partial y} = \frac{\partial}{\partial y}\left(\sum_i Y_i h_i\right) &= \sum_i Y_i\frac{\partial h_i}{\partial T}\frac{\partial T}{\partial y} + \sum_i h_i\frac{\partial Y_i}{\partial y} \\ &= \bar{c}_p\frac{\partial T}{\partial y} + \sum_i h_i\frac{\partial Y_i}{\partial y}.\end{aligned} \tag{2.8}$$

Rearranging Eq. 2.8 yields

$$\bar{c}_p\frac{\partial T}{\partial y} = \frac{\partial h}{\partial y} - \sum_i h_i\frac{\partial Y_i}{\partial y}. \tag{2.9}$$

Direct substitution into Eq. 2.7 now gives

$$\begin{aligned}\frac{k}{\mu\bar{c}_p}\mu\bar{c}_p\frac{\partial T}{\partial y} &= \frac{k}{\mu\bar{c}_p}\mu\left(\frac{\partial h}{\partial y} - \sum_i h_i\frac{\partial Y_i}{\partial y}\right) \\ &= \frac{k}{\mu\bar{c}_p}\mu\frac{\partial h}{\partial y} - \frac{k}{\mu\bar{c}_p}\mu\sum_i h_i\frac{\partial Y_i}{\partial y} \\ &= \frac{\mu}{\mathrm{Pr}}\frac{\partial h}{\partial y} - \frac{\mu}{\mathrm{Pr}}\sum_i h_i\frac{\partial Y_i}{\partial y}.\end{aligned} \tag{2.10}$$

Eq. 2.10 is an alternate form of the gas conduction term which is expressed in terms of enthalpy. Here it is pointed out that the Prandtl number notation is used to convey the *frozen Prandtl number*,

$$\mathrm{Pr} = \mathrm{Pr}_{frozen} = \frac{k}{\mu\bar{c}_p}. \tag{2.11}$$

Let the mass diffusion flux be approximated by the Fick's Law form such that

$$\sum_{i}^{ngs} \mathbf{J}_i h_i = \sum_{i}^{ngs} \rho_g \sum_{j} D_{ij} \frac{\partial Y_i}{\partial y} h_i \tag{2.12}$$

where the species diffusion coefficient D_{ij} must be computed for each chemical species i into species j. Now combine the enthalpy based conduction term with the mass diffusion term to arrive at

$$\begin{aligned}
k\frac{\partial T}{\partial y} + \sum_i \rho \sum_j D_{ij} \frac{\partial Y_i}{\partial y} h_i = \\
\frac{\mu}{\mathrm{Pr}} \frac{\partial h}{\partial y} - \frac{\mu}{\mathrm{Pr}} \sum_i h_i \frac{\partial Y_i}{\partial y} + \sum_i \rho \sum_j D_{ij} \frac{\partial Y_i}{\partial y} h_i = \\
\frac{\mu}{\mathrm{Pr}} \frac{\partial h}{\partial y} + \frac{\mu}{\mathrm{Pr}} \left(- \sum_i \frac{\partial Y_i}{\partial y} h_i + \frac{\mathrm{Pr}}{\mu} \sum_i \rho \sum_j D_{ij} \frac{\partial Y_i}{\partial y} h_i \right) = \\
\frac{\mu}{\mathrm{Pr}} \frac{\partial h}{\partial y} + \frac{\mu}{\mathrm{Pr}} \left[\sum_i \left(\frac{\rho \sum_j D_{ij} \mu \bar{c}_p}{k\mu} - 1 \right) \frac{\partial Y_i}{\partial y} h_i \right] = \\
\frac{\mu}{\mathrm{Pr}} \frac{\partial h}{\partial y} + \frac{\mu}{\mathrm{Pr}} \left[\sum_i \left(\mathrm{Le}_i - 1 \right) \frac{\partial Y_i}{\partial y} h_i \right].
\end{aligned} \tag{2.13}$$

The species Lewis number is also taken to be frozen, such that

$$\mathrm{Le}_i = \mathrm{Le}_{i,frozen} = \frac{\rho \sum_j D_{ij} \bar{c}_p}{k}. \tag{2.14}$$

The frozen species Lewis number must be defined such that the summation over all species yields a frozen Lewis number of unity. This gives

$$\mathrm{Le}_{frozen} = \sum_i \mathrm{Le}_{i,frozen} = 1. \tag{2.15}$$

Combining this frozen Lewis number of unity assumption with the negligible viscous work term gives the final diffusive flux term of the energy equation for the reduced similarity form of the boundary layer equations.

To reduce the momentum equation it is only necessary to assume that the streamwise pressure gradient term is negigible in the advective fluxes.

$$\frac{\partial P_e}{\partial x} = 0 \tag{2.16}$$

Recall that the y-momentum equation is known from the boundary layer edge conditions.

Finally, treatment of the *species* mass diffusion equations is likely the most complicated. Spalding's (28) general formulation for reaching the reduced similarity boundary layer equations was based strictly on the *elemental* mass diffusion equations which contained no source terms. Recall that the inhomogeneous source term $\dot{\omega}$ refers to the creation or destruction of the conserved quantity. Elements are only subject to change through nuclear transformations which do not occur in hypersonic flows. Under this framework, it is simple to assume that the elemental diffusion coefficients are equal, thus allowing a reduction of the mass equations. However, it is noted by Lees (29) that further treatment is necessary for the *species* mass diffusion equations.

First, the species diffusion coefficients must be considered equal. The zeitgeist of research in the early hypersonic era was centered around graphitic materials in air, and air was typically assumed to be a binary mixture of atoms and molecules. This assumption lead to the adoption of the binary diffusion coefficient (D_{12}). However, the contemporary assumption must be that for any given species the diffusion coefficients must be the same, such that

$$D_{ij} = D_{ji} = D. \tag{2.17}$$

Further, consider the reaction of a carbon surface with atomic oxygen,

$$\mathrm{C} + \mathrm{O} \rightleftharpoons \mathrm{CO} \tag{2.18}$$

where C is the elemental carbon within the ablating surface, O is the atomic species present in the boundary layer, and carbon monoxide CO is the resulting product of the oxidation reaction. Then for this reaction, the production terms are given by

$$\dot{\omega}_{\mathrm{O}} = -\frac{M_O}{M_{CO}}\dot{\omega}_{CO} \tag{2.19}$$

and

$$\dot{\omega}_{\mathrm{C}} = -\frac{M_C}{M_{CO}}\dot{\omega}_{CO} \tag{2.20}$$

where M_i is the molecular weight of the i species. Equations 2.19 and 2.20 both state that the production of a given atomic species (*element*) may be related to the destruction of its product by the ratio of molecular weights. Based upon this observation, start from the mass species diffusion equation

$$\rho u\frac{\partial Y_{CO}}{\partial x}+\rho v\frac{\partial Y_{CO}}{\partial y}-\frac{\partial}{\partial y}\left(\rho D\frac{\partial Y_{CO}}{\partial y}\right)=\dot{\omega}_{CO} \tag{2.21}$$

and multiply it by the mass oxygen fraction giving

$$\frac{M_O}{M_{CO}}\rho u\frac{\partial Y_{CO}}{\partial x}+\frac{M_O}{M_{CO}}\rho v\frac{\partial Y_{CO}}{\partial y}-\frac{M_O}{M_{CO}}\frac{\partial}{\partial y}\left(\rho D\frac{\partial Y_{CO}}{\partial y}\right)=\frac{M_O}{M_{CO}}\dot{\omega}_{CO} \tag{2.22}$$

Now add Eq. 2.22 to the mass species diffusion equation for the atomic species oxygen

$$\rho u\frac{\partial Y_O}{\partial x}+\rho v\frac{\partial Y_O}{\partial y}-\frac{\partial}{\partial y}\left(\rho D\frac{\partial Y_O}{\partial y}\right)=\dot{\omega}_O \tag{2.23}$$

yielding

$$\begin{aligned}\rho u\frac{\partial Y_O}{\partial x}+\frac{M_O}{M_{CO}}\rho u\frac{\partial Y_{CO}}{\partial x}+\rho v\frac{\partial Y_O}{\partial y}+\frac{M_O}{M_{CO}}\rho v\frac{\partial Y_{CO}}{\partial y}-\\ \frac{\partial}{\partial y}\left(\rho D\frac{\partial Y_O}{\partial y}\right)-\frac{M_O}{M_{CO}}\frac{\partial}{\partial y}\left(\rho D\frac{\partial Y_{CO}}{\partial y}\right)=\dot{\omega}_O+\frac{M_O}{M_{CO}}\dot{\omega}_{CO}.\end{aligned} \tag{2.24}$$

Noting that

$$\dot{\omega}_O+\frac{M_O}{M_{CO}}\dot{\omega}_{CO}=0 \tag{2.25}$$

and defining a new variable

$$\tilde{Y}_O=Y_O+\frac{M_O}{M_{CO}}Y_{CO} \tag{2.26}$$

then Eq. 2.24 becomes

$$\rho u\frac{\partial \tilde{Y}_O}{\partial x}+\rho v\frac{\partial \tilde{Y}_O}{\partial y}-\frac{\partial}{\partial y}\left(\rho D\frac{\partial \tilde{Y}_O}{\partial y}\right)=0 \tag{2.27}$$

which is the homogeneous form of the mass species diffusion equation given in terms of *pseudo mass fraction*. Lees points out that this procedure is applicable to any number of chemical reactions. The significance between this mass equation and the enthalpy equation will be explored again later in the text.

Summarizing, the advective fluxes become

$$\mathcal{F}_{adv} = \begin{pmatrix} \rho_{g_1} u & \rho_{g_1} v \\ \vdots & \vdots \\ \rho_{g_{ngs}} u & \rho_{g_{ngs}} v \\ \rho_g u^2 & \rho_g v u \\ \rho_g u h & \rho_g v h \end{pmatrix} \tag{2.28}$$

and the diffusive fluxes become

$$\mathcal{F}_{diff} = \begin{pmatrix} 0 & -\rho D \frac{\tilde{Y}_i}{\partial y} \\ \vdots & \vdots \\ 0 & -\rho D \frac{\partial \tilde{Y}_{ngs}}{\partial y} \\ 0 & -\mu \frac{\partial u}{\partial y} \\ 0 & -\frac{\mu}{\mathrm{Pr}} \frac{\partial h}{\partial y} \end{pmatrix} \tag{2.29}$$

where the y-momentum equation has been excluded as it is fully defined by the boundary conditions and the source terms are given by

$$\mathbf{S} = \mathbf{0} \tag{2.30}$$

since each of the conserved equations is now homogeneous. Condensing to vector notation gives

$$\rho \mathbf{U} \cdot \nabla \Gamma - \nabla \cdot \Phi \nabla \Gamma = 0 \tag{2.31}$$

where $\rho\mathbf{U}$ is the mass flux vector, Γ is a conserved property, and Φ is a transport coefficient. The *self similar* (i.e. transformed) version of Eq. 2.31 may be found in the literature, such as given by Hartnett and Eckert (30) with varying Prandtl and Schmidt numbers. This is the same general formulation framework given by Spalding, only with the added assumption of pseudo mass fractions as the dependent mass variable. Spalding points out that the solution to Eq. 2.31, Γ, is linear in the limit as the mass flux at the boundary wall approaches zero. Under the assumption

of a constant transport coefficient,

$$\lim_{\rho\mathbf{U}\to 0}\left[\rho\mathbf{U}\cdot\nabla\Gamma-\nabla\cdot\Phi\nabla\Gamma\right]=0 \tag{2.32}$$

becomes

$$\Phi\nabla^2\Gamma=0. \tag{2.33}$$

Mathematically, this gives the proportionality

$$\left(\Phi\frac{\partial\Gamma}{\partial y}\right)_0\propto\left(\Gamma_e-\Gamma_w\right) \tag{2.34}$$

which he establishes in order to define the *mass-transfer conductance*

$$g=\frac{\left(\Phi\frac{\partial\Gamma}{\partial y}\right)_0}{\left(\Gamma_e-\Gamma_w\right)} \tag{2.35}$$

which is relevant for any conserved property under the given assumptions. It should be noted that the suffix 0 refers to the gas-surface interface, and the subscript notations e and w refer to the limits of integration being the boundary layer edge and wall, respectively. Most importantly, the form of Eq. 2.35 is the common form of transfer coefficients. At this point, it is crucial to account for the plethora of assumptions required to reach this point. The following assumptions (beyond the boundary layer equation assumptions) were required to reach the form of Eq. 2.31:

1. Species mass diffusion coefficients are equal.
2. Psuedo species mass fractions as dependent variable in mass equations.
3. Streamwise pressure gradient is negligible.
4. Lewis number is unity.
5. Work done by shear forces is zero (i.e. $\mathrm{Pr}=1$).
6. Mass flux approaches zero at the wall.

7. Constant transport coefficients.

Under the given framework, it is now possible to identify the mass-transfer conductances for each of the conserved quantities:

$$g_{m,i} = \frac{\rho D \frac{\partial \tilde{Y}_i}{\partial y}\Big|_0}{\tilde{Y}_{e,i} - \tilde{Y}_{w,i}} \tag{2.36}$$

$$g_u = \frac{\mu \frac{\partial u}{\partial y}\Big|_0}{u_e - u_w} \tag{2.37}$$

$$g_e = \frac{\frac{\mu}{\mathrm{Pr}} \frac{\partial h}{\partial y}\Big|_0}{h_e - h_w} \tag{2.38}$$

Equation 2.36 is the definition of the species mass transfer conductance, Eq. 2.37 is the momentum transfer conductance, and Eq. 2.38 is the energy transfer conductance.

Interestingly, the Spalding form of the governing equations is not the simplest reduction available. Indeed, the modern *film coefficient* methodology derives its name from a form of the boundary layer equations further reduced from the Spalding form. This is known as Film Theory.

2.2 Film Theory

According to Eckert and Drake, the term film coefficient originated in heat exchanger theory (31). In a heat exchanger, the temperature of the liquid is known and the temperature gradient is assumed to only exist in a finite distance from the wall (Δ). To simplify this further, the actual temperature gradient may be replaced by a linear approximation, as illustrated in Fig. 2.1 at a distance from the wall called the film thickness (Δ_F). Thus, the heat flow to the wall becomes

$$Q = \frac{k}{\Delta_F} A \left(T - T_w\right) \tag{2.39}$$

where k is the thermal conductivity. It is assumed for these applications that the thermal conductivity is a constant, such that the internal temperature of the fluid is

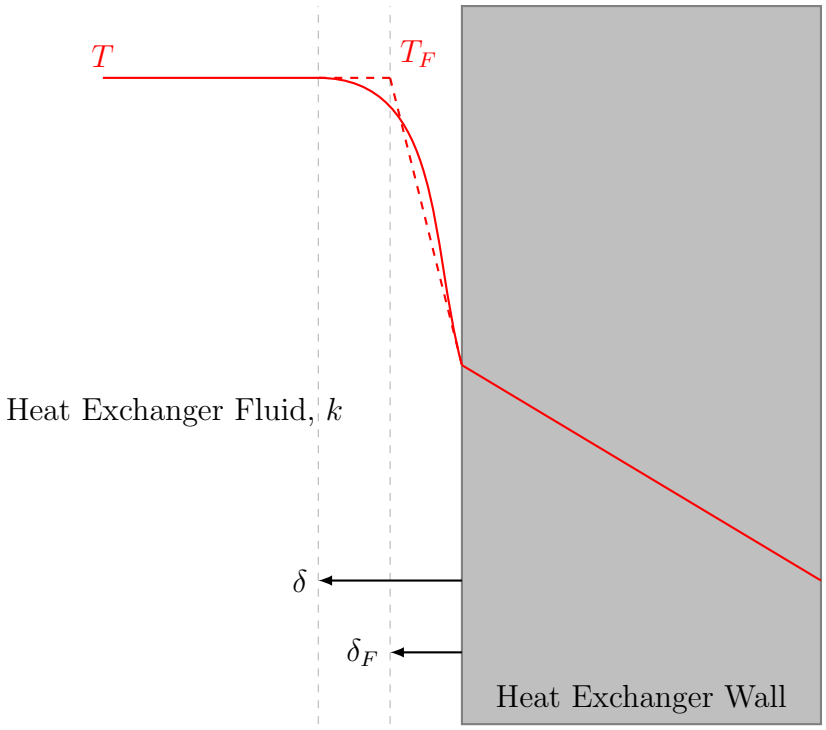

Figure 2.1: Film coefficient according to heat exchanger theory

also near constant. The customary practice in engineering, then became to compute the leading coefficient k/Δ_F as a single term, thus giving it the name film heat transfer coefficient.

In regard to aerothermodynamics, Mickley (32) provides a thorough description of the assumptions of film theory, and their relationship to the boundary layer equations. Conceptually, this requires that a film thickness be defined which is distinctly different than Prandtl's boundary layer (δ). As explained by Eckert and Drake, Mickley reiterates: *Film theory greatly simplifies the analytical treatment of a flow transport problem by means of an idealization which states that the transition between main-stream and wall conditions occurs entirely within a thin laminar film of thickness* Δ *lying immediately adjacent to the wall.* This film thickness is a differential distance normal to the surface (much thinner than the boundary layer). The concise assumptions which reduce the boundary layer equations to the film theory are:

1. Steady flow ($\frac{\partial}{\partial t} = 0$).

2. Laminar flow.

3. Flat to moderate curvature.

4. No-slip velocity.

5. Reasonably constant temperature and composition.

6. *Thin film* such that the mass flux in surface normal direction is constant.

7. The thin film is a constant film height.

8. Fluid density independent of streamwise coordinate.

9. No internal friction.

10. Constant transport coefficients: μ, k, D_{ij}.

11. Transport coefficients independent of body normal coordinate.

For the details of this reduction via application of the above assumptions see Appendix D. The boundary layer equations B.7- B.10 reduce to the follow system:

$$\mathcal{F}_{adv} = \begin{pmatrix} 0 & \rho_{g_i} v \\ \vdots & \vdots \\ 0 & \rho_{g_{ngs}} v \\ P_e & \rho_g v u \\ 0 & P \\ 0 & \rho_g v C_p \frac{\partial T}{\partial y} \end{pmatrix} \tag{2.40}$$

$$\mathcal{F}_{diff} = \begin{pmatrix} 0 & -\rho D \frac{Y_i}{\partial y} \\ \vdots & \vdots \\ 0 & -\rho D \frac{\partial Y_{ngs}}{\partial y} \\ 0 & -\mu \frac{\partial u}{\partial y} \\ 0 & -k \frac{\partial T}{\partial y} \end{pmatrix} \tag{2.41}$$

and

$$\mathbf{S} = \mathbf{0}. \tag{2.42}$$

Equations 2.40-2.42 represent the differential equations of film theory.

Note that all of the streamwise terms have been eliminated from the equation set except for the pressure gradient. Historically, these equations have been computed with favorable, unfavorable, and zero pressure gradients. With respect to understanding the models which comprise the contemporary film coefficient method, only the analysis of the zero pressure gradient is required. By neglecting the pressure gradient, the film theory reduced similarity form is reached. Following the sequence by Mickley, the final dimensionless similarity form is given by

$$\Gamma\left(\frac{d\beta}{dm}\right) = \frac{d^2\beta}{dm^2} \tag{2.43}$$

where β for the momentum, energy, and mass equations is given by

$$\beta_F = \frac{u}{u_e} \tag{2.44}$$

$$\beta_H = \frac{T_w - T}{T_w - u_e} \tag{2.45}$$

$$\beta_D = \frac{Y_{iw} - Y_i}{Y_{iw} - Y_{ie}}. \tag{2.46}$$

The algebraic details of the reduction are given in Appendix D. Note the relationship of the reduced equation set to Spalding's Eq. 2.31. First, because Lees' transformation of the mass dependent variable has not been applied, the mass equation is still in terms of the original mass fractions (Y_i). In the general formulation, the effect of chemical reactions is included in the mass variable transformation, whereas in film theory it is assumed away. Second, the mass flux in the streamwise advection term is zero in the film theory. By combining this observation with a zero pressure gradient, the system

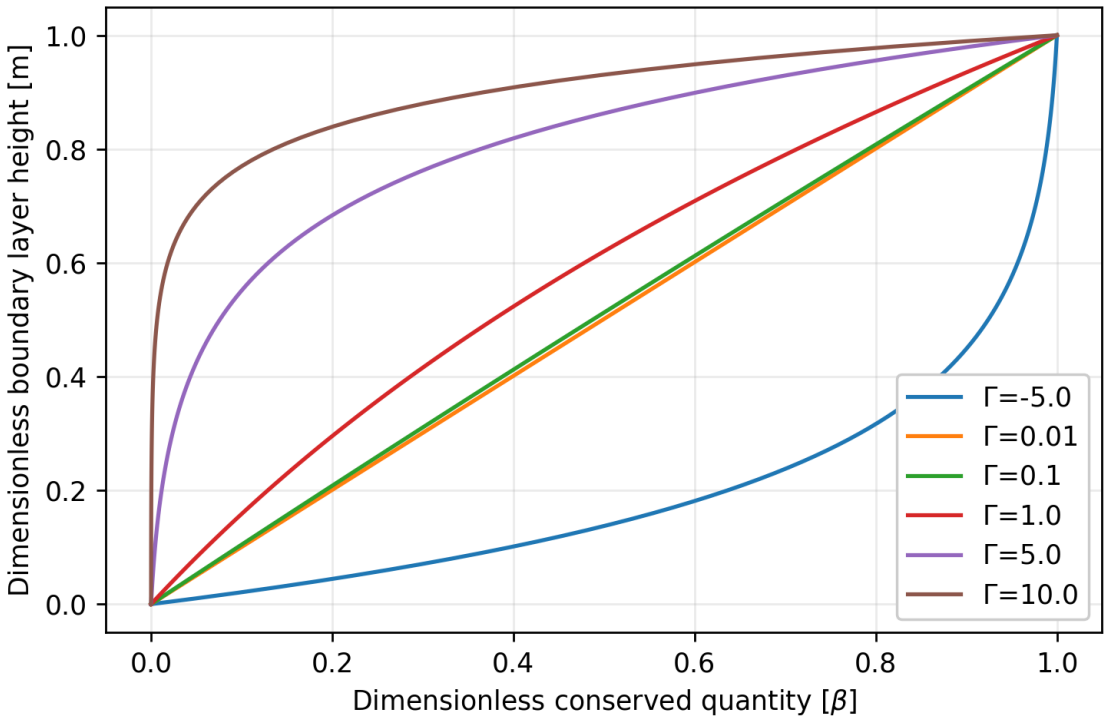

Figure 2.2: Variation of film theory profiles w.r.t. dimensionless mass transfer rate

becomes an ordinary differential equation system with a relatively simple analytical solution. The boundary conditions for these equations are now

$$\beta = 0, \qquad \text{when } m = 0 \tag{2.47}$$

$$\beta = 1, \qquad \text{when } m = 1 \tag{2.48}$$

where m is the dimensionless y-coordinate which maintains boundary layer edge properties and β is the dimensionless conserved variable. The solution to Eq. 2.43 is given by integration to be

$$\beta = \frac{e^{\Gamma m} - 1}{e^{\Gamma} - 1} \tag{2.49}$$

which yields the dimensionless velocity, temperature, and mass fraction profiles according to film theory.

Figure 2.2 demonstrates the behavior of Eq. 2.49 with various surface normal advection fluxes. The abscissa is the conserved quantity ($\beta = [Y_i, v, T]$) and the ordinate the dimensionless boundary layer height (m). The linear behavior described by Spalding occurs, as suggested, when the dimensionless mass transfer approaches zero. This is the same desired linear behavior described by Eckert and Drake concerning heat exchanger theory and illustrated in Fig. 2.1. As the mass transfer rate increases, the value of the conserved variable at the wall is reduced closer to the wall. The exact juxtaposition occurs for suction, where the dimensionless mass transfer is negative (blue line). This is the same result seen in classical studies of the Blasius/Falkner-Skan equations.

Another importantant result of the film theory is the so-called blowing correction. Equation 2.43 when differentiated with respect to m at the wall gives

$$\left(\frac{d\beta}{dm}\right)_w = \frac{\Gamma}{e^{\Gamma} - 1} \tag{2.50}$$

which introduces a relationship between the desired transfer coefficients and the mass transfer rate. Figure 2.3 shows that positive mass transfer reduces the associated gradient at the wall. This is the theoretical basis for the blowing correction used in contemporary material response codes. In the vicinity of zero mass transfer, the relationship is approximately linear and the reduction of the wall gradient actually slows as the mass transfer rate is increased. At extremely high mass transfer rates, the gradient can become zero, indicating that the fluid is no longer attached to the wall. In addition, the usual independent variable of the mass flux (Γ) may be alternatively defined as a blowing parameter, a convenient non-dimensionalized form of the mass flux normalized by the appropriate transfer coefficient.

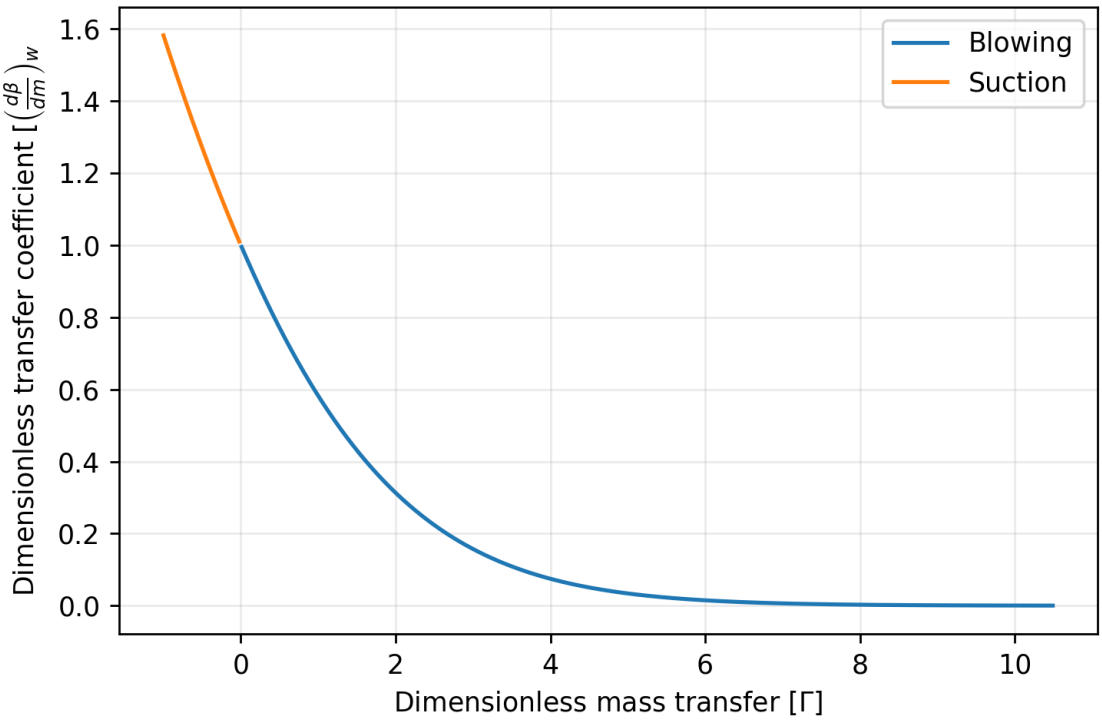

Figure 2.3: Transfer coefficients as a function of mass transfer rate

2.3 Transfer Coefficients and Blowing Parameters

The transfer coefficients are convenient non-dimensional quantities which emerge from the respective diffusive fluxes of the governing equations. Recall the diffusive transport terms of film theory:

$$\mathcal{F}_{diff} = \begin{pmatrix} -\rho D \frac{\partial Y_i}{\partial y} \\ -\mu \frac{\partial u}{\partial y} \\ -k \frac{\partial T}{\partial y} \end{pmatrix} \tag{2.51}$$

Now, take the ratio of the momentum diffusive transport term to the energy diffusive transport term. This yields

$$\frac{\dot{q}''}{\tau} = -\frac{k}{\mu} \frac{dT}{du} \frac{du}{dy} \left(\frac{du}{dy} \right)^{-1} \tag{2.52}$$

or simply

$$\frac{\dot{q}''}{\tau} = -\frac{k}{\mu} \frac{dT}{du}. \tag{2.53}$$

Next, integrating across the boundary layer gives

$$\frac{\dot{q}''}{\tau}\int_{u_w}^{u_e} du = -\frac{k}{\mu}\int_{T_w}^{T_e} dT \tag{2.54}$$

where the e subscript refers to the boundary layer edge and w refers to the wall. Under the thin film approximation (Mickley (32)), the ratio of the heat flux to the viscous transport, as well as the ratio of the thermal conductivity to the viscosity are constant. Directly integrating gives

$$\frac{\dot{q}''}{\tau}\left(u_e - u_w\right) = -\frac{k}{\mu}\left(T_e - T_w\right) \tag{2.55}$$

or under the no-slip boundary condition for the tangential component of the velocity

$$\frac{\dot{q}''}{\tau}u_e = -\frac{k}{\mu}\left(T_e - T_w\right). \tag{2.56}$$

Upon rearrangement

$$\frac{\dot{q}''}{\left(T_e - T_w\right)}\frac{\mu}{k} = \frac{\tau}{u_e} \tag{2.57}$$

the form of Spalding's transfer conductances appear. On the left is g_e and the right g_u, the energy and momentum transfer conductances. Next, recall the definition of the Prandtl number

$$\mathrm{Pr} = \frac{c_p\mu}{k} \tag{2.58}$$

and insert it into Eq. 2.57 giving

$$\frac{\dot{q}''}{\left(T_e - T_w\right)}\frac{\mathrm{Pr}}{c_p} = \frac{\tau}{u_e}. \tag{2.59}$$

Diving by the arbitrary $\rho_e u_e$ gives

$$\frac{\dot{q}''}{\rho_e u_e c_p\left(T_e - T_w\right)}\mathrm{Pr} = \frac{\tau}{\rho_e u_e^2}. \tag{2.60}$$

The resulting equation defines both the Stanton number and the skin friction coefficient:

$$\mathrm{C_H Pr} = \frac{\dot{q}''}{\rho_e u_e c_p\left(T_e - T_w\right)}\mathrm{Pr} = \frac{\tau}{\rho_e u_e^2} = \frac{\mathrm{C_f}}{2}. \tag{2.61}$$

To define the classical Reynolds' Analogy, let $\mathrm{Pr} = 1$. This important result relates the heat transfer coefficient (Stanton number, $\mathrm{C_H}$) to the momentum transfer coefficient (skin friction coefficient, $\mathrm{C_f}$). It also highlights that importance of the film theory framework, which allows the simplifications necessary to reach this form.

In an exactly analogous manner, the mass transfer coefficient may be reached. The species mass flux due to mass gradients may be given by Fick's Law

$$j_i = -\sum_j \rho D_{ij} \frac{\partial Y_i}{\partial y} \tag{2.62}$$

where the summation refers to all of the species j into which species i will diffuse. Dividing by the shear stress yields,

$$\frac{j_i}{\tau} = -\frac{\sum_j \rho D_{ij}}{\mu} \frac{dY_i}{du}. \tag{2.63}$$

Recall the definition of the Schmidt number for a species i is given by

$$\mathrm{Sc}_i = \frac{\mu}{\rho D_i}. \tag{2.64}$$

Integrating across the boundary layer height yields

$$\frac{j_i}{\tau} u_e = \frac{1}{\mathrm{Sc}_i} \left(Y_{i,e} - Y_{i,w} \right) \tag{2.65}$$

where the same no-slip boundary condition has been assumed. Rearranging and again arbitrarily dividing by the boundary layer edge mass flux, $\rho_e u_e$, gives

$$\frac{j_i}{\rho_e u_e \left(Y_{i,e} - Y_{i,w} \right)} = \frac{1}{\mathrm{Sc}_i} \frac{\tau}{\rho_e u_e^2}. \tag{2.66}$$

Equation 2.66 now becomes

$$\mathrm{C_{M_i}} = \frac{1}{\mathrm{Sc}_i} \frac{\mathrm{C_f}}{2}. \tag{2.67}$$

Upon inspection, Eqs. 2.61 and 2.67 are similar. The diffusion processes caused by thermal and mass gradients are both related to momentum transfer in the same manner under this set of assumptions, with a governing constant of proportionality being either the Prandtl number (for energy) or the Schmidt number (for mass).

Further, Eq. 2.61 may be inserted into 2.67 such that

$$\mathrm{C_H Pr} = \mathrm{C_M Sc}. \tag{2.68}$$

Rearranging gives

$$\frac{\mathrm{C_H}}{\mathrm{C_M}} = \frac{\mathrm{Sc}}{\mathrm{Pr}} = \mathrm{Le} \tag{2.69}$$

Based upon the assumptions introduced by film theory, Eq. 2.69 relates the heat transfer due to conduction and the mass transfer due to diffusion by a proportionality constant which is exactly the Lewis number. Recall that to reach the form of the governing equations which had solely conduction as the energy diffusive transport mechanism, the assumption was made that Le = 1. Inserting this identity into Eq. 2.69 gives

$$\mathrm{C_H} = \mathrm{C_M} \tag{2.70}$$

which states that the heat and mass transfer coefficients are the same and implies that the temperature or enthalpy boundary layers are similar to the concentration boundary layer. This is a *key feature of film theory* which is still adopted in contemporary design approaches.

The definition of the dimensionless transfer coefficients may be summarized by

$$\mathrm{C_M} = \sum_i \frac{j_i}{\rho_e u_e \left(Y_{i,e} - Y_{i,w}\right)} \tag{2.71}$$

$$\mathrm{C_f} = \frac{2\tau}{\rho_e u_e^2} \tag{2.72}$$

$$\mathrm{C_H} = \frac{\dot{q}''}{\rho_e u_e c_p \left(T_e - T_w\right)} \tag{2.73}$$

or

$$\mathrm{C_H} = \frac{\dot{q}''}{\rho_e u_e \left(h_e - h_w\right)} \tag{2.74}$$

Comparing Eqs. 2.71-2.74 to the transfer conductances of Spalding they vary only by the boundary layer edge mass flux, such that

$$g_i = \rho_e u_e C_i. \tag{2.75}$$

Under film theory, the advective flux is only present in the surface normal direction ($(\rho v)_w$) and is considered constant through the film. Thus, to non-dimensionalize this important parameter, the transfer conductances must be employed. This yields the blowing parameters

$$B_m = \frac{(\rho v)_w}{g_m} = \frac{(\rho v)_w}{\rho_e u_e \mathrm{C_M}} \tag{2.76}$$

$$B_u = \frac{(\rho v)_w}{g_u} = \frac{2\,(\rho v)_w}{\rho_e u_e \mathrm{C_f}} \tag{2.77}$$

$$B_e = \frac{(\rho v)_w}{g_e} = \frac{(\rho v)_w}{\rho_e u_e \mathrm{C_H}} \tag{2.78}$$

where again the subscripts m, u, and e stand for mass, momentum, and energy respectively. These blowing parameters provide a convenient non-dimensionalization which permits the solution of the surface mass balance equations, but also a basis for corrections due to a non-zero blowing. Since the linearity built into Spalding's transfer conductances is based on a mass flux approaching zero, these corrections are important to obtaining a reasonable solution.

2.4 Blowing Corrections

The most instrumental blowing correction in contemporary material response is the energy blowing correction. Therefore, in this section, it will be derived from the governing equations of film theory. It will be shown that the form of Eq. 2.50 may be reached using the previously defined blowing parameters.

The total enthalpy energy equation for the film theory is given by

$$\rho v \frac{dh_0}{dy} = \frac{d}{dy}\left(\frac{k}{\bar{c}_p}\frac{dh_0}{dy}\right). \tag{2.79}$$

where h_0 is the total enthalpy defined by $h_0 = h + V^2/2$ and $\bar{c}_p$ is the frozen specific heat. Introduce the definition

$$Y = \int_0^{\delta} \frac{\bar{c}_p}{k} dy \tag{2.80}$$

and the approximations

$$\rho v = (\rho v)_w \tag{2.81}$$

and

$$Y_\delta = Y_{\delta_0} \tag{2.82}$$

which are based on a thin, constant height film. Applying these definitions to Eq. 2.79 gives

$$(\rho v)_w \frac{dh_0}{dY} = \frac{d^2 h_0}{dY^2} \tag{2.83}$$

with boundary conditions

$$\begin{aligned} Y = 0, \qquad & u = 0 \\ Y = 0, \qquad & \frac{dh_0}{dY} = \dot{q}''_w \\ Y = Y_\delta, \qquad & h_0 = h_{0,e}. \end{aligned} \tag{2.84}$$

The solution to the non-zero mass transfer case then becomes

$$Y_\delta = \frac{1}{(\rho v)_w} \ln \left[\frac{\dot{q}''_w + (\rho v)_w h_{0,e}}{\dot{q}''_w} \right] \tag{2.85}$$

and the solution for the zero mass transfer case becomes

$$Y_{\delta_0} = \frac{h_{0,e}}{q_{w_0}}. \tag{2.86}$$

Equating the two expressions gives

$$\frac{(\rho v)_w h_{0,e}}{\dot{q}''_{w_0}} = \ln \left[\frac{\dot{q}''_w + (\rho v)_w h_{0,e}}{\dot{q}''_w} \right]. \tag{2.87}$$

The blowing augmentation for the energy equation requires the additional assumption of a cold wall, such that

$$h_{0,e} >> h_w \tag{2.88}$$

which makes the definition of the Stanton number (dimensionless energy transfer coefficient) become

$$\mathrm{C_H} = \frac{\dot{q}''_w}{\rho_e u_e h_{0,e}} \tag{2.89}$$

for the non-zero mass transfer case and

$$\mathrm{C_{H_0}} = \frac{\dot{q}''_{w0}}{\rho_e u_e h_{0,e}} \tag{2.90}$$

for the zero mass transfer case. Inserting the Stanton number definitions into Eq. 2.87 and simplifying gives

$$\frac{(\rho v)_w}{\rho_e u_e \mathrm{C_{H_0}}} = \ln\left[\frac{1 + \frac{(\rho v)_w}{\rho_e u_e \mathrm{C_H}}}{1}\right]. \tag{2.91}$$

Exponentiating and rearranging yields

$$\exp\left[\frac{(\rho v)_w}{\rho_e u_e \mathrm{C_{H_0}}}\right] - 1 = \frac{(\rho v)_w}{\rho_e u_e \mathrm{C_H}}. \tag{2.92}$$

Further rearranging gives

$$\mathrm{C_H} = \frac{\frac{(\rho v)_w}{\rho_e u_e}}{\exp\left[\frac{(\rho v)_w}{\rho_e u_e \mathrm{C_{H_0}}}\right] - 1} \tag{2.93}$$

and non-dimensionalizing by the zero mass transfer Stanton number gives

$$\frac{\mathrm{C_H}}{\mathrm{C_{H_0}}} = \frac{\frac{(\rho v)_w}{\rho_e u_e \mathrm{C_{H_0}}}}{\exp\left[\frac{(\rho v)_w}{\rho_e u_e \mathrm{C_{H_0}}}\right] - 1}. \tag{2.94}$$

Introducing the energy blowing parameters

$$B_e = \frac{(\rho v)_w}{\rho_e u_e \mathrm{C_{H_0}}} \tag{2.95}$$

gives

$$\frac{\mathrm{C_H}}{\mathrm{C_{H_0}}} = \frac{B_e}{\exp B_e - 1}. \tag{2.96}$$

It should come as no surprise that Eq. 2.96 comes in the same form as the film theory solution obtained in Eq. 2.50. It implies that a correction factor may be applied to the *unblown Stanton number* to account for the effects of blowing. In the next section, the theoretical foundation for modifying the film theory expression to account for hypersonic effects will be examined.

2.5 Recovery Factor

The velocity in a hypersonic flow generates an enormous amount of heat through viscous dissipation in the boundary layer. This may be considered the mechanical conversion of kinetic to thermal energy. The heat generated by viscous dissipation causes large temperature gradients in the gas, which in turn produces real gas effects, altering the characteristics of the flow.

To understand this effect of hypersonic flows, it is useful to employ a well known law that is relevant to low speed flows. Newton's Law of Cooling is given by the famous

$$\dot{q}'' = H\left(T_\infty - T_w\right) \tag{2.97}$$

where $\dot{q}''$ is the heat flux per area (W/cm^2), H is the heat transfer coefficient (W/cm^2/K), T_∞ is the freestream temperature (K), and T_w is the wall temperature (K). It states that the energy through a surface area per unit time is proportional to the temperature difference across the surface normal direction multiplied by a transfer coefficient.

The following illustrative example, expanded by the author from Eckert and Drake (31), shows the relationship between the solutions to the governing equations and Newton's low speed convective cooling equation. Consider Fig. 2.4 in a 2-dimensional coordinate system, where the x coordinate is in the direction of the flow and the y coordinate is perpendicular to the flow. The top plate (plate 1) is moved in the x-direction at a velocity u_1 while the bottom plate (plate 0) remains stationary. The conservation of momentum governing this flow is given by

$$\rho\frac{\partial u}{\partial t} + \rho u\frac{\partial u}{\partial x} + \rho v\frac{\partial u}{\partial y} = -\frac{\partial P}{\partial x} + \mu\left(\frac{\partial^2 u}{\partial x^2} + \frac{\partial^2 u}{\partial y^2}\right) + \rho\frac{\partial g}{\partial x} \tag{2.98}$$

where ρ is the density of the fluid, P is the pressure, g is the gravitational body force, and μ is the dynamic viscosity. Next, assume that the flow is steady, fully developed, and that gravity and pressure are both negligible. As well, assume that the flow is 1-dimensional, only moving in the x-direction, such that $v = 0$.

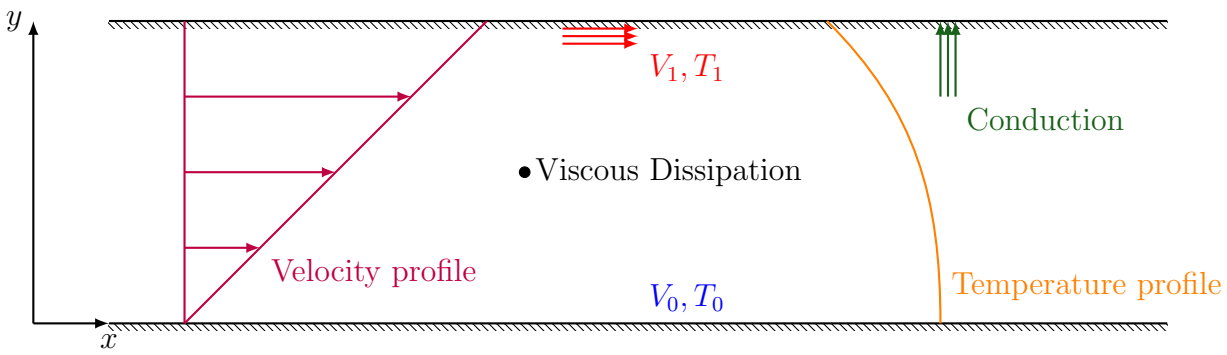

Figure 2.4: Hypersonic Couette flow

Under these circumstances the momentum equation becomes

$$\mu \frac{\partial^2 u}{\partial y^2} = 0 \tag{2.99}$$

which upon integration becomes

$$\frac{du}{dy} = c_1 \tag{2.100}$$

and

$$u = c_1 y + c_2 \tag{2.101}$$

where both c_1 and c_2 are constants of integration. Applying the boundary conditions

$$\begin{aligned} y = 0, \qquad & u = 0 \\ y = b, \qquad & u = u_1 \end{aligned} \tag{2.102}$$

gives

$$c_2 = 0 \tag{2.103}$$

and

$$c_1 = \frac{u_1}{b} \tag{2.104}$$

where b is the distance across the channel. This well known result is known as Couette flow and states that the velocity in the x-direction will be linear with respect to the distance across the channel (see Fig. 2.4).

$$u = \frac{u_1}{b} y \tag{2.105}$$

Next, consider the instance where the boundary conditions for the energy in the flow are given by

$$\begin{aligned} y = 0, \qquad & \tfrac{dT}{dt} = 0 \\ y = b, \qquad & T = T_1 \end{aligned} \tag{2.106}$$

where the stationary wall is adiabatic and the moving plate is being cooled to maintain a constant temperature, T_1. The work done by friction within the flow between a distance dy is given by

$$\frac{\partial}{\partial y}\left(u\mu\frac{\partial^2 u}{\partial y^2}\right)dy = \mu\left(\frac{\partial u}{\partial y}\right)^2 dy + u\mu\left(\frac{\partial^2 u}{\partial y^2}\right)dy \tag{2.107}$$

which has been expanded by the product rule. Recall that the second term of the RHS in Eq. 2.107 is zero and that $\left(\frac{\partial u}{\partial y}\right)^2 = \left(\frac{u_1}{b}\right)^2$. If the wall is adiabatic and the temperature assumed constant in the flow direction, then the energy must transfer toward the cooled plate by conduction. This gives the energy equation as

$$k\frac{\partial^2 T}{\partial y^2} + \mu\left(\frac{u_1}{b}\right)^2 = 0 \tag{2.108}$$

where k is the thermal conductivity of the fluid. Upon integrating, Eq. 2.108 becomes

$$\frac{\partial T}{\partial y} = -\frac{\mu}{2k}\left(\frac{u_1}{b}\right)^2 y + c_1 \tag{2.109}$$

and integrating again

$$T = -\frac{\mu}{2k}\left(\frac{u_1}{b}\right)^2 y^2 + c_1 y + c_2 \tag{2.110}$$

subject to the boundary conditions

$$\begin{aligned} y = 0, \qquad & \tfrac{\partial T}{\partial y} = 0 \\ y = b, \qquad & T = T_1. \end{aligned} \tag{2.111}$$

Since the first boundary condition reveals that $c_1 = 0$ and the second boundary condition yields

$$c_2 = T_1 + \frac{\mu}{2k}u_1^2 \tag{2.112}$$

Then Eq. 2.110 becomes

$$T = \frac{\mu u_1^2}{2k}\left(1 - \frac{y^2}{b^2}\right) + T_1 \tag{2.113}$$

or in terms of temperature difference

$$T - T_1 = \mathrm{Pr}\frac{u_1^2}{2c_p}\left(1 - \frac{y^2}{b^2}\right) \tag{2.114}$$

where $\mathrm{Pr} = \frac{\mu c_p}{k}$ is the Prandtl number and c_p the specific heat at constant pressure. Eckert states:

> The temperature which a surface assumes under the influence of internal friction is called *recovery temperature*.

Therefore, by Eckert's definition, at $y = 0$, Eq. 2.114 becomes

$$T_r - T_1 = \mathrm{Pr}\frac{u_1^2}{2c_p} \tag{2.115}$$

where T_r is the recovery temperature. If the temperature difference is made dimensionless, then it is called the *temperature recovery factor*. The recovery factor for Couette flow in the example, then is given by

$$r = \frac{T_r - T_1}{u_1^2/2c_p} = \mathrm{Pr}. \tag{2.116}$$

Now, continue the analysis by assuming the same situation but with prescribed temperatures at both plate 1 and plate 0. Then the boundary conditions for the problem become

$$\begin{aligned} y &= 0, \qquad T = T_0 \\ y &= b, \qquad T = T_1 \end{aligned} \tag{2.117}$$

where T_0 is the prescribed wall temperature. From the first boundary condition

$$T_0 = c_2, \tag{2.118}$$

and it follows that

$$c_1 = \frac{T_1 - T_0}{b} + \frac{\mu u_1^2}{2kb}. \tag{2.119}$$

If the heat flux into plate 0 is desired, then inserting Eq. 2.119 into Eq. 2.109 gives

$$\dot{q}''_w = k \left.\frac{\partial T}{\partial y}\right|_{y=0} = \frac{\mu u_1^2}{2b} + (T_1 - T_0)\frac{k}{b} \tag{2.120}$$

which becomes

$$\dot{q}''_w = \frac{k}{b}\left(\mathrm{Pr}\frac{u_1^2}{2c_p} + T_1 - T_0\right). \tag{2.121}$$

Now by substituting Eq. 2.116 into Eq. 2.121 the heat flux is given by

$$\dot{q}''_w = \frac{k}{b}(T_r - T_0) \tag{2.122}$$

which is the heat conduction through a semi-infinite slab with prescribed wall temperatures and no internal heat generation. This result implies that for high speed flow where the internal energy generation due to friction is large, *low speed convective heating laws may be applied with the caveat that the correct driving potential is used*. In this instance, the correct potential is the difference between recovery and wall temperatures. This idea of using low speed convective laws with appropriate driving potentials permeates throughout the literature and exists in engineering models in use today.

With this idea, Eckert and Drewitz (33) extend the recovery factor concept for high speed flows. Starting with the steady, laminar, boundary layer energy equation, following the original analysis by Pohlhausen (34),

$$u\frac{\partial T}{\partial x} + v\frac{\partial T}{\partial y} = \alpha\frac{\partial^2 T}{\partial y^2} + \frac{\mu}{\rho c_p}\left(\frac{\partial u}{\partial y}\right)^2 \tag{2.123}$$

where $\alpha = k/\rho c_p$ is the thermal diffusivity. Note that previously, *under film theory, the viscous dissipation term had been neglected.* Substituting the dimensionless temperature quantity

$$\theta_r = \frac{T - T_e}{V_e^2/2c_p} \tag{2.124}$$

into Eq. 2.123 yields

$$\frac{\partial^2 \theta_r}{\partial \eta^2} + \mathrm{Pr} f\left(\frac{\partial \theta_r}{\partial \eta}\right) + \frac{\mathrm{Pr}}{2}\left(\frac{\partial^2 f}{\partial \eta^2}\right)^2 = 0 \tag{2.125}$$

where f is the known Blasius solution of the momentum equation. The solution to Eq. 2.125 is given by the method of variation of parameters to be

$$\theta_r = \frac{\mathrm{Pr}}{2}\int_0^\infty \phi d\eta - \frac{\mathrm{Pr}}{2}\int_0^\eta \phi d\eta \tag{2.126}$$

where

$$\phi = \exp\left(-\mathrm{Pr}\int_0^\eta f d\eta\right)\left[\int_0^\eta \left(\frac{d^2 f}{d\eta^2}\right)^2 \exp\left(\mathrm{Pr}\int_0^\eta f d\eta\right) d\eta\right] \tag{2.127}$$

The value θ_r at the wall is precisely the recovery factor,

$$\theta_r(0) = \frac{\mathrm{Pr}}{2}\int_0^\infty \exp\left(-\mathrm{Pr}\int_0^\eta f d\eta\right)\left[\int_0^\eta \left(\frac{d^2 f}{d\eta^2}\right)^2 \exp\left(\mathrm{Pr}\int_0^\eta f d\eta\right) d\eta\right] d\eta. \tag{2.128}$$

Equation 2.128 is the definition of the recovery factor which was computed by Eckert (33) for the case of the flat plate over various flight conditions. Based upon the results of these computations, the curve-fitted value of the recovery factor is well fitted by

$$r \approx \mathrm{Pr}^{1/2}, \qquad 0.5 < \mathrm{Pr} < 5.0, \tag{2.129}$$

Turbulent boundary layers will be outside the scope of this document, but for completeness it is worth noting that the recovery factor is for these flows is typically taken as

$$r \approx \mathrm{Pr}^{1/3}, \qquad \mathrm{Pr} \approx 1. \tag{2.130}$$

Dorrance (35) provides an analytical treatment for both laminar and turbulent flows to reach precisely the same conclusions as the semi-empirical methods. Figure 2.5 is taken directly from Eckert's 1943 paper and shows the correlation between recovery factor and Prandtl number.

Based upon the previous observations, the *high velocity* convective heating may be computed with the low speed convection law, but with the *correct* driving potential. That is

$$\dot{q}'' = H\left(T_r - T_w\right) \tag{2.131}$$

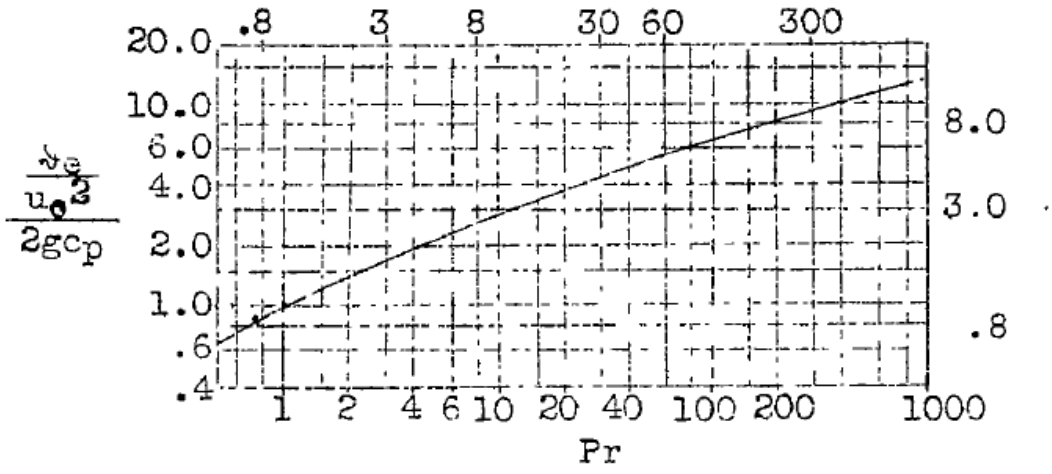

Figure 2.5: Data for Prandtl number derived recovery factor

where T_r is the recovery temperature given by

$$T_r = T_e + r\frac{V_e^2}{2c_p}. \tag{2.132}$$

In flows where the specific heat will vary considerably, as in the case of hypersonic flow, the c_p may no longer be considered constant. In this case, the correct driving potential uses the *recovery enthalpy*, defined by

$$h_r = h_e + r\frac{V_e^2}{2} \tag{2.133}$$

where h_e is the boundary layer edge static enthalpy, r is the dimensionless recovery factor, and V_e is the magnitude of the velocity. For hypersonic, strongly reacting flows, $h_r - h_w$ becomes the correct driving potential for estimation of convective heat transfer.

Note that this procedure for developing the correct driving potential did not use any assumptions not already present in the framework used to develop the leading coefficient term under the Spalding form or the film theory form of the governing equations. This includes constant thermal properties and unity similarity parameters (Le = Pr = Sc = 1). In fact, the reduced forms presented are ideal candidates for using the recovery factor concept strictly because they do ignore the viscous term

in the energy equation. In other words, the recovery enthalpy must be used when the underlying heat flux approximation did not account for viscous dissipation in the energy equation from which it was derived!

Furthermore, the Prandtl number definition of recovery factor is a curve-fit approximation to the numerical solutions of the non-dimensionalized energy equation with an adiabatic wall boundary condition (see Fig. 2.5). However, under it's strict definition see that

$$\begin{aligned} h_r &= h_e + r\frac{V_e^2}{2} \\ h_r &= h_e + \left(\frac{h_{aw} - h_e}{\frac{V_e^2}{2}}\right)\frac{V_e^2}{2} \\ h_r &= h_e + h_{aw} - h_e \\ h_r &= h_{aw}. \end{aligned} \tag{2.134}$$

This yields a more physical understanding of the recovery enthalpy. It states that the recovery enthalpy for a non-viscous derived heat flux correlation is the adiabatic wall enthalpy for when viscous dissipation is considered. Because an adiabatic wall boundary balances the viscous dissipation with the conduction in the fluid, the energy available at the wall will be that which remains from not being conducted through the boundary layer edge. In other words, the energy that is *recovered* from the total enthalpy. This makes itself evident in gases with Prandtl numbers less than unity, where the recovery factor simply reduces a portion of the kinetic contribution to the total energy content. A more succinct definition is given by van Oudheusden:

> ...the concept of *recovery* as the conversion of meanflow kinetic energy into thermal energy in the decelerated viscous flow.

This addresses only the contribution of viscous dissipation due to high velocity. What remains is to address the dynamic effects introduced by the temperatures and thermal gradients.

2.6 Reference Temperature Method

A very large portion of the boundary layer theory revolves around the transformations of the governing equations into partial non-linear ordinary differential equations. While these transformations are fundamental building blocks to understanding hypersonic theory, they are typically cast in a way that becomes confusing as to their original associated phenomena. For the purposes of this text, it need only be noted that an important parameter which arises from these transformations is the Chapman-Rubesin factor

$$C = \frac{\rho\mu}{\rho_e\mu_e} \tag{2.135}$$

which also appears as

$$C = \frac{\rho\mu}{\rho_w\mu_w} \tag{2.136}$$

due to Fay and Riddell. Figure 2.6 shows the computations of Fay and Riddell (36). The absicca is the non-dimensional enthalpy ratio $g = h/h_e$, and the ordinate a non-dimensional scale. The line starting at the top-left is the Chapman-Rubesin factor. The symbols in the figure are the equilibrium calculations made by the authors. This figure concisely demonstrates the need for variable coefficients in the boundary layer equations. The Chapman-Rubesin factor shows a variation of 80% over the specified enthalpy range. This observation, combined with the incorrect constant properties, could result in a large amount of error in the desired computation.

To compensate for this effect, but still allow a reasonable use of the developed flat plate theory, Rubesin and Johnson first offered the reference temperature method (37) which offers the solution of evaluating the properties of the flow at some average or *reference* temperature to compensate for high temperature effects. Typically, the literature will refer to Eckert as pioneering the use of the reference temperature correlation because his 1955 paper (38) provides a semi-empirical correlation based on the datasets at the time. While this is certainly true, and Eckert's correlation is

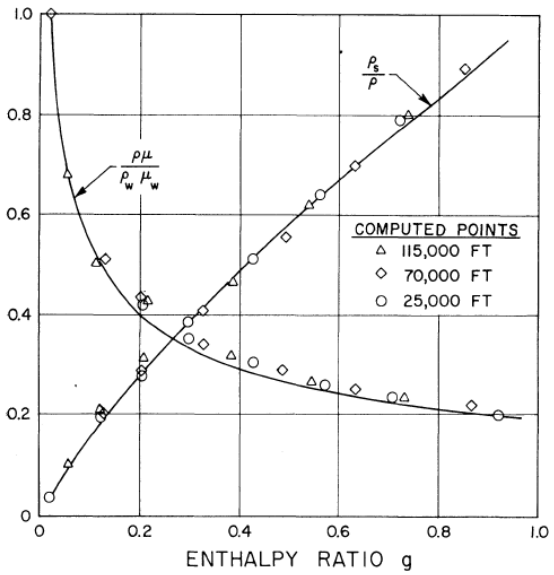

Figure 2.6: Variation of the Chapman-Rubesin factor computed by Fay-Riddell

widely used, it is useful to understand how the form of the relationship evolved from the underlying governing equations. To do so, examine the static enthalpy equation from the boundary layer equation set

$$\rho u \frac{\partial h_s}{\partial y} + \rho v \frac{\partial h_s}{\partial y} = \frac{\partial}{\partial y}\left(\frac{\mu}{\mathrm{Pr}}\frac{\partial h_s}{\partial y}\right) + \mu\left(\frac{\partial u}{\partial y}\right)^2. \tag{2.137}$$

If we do as Crocco and Busemann and assume that $h = h(u)$ then the relationship exists

$$\frac{\partial h_s}{\partial y} = \frac{\partial h_s}{\partial u}\frac{\partial u}{\partial y}. \tag{2.138}$$

Now inserting Eq. 2.138 into Eq. 2.137, assuming $\mathrm{Pr} = 1$ and the viscosity coefficient is constant, there yields

$$\rho u \frac{\partial h_s}{\partial u}\frac{\partial u}{\partial x} + \rho v \frac{\partial h_s}{\partial u}\frac{\partial u}{\partial y} = \frac{\partial}{\partial y}\left(\mu\frac{\partial h_s}{\partial u}\frac{\partial u}{\partial y}\right) + \mu\left(\frac{\partial u}{\partial y}\right)^2. \tag{2.139}$$

Expanding the first term on the RHS gives

$$\rho u \frac{\partial h_s}{\partial u}\frac{\partial u}{\partial x} + \rho v \frac{\partial h_s}{\partial u}\frac{\partial u}{\partial y} = \frac{\partial}{\partial y}\left(\mu\frac{\partial h_s}{\partial u}\right)\frac{\partial u}{\partial y} + \frac{\partial^2 u}{\partial y^2}\mu\frac{\partial h_s}{\partial u} + +\mu\left(\frac{\partial u}{\partial y}\right)^2. \tag{2.140}$$

Now moving the second term on the RHS to the LHS and commuting the enthalpy derivative with respect to velocity there is reached

$$\frac{\partial h_s}{\partial u}\left[\rho u\frac{\partial u}{\partial x}+\rho v\frac{\partial u}{\partial y}-\mu\frac{\partial^2 u}{\partial y^2}\right]=\frac{\partial}{\partial y}\left(\mu\frac{\partial h_s}{\partial u}\right)\frac{\partial u}{\partial y}+\mu\left(\frac{\partial u}{\partial y}\right)^2 \tag{2.141}$$

Immediately, it may be noticed, that the term within brackets is the simplified momentum equation with zero streamwise pressure gradient. Under this assumption, the LHS becomes exactly zero

$$0=\frac{\partial}{\partial y}\left(\mu\frac{\partial h_s}{\partial u}\right)\frac{\partial u}{\partial y}+\mu\left(\frac{\partial u}{\partial y}\right)^2. \tag{2.142}$$

Expanding the first term in the RHS gives

$$0=\frac{\partial}{\partial u}\frac{\partial u}{\partial y}\left(\mu\frac{\partial h_s}{\partial u}\right)\frac{\partial u}{\partial y}+\mu\left(\frac{\partial u}{\partial y}\right)^2 \tag{2.143}$$

which simplifies to

$$0=\frac{\partial^2 h_s}{\partial u^2}\mu\left(\frac{\partial u}{\partial y}\right)^2+\mu\left(\frac{\partial u}{\partial y}\right)^2 \tag{2.144}$$

or more simply

$$0=\left(\frac{\partial^2 h_s}{\partial u^2}+1\right)\mu\left(\frac{\partial u}{\partial y}\right)^2. \tag{2.145}$$

For the non-trivial solution to the above equation then,

$$\frac{\partial^2 h_s}{\partial u^2}=-1. \tag{2.146}$$

Upon integration, the expression becomes

$$h_s=-\frac{u^2}{2}+c_1u+c_2 \tag{2.147}$$

subject to boundary conditions at the vehicle wall and the boundary layer edge. The most obvious way to proceed is to assume a no-slip boundary condition at the wall such that $u_w=0$. Inserting into Eq. 2.147 gives

$$h_{s,w}=-\frac{u_w^2}{2}+c_1u_w+c_2 \tag{2.148}$$

or simply

$$h_w = c_2 \tag{2.149}$$

since the wall velocity vanishes and the total and static enthalpies are equal at the wall. Inserting the edge velocity then gives

$$h_{s,e} = -\frac{u_e^2}{2} + c_1 u_e + h_w \tag{2.150}$$

which undergoes further rearrangement to

$$\frac{h_{s,e} + \frac{u_e^2}{2} - h_w}{u_e} = c_1. \tag{2.151}$$

Inserting the constant of integration into the original expression then yields

$$h_s = -\frac{u^2}{2} + \left(h_{s,e} + \frac{u_e^2}{2} - h_w \right) \frac{u}{u_e} + h_w. \tag{2.152}$$

Finally, upon inserting the definition of total enthalpy, Crocco and Busemann's second integral is reached

$$h = (h_e - h_w) \frac{u}{u_e} + h_w. \tag{2.153}$$

From the form now given in Eq. 2.153 it is seen that under the assumption of Pr = 1 and zero pressure gradient, the *total* enthalpy is linear with respect to velocity through the boundary layer. This is a known result, but perhaps more interesting is rearranging the static enthalpy version of this integral, Eq. 2.152. Letting the specific heat be constant then gives

$$c_p T = -\frac{u^2}{2} + \left(c_p T_e + \frac{u_e^2}{2} - c_p T_w \right) \frac{u}{u_e} + c_p T_w. \tag{2.154}$$

Now dividing through by $c_p T_e$ yields

$$\frac{T}{T_e} = -\frac{u^2}{2 c_p T_e} + \left(\frac{T_e}{T_e} + \frac{u_e^2}{2 c_p T_e} - \frac{T_w}{T_e} \right) \frac{u}{u_e} + \frac{T_w}{T_e} \tag{2.155}$$

where the first two terms in the parenthesis are left unsimplified to illustrate the insertion of the total temperature definition.

$$\frac{T}{T_e} = -\frac{u^2}{2 c_p T_e} + \left(\frac{T_{o,e}}{T_e} - \frac{T_w}{T_e} \right) \frac{u}{u_e} + \frac{T_w}{T_e} \tag{2.156}$$

Now by assuming adiabatic flow and perfect gas there is inserted the Mach relation

$$\frac{T}{T_e} = -\frac{u^2}{2c_pT_e} + \left[\left(1 + \frac{\gamma - 1}{2}\mathrm{Ma}_e^2\right) - \frac{T_w}{T_e}\right]\frac{u}{u_e} + \frac{T_w}{T_e}. \tag{2.157}$$

Equation 2.157 may be further separated such that

$$\frac{T}{T_e} = -\frac{u^2}{2c_pT_e} + \left(1 + \frac{\gamma - 1}{2}\mathrm{Ma}_e^2\right)\frac{u}{u_e} + \left(1 - \frac{u}{u_e}\right)\frac{T_w}{T_e} \tag{2.158}$$

and continue rearranging terms to give

$$\frac{T}{T_e} = \left(\frac{u}{u_e} - \frac{u^2}{2c_pT_e}\right) + \left(\frac{\gamma - 1}{2}\mathrm{Ma}_e^2\right)\frac{u}{u_e} + \left(1 - \frac{u}{u_e}\right)\frac{T_w}{T_e} \tag{2.159}$$

At this point in the analysis, Eq. 2.159 bears the suitable form to understand where the forthcoming correlation emerges. The underlying assumption required is that u is some average value that represents the properties of the flow at elevated temperature and must be considered constant. For the purposes of this example, assume that $u = u_{avg} = 0.5u_e$. As well, since perfect gas relations have already been assumed, let the ratio of specific heats be $\gamma = 1.4$. Then Eq. 2.159 simplifies to

$$\frac{T}{T_e} = \left(0.5 - \frac{u_e^2}{8c_pT_e}\right) + 0.1\mathrm{Ma}_e^2 + 0.5\frac{T_w}{T_e} \tag{2.160}$$

or more generally

$$\frac{T}{T_e} = c_1 + c_2\mathrm{Ma}_e^2 + c_3\frac{T_w}{T_e}. \tag{2.161}$$

Equation 2.161 is the general form with variable coefficients which is used to correlate data by Eckert. It has been shown that the general form that the reference temperature takes is derived precisely from the boundary layer energy equation under a certain set of assumptions. However, it may be seen through the steps which were taken to arrive at such a form, that various groupings of the constants may allow the coefficients to vary.

Dorrance (35) provides a different analytical method of arriving at an *exact* reference temperature for the compressible laminar boundary layer which is contested by

Meador (39) as fortuitous. Never the less, Dorrance gives the reference temperature for a compressible laminar boundary layer as

$$\frac{T^*}{T_e} = 0.5 + 0.033M_e^2 + 0.5\frac{T_w}{T_e}. \tag{2.162}$$

Following the same line of analysis he arrives at

$$\frac{h^*}{h_e} = \frac{1}{2}\left(h_e + h_w\right) + 0.0833V_e^2 \tag{2.163}$$

for the reference enthalpy of an equilibrium air mixture. Eckert (38) gives

$$\frac{T^*}{T_e} = 0.5 + 0.038M_e^2 + 0.5\frac{T_w}{T_e} \tag{2.164}$$

and

$$\frac{h^*}{h_e} = \frac{1}{2}\left(h_e + h_w\right) + 0.0933V_e^2 \tag{2.165}$$

who cites heavily the work of Van Driest. Meador and Smart have provided an update as recently as 2005, which defines the reference enthalpy as

$$\frac{h^*}{h_e} = 0.45 + 0.16\sqrt{Pr^*}\left(\frac{\gamma - 1}{2}\right)\mathrm{Ma}_e^2 + 0.55\frac{h_w}{h_e} \tag{2.166}$$

and is grounded in the solutions of the boundary layer equations themselves, with no assumption on the wall enthalpy state.

The reference temperature/enthalpy method was originally used by Eckert to aid in correlating the skin friction and heat transfer results for compressible laminar flow over a flat plate. For the purposes of this text, it is used as an underlying assumption to define the Prandtl number, which is itself used to define the recovery factor. When utilizing a definition of the reference temperature or enthalpy (such as Meador-Smart) that depends on the recovery factor, then the equation becomes non-linear and subject to the relevant numerical iterative process for solution. For clarity, observe that the Meador-Smart equation becomes

$$0.45 + 0.16r(\mathrm{Pr}^*)\left(\frac{\gamma^* - 1}{2}\right)\mathrm{Ma}_e^{*^2} + 0.55\frac{h_w}{h_e} - \frac{h^*}{h_e} = 0 \tag{2.167}$$

where the solution for h^* is obtained in a single iteration, thus updating $r(\mathrm{Pr}^*)$ and the properties dependent upon the reference state, and permitting a solution based upon convergence criteria.

Chapter 3 Literature Review

This literature review considers relevant literature for solving the surface thermochemistry problem which couples the hypersonic flow field and thermal protection material computational domains.

3.1 Heritage Film Coefficient Model

The film coefficient model is first presented in NASA-CR-1064 (40, 41, 42, 43, 44, 45). A primary focus of the study is to enhance the fidelity of the solutions to the surface balance equations between a hypersonic chemically reacting compressible flow field and the decomposing ablative material. This is accomplished in one of two ways; a one-dimensional material response coupled to a chemically reacting, compressible boundary layer solver (the BLIMP program) and the same one-dimensional material response coupled to a film coefficient model of the boundary layer. The second is a *decoupled* approach which uses engineering correlations to produce static tables which permit economic calculation of the boundary layer state without actually computing the entire flow field. The process is as follows:

1. Compute as a function of time the mass transfer coefficient ($\rho_e u_e \mathrm{C_M}$), the pressure ($P_e = P_w$), and the relationship $\frac{\mathrm{C_M}}{\mathrm{C_H}} = \mathrm{Le}^{\gamma}$.

2. Insert the flat plate boundary layer approximation (remember elemental diffusion equation is homogeneous) into the elemental mass conservation equation as the mass diffusion flux. Rearrange the k^{th} elemental mass equations, assume chemical equilibrium, and tabulate functional relationships ($T_w, h_w, q_d = F(\dot{m}_c, \dot{m}_g, time)$).

3. Insert both engineering approximations for the fluid conduction and mass diffusion energy transport into the SEB. Allow the material response program to iteratively solve the SEB for the two independent variables (T_w and q_d) during solution run-time.

The first step is accomplished by crude engineering approximations and results in the input necessary to run the ACE/EST program, a surface thermochemistry solver. The method for acquiring the mass transfer coefficients and the pressure as a function of trajectory time is not explicitly detailed in the report. For contemporary purposes, the relationship between between the mass and heat transfer coefficients is almost always held as unity. However, this approach permits the flexibility to vary the scaling between mass and energy behavior throughout the trajectory.

The second step requires use of the elemental surface mass balance equation (eSMB)

$$-\left(\rho_w v_w\right)\tilde{Y}_{k,w} - \tilde{j}_{k,w} + \dot{m}_g \tilde{Y}_{k,g} + \dot{m}_c \tilde{Y}_{k,c} = 0 \tag{3.1}$$

where

$$\tilde{Y}_{k,j} = \sum_i \alpha_{ki} Y_{i,j} \tag{3.2}$$

is the mass fraction of element k and α_{ki} is the mass fraction of element k in chemical species i at the j^{th} state (such as the wall state, solid char state, etc). Further making the assumption that all elemental mass diffusion coefficients are equal, such

$$\rho_e u_e \mathrm{C}_{\mathrm{M}_i} = \rho_e u_e \mathrm{C}_{\mathrm{M}} \tag{3.3}$$

and inserting the flat-plate, incompressible, constant property relationship from boundary layer theory into Eq. 3.1 gives

$$-\left(\rho_w v_w\right)\tilde{Y}_{k,w} - \rho_e u_e \mathrm{C}_{\mathrm{M}} \left(\tilde{Y}_{k,e} - \tilde{Y}_{k,w}\right) + \dot{m}_g \tilde{Y}_{k,g} + \dot{m}_c \tilde{Y}_{k,c} = 0. \tag{3.4}$$

Next, define the dimensionless ablation terms to be the dimensionless pyrolysis gas flux

$$B'_g = \frac{\dot{m}_g}{\rho_e u_e \mathrm{C_M}}, \tag{3.5}$$

the dimensionless ablation flux

$$B'_c = \frac{\dot{m}_c}{\rho_e u_e \mathrm{C_M}}, \tag{3.6}$$

and the total dimensionless mass flux

$$B' = \frac{\dot{m}_g + \dot{m}_c}{\rho_e u_e \mathrm{C_M}}. \tag{3.7}$$

These B' (pronounced *Bee prime*) values were originally introduced by Lees (29) as non-dimensionalized parameters with the film coefficient ($\rho_e u_e \mathrm{C_H}$), where the prime notation designated them as the blowing parameters associated when mass transfer is present in the system. Normalizing by the mass transfer coefficient and rearranging yields

$$\tilde{Y}_{k,w} = \frac{B'_g \tilde{Y}_{k,g} + B'_c \tilde{Y}_{k,c} + \tilde{Y}_{k,e}}{1 + B'}. \tag{3.8}$$

By applying the known mass transfer coefficient and computing over a range of physical values for ablation and pyrolysis gas fluxes, coupled with the pressure, the relationship $T_w, h_w, q_d = F(\dot{m}_c, \dot{m}_g, time)$ may be tabulated for each time step. This is done external to the problem run-time.

For the fourth step, the convective heat flux is approximated by

$$q_{conv} \approx \rho_e u_e \mathrm{C_H} \left(h_r - h_w\right) + \rho_e u_e \mathrm{C_M} \left(\tilde{Y}_{k,e} - \tilde{Y}_{k,w}\right). \tag{3.9}$$

It is assumed that the same engineering correlations used to obtain the mass transfer coefficient as a function of time have also given crude approximations for the boundary layer edge state and chemical composition, to permit this evaluation. The fifth and final step uses a Newton method to iterate over the intial guess of an $\dot{m}_c$ value and the solid conduction term into the material.

3.2 Review of Computational Surface Thermochemistry

As early as 1994, Milos and Rasky (46) offer a milestone review of the contemporary efforts to accurately solve the surface balance equations for the strongly coupled hypersonic entry problem. The first relevant method described is deemed *Thermochemical ablation* by the authors, and this is the heritage methodology first developed by Aerotherm Corporation and described in the previous section (i.e. the heritage film coefficient methodology). In their description, the surface energy balance for a charring ablator is given to be

$$k_T \frac{\partial T}{\partial \eta} + k_v \frac{\partial T_v}{\partial \eta} + \sum_i^N \rho h_i D \frac{\partial Y_i}{\partial \eta} + q_r = \\ (1-\alpha)\, q_r + \sigma \epsilon T_w^4 + q_{cond} - \dot{m}_c'' h_c - \dot{m}_g'' h_g + \left(\dot{m}_c'' + \dot{m}_g''\right) h_w \tag{3.10}$$

where the terms on the LHS are the fluid conduction (contributions from both the translational and vibrational modes), the energy transported by mass diffusion, and the radiation heat flux. On the RHS, the first term is the absorptivity flux, the reradiation flux, the solid conduction into the vehicle, the flux due to surface (typically carbon) reactions, the flux carried by pyrolysis gas, and the advective flux generated by blowing on the fluid side of the boundary. Note that h_c is the solid char enthalpy, h_g is the pyrolysis gas enthalpy, and h_w is the enthalpy of the fluid at the wall temperature (assumed in local equilibrium). The film coefficient assumptions of equal species diffusion coefficients, equal heat and mass transfer coefficients, and the use of a boundary layer model blowing correction are all detailed.

As computational power increased, flowfield simulations for the boundary layer, viscous shock layer, partial Navier-Stokes and full Navier-Stokes all increased in complexity, allowing more physics models to be included in solutions. As an example, the BLIMPK code (47, 48) is a boundary layer code which includes ablation physics, a modern descendant from the boundary layer code described in NASA-CR-1064. It is noted that, at the time (1994) the current state-of-the-art is a full Navier-Stokes

simulation that includes full gas-phase kinetics and surface ablation modeling. As the authors state: *No CFD code currently handles the case of thermochemical ablation with or without surface reactions.*

As no fully-coupled CFD and MR simulation had yet to exist, the proposed solutions for advancing the state-of-the-art are semi-analytic methods. One method involves solving the heat integral balance along with the SEB and thermochemical ablation tables to create a transient thermal boundary condition that can be applied in a series of CFD simulations to account for heat conduction into the vehicle. The alternative proposed method is an approximate flow field boundary condition applied to material response. In this instance, the momentum energy integral technique solves the approximations of the boundary layer equations for the heat and mass transfer occurring at the surface. The main dependency is an accurate estimate of the pressure distribution obtained from inviscid flowfield solutions (which are much faster than including ablation physics). Both of these methods are still viable candidates for engineering design. However, it is noted that the HBI method, which most closely resembles the DHA method, still requires the use of thermochemical ablation tables for closure of the surface balance equations.

3.3 Diffusion coupling

As noted in NASA-CR-1064 documentation, an alternative approach to computing the gas-surface interaction for multicomponent chemically reacting boundary layers is to couple the flow field side to the surface/solid domain. In this body of work, this manner of coupling is coined *diffusion coupling* as its primary advantage is that it allows the calculation of the mass diffusion term to have an effect on the surface chemistry result.

In 2007, Bianchi (49) compared the film coefficient methodology to a diffusion coupled full Navier-Stokes solution for a graphitic flat plate. This was accomplished

by utilizing an iterative Newton method on the steady state surface energy balance (SSEB) and by assuming that the surface was in chemical equilibrium. The chosen flight condition was at $P_w = 1$ atm, $T_w = 4000$ K, and the typical freestream air mass fractions of $Y_{N_2} = 0.767$ and $Y_{O_2} = 0.233$. The agreement between the film coefficient method and the diffusion coupled method is found to be quite good, regardless of varying the Mach number between 2 and 6. There are two reasons this agreement appears. First, the flight condition is a high temperature and high pressure, which are favorable conditions for chemical equilibrium (the assumption underpinning the thermochemical ablation tables). Secondly, the geometry chosen is a flat plate. The boundary layer theory upon which the film coefficient is derived is based on approximations for flat plate geometry. Thus, the conditions chosen for comparison should be in very good agreement.

In 2011, de Muelenaere and Magin (7) formulated a stagnation line approximation of the Navier-Stokes equations to study the B' table formulation suggested by Kendall et al. The authors used as the material for comparison the phenolic-based carbon composites (see Chapter 6). The primary results presented are sensitivities of the B' tables, with respect to the species employed for equilibrium calculations, the thermochemical data source, and the diffusion and blowing approximations.

The authors found that between the physically realistic wall temperature range of 500-4000 K that the equilibrium calculations for a B' table were best represented by the following species: C, H, O, N, CH, CH_4, CO, CO_2, CN, C_2, C_2H, C_2H_2, C_3, C_4, C_5, HCN, H_2, H_2O, and N_2. They also found that by varying the data source for obtaining equilibrium constants that a large discrepancy in the sublimation (high temperature) regime of the B' table could be seen. This means for vehicles expecting sustained high wall temperatures that the choice of thermochemical tables may become an additional uncertainty in the analysis. Finally, a peripheral observation made by the authors is that by including homogeneous chemistry rates the effect on the wall state was not

significantly impacted. This is a re-iteration of a well known concept in boundary layer theory which posits that if the wall state is in chemical equilibrium it will be mostly insensitive to the homogeneous chemistry effects.

The result from this paper which is most relevant to the current work is the development of a stagnation line formulation of the Navier-Stokes equations which simulates a stagnation point boundary layer in a single dimension from the boundary layer edge to the vehicle wall. The governing equations are recast in primitive variables to permit the calculation of transport properties which are strong functions of temperature. The usual boundary layer transformation variables are avoided, but the boundary layer assumption of constant pressure through the surface normal direction, such that $P = P_e$ is constant, is maintained. The boundary conditions at the edge are given to be $\rho_{i,e}$, $\frac{du_e}{d\eta}$, $\frac{du_e}{dx}$, and T_e. The species densities at the boundary layer edge are computed from the state variables under a chemical equilibrium assumption.

The definition of the wall boundary conditions are critical. The wall normal blowing velocity is computed from the surface momentum balance such that

$$v_w = \frac{\dot{m}_c'' + \dot{m}_g''}{\rho_w}, \tag{3.11}$$

while the tangential velocity component is held at no slip conditions. The wall temperature is fixed for a given time step. Based upon this condition and $P_e = P_w$, the surface mass balance is solved where

$$Y_{k,w}\dot{m}_c'' = \frac{\dot{m}_g'' Y_{k,g} + \dot{m}_c'' Y_{k,c} - j_{k,w}}{\dot{m}_g'' + \dot{m}_c''} \tag{3.12}$$

the elemental mass diffusion flux is taken from the stagnation point solver as

$$j_{k,w} = \sum_i \nu_k^i \frac{M_k}{M_i} J_{i,w}. \tag{3.13}$$

As mentioned in the previous section, the surface mass balance requires a condensed phase chemical equilibrium solution for closure.

For clarity, the iteration procedure for obtaining the B'_c value, or dimensionless solid ablation rate, is repeated here. To begin, the stagnation line solver runs a cold wall case and computes the film coefficient as

$$\rho_e u_e \mathrm{C_H} = \frac{q''_w}{h_e - h_w} \tag{3.14}$$

remembering that for a stagnation point the kinetic portion of total enthalpy should be close to zero. Next, the authors employ the heat and mass transfer assumption

$$\rho_e u_e \mathrm{C_M} = \rho_e u_e \mathrm{C_H} \tag{3.15}$$

equating the transfer coefficients. The resulting mass transfer coefficient then scales a designated dimensionless pyrolysis gas flux through the relation,

$$\dot{m}''_g = \rho_e u_e \mathrm{C_H} B'_g, \tag{3.16}$$

yielding the dimensional pyrolysis gas flux. Taking the diffusional mass flux, $j_{k,w}$ directly from the stagnation point solver and using $\dot{m}''_g$ the SMB (Eq. 3.12) is solved for the dimensional ablation mass flux $\dot{m}''_c$ and the wall mass fractions. This, in turns, yields the wall normal velocity through the surface momentum balance (Eq. 3.11). The wall mass fractions and the wall normal velocity (primitive variables at the wall) are fed back to the stagnation point solver which holds the remaining primitive variable T_w constant, and the sub-iteration loop continues until the scaled form of the dimensionless ablation flux B'_c is acquired.

For the primary analysis, the equilibrium species were reduced to the following set: C, H, O, N, CO, CN, C_2, C_2H, C_3, H_2, and N_2. The heritage method of computing the dimenionless ablation flux B'_c was compared to the iterative stagnation point solver scheme. The pressure chosen was atmospheric. The range of temperatures were between 500-4000 K. It is unclear whether or not the blowing correction is added to the traditional B'_c calculation. It is also worth noting that due to the removal of carbon dioxide, there is no kinetically dominated area in the lower temperature regime. It

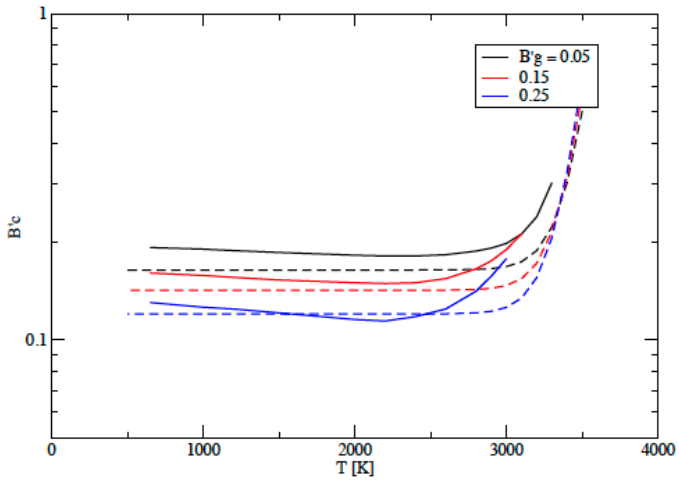

Figure 3.1: Comparison of diffusion coupled vs. transfer coefficient surface thermochemistry ablation tables: Reference (7)

would be interesting to see how these two approaches differ in the kinetically-limited area of the B' tables.

The heritage B' table shows an expected behavior, where beyond 3000 K the sublimation regime begins to asymptote. The stagnation point solver shows signs of asymptotic behavior at much lower temperatures than the heritage counter part. The heritage method plateaus and remains constant over the entire temperature range, varying in value only due to the pyrolysis gas injection. The higher blowing rates decrease the ablation, as the hydrogen present in the control volume at the gas-surface interface oxidizes faster than the carbon, thereby limiting carbon monoxide production. However, the stagnation point solver shows an important trend which contrasts this temperature independence. By introducing the mass diffusion flux, the constant mass diffusion coefficient value (per elemental equation) now varies according to element. Thus, a temperature dependent elemental presence is included in the calculation. This elemental variation in the SMB is directly reflected in the curvature of the produced stagnation point solver B' table. It would be interesting to see this variation in the B' tables explored further.

Keeping in mind that the iterative scheme in the stagnation point solver requires

that the heat and mass tranfer analogy and chemical equilibrium at the wall are still assumed, *this is important numerical evidence that coupling mass diffusion physics to the fluid flow field will change the wall state and in so doing, the desired boundary condition of the material response solver.*

Johnston (12) provides an instructive contemporary study of two of the film coefficient methodology assumptions. Based on the Orion multi-purpose crew vehicle (MPCV), whose chosen thermal protection system is Avcoat, he assesses both the blowing correction and the heat and mass transfer analogy in a systematic fashion. The MPCV is approximated by a 3.6 m radius sphere with the flight conditions being a freestream velocity of 6.0 km/s (Case 1) and 8.0 km/s (Case 2) and the freestream density 3.0×10^{-4} kg/m^3. The Avcoat material, whose char and pyrolysis gas elemental composition is required, is separated into 3 formulations (see Table 1 (12)), respectively A, B, and C. In addition, two body points are evaluated. The stagnation point at $s = 0.0$ m, and a downstream point located at $s = 2.0$ m. One additional permutation is a reduction of the pyrolysis gas blowing for case 1A. This results in a matrix of cases, as defined in the first column of Table 3.1.

The wall boundary conditions are given by first assuming a steady-state ablation at the wall to obtain a reasonable first approximation. This approach is similar to radiative equilibrium, except instead of neglecting the conduction into the vehicle, it approximates this term by assuming a steady recession rate has been achieved between the surface recession and the pyrolysis decomposition front.

Johnston computes 3 separate CFD simulations using the LAURA code; an *uncoupled* approach which is the contemporary form of the film coefficient engineering methodology, a *partially coupled* CFD solution which removes the blowing correction, and a *fully coupled* approach which removes the blowing correction and the heat and mass transfer analogy. The elemental mass flux is computed from the concentration gradients and diffusion coefficients within the CFD solution. Because of the removal

of this assumption, it is no longer possible to solve the elemental surface mass balance. Instead, Johnston uses a procedure developed by Gnoffo (50), which utilizes a transformation matrix on the elemental mass balance equations such that

$$F_{ij}\rho_j v - \dot{m}'' Y_{k,c} = F_{ij}\rho D_j \frac{\partial X_j}{\partial y}. \tag{3.17}$$

In Eq. 3.17, F_{ij} is the transformation matrix described in the paper, $Y_{k,a}$ is the elemental mass fraction of ablation products, D_j is the effective mass diffusion coefficient for species j, and X_j is the molar fraction of species j. Due to the transformation, the mostly species dependent mass equations may be solved under the assumption of chemical equilibrium. By adding the equation

$$\rho_w \frac{Y_{w,c}}{M_c} = K_{eq,C} \tag{3.18}$$

where $Y_{w,c}$ is the mass fraction of atomic carbon at the wall, M_c is the molecular weight of carbon, and $K_{eq,C}$ is the equilibrium constant for the heterogeneous sublimation reaction, in dimensions of kg·mol/m^3. Inclusion of this equation permits calculation of the solid ablation rate $\dot{m}''_c$ at the wall.

The significant aerothermal quantities of solid ablation flux ($\dot{m}''_c$) and convective heat flux (q''_{conv}) may be directly compared from these numerical experiments. They may be tabulated as non-dimensionalized percentages, such that

$$\Delta = \frac{x_{fullycoupled} - x_{uncoupled}}{x_{fullycoupled}} \times 100\% \tag{3.19}$$

where fully coupled is the equilibrium wall solution including computed diffusion and blowing and uncoupled is the film coefficient approach with both approximations. Johnston finds that the partially uncoupled simulations are out of family. This is because the two film coefficient approximations counteract one another and are meant to be incorporated together. In this regard, the partially uncoupled results are not re-stated here. The results relevant to this discussion are summarized in Table 3.1.

Case Description	$\Delta\dot{m}''_c$ %	$\Delta q''_{conv}$ %
1A, $s = 0$, laminar	-1.45	-7.14
1A, $s = 2$, laminar	0.71	-10.27
1B, $s = 0$, laminar	5.49	-4.79
1B, $s = 2$, laminar	7.17	-15.38
1C, $s = 0$, laminar	-3.53	-6.06
1C, $s = 2$, laminar	-1.45	-9.16
1A, $s = 0$, laminar, $0.33 \cdot \dot{m}''_g$	3.73	-10.34
1A, $s = 2$, laminar, $0.33 \cdot \dot{m}''_g$	4.98	-11.76
2A, $s = 0$, laminar	-1.32	-1.57
2A, $s = 2$, laminar	0.19	-3.94
2B, $s = 0$, laminar	2.99	-13.17
2B, $s = 2$, laminar	4.44	-13.18
2C, $s = 0$, laminar	-4.05	0.81
2C, $s = 2$, laminar	-3.12	-1.72

Table 3.1: Aerothermal quantities from film coefficient assumption study (12)

First, consider the convective heat flux predicted by the varying cases. In all but a single instance, the film coefficient predicts a higher convective heat flux, resulting in negative percentage values through the table. From a design perspective this may be a desirable effect, inferring that there is conservatism built into the film coefficient approximations. The one case that does not have a higher convective heat flux is within 1 percent of the fully coupled prediction. One following question would be, is whether or not this apparent conservative nature changes with respect to flight condition or the wall equilibrium assumption (or both).

Furthermore, the higher prediction of convective heat flux is consistently larger at the downstream location. In other words, the film coefficient approximations become *more* conservative at a downstream location, all other assumptions held constant. The approximations of *thin film* boundary layers may be less relevant to locations the further downstream they are, as the boundary layer thickens in the streamwise direction. While the convective heating is larger higher according to the film coefficient simulation, the ablation flux is increases with respect to the fully coupled

simulation. In other words, although the film coefficient simulation has a higher heat flux than the fully coupled, the difference between the two ablation fluxes decreases as a function of downstream distance. This may be consistently observed in each of the varying cases.

The numerical data suggests that the ablation rate is strongly dependent upon the elemental composition. Recall that both simulations use the chemical equilibrium assumption, and therefore the strong preference for one simulation against another must be entirely due to the diffusion mechanism or the scaling of the dimensionless ablation parameter (B'_c). Noticeably, Avcoat material B, whose elemental hydrogen is replaced by fractions of carbon and oxygen in the pyrolysis gas, shows a higher ablation flux in the fully coupled simulation. In both Avcoat materials A and C, the presence of hydrogen (a light element) is at or above 9%. Perhaps counterintuitively, this suggests that there is better agreement between the film coefficient and the fully coupled method when light elements are computed as part of the variable mass diffusion coefficients. This higher ablation rate also occurs when the surface of the fully coupled simulation experiences a comparatively lower convective heat flux than the film coefficient simulation.

Avcoat material A provides further insight into the comparative behavior of the approaches. At both the low and high velocity cases, the ablation fluxes for both methods are approximately within 2% of one another. But, if the pyrolysis blowing rate is artificially reduced by 33%, then the fully coupled simulation predicts a significantly higher amount of recession. This, against, must be attributable to the variability of the diffusion coefficients in the equilibrium calculation.

Avcoat material C shows a different behavior when comparing the models. This material includes a large amount of elemental hydrogen in the pyrolysis gas, and a simple char fraction of 100% carbon (excluding the difficult to handle silicon). For both flight cases, the film coefficient method predicts a higher ablation flux rate than

the fully coupled method. It is impossible to differentiate if this is solely due to the large presence of hydrogen or a combinatorial effect due to missing oxygen and silicon in the char elemental fractions.

Generally speaking, there is clearly a strong sensitivity to the chosen elemental mass fractions for equilibrium calculations. By altering these mass fractions, the mass loss rates vary between -4.05% and +7.17%. The film coefficient tends to predict higher convective heat fluxes, regardless of the variability in ablation rates. The range is found to be between -15.38% and +0.81%.

The two previous studies looked at variations in the film coefficient methodology assumptions. In the case of de Muelenaere, the mass diffusion flux was directly included in generating a B' table. In the case of Johnston, the blowing correction was tested, as well as the heat and mass transfer analogy. In both instances, a wall in chemical equilibrium underpins the results. In practice, this assumption is often used as the only efficient means of computing surface thermochemistry.

Candler (51, 52) provides a comparison of equilibrium and kinetic surface chemistry models. In his paper, an air-carbon system has been examined using both the heritage methodology of incorporating the saturated thermodynamic equilibrium assumption (B' model) and the non-equilibrium reaction mechanisms. A critical detail to mention, is that the B' model is coupled to the fluid dynamic simulation, such that mass diffusion and homogeneous reactions are included in the overall solution. This varies from the static B' tables generated under the film coefficient methodology, which are computed in isolation, and deployed in the material response.

A 10 cm, 8° sphere-cone geometry flying at a freestream velocity of 7 km/s at altitudes of 20, 25, 30, and 40 km is used for the study. These flight conditions cause a large extent of dissociation, while at the same time avoiding the complexity of ionization effects. A spatial thermal distribution is dictated, as opposed to solving the actual surface energy balance. Compared to the B' model is the kinetic ZA model (53)

with three different gas-phase models. The first gas phase model is due to Park (54, 55), the second is the Park model but with additional sublimation reactions, and the third is due to additional nitridation reactions identified by Martin and Boyd (56). The most relevant flight condition for a returning spacecraft would be the highest altitude case of 40km. Below this altitude, the vehicle should be moving significantly slower than the freestream velocity chosen. The peak surface temperature for this flight condition is chosen to be approximately 2700 K, which decays in the downstream direction.

At these flight conditions, the total surface mass flux is seen to be as much as 25% higher for the B' model than the ZA model at the stagnation point of the vehicle. This difference decreases downstream. It is irrespective of the gas phase model associated with the ZA kinetics.

Looking further at the species distribution that cause this discrepancy between models, it is seen that only CO_2 and CO are formed. The B' equilibrium model predicts nearly all of the associated surface mass flux due to CO diffusing away from the surface. The ZA model shows a mass flux of CO molecules *toward* the vehicle wall. This appears as a negative species mass flux. Contrastingly, the ZA model produces positive CO_2 species mass fluxes. This CO_2 production differs significantly depending on the homogeneous reactions considered. But when the B' model is utilized, there is no CO_2 production at all. The negative carbon monoxide fluxes reduce the total surface mass flux such that the ZA model predicts a lower surface ablation rate. As a function of downstream coordinate, only the areas close to the spherical cap are affected and oxidation effects are minimal (though non-zero in some cases) along the conical portion of the body.

Based on these observations, not only do the saturated equilibrium model and the kinetic models produce an appreciable difference in total surface mass fluxes, but they do so in a mechanistically different manner. The context of the current body of work

is to improve the numerical predictions of aerothermal modeling so that currently unmodeled phenomena are captured in that prediction. In light of the results of this paper, it may be seen that utilizing kinetic mechanisms at the surface can produce different characteristics of the CFD solutions, regardless of whether the macroscopic aerothermal quantities are quantitatively similar. Thus the question becomes whether or not CFD-based methods utilizing kinetic boundary conditions for vehicle design can still produce results similar to the heritage methods that have a long history of use.

3.4 Full coupling

In 1999, Olynick et al. (57) compute the coupled ablation modeling of the Stardust sample return capsule (SRC). Due to the high velocity entry and resulting peak heat flux, as well as the PICA heatshield TPS, a large number of relevant physics were modeled. The iteration process to construct an accurate boundary condition requires solving the surface balance equations by passing information between the CFD solver GIANTS and the MR solver, FIAT. It also included the effect of radiation within the flow field, due to the code NOVAR. The CFD passes heat flux, transfer coefficients, and pressure to FIAT to obtain enthalpy and B' values, which then solve a surface energy balance. The criteria for ending the iteration process then depends on the comparison of surface heat flux computed by the CFD against that produced by the MR solver. When within 5% of each other, the solution process marches to the next trajectory point of the simulation.

Perhaps the most impressive part of this study, is that it directly informed the aerothermal heatshield design sizing process for the Stardust vehicle. Importantly, this is due to the small size of the vehicle which also maintains a smooth body outer mold line. Quantitatively, it also demonstrated that for intense flight conditions, the ablation mechanisms present in surface thermochemistry could reduce the peak

heating up to 35%.

In 2001, Kuntz et al. (23) found considerable difficulty in coupling the surface balance equations for the surface thermochemistry problem. The iterative procedure set forth still represents a state-of-the-art methodology for computing the coupled problem. For the IRV analyzed, the largest difficulty, restated at the end of the paper, was in handling the film coefficient. The value of the film coefficient has in the denominator the recovery enthalpy and the wall enthalpy. The first chosen trajectory had relatively low velocities near the end of the flight, resulting in a singularity being produced as the wall enthalpy approached the same value as the recovery enthalpy. Kuntz notes that they circumvented this problem in two different ways. First, although not detailed rigorously, the authors state that they shifted the ablation model from the MR simulation to the CFD code. This is precisely the idea behind the DHA model. The second option that was available was to compute a different trajectory with a much higher impact velocity, such that the two enthalpies did not produce a singularity.

Martin and Boyd, 2009 (58), Nompelis and Candler, 2009 (59), Upadhyay et al., 2010 (60) all provide literature examples of loosely coupled CFD and MR simulations where the boundary condition to the CFD becomes a 1-dimensional material response solution. In the case of Martin and Boyd, a moving mesh algorithm is implemented presumably with a surface ablation model. Nompelis incorporates a fully-equilibrium flow field and the heritage film coefficient transfer coefficient model. Upadhyay offers a preliminary sensitivity analysis that shows that rate controlling parameters, as well as the species mass diffusion coefficients and virgin densities, are the primary drivers in a coupled surface thermochemistry problem.

Chen and Milos (61) chose to loosely couple the TITAN material response and DPLR CFD codes, maintaining the heritage film coefficient methodology as the boundary condition between the two solvers. The test bed for this coupling is an

arcjet experiment. In their work, the CFD provides the film coefficient and pressure distribution, passing it to TITAN which computes a time accurate MR simulation. It is interesting to see in their process that they prescribe a surface recession limit, presumably from knowledge of the arcjet experiments they are trying to replicate. When TITAN reaches this recession limit, it computes the shape change and passes this back to DPLR. DPLR's internal utility for shock adapting its grid is used through each iteration of this process. The results are shown to compare with previous implementations of this model using different codes. However, an important concept taken from this coupling is that shape change of the ablated material will signficantly affect the resulting aerothermal quantities evaluated at the surface. This is something that the new decoupled methodology cannot strictly address.

Furthermore, Weng and Martin (62) have taken an original approach that solves both domains at the same time. Both porous and conventional plain flow are modeled by interpolating between the region's local porosity, solid density, tortuosity, and permeability. The governing equations for both domains are tightly coupled by not only surface mass and energy balances, as per standard coupling schemes, but also by a surface momentum balance. This approach has been verified using analytical benchmark cases, and validated by comparison to flow tube experiments, but has not yet been implemented into vehicle design.

3.5 Molecular beam data models

The two most established heritage, kinetic carbon ablation models are due to Park (13) and Zhluktov and Abe (53). The Park model originated as an improvement on that given by Metzger (63), whose original model was derived from empirical data collected in electric arc facilities. Park compiled data from multiple experimental data sources over a broad range of carbon morphologies and offered new Arrhenius style rates for the oxidation mechanisms which would provide more conservative estimates of surface

recession in regimes applicable to hypersonic flight. While Park relied on numerical solutions to the boundary layer equations to determine integrated recession rates, Zhluktov and Abe applied a viscous shock layer (VSL) code to arrive at a suggested set of kinetic mechanisms. While the Park model only contains carbon monoxide, the Zhluktov-Abe (ZA) model contained 12 surface reactions which included additional species such as carbon dioxide and the sublimate C_3. Multiple authors have studied variations of these two models in attempts to match data, a primary example being the passive ablation nose-tip technology (PANT) experiment (64, 65).

Poovanthingal (66) et al. derived a finite-rate oxidation model from molecular beam experiments, with carbon as the system substrate. This new finite rate model is based on the physical competition between CO formation and O atom desorption. In their study, the Marschall and MacLean kinetic solver framework was used to implement their kinetic model into the US3D CFD code and subsequently compare it to the ZA-MacLean-mobile model. The flight vehicle and conditions were the exact same conditions as used by Candler. This is convenient because it allows a direct comparison between both numerical studies. See figures 10 (51) and 12 (66) of the respective papers.

The new molecular beam model shows a similar disagreement with the ZA model as the B' model. What is more interesting is the comparison between the B' model and the new model. The B' model predicts essentially no carbon dioxide at the stagnation point, continuing to about 1.5 non-dimensional surface units. At this location on the vehicle, a positive CO_2 flux is generated and remains fairly constant, suggesting that surface conditions have reached the lower temperature carbon dioxide plateau. The carbon monoxide mass flux in the B' model starts at approximately 0.28 $kg/m^2/s$ at the stagnation point and decreases until it reaches the critical location on the vehicle where CO_2 production begins. At this point, the CO mass flux becomes slightly negative and is fairly constant along the remainder of the vehicle body. This

indicates that CO is being consumed in the production of CO_2, hinting at an exchange reaction. In contrast, the new molecular beam model produces a CO flux closer to 0.25 kg/m^2/s. The lower carbon monoxide flux is possibly a result of the negative mass flux of atomic oxygen, suggesting that a considerable amount of O atoms are adsorbed to the surface. The presence of CO_2 is nowhere in the molecular beam model, which should occur through a surface exchange reaction with these adsorbed atoms does not seem to take place, and thus no CO_2 is observed.

Ongoing work from Prata et al. (67) is extending the molecular beam data to systems that involves nitrogen, and therefore also carbon nitridation. The theoretical kinetic rates developed match the molecular beam data, and limited data from inductively coupled plasma wind-tunnel facilities. Prata et al. show that CO is the dominant reaction product, with CO_2 only being a minor product. In addition, recombination of O to O_2 becomes negligible at moderate to high pressure conditions, while the N atom recombination is suggested to occur at a probability of approximately 0.1. With regards to CN, it was found to have a low reaction probability except for under low flux conditions. Perhaps most importantly, nearly all reaction products displayed non-Arrhenius behavior which was dependent not only upon surface temperature but also on surface coverage. This coincides with behavior described by Poovathingal. At this time, the current author wishes to incorporate these state-of-the-art methods in a CFD code and validate the models against a flight experiment. However, this research represents the framework which enables these new models to be implemented into an entire vehicle design process.

3.6 Concluding remarks for literature review

This brief survey of the literature cannot exhaustively cover all methods for coupling the hypersonic heating problem. Emphasis has been placed on key elements in the literature that offer insight into the fundamental problems associated with the film

coefficient engineering methodology assumptions.

Most of the literature coupling methods may be centered around the idea that one of the two domains becomes a boundary condition for the other. This idea was clearly stated by Milos and Rasky. Of the two, the most common seems to be utilizing the material response simulation as a boundary condition for the flow field solver. This may be the case since the flow field solver requires a smaller time step to resolve the relevant physics. However, nowhere in the literature has another approach been suggested that strictly *decouples* the two domains. An examination of diffusion coupling schemes highlights that this is possible with the state-of-the-art models currently available.

By coupling the diffusion processes of the flow field simulation to the construction of B' tables, the surface thermochemistry result qualitatively and quantitatively changes. The sensitivity study by Johnston showed that at considerable Mach number the film coefficient approach produced higher convective heat fluxes than a fully coupled simulation. Furthermore, the author showed this while holding the chemical equilibrium assumption constant, implying that the blowing correction, diffusion coupling, and the heat and mass transfer analogy were all a part of this effect.

Finite rate carbon oxidation models continue to increase in fidelity with data being imported from ongoing molecular beam experiments. Comparisons between equilibrium and finite rate mechanisms suggest that the surface and boundary layer species are quite different, even when total ablation fluxes may be quantitatively similar. This is a very important finding, as the species present at the wall determine the mass diffusion fluxes that can comprise a large percentage of the total wall heat flux.

The decoupled methodology presented in this work seeks to eliminate the deficiencies of the heritage film coefficient engineering model, which is currently the only identified decoupled engineering methodology which is capable of modeling ablation

physics. It will eliminate the use of the blowing correction model, the heat and mass transfer analogy, and the saturated chemical equilibrium model, all while maintaining a strictly decoupled approach.

Chapter 4 Methodologies

4.1 Film coefficient methodology

To the author's knowledge, a contemporary form of the film coefficient engineering methodology has not been outlined in the literature, to the degree that it would allow implementation in an engineering design program. At its simplest, the film coefficient engineering methodology states that the transfer of mass and energy across a gas-surface interface may be expressed as a function of a transfer coefficient and a driving potential. The origin of these ideas have been outlined in Chapters 2.1-2.3. What follows is the author's best attempt at including a detailed level of description which will permit implementation across industry.

Flow field calculations

The implementation of the film coefficient engineering model begins by computing the flow field of the vehicle for a given trajectory point. Throughout the body of this thesis, the CFD considered is laminar, fully viscous, two-temperature thermal non-equilibrium, and chemically reacting. The unblown, hypersonic film coefficient may be calculated at a given body point on the vehicle as

$$\rho_e u_e \mathrm{C}_{\mathrm{H}_0} = \frac{q_w^{\mathrm{CFD}}}{h_r^* - h_w} \tag{4.1}$$

where the superscript CFD refers to a value which is extracted from the CFD solution directly. The asterisk superscript $(*)$ refers to the recovery enthalpy being a model based on flat plate boundary layer theory which replaces the adiabatic wall enthalpy (see Chapters 2.5 and 2.6).

The quantity q_w^{CFD} may be acquired from the CFD surface energy balance which

may be stated as

$$q_w^{\text{CFD}} = \left[-k_w \frac{\partial T}{\partial y} - \sum_i j_i h_i + q_{\text{rad}} \right]_{\text{fluid}} = \left[q_{\text{cond}} \right]_{\text{solid}} + \left[\epsilon\sigma \left(T_w^4 - T_\infty^4 \right) \right]_{\text{surface}}. \quad (4.2)$$

The first term is the conduction from the fluid to the surface, the second term is the mass diffusion flux, and the third term is the radiation from the hot gas in the flow field to the surface. On the RHS, the first term is the solid conduction into the wall, and the second term is the reradiation from the surface to the far-field. When entry velocities remain below 9.5 km/s, Brandis and Johnston (9) note that radiation from the gas will not be a significant contributor. Additionally, the radiative equilibrium model assumes that the solid conduction into the vehicle wall is negligible. While this is not physically consistent, it has the advantage of closing the surface mass and energy balance equations such that they may be solved numerically, as opposed to dictating wall values. Combining these two observations, the surface energy balance, and therefore the wall heat flux from the CFD reduces to

$$q_w^{CFD} = \left[-k_w \frac{dT}{dy} - \sum_i j_i h_i \right]_{\text{fluid}} = \left[\epsilon\sigma \left(T_w^4 - T_\infty^4 \right) \right]_{\text{surface}} \quad (4.3)$$

where it must be noted that the conduction and the mass diffusion (both equal to the reradiation) are the physical components of the flux which get transferred through this relation. As well, the thermal conductivity, the species mass fluxes and enthalpies will all vary according to the models used in the CFD. To determine the mass diffusion flux, the surface mass balance (SMB) equation is needed. Under the film coefficient methodology this takes the form

$$\left[-j_i \right]_{\text{fluid}} = \left[M_i \dot{\omega}_i \right]_{\text{surface}} \quad (4.4)$$

where the $\dot{\omega}_i$ term is the production term of chemical species i. Notably, there is no advection term. The mass diffusion flux is frequently modeled using Fick's Law which sets it proportional to the species mass gradient. This requires an accurate way to compute the multi-component species diffusion coefficients, for example the

self consistent effective binary diffusion model (68) (SCEBD). The production term under the film coefficient methodology refers to the catalytic model chosen to predict the atomic recombination (and its exothermic release) at the vehicle wall, for example see Park (69) or Stewart (70). The solution of the $i+1$ equations formed by Eq. 4.3 and Eqs. 4.4 constitutes the boundary condition, coupled to the interior of the CFD solution by the surface normal gradients, which ultimately yields the heat flux in the film coefficient numerator.

The recovery enthalpy is described by

$$h_r = h_e + rV_e^2/2 \tag{4.5}$$

where h_e is the static enthalpy at the boundary layer edge and V_e is the magnitude of the velocity in the same location. The component r is the recovery factor (Chapter 2.5), computed by

$$r = \sqrt{\mathrm{Pr}^*}. \tag{4.6}$$

The reference Prandtl number (Pr^*) is computed at the reference state (Chapter 2.6). In practice, this may be accomplished by first computing the reference temperature (for example, Eq. 2.164). The reference temperature may then be used to compute the flow field properties with an equilibrium solver to obtain the specific heat, thermal conductivity, and viscosity which comprise the reference Prandtl number.

The wall enthalpy in Eq. 4.1 may be calculated as a function of chemical state, such that

$$\begin{aligned} h_w\,(\text{equilibrium}) &= F\left(T_w, P_w, X_k^\infty\right) \\ h_w\,(\text{non-equilibrium}) &= F\left(T_w, P_w, Y_i\right) \end{aligned} \tag{4.7}$$

where if a chemical equilibrium state is assumed it becomes a function of the state variables and the freestream elemental mole fractions. If chemical non-equilibrium is chosen, then the quantity is calculated as a function of the local state variables and mass composition within the CFD.

Material response calculations

For a carbon-based surface ablator, the surface energy balance computed by the material response solver is given by

$$q_{cond} = \left[q_{\text{aero}} - (\rho v)_w h_w\right]_{\text{fluid}} - \left[\epsilon\sigma\left(T_w^4 - T_\infty^4\right)\right]_{\text{surface}} + \left[\dot{m}_c'' h_c\right]_{\text{solid}} \tag{4.8}$$

where q_{cond} is the quantity of interest, the conduction flux into the vehicle. The aeroheating flux is the heat flux contributed to the SEB by the film coefficient model; it models the conduction from the fluid to the surface, the mass diffusion, the ablative species presence in the boundary layer, and advection. The second term is the advection contribution as computed in the material response due to chemical reactions at the surface. This term is negative as derived since it typically carries energy away from the wall. The third term is the reradiation of energy from the surface to the far-field. The final term is the ablation flux due to chemical reactions with the bulk phase (the TPS material).

The aeroheating flux may be defined as

$$q_{aero} = \rho_e u_e \mathrm{C}_{\mathrm{H}_0}\left(\frac{\mathrm{C}_{\mathrm{H}}}{\mathrm{C}_{\mathrm{H}_0}}\right)(h_r - h_w) = q_w^{\mathrm{CFD}}\left(\frac{\mathrm{C}_{\mathrm{H}}}{\mathrm{C}_{\mathrm{H}_0}}\right)\left[\frac{h_r - h_w^{\mathrm{MR}}}{h_r - h_w^{\mathrm{CFD}}}\right] \tag{4.9}$$

where two separate definitions have been given. The first definition is encountered frequently in practice, as it is often how the film coefficient model is applied from a thermal analyst perspective. From left to right it consists of the unblown film coefficient, the blowing correction, and the enthalpy potential. The recovery enthalpy is directly extracted from the CFD and the wall enthalpy is computed based on surface thermochemistry tables which relate the state variables and the mass composition at the wall. The second definition is the theoretical definition which helps illustrate how the film coefficient approximates the physics. In this formulation, the first term is the base heat flux, as extracted from the CFD. The second term is the blowing correction. The third term is an enthalpy ratio, where the enthalpy potential in the

denominator is from the CFD and the numerator is that computed in the material response. This immediately illustrates that the film coefficient model is composed of a proportionality constant and a linear correction. The proportionality constant is the blowing correction, for most physical problems being between 0 and 1. This term approximates the effect of advection on the estimated base heat flux. The second term is the enthalpy correction term, which not only approximates the variation in energy state due to the presence of ablating species (which are not present in the film coefficient CFD), but also the difference in wall temperature.

The second term in both definitions is the blowing correction. This takes the form

$$\frac{\mathrm{C_H}}{\mathrm{C_{H_0}}} = \frac{2\lambda B'}{\exp\left(2\lambda B'\right) - 1} \tag{4.10}$$

which varies from the thin film derived form presented in Chapter 2.4 in two ways. First, the blowing parameter used is the B' parameter, where the prime notation given by Lees (29) is used. This implies that the denominator of the blowing parameter is taken to be the *blown* film or mass transfer coefficient. Secondly, the factor 2λ appears in front of the blowing parameter, which refers to an empirical best fit of data based on flow state. For the relative flow state then

$$\begin{aligned} \lambda &= 0.4, \qquad \text{turbulent}, \\ \lambda &= 0.5, \qquad \text{laminar}. \end{aligned} \tag{4.11}$$

The only undescribed enthalpy in the aeroheating term is the wall enthalpy evaluated during the run-time of the material response solver. This is the wall enthalpy appearing in the numerator of the second definition. Unlike the wall enthalpy in the denominator, which consists of gas phase species only, this wall enthalpy represents the chemical equilibrium mass composition given by solving the multi-phase equilibrium problem, which includes gas-surface interactions. Thus, for example, the presence of carbon monoxide (or any of other various ablative species) will express their effect on the wall energy state through this term. This term will also relate the

change in energy state from the CFD, which was computed at a given wall temperature, with the wall temperature of the material response.

To close the boundary condition equation set, the surface mass balance equations must be utilized in a manner similar to the heritage method (Chapter 3.1). The total mass balance for a surface ablator is given by

$$(\rho v)_w = \dot{m}'' = \dot{m}_c'' \tag{4.12}$$

since the diffusion term vanishes when summed over all species. The elemental surface mass balance gives

$$j_k + (\rho v)_w Y_{k,w} = \dot{m}_c'' Y_{k,c} \tag{4.13}$$

where j_k refers to the elemental mass diffusion flux, and $Y_{k,w}$ refers to the mass fraction of a given element k at either the gaseous state at the wall (w) or the carbon surface (c). Under the approximations (Chapters 2.1, 2.2, 2.3) of equal species mass diffusion coefficients and Le = 1, then from boundary layer analysis the elemental mass diffusion flux may take the form

$$j_k \approx \rho_e u_e \mathrm{C_M} \left(Y_{k,w} - Y_{k,e}\right) \tag{4.14}$$

noting that the elemental equations are homogeneous. The leading coefficient $\rho_e u_e \mathrm{C_M}$ is the mass transfer coefficient, while the subscripts w and e refer to the vehicle wall and the boundary layer edge, respectively. Nonequal diffusion coefficients have also been explored which replace the mass fractions presented in Eq. 4.14 by so-called *diffusion driving forces* (41). These potentials are based on empirical factors that depend on the binary diffusion coefficients between two elements and temperature. However, this approach is not considered in this work.

Inserting Eq. 4.14 into Eq. 4.13 and dividing through yields

$$\left(Y_{k_w} - Y_{k_e}\right) + \frac{(\rho v)_w}{\rho_e u_e \mathrm{C_M}} Y_{k_w} = \frac{\dot{m}_c''}{\rho_e u_e \mathrm{C_M}} Y_{k_c} \tag{4.15}$$

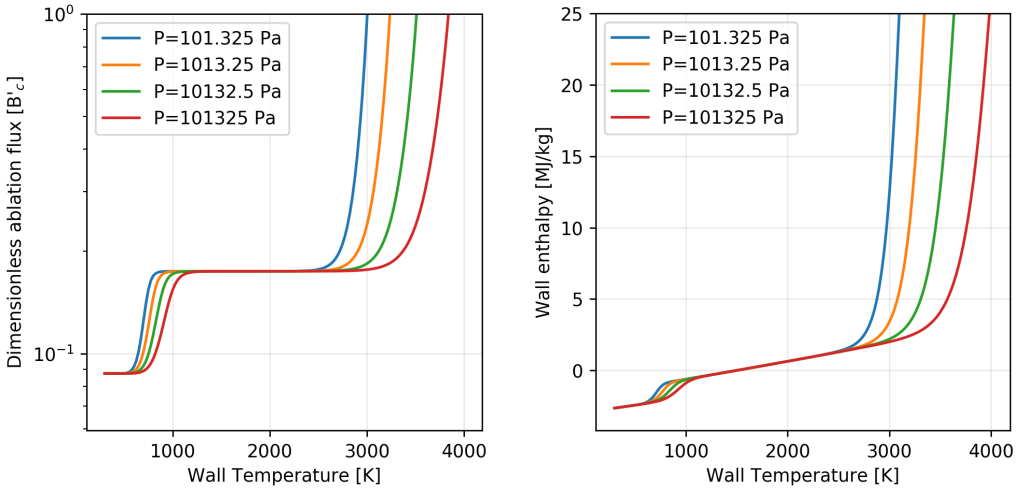

(a) Dimensionless ablation flux

(b) Wall enthalpy

Figure 4.1: Standard carbon-air surface thermochemistry tables

which by noting that in the absence of pyrolysis gas blowing that

$$B' = \frac{(\rho v)_w}{\rho_e u_e \mathrm{C_M}} = \frac{\dot{m}_c''}{\rho_e u_e \mathrm{C_M}} = B_c' \tag{4.16}$$

further reduces to

$$(Y_{k_w} - Y_{k_e}) + B' Y_{k_w} = B_c' Y_{k_c}. \tag{4.17}$$

Upon rearrangement there yields

$$B_c' = \frac{Y_{k_e} - Y_{k_w}}{Y_{k_w} - Y_{k_c}} = \frac{1}{1 - Y_{C_w}} \tag{4.18}$$

where it is assumed that the carbon elemental presence is zero ($Y_{C_e} = 0$) at the boundary layer edge and the carbon fraction in the bulk phase is unity ($Y_{C_c} = 1$). The system of equations for k elements may then be solved by numerical iteration for the wall composition, which in turn yields the dimensionless ablation flux (B_c') and the wall enthaly (h_w). There are numerous schemes for solving the equilibrium composition (though fewer for the multi-phase problem) and the reader is referred to Smith and Missen (71) for details. The dimensionless ablation flux and wall enthalpy values for a carbon-air multi-phase system are shown in Figs. 4.1(a) and 4.1(b). The

physical mechanisms which determine the qualitative nature of the thermochemistry tables are discussed in the succeeding analysis.

With both parameters now defined as tabulated functions of the state variables (and the dimensionless pyrolysis blowing rate in the case of a decomposing ablator), the only remaining relation required for closure of the boundary condition equation set is the *mass/heat transfer analogy*.

$$\rho_e u_e \mathrm{C_M} \approx \rho_e u_e \mathrm{C_{H_0}} \left(\frac{\mathrm{C_H}}{\mathrm{C_{H_0}}} \right) \tag{4.19}$$

The theory behind making this assumption has been derived in Chapter 2.3, however the scrupulous reader will note that the blowing correction has been added to Eq. 4.19. This equates the mass transfer coefficient to the blown film coefficient (corrected for advection). With this relation, the solid ablation flux may be immediately written

$$\dot{m}_c'' = \rho_e u_e \mathrm{C_M} B_c' \approx \rho_e u_e \mathrm{C_{H_0}} \left(\frac{\mathrm{C_H}}{\mathrm{C_{H_0}}} \right) B_c' \tag{4.20}$$

This closes the system of equations comprising the boundary conditions for the film coefficient engineering method. For an extended discussion on the two definitions of the aeroheating boundary condition, see Appendix F.

4.2 Direct heating and ablation methodology

Flow field calculations

The Direct Heating and Ablation (DHA) method translates information about the convective heat and mass transfer from the CFD *directly* to the material response. Contrary to the film coefficient method, which computes only the convective heat transfer from air species on the CFD side, under the DHA method, the vehicle's TPS now introduces surface ablation species through the use of a kinetic reaction mechanism framework (such as that developed by Marschall-Maclean (72), (73)).

The surface energy balance in the CFD, for the DHA method, then becomes

$$q_w^{\text{CFD}} = \left[-k\frac{dT}{dy} - \sum_i j_i h_i - (\rho v)_w h_w \right]_{\text{fluid}} = \left[\epsilon\sigma \left(T_w^4 - T_\infty^4 \right) \right]_{\text{surface}} \tag{4.21}$$

noting that a negatively signed conduction term increases energy at the surface (same case for mass diffusion) and is comprised of both contributions from the two-temperature model. Both the fluid conduction and the mass diffusion terms, while identical in form as the film coefficient SEB, are now calculated with ablative species present in the fluid mixture directly adjacent to the wall. This can change the mixture thermal conductivity, density, species mass diffusion coefficients, and the mass gradients. Furthermore, the advection term is now present in the calculation of the CFD-based wall heat flux, which means that no blowing correction model must be implemented. To close the CFD boundary condition equation set, the species surface mass balance is required.

$$\left[-\rho D_i \frac{\partial Y_i}{\partial y}\bigg|_w + (\rho v)_w Y_{i,w} \right]_{\text{fluid}} = \left[M_i \dot{\omega}_i \right]_{\text{surface}} \tag{4.22}$$

On the LHS of Eq. 4.22 is the mass diffusion flux due to species i and the species advection flux. On the RHS is the production term. This differs from the film coefficient model where the production term describes the catalytic model. In the DHA framework, this includes any kinetic reactions which may or may not include catalytic recombination. The production term takes the form

$$\dot{\omega}_i = \sum_k \dot{\omega}_{i,k} = \sum_k \Omega_{ns} v_{i,k} \left[k_{f,k} \prod_{i=1}^{K} X_i^{v'_{i,k}} - k_{b,k} \prod_{i=1}^{K} X_i^{v''_{i,k}} \right] \tag{4.23}$$

where the subscript i refers to chemical species and the subscript k refers to a given chemical reaction which occurs at the gas-surface interface. The Ω_{ns} term is the surface phas fraction, which takes a value between 0 and 1. The $v'_{i,k}$ and $v''_{i,k}$ terms are the reactant and product stoichiometric coefficient for species i in reaction k. The X_i terms are the molar concentrations, which may vary in unit depending upon which phase species i is in. The $k_{f,k}$ and $k_{b,k}$ are the forward and backward rate coefficients

which take various forms according to the defined reaction. The current work uses the model set forth by Marschall and Maclean (72, 73). From the production rates, the solid ablation flux may be directly obtained.

$$\dot{m}_c'' = -\sum_{nb=1}^{N_b}\sum_{i=1}^{I} M_i\dot{\omega}_i \tag{4.24}$$

Summation over all species and rearrangement yields the surface normal velocity

$$v_w = \frac{1}{\rho}\sum_i M_i\dot{\omega}_i. \tag{4.25}$$

Equations 4.21, 4.22, and 4.25 constitute the boundary conditions for the DHA CFD. From a single CFD solution, the quantities of interested may be obtained as

$$\begin{aligned} \dot{m}_c'' &= F\left(t, T_w, \mathbf{x}\right) \\ q_w^{\mathrm{CFD}} &= F\left(t, T_w, \mathbf{x}\right) \\ P_w &= F\left(t, T_w, \mathbf{x}\right) \end{aligned} \tag{4.26}$$

which are extracted directly from the CFD solution. In other words, for a given body point in physical space ($\mathbf{x}$), the solid ablation flux ($\dot{m}_c''$), the wall heat flux (q_w^{CFD}), and the pressure at the wall (P_w) are tabulated as a function of time and wall temperature (T_w). To construct a tabulated environment for the material response, the CFD is repeated over a range of surface emissivity values, which artificially modifies the spatial temperature distribution at the wall of the vehicle. The resulting tabulated properties are interpolated within the material response.

Material response calculations

The energy boundary condition for the material response now becomes

$$q_{\mathrm{cond}} = \left[q_w^{\mathrm{CFD}}\right]_{\mathrm{fluid}} - \left[\dot{m}_c'' h_c\right]_{\mathrm{solid}} - \left[\sigma\epsilon\left(T_w^4 - T_\infty^4\right)\right]_{\mathrm{surface}} \tag{4.27}$$

where both the heat flux and the solid ablation flux are linearly interpolated quantities from the DHA tables. The advective reduction of energy, the ablation species effect

on mixture properties, and the mass diffusion have all been included in this new heat flux term. The solid ablation flux provides the surface recession rate through the usual expression

$$\rho_s \dot{s} = \dot{m}_c''. \tag{4.28}$$

Of primary interest is that all of the complicated models have been removed from the material response side of the engineering method. There is no need for the thermal analyst to perform any work other than application of the boundary condition to the thermal problem.

Chapter 5 Results

5.1 Convective heat transfer in the film coefficient methodology

To build an intuition for the sensitivities associated with the film coefficient method, the simplest case of convective heat transfer is examined. From Eq. 4.9, it is evident that the computed heat flux (q_w^{CFD}) from the CFD simulation will be a large sensitivity in the downstream material response heat flux. Regardless of the fidelity of the computational tools being used for the design process, they should be verified and/or validated against higher fidelity methods to develop adequate safety margins for vehicle heating. This is essentially a practice in mitigating the sensititivity associated with the q_w^{CFD} term. Aerothermal margins may be established by comparison of computational tools against experimental data (such as wind tunnel or flight). Alternatively, higher fidelity computational methods may help establish confidence in aerothermal margins dictated for lower fidelity models. The method of determining proper margins is outside the scope of this paper and therefore the sensitivity of q_w^{CFD} is not assessed.

However, a final comment on the q_w^{CFD} term is necessary for the following discussion. The q_w^{CFD} term is evaluated at a single wall temperature for a given body point in the CFD solution and remains constant. While the *relative value of* q_w^{CFD} *to reality* is not assessed, the effect of the chosen wall temperature and the assumed linearity of the model are. The remaining bracketed term in Eq. 4.9 may then be thought of as a correction factor for the wall temperature assumed by the material response (MR) calculation. When extended to systems with mass transfer, the bracketed term then includes the effect of having ablative species present at the vehicle wall as well as for variable wall temperature.

It is useful to analyze each term in a piecewise fashion before examining the

Parameter	Value	Units
Initial Velocity	6	km/s
Flight path angle	-1	degree
Altitude at interface	125	km
Angle of attack	0	degrees
Nose radius	2.5, 0.5	m
Body shape	Sphere	
Vehicle mass	8000	kg

Table 5.1: Demonstration entry conditions

cumulative downstream effect on the material response, since multiple components contribute to the resulting heat flux. This study examines the *effect of the CFD assumptions on the engineering model* and the subsequent effects on material response. The following effects are discussed:

1. Boundary layer edge properties and recovery factor
2. Chemical equilibrium at the wall
3. Constant film coefficient (functional dependence on h_w)
4. Energy boundary condition (wall temperature)
5. Cumulative effect on material response wall heat flux

To perform the sensitivity study, an arbitrary sphere-shaped flight vehicle of nose radius 2.5 m and point mass of 8000 kg is chosen. A ballistic, non-lifting trajectory at zero angle of attack, with parameters given in Table 5.7, is modeled using the Kentucky Trajectory Modeling Program (KTMP) (74). The trajectory is chosen so that the peak heating produces significant aerothermal heating without the effects of ionization within the fluid flow.

By using the Sutton-Graves (75) heating indicator for an Earth atmosphere, the altitude and inertial velocity for the peak heating may be estimated. The altitude may be used to compute the freestream mass fractions and temperature using the Standard

Atmosphere (22) model. These freestream parameters serve as inputs for the Data Parallel-Line Relaxation (76) (DPLR) CFD simulation. The grid is 2-dimensional, the simulation performed is axisymmetric, and the usual grid convergence practices were followed in resolving flow features. The body points under consideration for the vehicle are the stagnation point and the 90° shoulder shown in Fig. 5.1. The stagnation point is a unique, high heating location on the body which decelerates the flow, thereby converting inertial energy to thermal energy. The 90° shoulder location is included to illustrate the thermal recovery concept, well described by van Oudheusden (77), as well as other downstream effects seen by variation of the model parameters. Other simulation parameters in the study are given in Table 5.2. Non-numerical values given in the table refer to the chosen model, where NASA-9 refers to the equilibrium coefficients being calculated by temperature curve fits from the NASA-9 dataset out of Glenn Research Center (78), and Yos Mixing refers to the Gupta-Yos transport coefficient mixture model (79). The chosen homogeneous model is given by Park (54) 5-species air, which includes the nitric oxide product. Recall that earlier engineering approximations, such as those by Lees and Fay, modeled air as a binary mixture of molecules (N_2, O_2) and their dissociated atoms (N, O). See Park (54) for a description of the homogeneous reaction set. The thermal field is modeled in thermal non-equilibrium with the two temperature model (80), which permits the expected vibrational excitation that occurs before molecular dissociation.

Boundary layer edge properties and recovery factor

Recall that the recovery enthalpy is defined as

$$h_r = h_e + r\frac{u_e^2}{2} \tag{5.1}$$

where the recovery factor r is well approximated by

$$r \approx \sqrt{\mathrm{Pr}^*} \tag{5.2}$$

Parameter	Value	Units
Altitude	32.5	km
Freestream Velocity	4721.19	km/s
Freestream Density	0.0130462	kg/m^3
Freestream Temperature	228.89	K
Initial Mass Fraction [N2]	0.767	kg/kg
Initial Mass Fraction [O2]	0.233	kg/kg
Surface Emissivity	0.88	
Equilibrium Coefficients [K_{eq}]	NASA-9	
Thermal Properties	NASA-9	
Viscosity Model	Yos mixing	
Thermal Conductivity	Yos mixing	
Flow State	Laminar	

Table 5.2: CFD parameters for 5 species, chemically reacting, laminar air

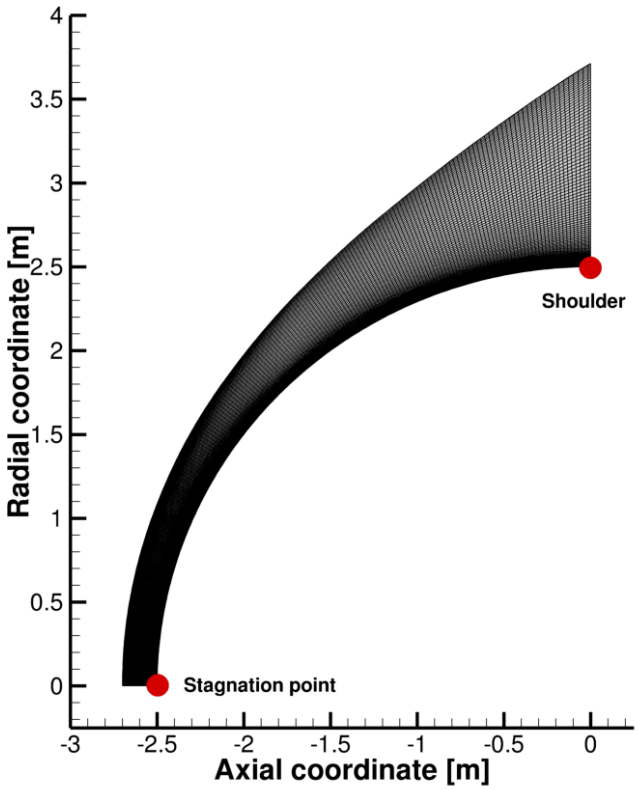

Figure 5.1: Vehicle body points and shock-adapted, axisymmetric grid

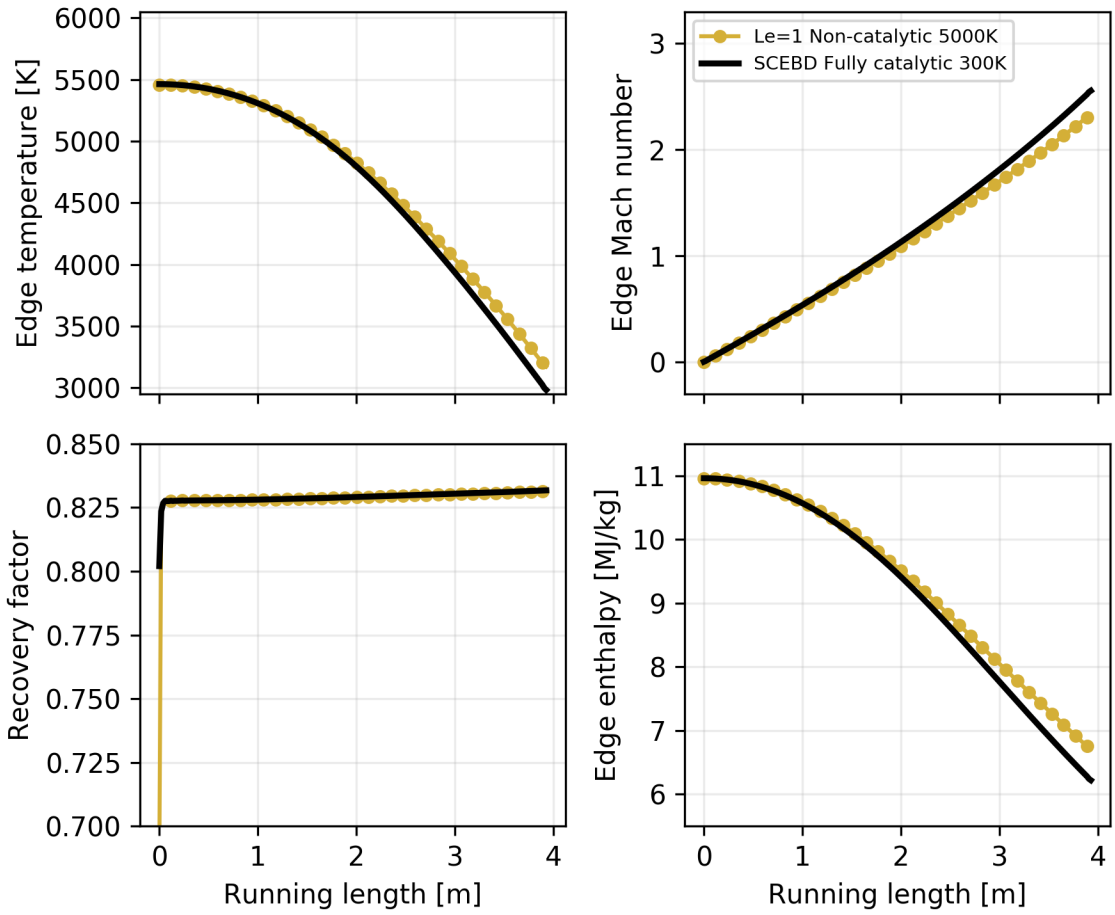

Figure 5.2: Boundary layer edge properties

and Pr^* is the Prandtl number evaluated at a reference temperature given by

$$T^* = 0.4T_e + 0.6T_w + 0.11r\left(\gamma^* - 1\right)M_e^2. \tag{5.3}$$

Figure 5.2 shows boundary layer edge temperature, Mach number, static enthalpy, and recovery factor. Two extremes of the chosen modeling assumptions, the SCEBD diffusion model with a fully catalytic wall at 300 K and the Lewis number unity, non-catalytic wall at 5000 K, are chosen to distinguish that the boundary layer edge properties are insensitive to modeling assumptions.

At the stagnation point of the vehicle, the flow field has decelerated outside of the boundary layer to approximately zero. Due to this same deceleration, the static

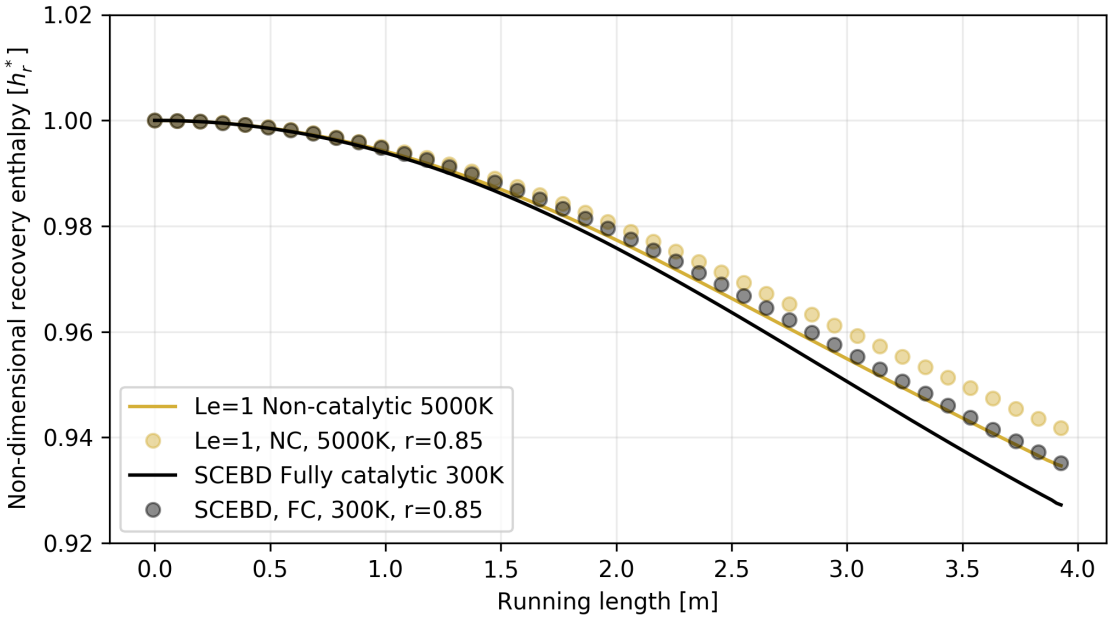

Figure 5.3: Recovery enthalpy distribution along the boundary layer edge

enthalpy is at a maximum at the stagnation point and the Mach number is zero. Along the running length of the vehicle, the increasing Mach number reflects the kinetic contribution to the total enthalpy. The slight increase in enthalpy approaching the shoulder for the 5000 K isothermal wall assumption is due to the vehicle being hot enough to heat the boundary layer in that area (i.e. the conduction term in the SEB is negative). This also appears as a reduction in the edge Mach number.

The change in recovery factor, a function of both wall and edge properties, is less than 0.005 across the body of the vehicle. The insensitivity of the recovery factor is not due to the calculation of the reference temperature, but rather due to the Prandtl number approximation. This is because the properties comprising the Prandtl number behave in dissimilar ways with increasing temperature and tend to compensate for one another. The fall off seen close to the stagnation point is a numerical artifact. The theoretical value of the recovery factor should be exactly equal to unity at the stagnation point, as all of the thermal energy is recovered due to deceleration in the

flow. Therefore, in the vicinity of the stagnation point there is a discrepancy between the Prandtl number approximation and the theoretical value, which is not considered further.

The non-dimensional recovery enthalpy is given by

$$h_r^* = \frac{h_r}{h_0} \tag{5.4}$$

where h_0 is the stagnation enthalpy, as a function of the running length of the vehicle wall. The two limiting cases are plotted in Fig. 5.3, with and without a constant recovery factor of $r = 0.85$. In the region close to the stagnation point, there is no discernable difference in recovery enthalpy. As the conditions change along the running length of the vehicle, the two limiting extremes diverge by at most 2% at the shoulder. This small variation in recovery enthalpy justifies the assumption of a constant recovery factor.

Examining Fig. 5.4 gives the mass composition as it has reached the boundary layer edge. Again, the two extremes of modeling assumptions are chosen to demonstrate the relative insensitivity to the diffusion model and wall assumptions. However, it is also important to note that the edge properties will vary with respect to the running length of the vehicle. It is seen that the molecular oxygen is nearly fully dissociated at the stagnation point, and the degree to which it is dissociated decreases as the temperature decreases in the running length direction. The discrepancy in the extent of dissociation of molecular oxygen between the two models is the reason for the disagreement in the edge *static* enthalpy (seen in Fig. 5.2) at the shoulder compared to the stagnation point. The amount of NO lost at the shoulder, in concert with decreasing levels of O and N results in a higher percentage of molecular oxygen and nitrogen in that location.

While the recovery enthalpy does not change significantly across the boundary layer edge (approximately 6%), the edge temperature (top plot, Fig. 5.2) and the edge mass fractions (Fig. 5.4) change significantly. These quantities will determine the

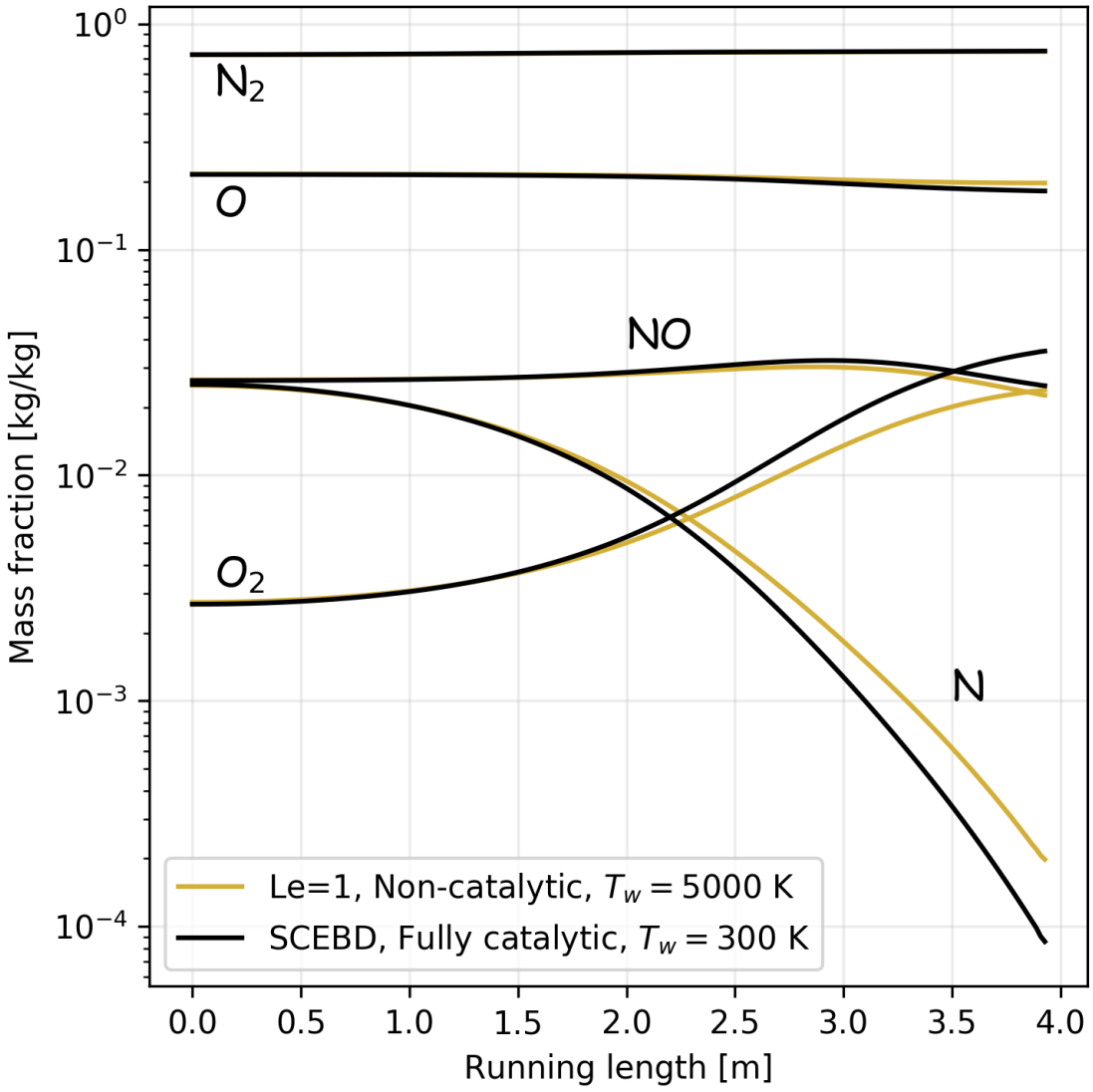

Figure 5.4: Boundary layer edge mass fractions

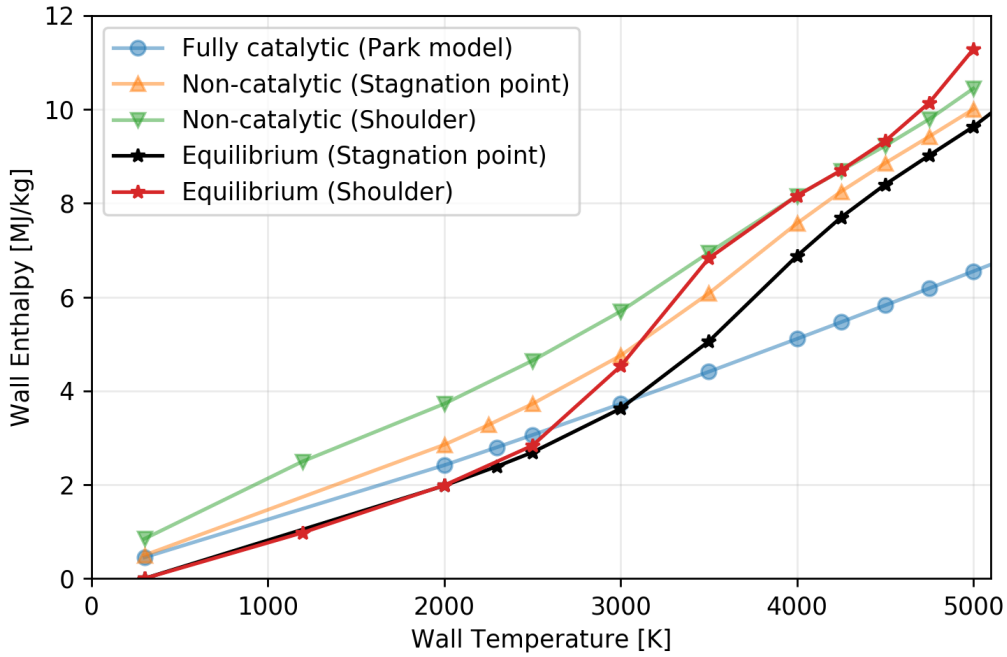

Figure 5.5: Mass boundary condition effect on wall enthalpy for Earth atmosphere

overall thermal and mass gradients which control the conduction and mass diffusion terms in the SEB.

It is concluded from the above analysis that (for this flight condition, for a given body point) the engineering model is not sensitive to the boundary layer edge properties, except in the case of the hot wall at the shoulder, and that an assumed constant recovery factor value will not skew the results.

Chemical equilibrium wall enthalpy assumption

In hypersonic viscous flow, high velocity fluid undergoes rapid viscous dissipation in the boundary layer, which generates a large amount of heat. In this highly energized state, it is appropriate to use enthalpy as an energy metric of the flow due to variable thermodynamic properties (namely specific heat). The heat transfer now becomes functionally dependent upon the mass composition.

Figure 5.5 shows the wall enthalpy as a function of wall temperature for an equi-

librium 5-species air mixture at $P = 2.77798 \times 10^5$ Pa (black, stagnation point) and at $P = 1.0476 \times 10^4$ Pa (red, shoulder). Also included are a non-catalytic CFD based wall enthalpy for both the stagnation point (orange) and the shoulder (green), and a CFD based wall enthalpy computation based on the wall species when a *fully catalytic* Park model is implemented (blue, stagnation point).

The wall enthalpy for each of the three models is monotonically increasing with respect to wall temperature. At low wall temperatures (for example 300 K), the non-catalytic and *fully catalytic* mass boundary conditions permit an appreciable amount of nitric oxide to reach the wall, thereby slightly increasing the wall enthalpy. Additionally, because of the first order nature of the *fully catalytic* model, it takes on a linear form, lacking the curvature of the other two models. This means forcing molecular recombination in a physically inconsistent manner, which results in much lower wall enthalpies at high wall temperatures. The equilibrium wall enthalpies both display a curvature at moderate wall temperatures, reflecting the point where atomic species increase in the mixture. However, since the chemical time scale is finite for a non-catalytic wall (which relies on kinetic mechanisms in the homogeneous phase), there is only one wall temperature range where the shoulder body point reaches equilibrium using the non-equilibrium rates. The stagnation point never fully reaches the chemical equilibrium state.

Figure 5.6 shows the quantitative species comparison between the kinetic and equilibrium compositions. Figure 5.6(a) is for the stagnation point of the vehicle and Fig. 5.6(b) is for the shoulder. The percentages are calculated by

$$\frac{\left(X_{i,w}^{\mathrm{CFD}} - X_i^{\mathrm{EQ}}\right)}{X_i^{\mathrm{EQ}}} \times 100.0 \tag{5.5}$$

where X_i^{EQ} is the equilibrium species mole fraction based on freestream elemental mole composition and i is a given chemical species. The wall boundary condition is chosen to be the hot wall at 5000 K to allow a maximum amount of energy through

the boundary layer, in an effort to artificially drive the homogeneous rates as close to equilibrium as possible.

Under these conditions, the stagnation point species' relative error with respect to the equilibrium mole fraction is within 3% for each species. This corroborates the small difference at 5000K in Fig. 5.5, between the orange and black lines. Looking to Fig. 5.6(b), a larger variation from equilibrium composition at the shoulder reinforces the observed behavior of the non-catalytic wall enthalpy seen in Fig. 5.5 (green line) versus the equilibrium enthalpy (red line). The large excess of atomic nitrogen, N, and the smaller percentages of molecular oxygen and nitric oxide result in a higher mixture enthalpy. The point to be made here, is that even at extremely high wall temperatures and moderate pressures, the homogeneous rates do not reach full chemical equilibrium.

Constant film coefficient

This section investigates the assumption that

$$\frac{\partial}{\partial h_w}\left(\rho_e u_e \mathrm{C_H}\right) = const. \tag{5.6}$$

for a given trajectory point. Since the film coefficient is the negative slope of the heat flux, this implies no curvature is present in the relationship between the wall heat flux and the wall enthalpy. Figure 5.7 plots the film coefficients for the various diffusion models and mass boundary conditions as a function of the wall enthalpy. Each marker indicates a CFD solution.

Figure 5.7(a) shows the film coefficients constructed using a non-equilibrium wall enthalpy in the denominator. This grouping is intentionally designed to illustrate the effect of adding the diffusive contribution to the surface energy balance (SEB). The solid lines represent a non-catalytic wall, which requires that the source term in the surface mass balance equals zero. This, in turn, nullifies the diffusive term in the SEB, guaranteeing that the total heat flux at the surface is simply the conduction

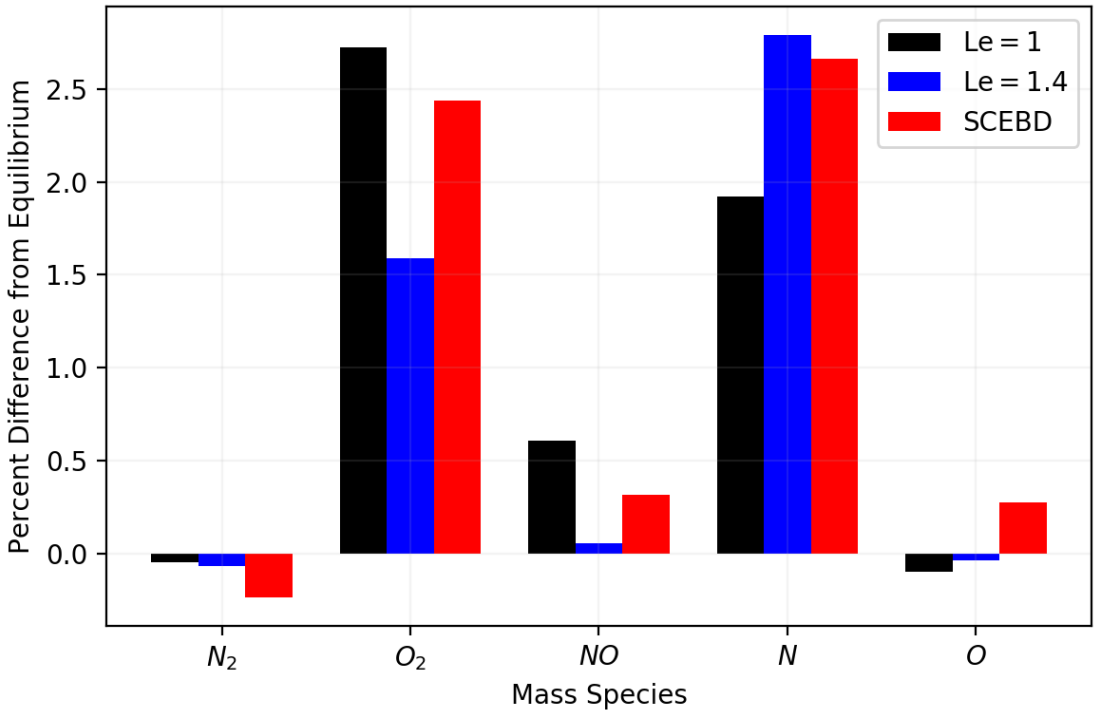

(a) Stagnaton point: $T_w = 5000$ K, $P_w = 2.77798 \times 10^5$ Pa, isothermal wall

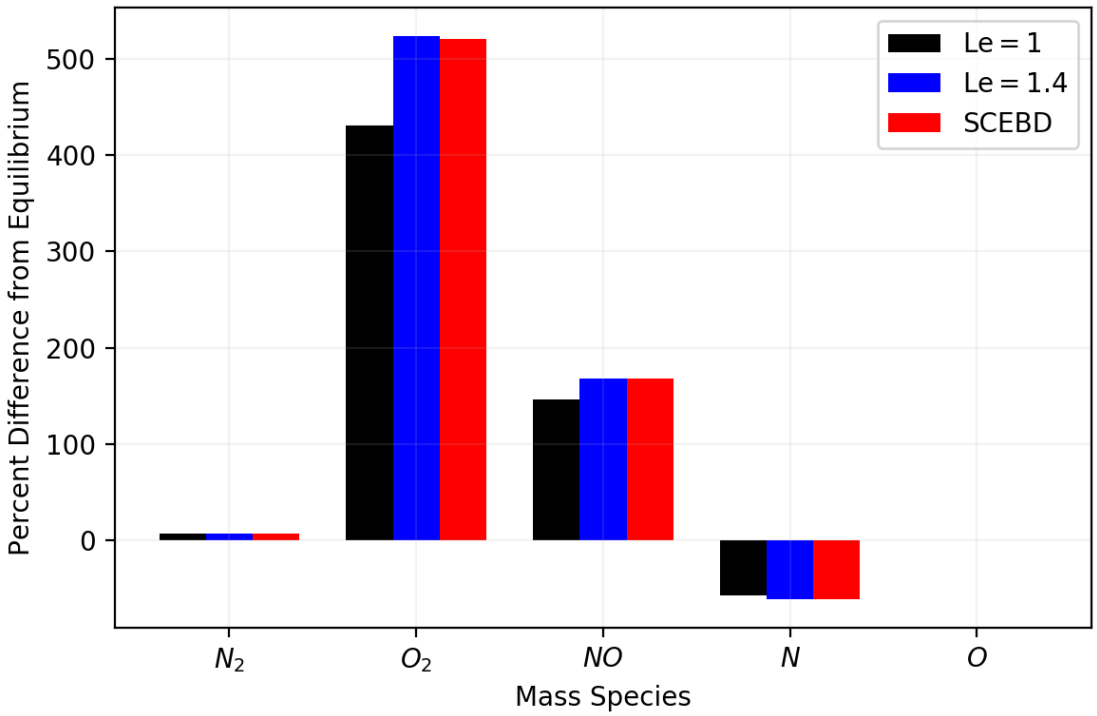

(b) Shoulder: $T_w = 5000$ K, $P_w = 1.0476 \times 10^4$ Pa, isothermal wall

Figure 5.6: Molar fraction difference of CFD composition vs. equilibrium

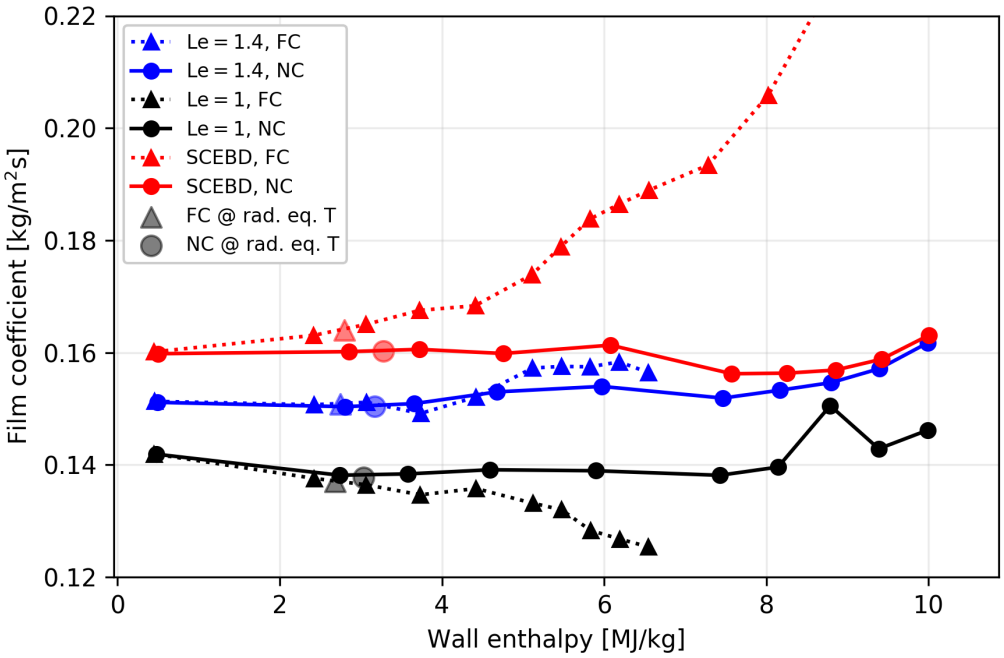

(a) Non-equilibrium wall enthalpy based film coefficients

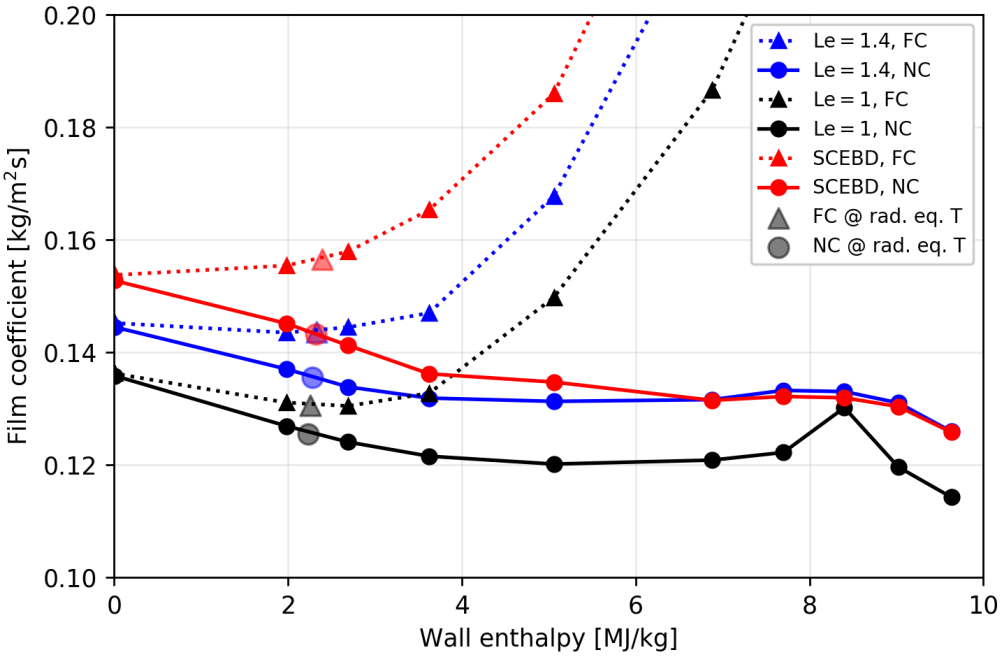

(b) Equilibrium wall enthalpy based film coefficients

Figure 5.7: Stagnation point film coefficient sensitivity

flux. The relative values of the film coefficients between diffusion models may be attributed to their sensitivity to q_w^{CFD}. However, more important, is that when only conduction is considered (solid lines), the increase in non-equilibrium wall enthalpy (see Fig. 5.5) and subsequent decrease in enthalpy potential balances the decrease in the wall heat flux as the wall temperature increases.

In contrast, the dotted lines of Fig. 5.7(a) include the effect of the *fully catalytic* Park model. By this inclusion, diffusion now contributes to the total heat flux at the wall through both the Fick's Law mass diffusion term and the catalytic source term ($\dot{\omega}$). In this instance, the various diffusion models begin to behave differently. For any given wall temperature, the *fully catalytic* model will have an enthalpy potential ($h_r - h_w$) equal to or less than the non-catalytic model (Fig. 5.5, blue line vs. orange line). At the same time, the q_w^{CFD} term will be affected by the inclusion of the surface mass balance terms. As the wall temperature increases, a decrease in conduction takes place (to the point of heating the boundary layer) coinciding with an increased diffusion contribution. The reason for seemingly disparate behaviors in the three diffusion models is due to *the rate at which the diffusion contribution increases* with respect to wall temperature. For Le = 1 the increase in the diffusion term cannot keep pace with the reduction of heat flux, and therefore the film coefficient decreases. For the SCEBD model, the diffusion outpaces the reduction in conduction, resulting in higher and higher film coefficients. This occurs because the *fully catalytic* Park model has no constraint, where the limiting case should be chemical equilibrium at the wall.

Figure 5.7(b) shows the film coefficients computed for a film coefficient calculated with an equilibrium wall enthalpy. Again, examining the non-catalytic case (solid lines) first, as the case of pure conduction, the lower wall enthalpy compared to a non-equilibrium wall enthalpy allows the reduction in the conduction term to decrease the film coefficients as wall temperature increases. The *fully catalytic* model (dotted

lines) demonstrates a large increase in the overall q_w^{CFD} term. In the previous example, the decreasing enthalpy potential (due to the large increase in atoms) helped balance the increasing diffusion contribution. However, in this case, the equilibrium enthalpy potential is much lower, resulting in a large increase in the film coefficients.

In summary, at the stagnation point of the vehicle it may be seen that for a non-catalytic wall, the assumption of a constant film coefficient is a fair approximation of the calculated results. With an equilibrium wall enthalpy, the film coefficient decreases slightly as the wall temperature increases. However, with the implementation of a catalytic model with no energy limit, at high wall temperatures the linearity of the model no longer applies and the film coefficient computation begins to change more rapidly with respect to wall enthalpy.

Figure 5.8 shows the film coefficients at the 90° shoulder as a function of wall enthalpy. Figure 5.8(a) is the film coefficient computed with a non-equilibrium wall enthalpy. Notably, all of the film coefficients are an order of magnitude lower than the stagnation point. The thermal energy available in the boundary layer edge has dropped from the stagnation point to the shoulder. This considerably reduces the temperature distribution through the boundary layer and subsequently the thermal gradient at the wall controlling the conduction term. Therefore, for the pure conduction (solid lines), a constant decrease is observed in the film coefficient due to the increase in wall temperature. Eventually, the adiabatic wall temperature is passed and the conduction term becomes negative.

As well, the *fully catalytic* model now does not display the divergent behavior between diffusion models as in the case of the stagnation point. In fact, each of the diffusion models seems to be trending down. Just as the conduction term is smaller due to the edge temperature, so too is the mass diffusion term due to the concentration gradients which exist through the boundary layer height. As evidenced from Fig. 5.2, an increase in molecular oxygen by an order of magnitude from the

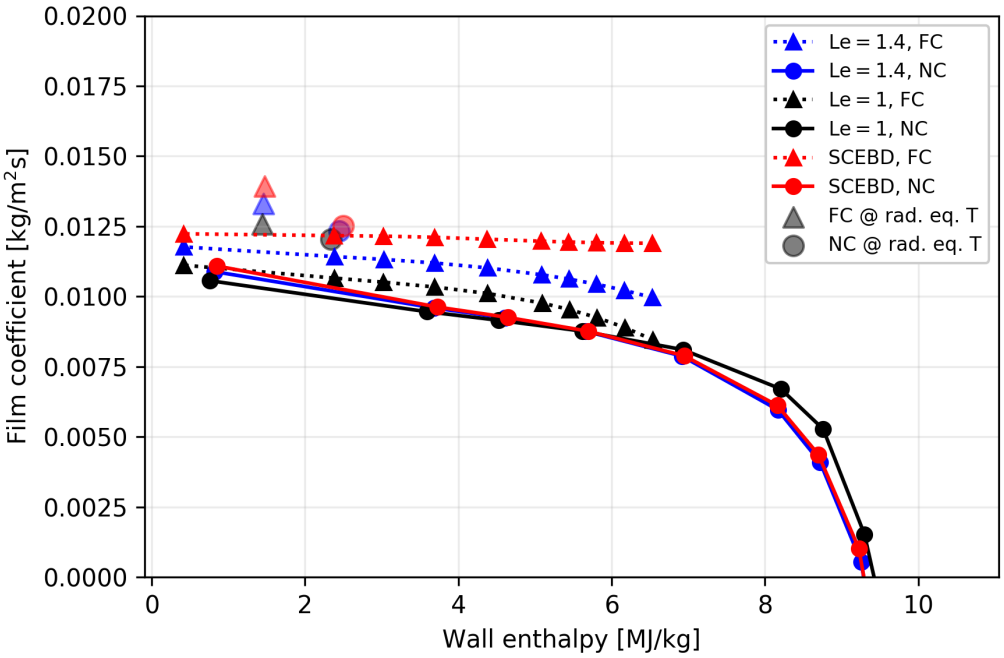

(a) Non-equilibrium wall enthalpy based film coefficients

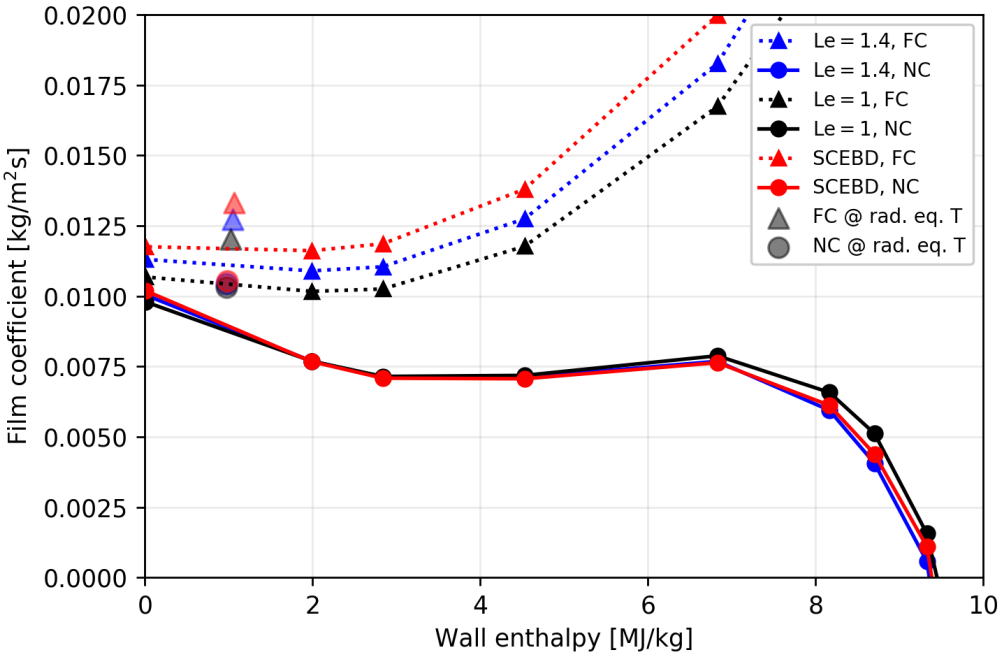

(b) Equilibrium wall enthalpy based film coefficients

Figure 5.8: Shoulder film coefficient sensitivity

stagnation point to the shoulder helps keep the diffusion term small. Consequently, the divergence between predicted film coefficients for the *fully catalytic* case is less severe and trending lower with respect to wall enthalpy.

Figure 5.8(b) shows the film coefficients at the shoulder computed with an equilibrium wall enthalpy. The non-catalytic film coefficient (solid line) again reflects the balance between enthalpy potential and computed CFD wall heat flux. After dropping from the cold wall film coefficient (furthest left), the film coefficient becomes approximately constant over a given wall enthalpy range. As the wall state approaches higher energies, the thermal gradient becomes smaller and smaller. Between a wall enthalpy value of 0.8 and 1.0×10^7 J/kg, the vehicle *begins to heat the boundary layer* at the shoulder. However, in the case of the *fully catalytic* model (dotted lines), now the diffusion term in q_w^{CFD} increases faster than the decrease in the conduction term. This results in behavior similar to Fig. 5.7(b). The point where the signs flip for both non-catalytic and *fully catalytic* models indicates that the wall enthalpy has surpassed the recovery enthalpy. For the non-catalytic case this means returning the sign of the film coefficient to positive, while for the *fully catalytic* the film coefficient now becomes negative.

Summarizing the shoulder location, it may be seen that a non-catalytic wall (solid lines) will produce a film coefficient which decreases slightly with respect to wall enthalpy. Approaching the recovery state, it will begin to decrease rapidly, not due to the enthalpy state values' proximity to one another, but due to the conduction term dropping as the wall temperature increases. In the case of the *fully catalytic* model, milder conditions suggest that the divergent behavior seen at the stagnation point is a product of the strong temperature and mass gradients within the stagnation boundary layer. However, the *fully catalytic* model repeats an unphysical behavior seen at the stagnation point when coupled with an equilibrium wall enthalpy.

Finally, it is interesting to note the behavior of the radiative equilibrium wall

boundary condition at the shoulder location. Figures 5.8(a) and 5.8(b) both have semi-transparent CFD markers for each case. These may be seen between 1-3 MJ/kg in Fig. 5.8(a) and between 0-2 MJ/kg in Fig. 5.8(b). This is a notable feature of the radiative equilibrium boundary condition which creates a thermal distribution as a function of streamwise direction. This leads to a similar thermal distribution as encountered at the boundary layer edge, where the maximum temperature exists at the stagnation point and decreases in the streamwise direction. The transport of upstream energy to downstream body points directly leads to a higher q_w^{CFD}. This is why these CFD markers appear to break the trend of their respective isothermal cases, producing slightly larger film coefficients. This raises the question of which wall energy boundary condition to choose for a given CFD solution, which is investigated next.

Model effect on material response wall heat flux

In Figs. 5.7 and 5.8, each marker represents a given CFD solution for a set of assumptions. A single marker must be chosen to represent the heat transfer for that flight condition. In the previous sections, the entire range of wall temperatures were computed to demonstrate the dependence of the mass boundary condition on the wall energy state. In this section, three energy boundary conditions are employed; a *cold wall* case of an isothermal wall at 300 K, a radiative equilibrium case, and a *hot wall* case of an isothermal wall at 5000 K.

During calculation in the material response code, the only unknown is the wall temperature upon which the h_w^{EQ} depends. In physical terms, if the wall temperature in the material response lags behind the CFD wall temperature (perhaps on the way up the heat pulse), then the result of the model will be to add more heat through the surface. If the vehicle wall is hotter than the evaluated wall temperature in the CFD (perhaps during the convective cooling phase), then the heat transfer will be

reduced.

To examine the cumulative impact of the engineering model, the quantities

$$q^{\Delta}_{\mathrm{EQ}} = \frac{q^{\mathrm{MR}}_{\mathrm{EQ}} - q^{\mathrm{CFD}}_{w}(T_w)}{q^{\mathrm{CFD}}_{w}(T_w)} \times 100.0 \tag{5.7}$$

and

$$q^{\Delta}_{\mathrm{NE}} = \frac{q^{\mathrm{MR}}_{\mathrm{NE}} - q^{\mathrm{CFD}}_{w}(T_w)}{q^{\mathrm{CFD}}_{w}(T_w)} \times 100.0 \tag{5.8}$$

may be computed, where $q^{\mathrm{MR}}_{\mathrm{EQ}}$ is the material response heat flux produced by the film coefficient model with an equilibrium wall enthalpy, $q^{\mathrm{MR}}_{\mathrm{NE}}$ is the material response heat flux produced by the film coefficient model with a non-equilibrium wall enthalpy, and $q^{\mathrm{CFD}}_{w}(T_w)$ is the CFD heat flux, using the same set of assumptions as the film coefficient CFD at the isothermal wall temperature. In other words, this metric computes how close the prediction of the film coefficient model will be to the CFD heat flux, if the CFD were run at the material response wall temperature. Recall, that this does not guarantee the q^{CFD}_{w} term be close to reality.

In the following figures, the blue lines refer to film coefficient heat flux predictions based on a CFD solution with an isothermal wall at 300 K (or *cold wall*). The orange lines refer to film coefficient heat flux predictions based on a CFD solution with a radiative equilibrium wall, which for these flight conditions corresponds to a spatial distribution in the temperature range [1000-3000] K. The red lines refer to film coefficient heat flux predictions based on a CFD solution with an isothermal wall at 5000 K (or *hot wall*), which approximates an adiabatic wall temperature condition (but permits catalysis). The solid lines in the figure refer to a non-equilibrium (NE) wall enthalpy being used in the denominator of the film coefficient, while the dashed lines refer to an equilibrium wall enthalpy (EQ) based on the state variables at the wall and the freestream elemental mole fractions.

Figure 5.9(a) is for the non-catalytic wall boundary condition, using the Le = 1 diffusion model. This is consistent with the boundary layer assumption mentioned

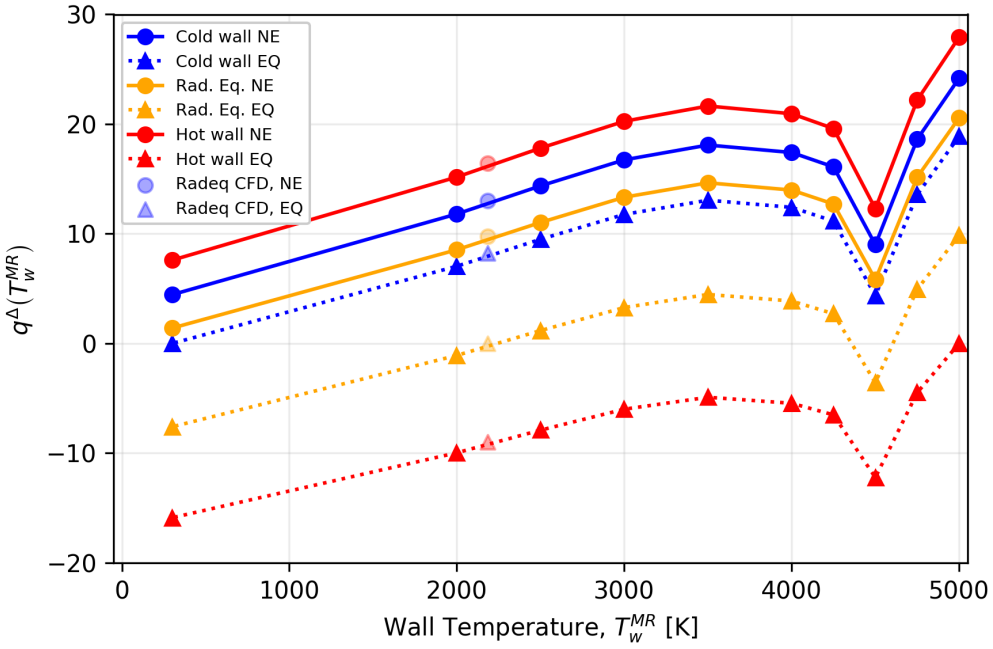

(a) Non-catalytic wall

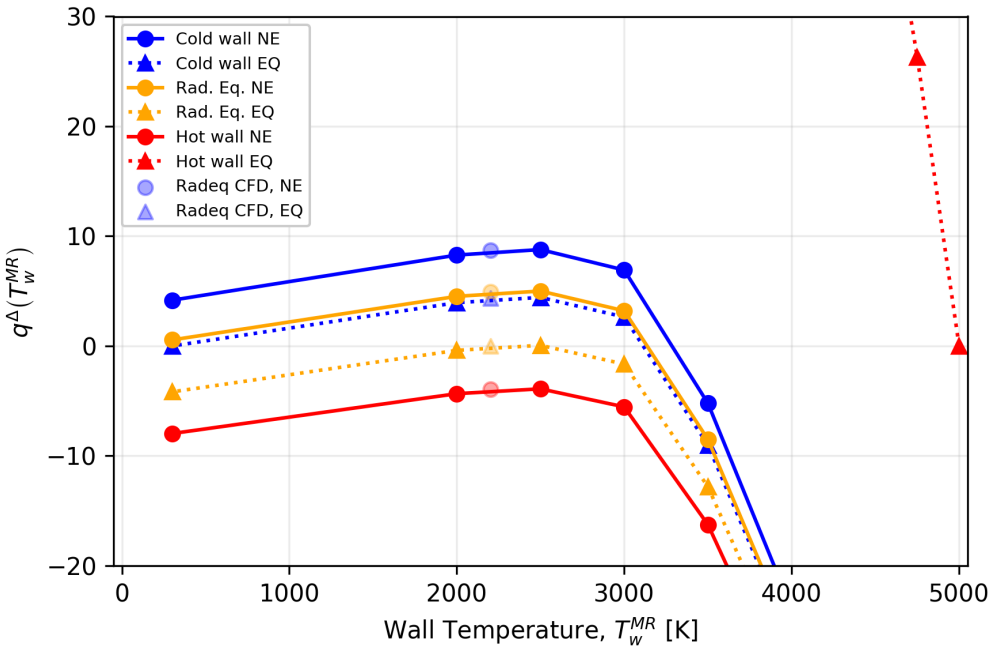

(b) *Fully catalytic* wall (Park model)

Figure 5.9: Stagnation point, Le = 1

previously, where heating due to mass diffusion is not present. With conduction as the primary means of heat transfer, Fig. 5.9(a) demonstrates that the film coefficient model will conservatively bound the CFD prediction for all three energy assumptions if the film coefficient is constructed with a non-equilibrium wall enthalpy. On the other hand, the film coefficients constructed with an equilibrium wall enthalpy ($\rho_e u_e C_H^{EQ}$) predict lower heat fluxes than the non-equilibrium ($\rho_e u_e C_H^{NE}$) counterparts. This results in areas where the model will underpredict the CFD solution for a given wall temperature.

Figure 5.9(a) also demonstrates qualitative similarity between the q_{EQ}^{MR} and q_{NE}^{MR} predictions. Both exhibit an increase from cold wall temperatures up to around 3500 K before reversing curvature. The dip is due to the exponentially decreasing fluid conduction term at high wall temperatures. Further, it is observed that the equilibrium wall enthalpy curves are all lower than their non-equilibrium wall enthalpy counterparts.

Figure 5.9(b) is for the *fully catalytic* boundary condition at the stagnation point, again using the Le = 1 diffusion model. Most immediately noticeable is the poor performance of the hot wall, equilibrium wall enthalpy film coefficient. This is directly attributable to Chung's observation that a first order catalytic model should not be employed at wall temperatures much higher than 2000K. This results in unphysical mass compositions which deviate strongly from chemical equilibrium.

However, it may be noticed that, at the 5000 K wall temperature, the percent difference is zero. This occurs because the equilibrium wall enthalpy in the denominator of the film coefficient is the same as the wall enthalpy in the numerator. This condition also exists for the cold wall film coefficient (blue) at 300 K and the radiative equilibrium film coefficient between 2000 and 2500 K, and is true for every set of assumptions given only an equilibrium wall enthalpy be used in the film coefficient model.

A qualitative inspection of Fig. 5.9(b) reveals that each of the remaining sets of assumptions gradually increase their prediction of heat flux with respect to wall temperature, reaching a maximum approximately between 2200 and 2500 K. The curvature shifts and the difference of the model against the CFD begins to decrease until at 4000 K it is below 20% of the CFD prediction. This is due to the enthalpy correction term *over-correcting* the CFD predicted heat flux (q_w^{CFD}). However, the film coefficient predictions for each of the sets of assumptions remains within $\pm 10\%$ when below this wall temperature.

Looking to Fig. 5.10, the stagnation point CFD heat flux difference is plotted, now with the SCEBD model. For the case of the non-catalytic wall (Fig. 5.10(a)), unlike the constant Lewis number diffusion model, there is no sharp curvature in between 4000 and 5000 K wall temperatures. Between the two diffusion models, the SCEBD model produces the higher of the two wall heat fluxes, indicating a steeper thermal gradient. This higher gradient at the wall means a less severe decrease in the conduction term, and thus no *dip* in the film coefficient prediction. The *fully catalytic* wall (Fig. 5.10(b)) shares similar attributes to the constant Lewis number, but in the lower to moderate wall temperatures, where the Le = 1 model increases heat flux to a point, the SCEBD diffusion model is monotonically decreasing.

Next, consider the surface heat flux predicted by the film coefficient model at the shoulder location. See Figs. 5.11(a) and 5.11(b) for the Le = 1 diffusion model. In this case, the hot wall produces applied heat fluxes outside an acceptable range.

The cold wall and radiative equilibrium film coefficients produce behaviors similar to the stagnation point location, noting only that now the y-axis range has increased considerably. In Fig. 5.11(a), both wall energy models increase, regardless of enthalpy assumption to a certain point. At the lower pressure shoulder location, the dip previously seen at the stagnation point occurs at a lower temperature. Beyond this critical temperature, the heat flux values from the lower wall temperature CFD solutions be-

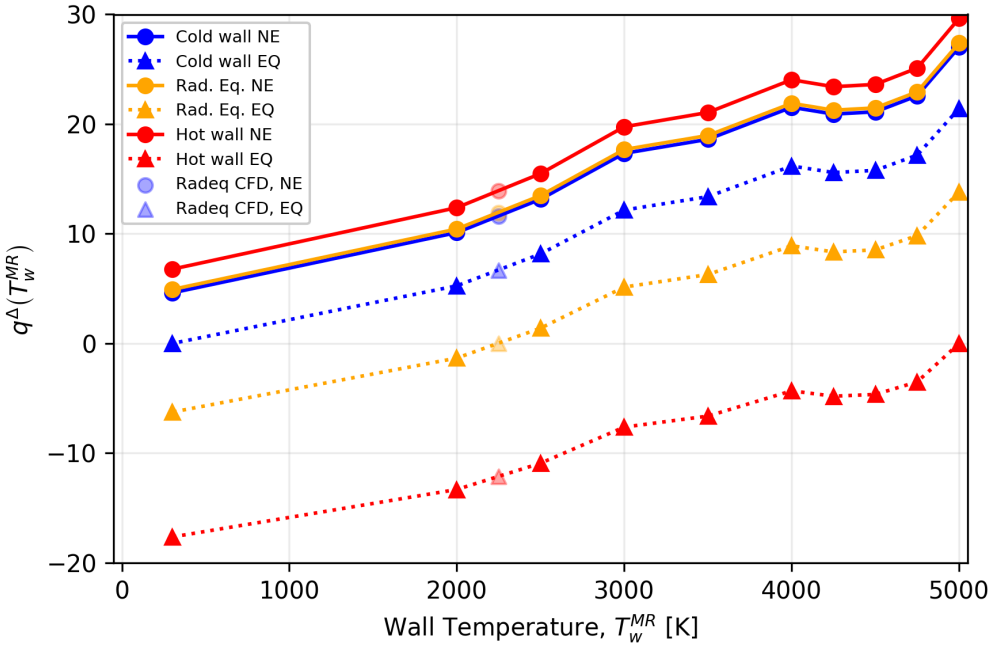

(a) Non-catalytic wall

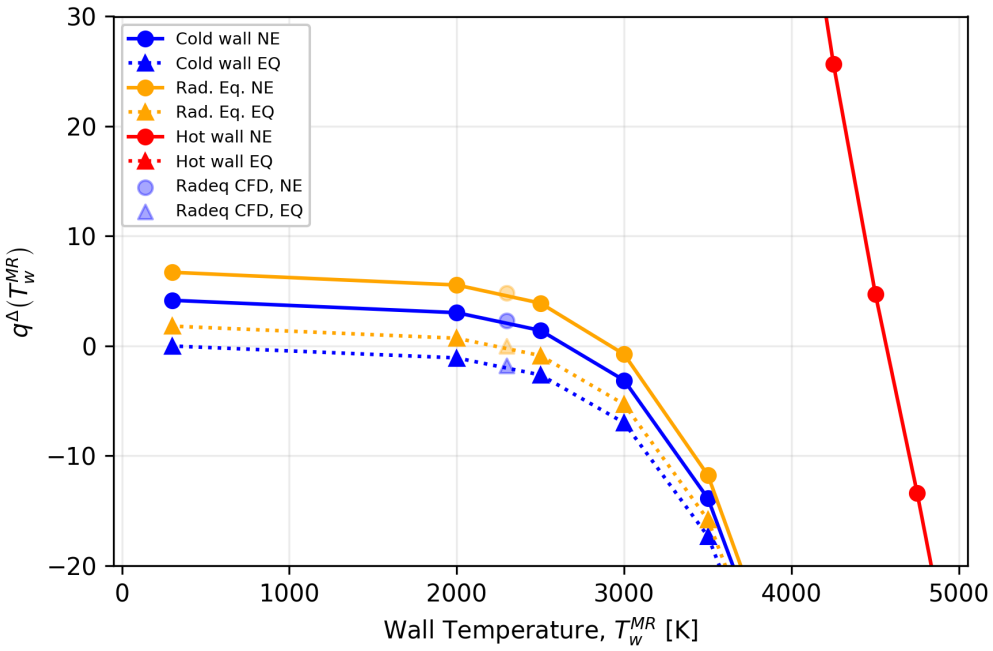

(b) *Fully catalytic* wall (Park model)

Figure 5.10: Stagnation point, SCEBD model

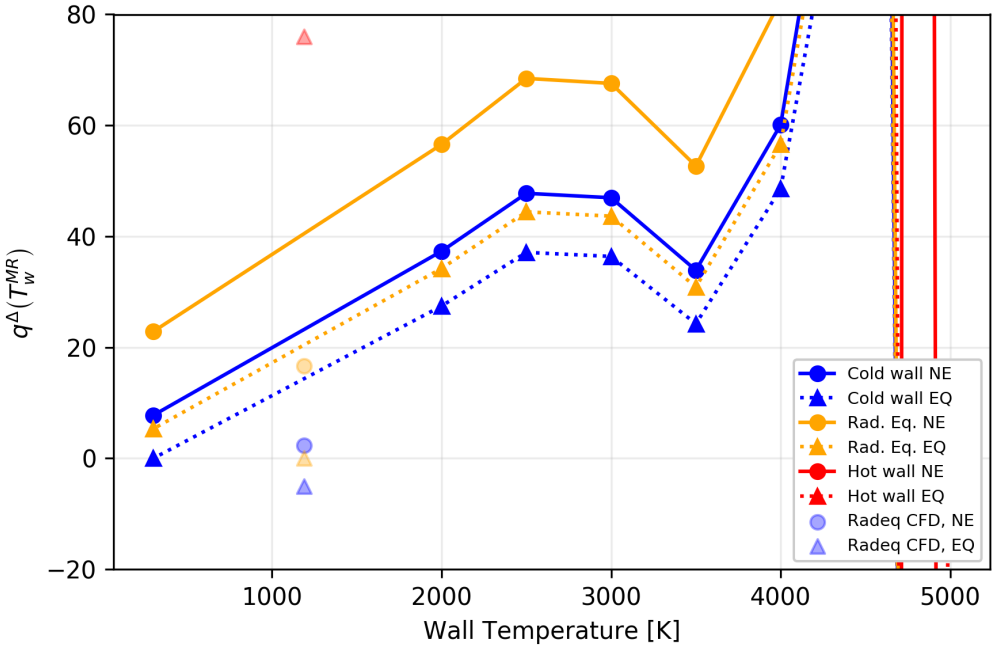

(a) Non-catalytic wall

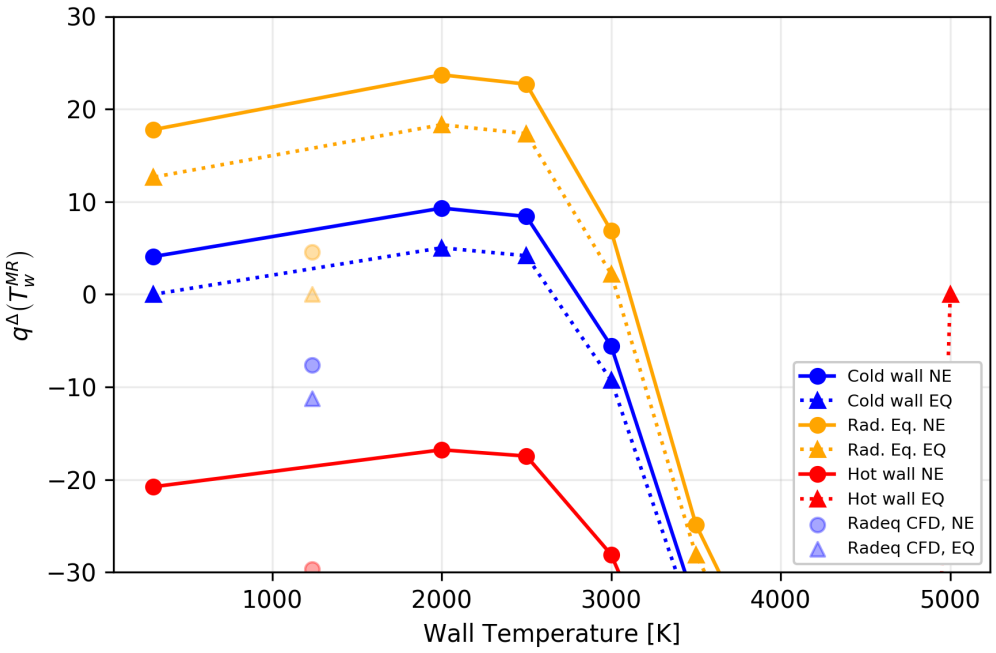

(b) *Fully catalytic* wall (Park model)

Figure 5.11: Shoulder, Le = 1

come exponentially larger than the material response wall temperatures, resulting in a large amount of conservatism at this body location. Again, the equilibrium wall enthalpy film coefficients produce applied heat fluxes which are lower than their non-equilibrium counterparts for previously mentioned reasons. This body location also demonstrates the radiative equilibrium cumulative effect. The semi-transparent markers are located below their isothermal counterparts. Since the heat flux associated with a radiative equilibrium is *higher* than an isothermal wall case, the difference between the material response wall temperature will be smaller. This results in a smaller prediction of the applied surface heat flux.

When the wall is *fully catalytic*, as in Fig. 5.11(b), the behavior is qualitatively similar to the stagnation point. Again, the cold wall and radiative energy conditions increase with respect to wall temperature up to around 2500 K before getting less and less conservative. Again, the radiative equilibrium cases are shown to be lower than their isothermal counterparts at this body location. The results for the Le = 1.4 and the SCEBD model are quite similar and not reproduced here.

Remarks on convective heat transfer in the film coefficient methodology

The film coefficient engineering model for evaluating aerothermal heating to a non-ablating, non-decomposing thermal protection system in a laminar, chemically reacting, dissociated flow is presented. Extensions to the film coefficient model such as mass injection, blowing, roughness augmentation, etc. were not assessed. The following conclusions may be drawn.

Edge properties

1. For a given body point, for a given trajectory point, the recovery enthalpy is essentially constant and insensitive to the tested assumptions. One exception

is an extremely hot wall (i.e. $T_w >> T_e$) which can cause conductive heating from the vehicle to the boundary layer at downstream locations.

2. The recovery factor is approximately constant for the tested set of assumptions and in the streamwise direction, due to the Prandtl number model.

Diffusion model

1. Generally, the SCEBD model produced higher film coefficients, followed by the Le = 1.4 and then the Le = 1.

2. Non-equilibrium wall enthalpy based film coefficients at the stagnation point (severe conditions) showed divergent behavior between the three diffusion models, attributable to the rate of increase of the mass diffusion term relative to the rate of decrease of the conduction term.

Mass boundary condition

1. Chemical equilibrium is not necessarily ensured with a kinetic model, even at harsh flight conditions.

2. The degree of non-equilibrium at the wall will increase the film coefficient heat flux prediction if the non-equilibrium wall enthalpy is greater than the equilibrium wall enthalpy, and conversely, decrease the heat flux prediction if the non-equilibrium wall enthalpy is less than the equilibrium wall enthalpy.

3. At high wall temperatures, the choice of heterogeneous models paired with an equilibrium wall enthalpy can produce unphysically large film coefficient values.

4. The conduction term and the mass diffusion term are inversely related to one another. As the wall temperature increases, the heterogeneous rates will increase (and in the case of recombination, release energy), while the thermal

gradient decreases. This process should be limited by chemical equilibrium, which depends on the chosen model for a mass boundary condition.

Energy boundary condition

1. Cold wall temperatures in nearly all cases produce material response heat fluxes conservative compared to the CFD predicted heat flux. The caveat associated with this boundary condition is the steep gradients produced by the low wall temperature, which may affect other boundary layer properties (such as integrated values to determine transition).

2. Hot wall temperatures under certain sets of assumptions will produce non-physical results and should be avoided when using the film coefficient model.

3. Radiative equilibrium BC produces a thermal distribution as a function of streamwise direction which increases the available energy at downstream body locations on the vehicle (relative to an isothermal solution).

Overall performance

1. The cold wall and radiative equilibrium energy boundary conditions with a non-catalytic wall and a non-equilibrium wall enthalpy will ensure a conservative estimate of the heat flux is produced by the film coefficient model.

2. The cold wall and radiative equilibrium energy boundary condition with a *fully catalytic* wall and non-equilibrium wall enthalpy will produce a conservative estimate of the heat flux up to approximately 3000 K.

If considering the film coefficient model as a Taylor Series expansion about the q_w^{CFD} term with respect to wall enthalpy (see Appendix F), then the best choice for an energy boundary condition would be radiative equilibrium. This not only produces a more physical temperature distribution at the wall, but also ensures that the initial

starting point of the CFD calculation will be in close proximity to the energy state in the material response. Therefore, the q_w^{CFD} term will need less of a correction. Compare this to the extreme corrections required using either too cold or too hot of an isothermal wall temperature. Further, it has become clear from this investigation, that an effort should be made to limit the chosen mass boundary condition at chemical equilibrium to avoid large discrepancies between the film coefficient prediction and the CFD calculation.

A primary focus of this investigation is to inform future aerothermal design of spacecraft. The majority of this analysis was conducted for a single flight condition and flight configuration. It may be extended to further flight space and numerous flight configurations, as appropriate for application. The role of spatial thermal distributions was evident at downstream locations, and this analysis could be repeated by comparing to CFD solutions using a radiative equilibrium boundary condition with non-physical emissivity values to replicate various wall energy states (instead of isothermal). In addition, a myriad of CFD parameters may be varied and investigated for downstream impact on the film coefficient model (such as radiation coupling, thermal and transport property models, for example). Of particular interest may be the continued analysis of diffusion vs. conduction effects as a function of wall temperature when better surface reaction models are available to characterize surface catalysis. It is also worth mentioning that nonlinear temperature dependent catalysis models (such as proposed by Stewart (81)) can lead to a non-conservative film coefficient (see Appendix G).

5.2 Examination of the heat and mass transfer analogy

This section investigates the scaling assumption which requires the heat and mass transfer analogy. It is given by

$$\dot{m}''_c = \rho_e u_e \mathrm{C_M} B'_c \approx \rho_e u_e \mathrm{C_{H_0}} \frac{\mathrm{C_H}}{\mathrm{C_{H_0}}} B'_c \tag{5.9}$$

where the mass transfer coefficient has been replaced by the film coefficient multiplied by the blowing correction. As the B'_c parameter is a function of the blown film coefficient, this re-normalizes the value to a physically scaled value in units of $\mathrm{kg/m^2/s}$. To isolate the effect of the assumption, multiple ballistic trajectories are flown and the peak heating flight condition is approximated. As this location in the trajectory is most likely to be in chemical equilibrium at the surface of the vehicle, an *accelerated* kinetic model (explained in the next sections) and the B' surface thermochemistry model are both evaluated. If the mass fractions produced by both surface chemistry models are roughly equivalent, then the difference in the solid ablation flux is due to the heat and mass transfer assumption.

Vehicle

Consider a perfect sphere with an undetermined thickness of Fiberform (a graphitic, non-charring TPS material) flying through a given trajectory in the Earth atmosphere. The sphere adopts a mass relevant to historic space capsules of 8000 kg, such as Apollo and the more recent Orion. The vehicle is modeled as a point mass in the trajectory code, and as a quarter arc in the flow field simulation. Each trajectory is considered ballistic, which results in no skip and a constant angle of attack of 0°.

Trajectories

The Kentucky Trajectory Modeling Program (KTMP) is used to compute a family of trajectories. See Appendix I for details on the required assumptions and the governing

Parameter	Value
Altitude at interface	125 km
Angle of attack	0°
Nose radius	2.5 m
Body shape	Spherical
Vehicle mass	8000 kg

Table 5.3: Common parameters for mass and heat transfer analogy study

Case	Entry Velocity [km/s]	Flight Path Angle [°]
A1	6	-4
A2	6	-10
B1	7	-1
B2	7	-10
C1	8	-2
C2	8	-4
C3	8	-8
D1	9	-4
D2	9	-6

Table 5.4: Dispersion conditions for mass and heat transfer analogy study

equations of motion. The attributes common to each trajectory are provided in Table 5.3. The dispersion conditions are listed in Table 5.4. By evaluating multiple flight conditions, it is possible to interpolate a generalized effect over a given flight space of interest. The flight corridor and peak heating locations are shown in Fig. 5.12. Notably, the 9 km/s, shallow entry angle case is a high enough velocity that even on a ballistic trajectory it tends to skip, a perhaps interesting case compared to the others which results in a rather high altitude, high velocity flight location.

Grid

A grid is hyperbolically extruded from the quarter arc of a 2.5 m circle. Grid convergence is ensured by doubling the node locations and comparing streamline values at the stagnation point and shoulder. The shock-adapted grid is shown in Fig. 5.1.

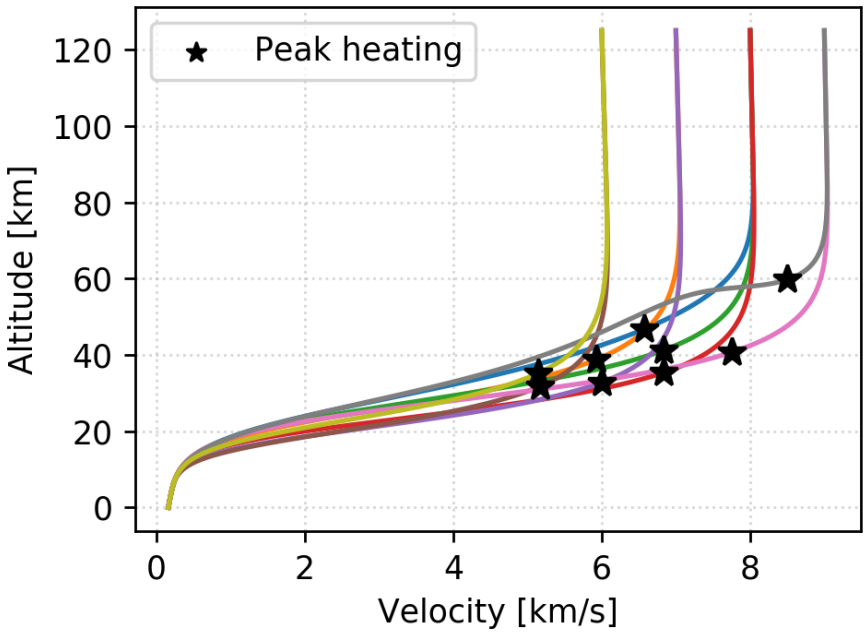

Figure 5.12: Analysis flight corridor with marked locations of peak heating

CFD

The flow field is computed and the axisymmetric grid adapted using the Data Parallel Line Relaxation (76) (DPLR) computer program. The atmospheric density for each CFD case is a function of altitude, using the Standard Atmosphere(22). The initial mass fractions are $N_2 = 0.767$ and $O_2 = 0.233$, neglecting trace elements. The viscosity and thermal conductivity are computed using the Gupta-Yos mixing model(79). The two-temperature model of Park is adopted for thermal non-equilibrium(80). Homogeneous equilibrium constants are computed from the NASA-9(78) data set. Each CFD solution is computed to a global density residual (as low as permitted by the solver), grid adapted, and then re-converged to a lowest possible error value. Each of the necessary initial conditions for the CFD solution are listed in Table 5.5. A standard contour plot is shown in Fig. 5.13, with a mirrored temperature and pressure field.

Case	Velocity [km/s]	Altitude [km]	Density [kg/m^3]	Temperature [K]
A1	5.140	35.158	8.25933e-03	236.951
A2	5.173	31.789	1.39981e-02	228.281
B1	5.927	38.788	4.77384e-03	246.998
B2	5.998	32.781	1.19820e-02	230.366
C1	6.574	46.762	1.54546e-03	269.027
C2	6.837	41.244	3.33708e-03	253.789
C3	6.829	35.332	8.04078e-03	237.433
D1	8.499	59.699	3.22691e-04	247.93
D2	7.756	40.721	3.59848e-03	252.343

Table 5.5: Initial conditions for mass and heat transfer analogy study

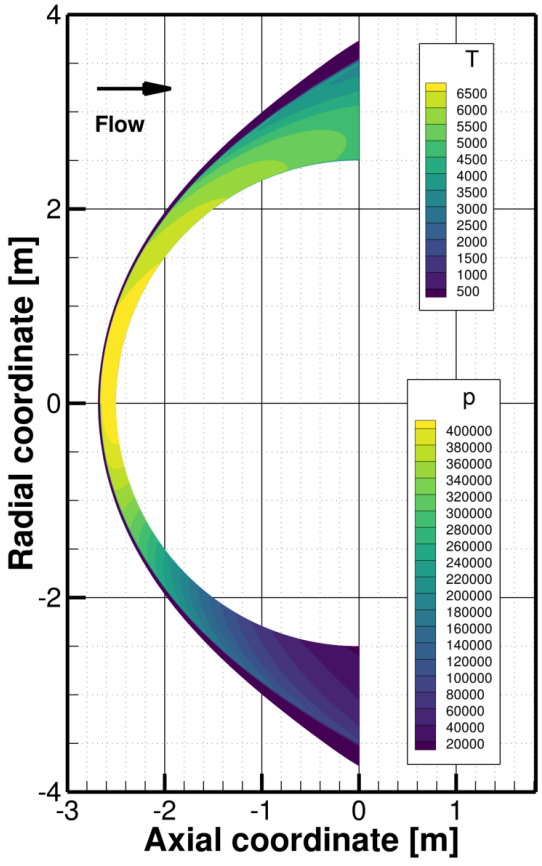

Figure 5.13: Grid-adapted CFD solution for sphere shaped vehicle analysis – temperature and pressure field contours

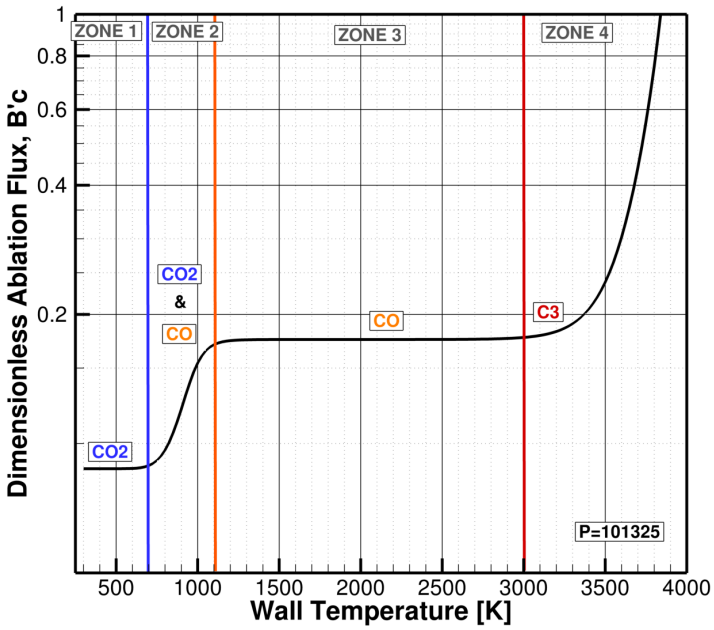

Figure 5.14: Film coefficient surface thermochemistry table for a carbon-air mixture

Chemistry models

To understand how to make a comparison of ablation rates using the two methodologies, it is essential to understand the film coefficient surface thermochemistry tables. Reproduced in Fig. 5.14 is the B' table for a carbon-air mixture with separate zones labeled for clarity. On the abscissa is the wall temperature, and the ordinate gives the dimensionless ablation flux value defined by

$$B'_c = \frac{\dot{m}''_w}{\rho_e u_e \mathrm{C_M}} \tag{5.10}$$

where for a surface ablator under the film coefficient methodology it is approximated as

$$B'_c = \frac{\dot{m}''_c}{\rho_e u_e \mathrm{C_{H_0}} \left(\frac{\mathrm{C_H}}{\mathrm{C_{H_0}}} \right)}. \tag{5.11}$$

Starting at low wall temperatures, Zone 1 is defined by the kinetically limited oxidation reaction of carbon to carbon dioxide. By kinetically-limited it is implied that the limiting factor is the speed of the reaction. In Zone 2, the production of

CO_2 and CO begins to occur. The speed at which the carbon monoxide is produced is faster than the CO_2 and produces twice as much ablation product as it requires only a single atomic oxygen. Thus, it increases the dimensionless ablation flux value to the approximate plateau value of $B'_c = 0.174855$, a commonly cited and well-known value from the literature. The plateau value marks Zone 3, the diffusion limited regime where the amount of ablation occurring at the surface is limited by the availablity of atomic oxygen reaching the surface through mass diffusion. Under the film coefficient methodology, the equilibrium solver only gives the mass composition and the re-scaling of the dimensionless ablation flux is the part of the calculation that introduces the effect of mass diffusion. Finally, Zone 4 is when the surface becomes energetic enough to permit intramolecular reactions between the carbon atoms that directly produce a sublimate.

To provide a one-to-one comparison between chemistry models, a novel kinetic reaction scheme is devised for the DHA methodology. The reaction set includes the 4 surface reactions from the Park 1976 model, as well as an additional surface catalyzed nitric oxide dissociation reaction.

$$O_2 + (s2) + C(b1) \leftrightarrow CO + O + (s2) \tag{5.12}$$

$$O + (s2) + C(b1) \leftrightarrow CO + (s2) \tag{5.13}$$

$$O + (s1) \leftrightarrow O(s1) \tag{5.14}$$

$$O + O(s1) \leftrightarrow O_2 + (s1) \tag{5.15}$$

$$NO + (s2) \leftrightarrow N + O + (s2) \tag{5.16}$$

Equation	Reaction Type	Reaction coefficient (1/s)	Activation Energy, E_a (J/kg)
5.21	Eley-Rideal	$\gamma_0 = 1.00$	0.00
5.22	Eley-Rideal	$\gamma_0 = 1.00$	9.644×10^3
5.23	Adsorption	$S_0 = 1.00$	9.644×10^3
5.24	Eley-Rideal	$\gamma_0 = 1.00$	9.644×10^3
5.16	Eley-Rideal	$\gamma_0 = 1.00$	0.000

Table 5.6: *Modified* Park model for artificially enforced chemical equilibrium

The reaction parameters have been modified to the values given in Table 5.6. As will be shown in the forthcoming analysis, the result of modifying the reaction parameters is a model which forces oxidation of atomic oxygen species, while freeing nitrogen to recombine to its molecular form. To further guarantee this, and ensure numerical stability, no reverse reactions are used in the kinetic scheme. Reaction 5.16 was added because it was found through numerical experimentation that the nitric oxide formed upstream would persist along a given streamline all the way to the wall. This tied up oxygen and nitrogen so that other equilibrium products could not be formed.

Analysis

As defined by Eq. 4.24, the solid ablation flux is comprised of the carbonaceous species from the bulk phase. Logically, this makes sense as the more carbon which is liberated from the bulk phase as a gaseous species equates to a higher amount of surface recession. Based on the previous discuss about the surface thermochemistry tables, the expected products are carbon dioxide, carbon monoxide, and C_3 (also referred to as tricarbon). As only carbon monoxide will be produced by the modified park surface reactions, the mole fraction of carbon monoxide can provide an important baseline for interpretation. Figure 5.15 shows the mole fraction, denoted (by X_CO) on the y-axis plotted against the wall temperature from the DHA CFD. The blue circle markers are the carbon monoxide produced for each different case at varying flight conditions and

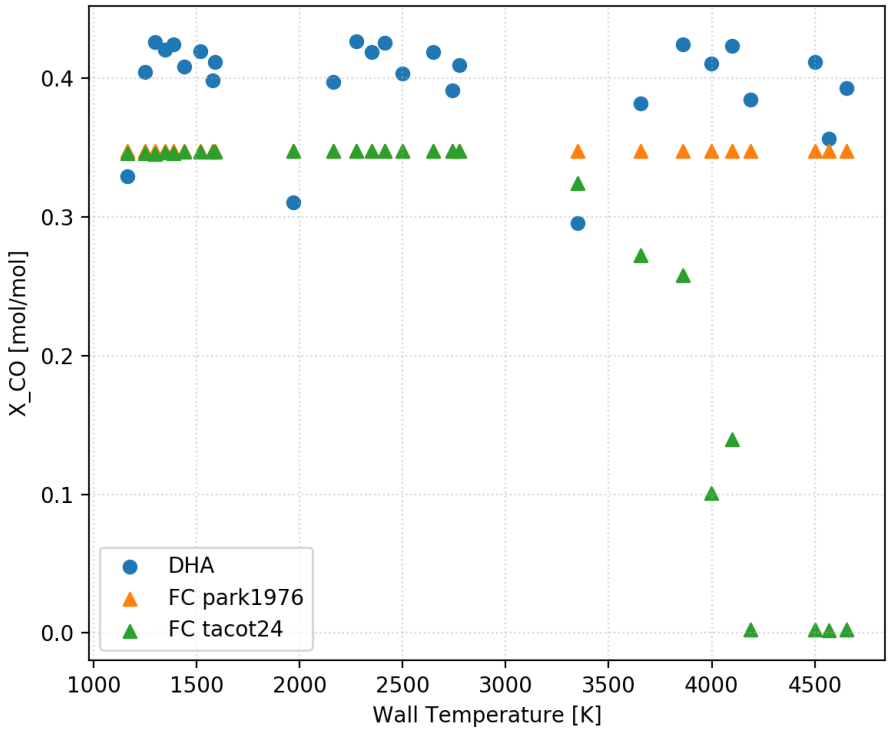

Figure 5.15: Variation in carbon monoxide mole fractions at stagnation point

epsilons. The orange triangle markers represent the carbon monoxide mole fraction given by a surface thermochemistry table only using the species available in the park 1976 surface chemistry model (strictly CO). The green triangle markers represent the carbon monoxide mole fraction using all of the available species associated with the TACOT species (24 of them, hence tacot 24), which permits CO_2 and C_3.

With the exception of a single trajectory point (the lofted case), the accelerated kinetic mechanism has produced a high relative amount of carbon monoxide. The B' table developed with only park 1976 species shows a nearly constant value which represents the carbon monoxide plateau. This initial finding may have been predicted, but it is also extremely important. With no backward reactions, a large excess of carbon has been oxidized, and the amount of carbon being oxidized should be proportional to the amount of surface ablation occurring. If this is the case, then it would stand that for all instances where ablating CFD has been computed, that the solid

ablation flux should be larger.

Adding the other available species to the B' calculation allows some divergences from this behavior in the kinetically controlled region (low wall temperature). In this instance, some CO_2 is now beginning to form at these flight conditions. At the other end of the temperature spectrum, as the 3000 K threshold is crossed, the CO mole fraction begins to decrease rapidly. This indicates a transition to the sublimation regime, where tricarbon is now being produced instead of carbon monoxide.

An important note about this tricarbon production, is that the extreme high temperatures seen in this analysis are due to the logarithmic range of the epsilon parameter. The very low value of $\epsilon = 0.1$ physically acts to contain energy at the surface (decreasing the reradiation term). More physical temperature estimates will be close to $\epsilon = 1$ and this should be kept in mind when choosing not only the epsilon range, but also the surface reaction scheme.

Bearing these considerations in mind, the percent difference between the DHA and FC solid ablation fluxes is proposed as an analysis metric,

$$\Delta = \frac{\dot{m}_c''\,(\mathrm{DHA}) - \dot{m}_c''\,(\mathrm{FC})}{\dot{m}_c''\,(\mathrm{DHA})} \times 100 \tag{5.17}$$

where the solid ablation flux $\dot{m}_c''$ has been directly extracted from the DHA method and the film coefficient solid ablation flux is calculated according to Eq. 5.9. The B' value obtained for the film coefficient must be a function of the wall temperature and pressure as calculated by the DHA method to make the comparison one-to-one.

Figure 5.16 shows this metric plotted against the wall temperature. Results for wall temperatures above 3000 K have been removed as the kinetic mechanism has no reaction capable of producing tricarbon and thus the comparison is no longer one to one. In the temperature range which is more applicable to space flight, the results of the comparison show that the film coefficient predicted solid ablation flux is consistently higher than that predicted by the DHA method. The comparisons with non-catalytic film coefficients show a variation between roughly 20 and 80 percent.

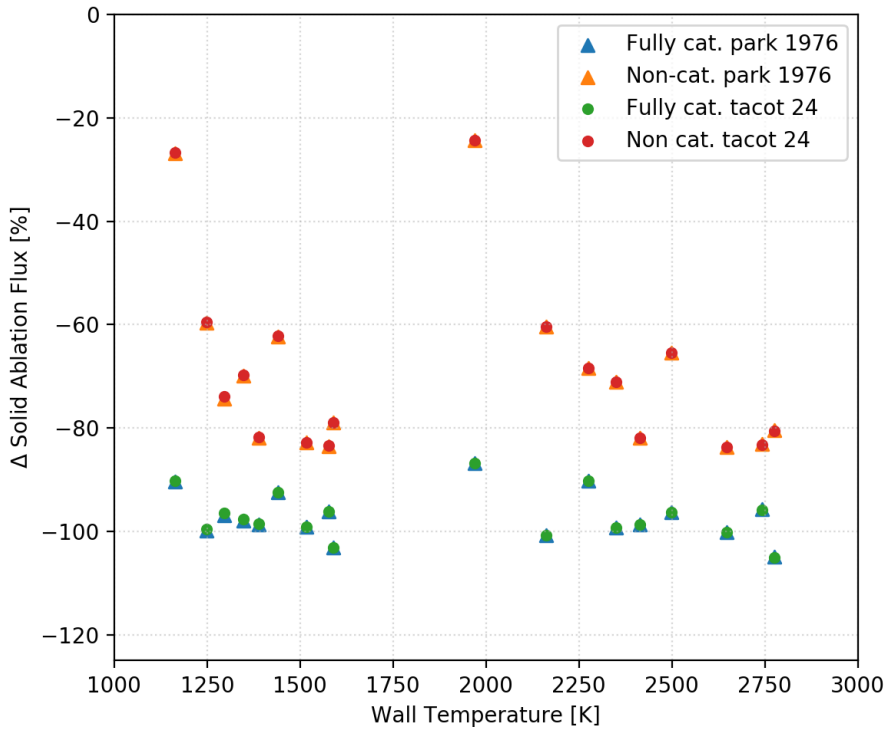

Figure 5.16: Percent difference between film coefficient predicted solid ablation flux and the DHA method at the stagnation point

The family of solid ablation fluxes constructed with a fully catalytic tend to predict 80 to 100 percent more solid ablation, roughly speaking.

This is counter-intuitive to the results obtained in Fig. 5.15. Those results showed the DHA method with *more* carbon monoxide than the FC method in the wall adjacent fluid. The only way the FC method can obtain a higher solid ablation flux is through the scaling parameter, the blowing corrected film coefficient.

Therefore, for the stagnation point, for the chosen flight conditions, it may then be concluded that even with an unreasonably fast kinetic mechanism which over-shot chemical equilibrium mole fractions of carbon monoxide, the practice of re-scaling the non-dimensional blowing parameter with the corrected film coefficient is largely conservative. If a kinetic mechanism which perfectly replicated chemical equilibrium was used, the result would be an even larger discrepancy between solid ablation fluxes.

The exact same process may be applied to the downstream shoulder location.

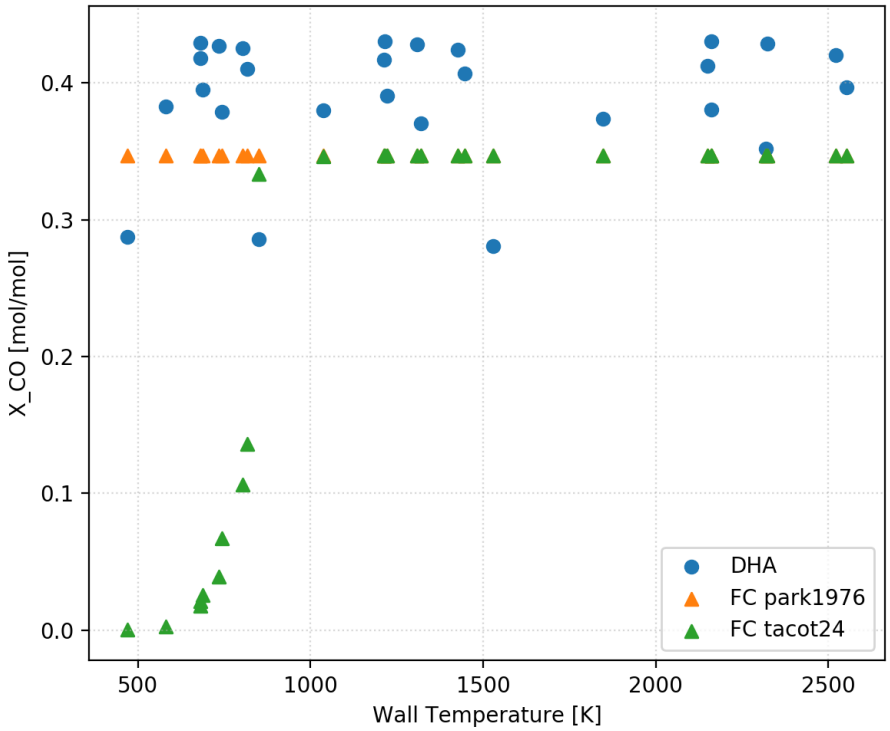

Figure 5.17: Variation in carbon monoxide mole fractions at shoulder location

Figure 5.17 shows the carbon monoxide mole fractions at the shoulder for each engineering method. Again, the lofted case for the DHA method produces a lower carbon monoxide fraction. More interesting is the low temperature range, which demonstrates the kinetically-limited carbon dioxide regime. The film coefficient carbon monoxide production decreased rapidly at temperatures between 500 and 1000 K, exactly where the B' table diverges. As seen in the B' table, this causes the ablation rate to decrease as a function of the amount of oxygen which needs to be consumed for a single carbon atom. In the figure, this translates to a rapid drop in CO as CO_2 becomes the dominant product.

Figure 5.18 shows the percentage difference in ablation as a function of wall temperature. Again, the lower wall temperature range which reflects CO_2 production is not compared (although the trend is quite similar) as the comparison is not one-to-one. In the wall temperature range where carbon monoxide is the dominant product,

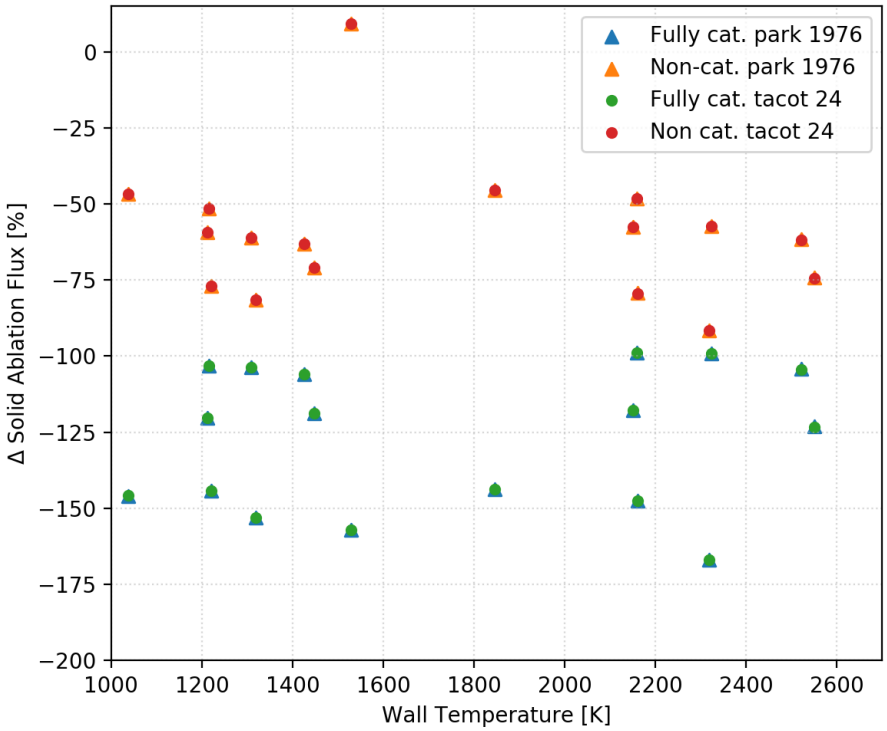

Figure 5.18: Percent difference between film coefficient predicted solid ablation flux and the DHA method at the shoulder location

the trend clearly shows a higher amount of solid ablation flux according to the film coefficient methodology. Again, the non-catalytic cases have a smaller percent difference than the fully catalytic cases. Some of the fully catalytic cases exceed 150% difference.

Notably, a single point through the flight space has a kinetic solid ablation flux higher than film coefficient. Recall that there were three lofted cases for variable emissivities that had lower carbon monoxide mole fractions. The emissivity values of $\epsilon = 1$ and $\epsilon = 10$ both yielded wall temperatures in the CO_2 range, so they are not included in the figure. The low emissivity value of $\epsilon = 0.1$ maintains a large amount of energy, resulting in a warmer surface temperature than the other two cases. This case predicts a DHA solid ablation flux that is approximately 10% higher than the film coefficient case.

From flat plate boundary layer theory, there also exists the relation

$$\frac{C_H}{C_M} = Le^{2/3} \tag{5.18}$$

which is sometimes encountered for non-similar, chemically reacting flows (40). Taking a Lewis number of 1.4 this equates to a 20% reduction which shifts the solid ablation prediction of the film coefficient method in the correct direction. As Le = 1.4 is for air, this number may change at the wall where a large number of ablating species are present. In the author's experience, carbon ablators tend to reduce the Lewis-Semenov number to a value closer to unity which does not make the above relation useful.

Remarks on mass and heat transfer analogy analysis

In summary, a small subset of CFD solutions were assessed for a family of dispersed trajectories. The peak heating location in the trajectory, chosen as the most amenable to the chemical equilibrium condition, provided a wide range of velocities, altitudes, and wall temperatures. Using a kinetic mechanism which rapidly oxidizes carbon to levels beyond that predicted by a chemical equilibrium solver, it was found that the excess carbonaceous species did not exceed that predicted by the film coefficient method. The only way this can be possible is through the scaling mechanism inherent in the film coefficient methodology. This is numerical evidence that the film coefficient method predicts large values of solid ablation flux relative to directly computed ablation rates due to assumptions inherent to the method itself.

While conservative estimates of solid ablation flux may be designed to in a flight program, other problems may arise from excess shape change. For example, the prediction of burn-through in localized regions that have augmented heating on a vehicle. Another example would be smaller vehicles with vectorized thrust which may require accurate prediction of ablating shape change for guidance considerations.

This analysis may be further extended by coupling the surface thermochemistry tables directly to a CFD solver and solving the resulting system of equations with the computed mass diffusion fluxes. As reported in the Chapter 3.3, this was has been performed by de Muelenaere and Magin (7), but the discrepancy was not rigorously investigated further. This approach could be used to develop static B' tables that include the mass diffusion effects as a function of flight space.

5.3 Numerical case study: Spherical geometry

The current section investigates how the primary quantities of interest, the surface temperature and recession rate (a function of the solid ablation flux), in an engineering design analysis cycle will vary under the Film Coefficient (FC) and the Direct Heating and Ablation (DHA) methodologies for a fixed heatshield thickness. The methodologies are further compared by using an iterative heatshield sizing tool to determine the necessary thickness for reaching a maximum bondline temperature.

Trajectory and vehicle

Consider a perfect sphere with an undetermined thickness of Fiberform (a graphitic, non-charring TPS material) flying through a given trajectory in the Earth atmosphere. The sphere adopts a mass relevant to historic space capsules, such as Apollo and the more recent Orion. The Kentucky Trajectory Modeling Program (KTMP, Appendix I) is used to compute a target trajectory in conjunction with the Sutton-Graves heat flux correlation (75). Based upon engineering judgement, the trajectory parameters given in Table 5.7 should lead to dissociation of both molecular species and the formation of nitric oxide without reaching conditions energetic enough to promote ionization.

Locations along the computed trajectory are selected to capture the curvature of the correlation heat flux. Figure 5.19 shows the altitude, velocity, and heat flux as

Parameter	Value	Units
Initial Velocity	6	km/s
Flight path angle	-1	degrees
Altitude at interface	125	km
Angle of attack	0	degrees
Nose radius	2.5, 0.5	m
Body shape	Spherical	
Vehicle mass	8000	kg

Table 5.7: Demonstration test-case entry conditions

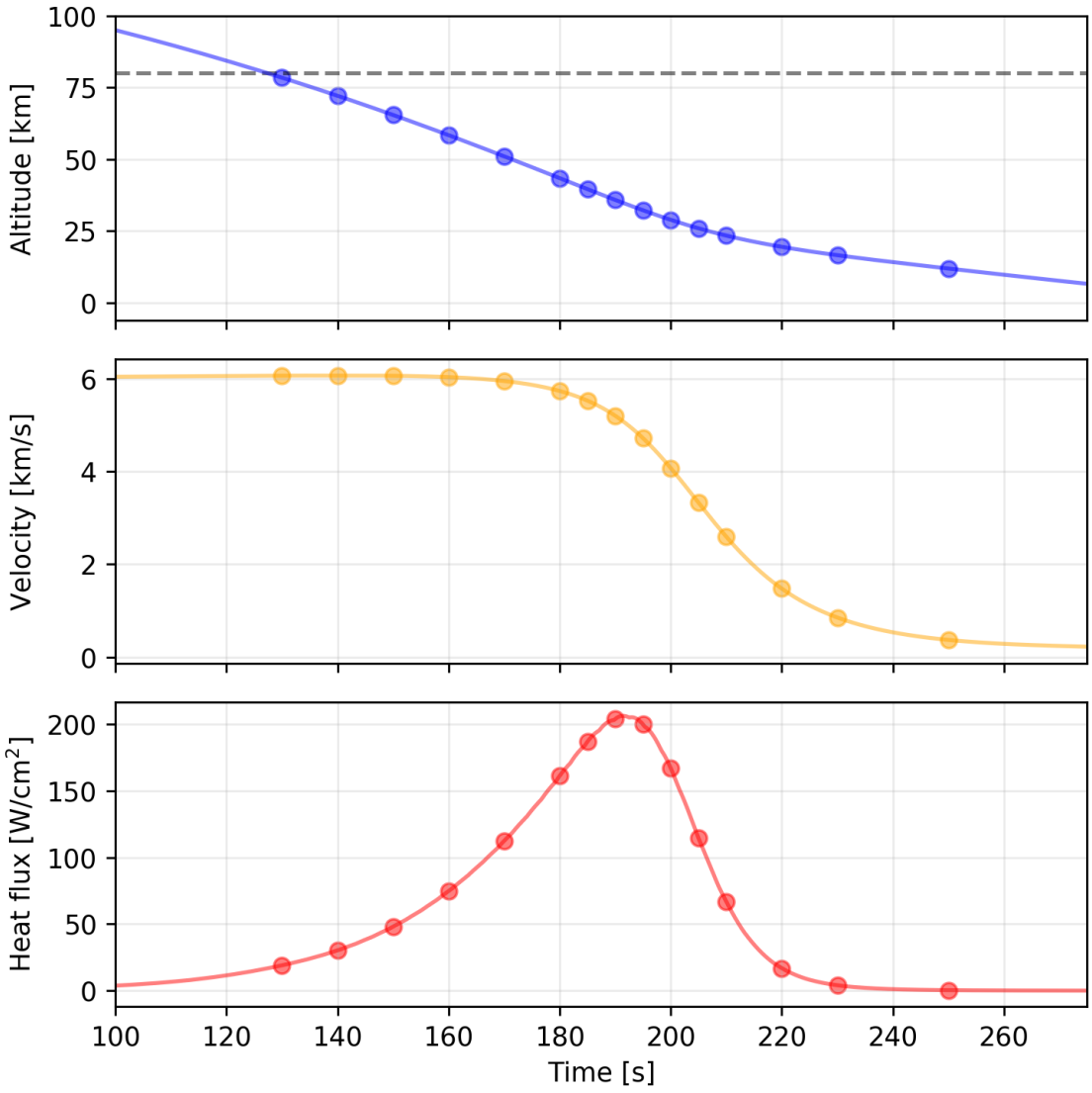

Figure 5.19: Trajectory data for $v_i = 6$ km/s and $\gamma = 1°$.

Time [s]	Altitude [m]	Velocity [m/s]	Density [kg/m^3]	Temperature [K]
1.3000e+02	7.8476e+04	6.0694e+03	2.7206e-05	201.612
1.5000e+02	6.5485e+04	6.0677e+03	1.7302e-04	231.962
1.7000e+02	5.1051e+04	5.9549e+03	1.0568e-03	270.650
1.8000e+02	4.3441e+04	5.7398e+03	2.7097e-03	259.859
1.8500e+02	3.9618e+04	5.5310e+03	4.5442e-03	249.293
1.9000e+02	3.5856e+04	5.2049e+03	7.7853e-03	238.884
1.9500e+02	3.2247e+04	4.7212e+03	1.3430e-02	228.886
2.0000e+02	2.8906e+04	4.0754e+03	2.2674e-02	225.425
2.1000e+02	2.3402e+04	2.5964e+03	5.4477e-02	219.966
2.2000e+02	1.9474e+04	1.4753e+03	1.0428e-01	216.650
2.3000e+02	1.6565e+04	8.5089e+02	1.6920e-01	216.650
2.5000e+02	1.1912e+04	3.6785e+02	3.3349e-01	216.650

Table 5.8: CFD initial conditions for chosen trajectory points of Sphericus flight.

a function of time. The earliest point in the trajectory is dictated by the continuum condition, denoted in the top subfigure by a dashed gray line. The relevant quantities required for initializing CFD solutions for a given trajectory point are given in Table 5.8.

Grid

A grid is hyperbolically extruded from the quarter arc of a 0.5 m and 2.5 m circle. Grid convergence is ensured by doubling the node locations and comparing streamline values at the stagnation point and shoulder. Two body points on the vehicle are analyzed, the stagnation point and the 90° shoulder, shown in Fig. 5.1. For the material response simulations that require a fixed depth, a 1-dimensional grid was generated with a stretching ratio of 1.02 starting from a front element sized at 1×10^{-8} m. This is placed on top of a $1/8^{\text{th}}$ inch aluminum substructure, gridded by inheriting the final cell of the carbon layer as the first element size, with a stretching ratio of 5%. The fixed depth for this analysis was 2 inches, regardless of the vehicle nose diameter or methodology being used.

Parameter	Film Coefficient	Direct Heating & Ablation
Wall Mass BC	Full/Non-catalytic	Park 1976
Wall Energy BC	Rad. Eq.	Rad. Eq. (ablative species)
Available Species	N_2, O_2, NO, N, O	N_2, O_2, NO, N, O, CO, C_2, CN, C
Surface Emissivity	0.88	[0.1,7.0]

Table 5.9: Variable CFD parameters

CFD

The flow field is computed and the axisymmetric grid adapted using the Data Parallel Line Relaxation (76) (DPLR) computer program. The atmospheric density for each CFD case is a function of altitude, using the Standard Atmosphere(22). The initial mass fractions are $N_2 = 0.767$ and $O_2 = 0.233$, neglecting trace elements. The viscosity and thermal conductivity are computed using the Gupta-Yos mixing model(79). The two-temperature model of Park is adopted for thermal non-equilibrium(80). Homogeneous equilibrium constants are computed from the NASA-9(78) data set. Two body points on the vehicle are analyzed, the stagnation point and the 90° shoulder, shown in Fig. 5.1. Between the two models, the varying parameters are given in Table 5.9. The surface emissivity range defined in the DHA column of Table 5.9 is non-physical above 1. These non-physical values are used to reach lower wall temperatures, while maintaining the influence of the flow field physics on the spatial temperature distribution. Each CFD solution is computed to a global density residual (as low as permitted by the solver), grid adapted, and then re-converged to a lowest possible error value.

Chemistry models

The homogeneous model used by the film coefficient method is due to Park (54) and colloquially called 5-species air. The surface chemistry in the CFD is modeled as either non-catalytic, such that the mass fraction gradient at the wall is zero, or using

the Park model (69). This model suggests that the chemical production term in the species equation may be modeled by

$$\dot{\omega}_i = \rho_i \gamma_i(T_w) \sqrt{\frac{RT_w}{2\pi M_i}} \tag{5.19}$$

where ρ_i is the species density, T_w is the wall temperature, R is the universal gas constant, and M_i is the molecular weight of species i. The probablistic term in Eq. 5.19 is defined as

$$\gamma_i\left(T_w\right) = \gamma_{i_0} \exp \frac{T_{ac}}{T_w} \tag{5.20}$$

where T_{ac} is the activation energy divided by the gas constant, and γ_{i_0} is the accommodation coefficient. This model requires that γ_{i_0} has a constant value of unity (i.e. *fully catalytic*), for all molecules except NO. Due to a lack of catalytic data, the nitric oxide species considered for the Park model is $\dot{\omega}_{NO} = 0$.

To simulate the Fiberform material, the charred material properties of TACOT (82) are employed. This is a theoretical material used to simulate low-density porous ablators whose carbon substrate is Fiberform. The surface thermochemistry therefore becomes the associated B' table with the constraint that the pyrolysis gas term is strictly zero. For an example of the B' and wall enthalpy curves associated with this material, see Fig. 4.1.

The DHA method uses an extended form of the same Park model, using the reactions listed in Table 5.11. The surface thermochemistry model adopted by the DHA method is the Park 1976 carbon oxidation model (13), given by the following four surface reactions:

$$\mathrm{O}_2 + (s2) + \mathrm{C}(b1) \leftrightarrow \mathrm{CO} + \mathrm{O} + (s2) \tag{5.21}$$

$$\mathrm{O} + (s2) + \mathrm{C}(b1) \leftrightarrow \mathrm{CO} + (s2) \tag{5.22}$$

$$\mathrm{O} + (s1) \leftrightarrow \mathrm{O}(s1) \tag{5.23}$$

Parameter	Variable	Value	Units
Number of surface phases	nsp	2	
Number of bulk phases	nbp	1	
Number of gas species	ngps	3	
Surface site density	Φ	7.5×10^{-6}	mol/m^2
Carbon solid density	ρ_s	175	kg/m^3
O_2 Dissociation Energy	E_{diss}	0.493440	MJ/mol
CO Dissociation Energy	E_{diss}	1.071726	MJ/mol
Eq. 5.21 Eley-Rideal reaction efficiency	γ_0	0.01	
Eq. 5.22 Eley-Rideal reaction efficiency	γ_0	0.63	
Eq. 5.23 Sticking coefficient	S_0	0.63	
Eq. 5.24 Eley-Rideal reaction efficiency	γ_0	0.63	
Eq. 5.21 Eley-Rideal energy barrier	E_{er}	0	J/mol
Eq. 5.22 Eley-Rideal energy barrier	E_{er}	9.644×10^3	J/mol
Eq. 5.23 Adsorption energy barrier	E_{ad}	9.644×10^3	J/mol
Eq. 5.24 Eley-Rideal energy barrier	E_{er}	9.644×10^3	J/mol

Table 5.10: Park 1976 (13) surface reaction model parameters

$$O + O(s1) \leftrightarrow O_2 + (s1) \tag{5.24}$$

The parameters associated with these surface reactions are given in Table 5.10 with the same nomenclature as dictated by Maclean and Marschall.

Fixed depth analysis

For the case of a uniform, 2 inch Fiberform heatshield on the spherical spacecraft, the surface temperature and solid ablation flux values have been plotted as they occur in the material response simulation. The FC method is plotted as a range (the gray area) between the Park fully catalytic model (black line) and the non-catalytic model (blue line). This provides a range of applicability, with exception to the super-catalytic boundary condition. The gold line represents the result of the DHA method using the Park oxidation model.

Figure 5.20 shows the surface temperature results for the two body locations, for both nose radii. Figures 5.20(a) and 5.20(b) show the resulting surface temperature

Dissociation Reactions
$N_2 + M \leftrightarrow N + N + M$
$O_2 + M \leftrightarrow O + O + M$
$C_2 + M \leftrightarrow C + C + M$
$CN + M \leftrightarrow C + N + M$
$NO + M \leftrightarrow N + O + M$
Exchange Reactions
$N_2 + O \leftrightarrow NO + N$
$NO + O \leftrightarrow O_2 + N$
$CO + C \leftrightarrow C_2 + O$
$CO + O \leftrightarrow O_2 + C$
$CO + N \leftrightarrow CN + O$
$N_2 + C \leftrightarrow CN + N$
$CN + O \leftrightarrow NO + C$
$CN + N \leftrightarrow C_2 + N$

Table 5.11: Park modified with carbon species reactions

histories for the stagnation point. The DHA method and the fully catalytic FC method produce similar temperatures, while the non-catalytic is noticeably lower in the early trajectory and up to peak heating. This suggests, at stagnation conditions (higher pressure and temperature), that the ablative species in the boundary layer are increasing the conduction and diffusion fluxes in an amount close to the exothermic energy release of the catalytic recombination.

Beyond peak heating, all three predictions converge to an approximately equal value. The convergence of the two mass BC's of the FC method suggests that catalysis has essentially stopped around 210 seconds. This further indicates that conditions have changed in the boundary layer such that atomic species are no longer reaching the wall. Similarly, the DHA method mass BC is a function of both wall temperature and atomic species concentrations (or densities). As advective currents carry away carbonaceous species, and fewer and fewer atomic species arrive at the wall, the DHA method will essentially yield a surface temperature due to an air environment. The convergence of the three methods suggests that this is occurring late in the trajectory.

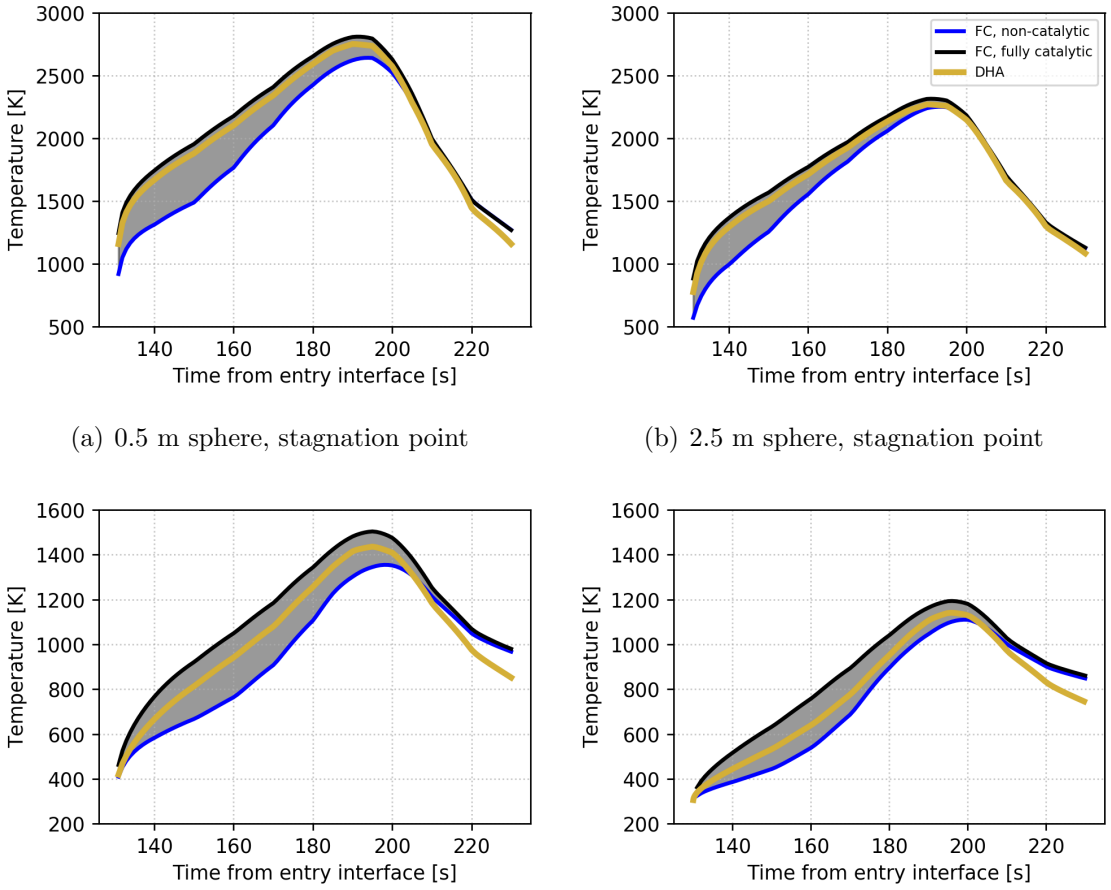

(a) 0.5 m sphere, stagnation point

(b) 2.5 m sphere, stagnation point

(c) 0.5 m sphere, shoulder

(d) 2.5 m sphere, shoulder

Figure 5.20: Surface temperature comparison between FC and DHA methods

It may also be pointed out that the equilibrium assumption of the film coefficient method produces a finite ablation flux, but it is not of sufficient magnitude to drive the surface temperature.

The shoulder surface temperature predictions seen in Figs. 5.20(c) and 5.20(d) demonstrate a similar range within the two mass boundary conditions selected for the FC method. However, at this body location, the DHA method predicts a surface temperature roughly in between the two ranges of catalycity. This is an important feature, as it introduces the concept that the DHA method will alter the surface temperature depending on the physics that are occurring at a given body location on the vehicle. In other words, at the stagnation point, the vehicle's surface may be

in chemical equilibrium. But moving away from the stagnation point to downstream regions, the lower temperatures and pressures, accompanied by a thicker boundary layer, may not be in chemical equilibrium. This effect may also be deduced from the fact that the smaller nose radius vehicle has a DHA prediction closer to fully catalytic than the 2.5 m nose radius. This is because, the 0.5 m vehicle has temperatures higher at any given point in the trajectory (a result known from classical boundary layer theory).

The convective cooling phase of flight at the body shoulder location also exhibits interesting behavior. The FC method predictions converge, as they did at the stagnation point. However, the DHA method continues to decrease below the FC prediction. As has already been suggested, catalysis has ended at this point in the trajectory. The difference is the evaluation of the wall enthalpy. The wall enthalpy used in the aeroheating boundary condition is an interpolated result from the chemical equilibrium surface thermochemistry tables. In contrast, the DHA method will give the wall heat flux *directly* from the CFD, which means that it is a function of the non-equilibrium wall enthalpy. In severe cases, the chemical equilibrium assumption will make the surface temperature plateau, a modeling error known as *endgame recession*. This often results, in engineering practice, in the development of complicated surface thermochemistry tables that include a switch to non-equilibrium conditions at certain a Mach number. This modeling inaccuracy is completely avoided by the DHA method.

Figure 5.21 uses the same format to present the solid ablation flux predictions of both methods. Notably, the ordinate is plotted in the log scale to facilitate ease of comparison for the DHA method. The general trend in Fig. 5.21 suggests that the ablation rate from the Park 1976 carbon oxidation model most closely resembles the B' value scaled by a fully catalytic film coefficient. In Fig. 5.21(d) the kinetic rate even exceeds the equilibrium condition, due to the model not computing backward

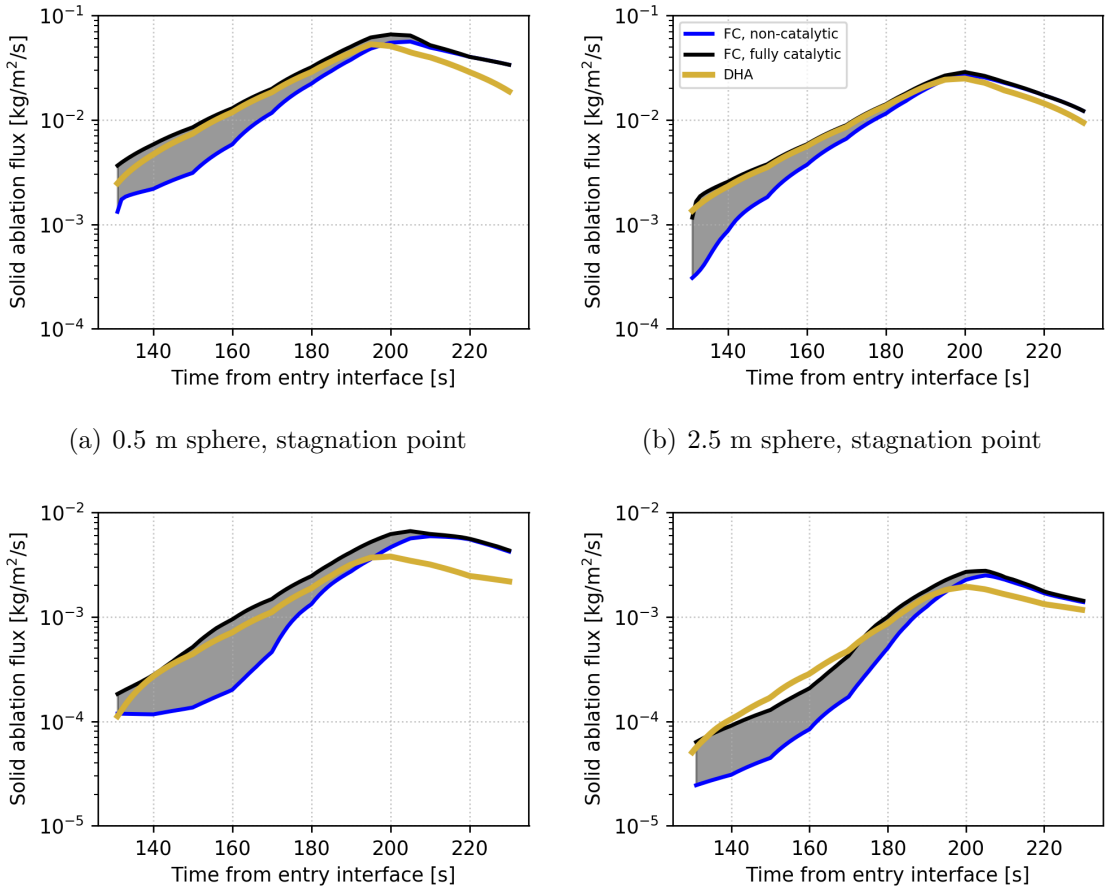

(a) 0.5 m sphere, stagnation point

(b) 2.5 m sphere, stagnation point

(c) 0.5 m sphere, shoulder

(d) 2.5 m sphere, shoulder

Figure 5.21: Solid ablation flux comparison between FC and DHA methods

rates.

Another noticeable feature is the decline in ablation after peak heating. All four subplots show that ablation decreases more rapidly under the Direct Heating and Ablation methodology. This is significant, again, because it demonstrates the ability of the DHA method to change with the expected physics. During the late trajectory, the surface temperature rapidly cools, the dynamic pressure drops, and conditions are more suitable for chemical non-equilibrium. The film coefficient methodology does not recognize this sudden change, and instead offers a conservative estimate based on scaling and chemical equilibrium. In predicting burn-through, the transience of the ablation may be an important detail that cannot be overlooked.

Finally, another notable difference in the solid ablation flux trends is seen in all subplots except Fig. 5.21(b). For the FC method, the maximum value of solid ablation flux along the trajectory occurs around 200 seconds. However, the DHA method shows a peak around 190-195 seconds. Contrasting this with the behavior of the surface temperature, the peak surface temperature for both methods (and for all body locations/nose radii) occurs at the same time as the peak solid ablation flux for the DHA method. When considering the B' tables associated with a carbon-air mixture, the CO plateau occurs across the surface temperatures experienced over the trajectory. This constant value is rescaled into dimensional form by the film coefficient. On the contrary, the DHA method predicts instantaneous solid ablation flux values *directly* in the CFD, which yields a strong correlation to the surface temperature.

Heatshield sizing analysis

For a proposed *given* heatshield thickness, the previous analysis is adequate. However, for determination of the heatshield thickness, the surface recession and heat flux are inputs into the sizing process. The CHAR program is capable of finding the optimal thickness for given boundary conditions, based on the known failure temperature of the substructural material. The sizer option minimizes material thickness in order to meet the user-specified temperature constraints.

Consider then a substructural material of aluminum with a bondline temperature requirement of 450° Fahrenheit. Tables 5.12 and 5.13 show the resulting recession data for sizing the Fiberform heatshield of the 2.5 m and 0.5 m vehicles. The first two rows give the recession measurement and sizing for the stagnation point, and the last two rows give the same measurements for the shoulder. The first three columns are the DHA method, and the FC method with a fully catalytic and non-catalytic mass BC in the CFD. The last two columns are the percentage difference between

Parameter	DHA [mm]	FC [mm] fully cat.	FC [mm] non-cat.	Δ [%] fully cat.	Δ [%] non-cat.
Stag. recess	6.793	7.629	6.713	10.96	-1.192
Stag. sizing	25.67	26.12	24.39	1.723	-5.248
Shoulder recess	0.514	0.635	0.502	19.06	-2.390
Shoulder sizing	12.94	14.51	11.99	10.82	-7.923

Table 5.12: Recession depth and heat shield sizing for 2.5 m nose radius sphere

Parameter	DHA [mm]	FC [mm] fully cat.	FC [mm] non-cat.	Δ [%] fully cat.	Δ [%] non-cat.
Stag. recess	14.08	17.64	14.08	20.18	0.0
Stag. sizing	29.76	30.61	27.58	2.777	-7.904
Shoulder recess	1.038	1.719	1.319	39.62	21.30
Shoulder sizing	17.62	18.81	15.99	6.326	-10.19

Table 5.13: Recession depth and heat shield sizing for 0.5 m nose radius sphere

the DHA method prediction and the FC method.

Looking to Table 5.12, it is seen that the DHA method predicts recession and sizing below the fully catalytic film coefficient, and above the non-catalytic film coefficient at both body locations. By comparing the DHA method to the fully catalytic film coefficient, it is seen that the sizing at the stagnation point is less sensitive to the recession rate than the shoulder. A 10% difference in recession at the stagnation point causes a nearly 2% sizing difference. Conservely, at the shoulder, a 20% difference in recession causes a nonlinear jump up to almost 11% sizing difference. Since the total recession is a significant portion of the total thickness, a considerable amount of thermal mass is lost through the trajectory, resulting in higher temperatures. Comparing to the non-catalytic results, the scaling due to the film coefficient greatly reduces the overall recession. However, the relatively small difference in recession at both locations (1-2%) does not drive the variation in heatshield thickness. In this instance, the energy contribution from the surface ablation is so small, the driving factor becomes the incorporation of the ablative species into the conduction

and mass diffusion fluxes. As will be shown later, the percentage of energy contribution from various component fluxes shifts dramatically when the ablative species are included in the CFD calculation. This indicates that the physics are driving the heatshield sizing, instead of an arbitrary mass transfer assumption at the wall.

Next, the radius of the vehicle is decreased. Table 5.13 shows the sizing analysis results for the 0.5 m vehicle. As predicted by the classical result of Allen and Eggers (83), this increases the heating. The elevated heating levels have concurrently higher recession and sizing values. At the stagnation point, the chemical equilibrium assumption predicts 20 to 40% more recession than the kinetic model. Interestingly, the shoulder location seems to be less sensitive to the recession than for the larger diameter vehicle. The smaller vehicle and larger vehicle both had doubled increases in recession moving from stagnation point to shoulder. However, the smaller vehicle's shoulder sizing thickness difference between methods increased by only 6%. This, again, alludes to the modified conduction and diffusion fluxes taking into account the ablative species in the boundary layer.

Comparison of the DHA method to the non-catalytic film coefficient reveals some chemical non-equilibrium effects for the 0.5 m vehicle. Decreasing the nose radius of the vehicle reduces the advective time scale, and consequently, it is seen that the non-catalytic film coefficient predicts a higher total recession amount than DHA method. In this instance, the ablation predicted by the DHA method is less than or equal to (rounded) the non-catalytic case, and yet despite losing more mass it has a smaller heatshield sizing thickness. This re-iterates the central theme of the DHA method, the ablative species are modeled in the CFD and transferred to the material response without the use of a correction model.

From a bird's eye view, looking at both Tables 5.12 and 5.13, it is also necessary to point out that all engineering methodologies wound up within $\pm$ 10% of one another. This simply demonstrates the margin associated with the entire adoption of the DHA

process relative to the heritage process.

Blowing correction assessment

In Fig. 5.22, the film coefficient blowing correction for the 0.5 m spherical vehicle is plotted to demonstrate it's dependence on the B'$_c$ quantity. The 0.5 m vehicle is chosen as it experiences the largest heat flux and should thus produce a more quantifiable blowing condition. On the abscissa is shown the blowing correction computed as

$$\Omega_{film} = 1 - \mathrm{C_H}/\mathrm{C_{H_0}} \tag{5.25}$$

which conveys the percentage of the aeroheating flux which should constitute the predicted advective flux. On the ordinate is the trajectory time. The blue shaded region is the stagnation point of the vehicle and the orange is the shoulder.

At the stagnation point, the value immediately jumps to approximately 6.5% of the aeroheating flux. This value remains constant, as it relates to the CO plateau found in the B' table. The very minor discrepancy at the beginning of the trajectory is due to the wall temperature being in the vicinity of the 1000 K value, where the transition zone ends. Likewise, the wall temperature is quite low for the shoulder location early in the trajectory. This leads to an initial B'$_c$ value in the CO_2 plateau. As the vehicle descends into the atmosphere, the surface heats up and the blowing correction follows the transition from CO_2 to CO. At the end of the trajectory, the wall temperature begins to cool, allowing a drop away from the 6.5% value. The non-catalytic film coefficient at the shoulder lags behind the fully catalytic, as it has less energy and therefore takes more time to reach the optimal wall temperature for carbon oxidation.

The advective flux may be estimated by taking this percentage value and multiplying it by the aeroheating flux computed in the material response. This value is shown in the top subplot of Fig. 5.23, with the wall temperature co-plotted beneath

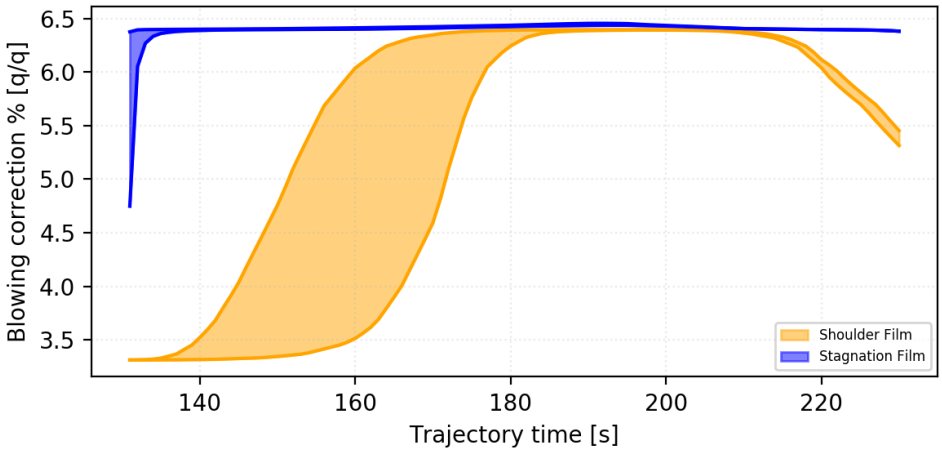

Figure 5.22: Film coefficient blowing correction expressed as percentage (i.e. C_H/C_{H_0}) of aeroheating flux.

it. In the case of a ballistic entry trajectory, which yields a single heat pulse through the atmosphere, the constant blowing correction takes on the qualitative behavior of the aeroheating flux. This means it rises to a peak value and then falls. This behavior may, as well as the peak advective flux value, be contrasted with the behavior of the DHA CFD-computed advective fluxes.

In Fig. 5.24, the top row is the stagnation point of the vehicle and the bottom row is the shoulder. The left column is the advective flux plotted against the trajectory time and the right column is the wall temperature plotted against trajectory time. The blue lines are the low emissivity ($\epsilon = 0.1$) DHA computed advective fluxes, linearly interpolated between trajectory points. The orange lines are the unity emissivity cases. The green lines are the high emissivity ($\epsilon = 10$) cases. The black line is the wall temperature computed by the material response when using the DHA boundary condition. This is the temperature used to calculate the interpolated advective flux duing the material response run time.

At the stagnation point, the wall temperature from the material response strongly tracks with the $\epsilon = 1$ DHA wall temperatures. This means a fairly good approximation is simply the $\epsilon = 1$ advective flux. The DHA advective flux peaks around 200

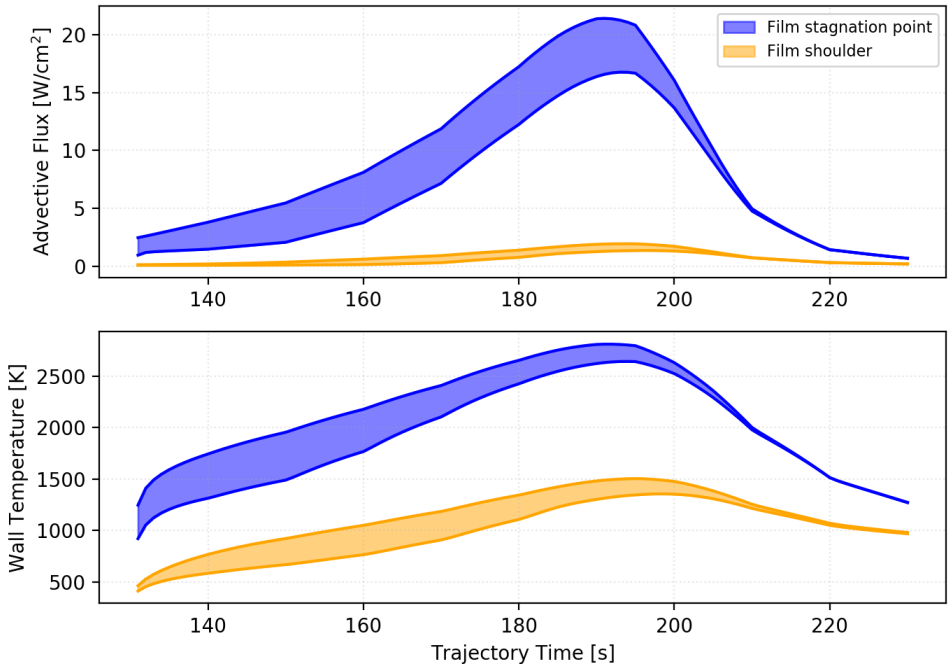

Figure 5.23: Film coefficient predicted advective flux

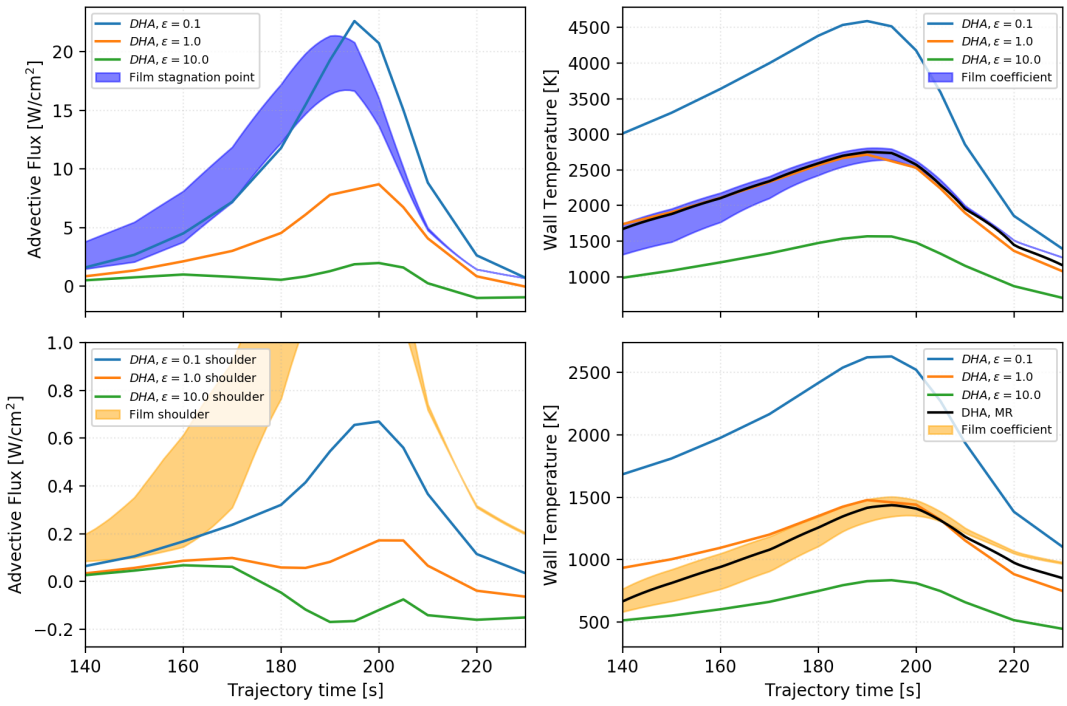

Figure 5.24: DHA computed advective fluxes for variable wall temperatures

seconds (maybe at 195 seconds, but this CFD case failed), well below 10 W/cm^2. In contrast, the FC-predicted advective flux peaks around 190 seconds at values above 15 and 20 W/cm^2. In other words, the film coefficient will predict a larger advective flux, and thus a larger reduction to overall heating, as compared to computing the advection (and the wall mass composition) in the CFD.

Looking to the shoulder of the vehicle (bottom row of Fig. 5.24, the wall temperature of the material response is between the emissivity values of 1 and 10. This means the interpolated value used in the material response will be between the orange and green lines in the advective flux subplot, in the bottom left. This subplot shows an example of how the DHA method computing the physics begins to deviate from correction models. In this figure, it is seen that as the surface temperature increases the blowing increases. However, this leads to a change in the mass composition adjacent to the wall, where now carbonaceous species are present and continuing to increase. This injection of ablation species *decreases* the wall enthalpy, which is one of the terms in the advective flux. Therefore, at low temperatures, this competition between wall temperature and carbon content creates an unusual trend. In fact, in both the orange and green lines, it is seen that the carbon content leads to a negative wall enthalpy and thus a negative advective flux.

This is a clear example of how avoiding gross assumptions, such as saturated chemical equilibrium at the wall, leads to a more accurate characterization of the physics. It is quite unlikely that the wall temperatures presented at the shoulder will result in chemical equilibrium, and therefore, the non-equilibrium nature of the problem, as well as the true mass composition at the wall needs to be taken into account.

Surface energy balance assessment

To assess the important observation about the change in fluxes due to ablative species, examine the surface energy balance that is applied to the material response simulation for both engineering methods. For the film coefficient, the following surface energy balance exists

$$q_{\text{aero}} + q_{\text{abl}} - q_{\text{rerad}} = q_{\text{cond}} \tag{5.26}$$

where the first term is the so-called aeroheating term, which approximates the conduction and mass diffusion fluxes, the second term is the ablation flux due to surface mass loss, the third term is energy reradiated from the surface, and the final term on the RHS is the solid conduction into the vehicle. It is useful to recast the definition of the aeroheating flux as the CFD computed heat flux from the film coefficient CFD, and the corrections to that heat flux (see Appendix F). Let the aeroheating term take the form

$$q_{\text{aero}} = q^{\text{CFD}} \times \Omega \times \Gamma \tag{5.27}$$

where the first term is the CFD computed heat flux which is purely fluid conduction in the case of a non-catalytic BC and conduction plus mass diffusion in the case of a catalytic BC. The second term Ω is the blowing correction and the third term is the enthalpy correction, which is given by

$$\Gamma = \frac{h_r - h_w^{\text{MR}}}{h_r - h_w^{\text{CFD}}} \tag{5.28}$$

where the wall enthalpy in the denominator is evaluated at the material response wall conditions and the wall enthalpy in the denominator is evaluated at the CFD wall conditions. The blowing correction is meant to correct the lack of wall normal velocity in the CFD, which reduces the effective heat flux. The enthalpy correction is applied to correct for the lack of ablative species in the CFD. The resulting corrected heat flux cannot discern between contributions from conduction, mass diffusion, and advection. Instead, it always appears as a single term.

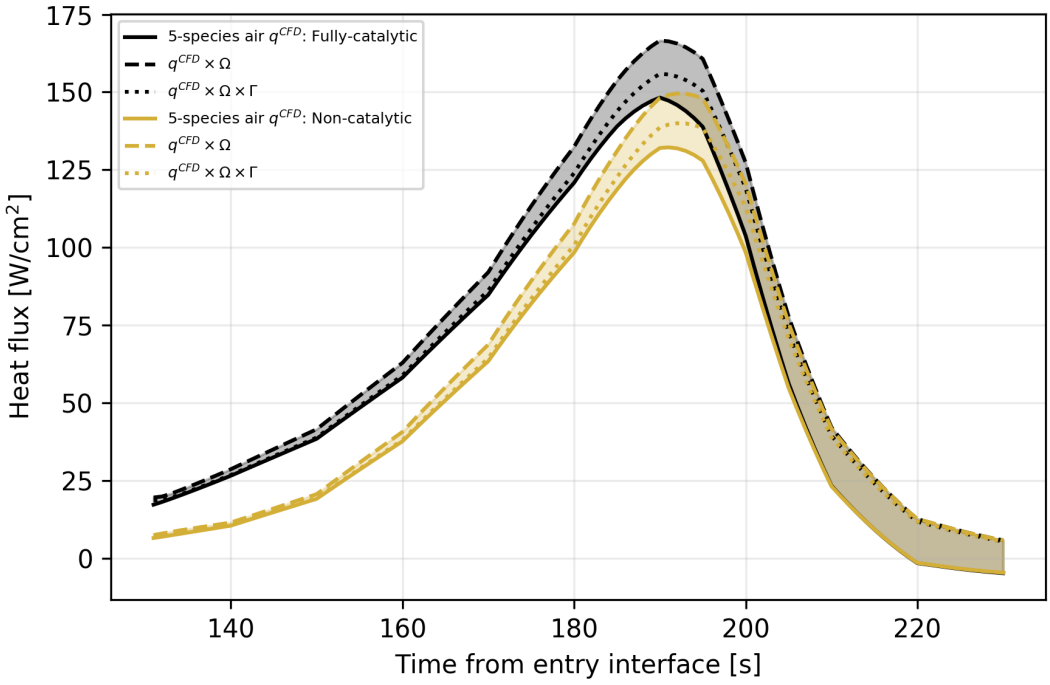

Figure 5.25: Film coefficient corrections for the stagnation point of the 2.5 m nose radius vehicle

To visualize how the corrections in the film coefficient affect the applied heat flux through the course of the trajectory, they are co-plotted in Fig. 5.25 with the CFD-extracted base heat flux from the 5-species air simulation. The x-axis is the time from entry interface, measured in seconds, and the y-axis is the heat flux, measured in W/cm^2. The gold lines are the CFD simulations with a non-catalytic wall BC and the black lines are the fully catalytic BC. The non-catalytic wall is the case of pure fluid conduction, while the fully catalytic is a combination of fluid conduction and mass diffusion due to catalysis. Early in the trajectory, the catalytic assumption substantially increases the heat flux produced by the method. This offset continues into the peak heat flux, and then afterwards tapers such that the two catalytic conditions converge. This is the result of the convective cooling phase no longer providing adequate conditions for dissociation.

The dashed lines represent the application of the enthalpy correction. The CO

content in the material response simulation decreases the wall enthalpy (enthalpy of the gaseous molecules adjacent to the wall, at the wall temperature). The decreasing wall enthalpy in the numerator of Eq. 5.28 makes the *difference* larger, thereby increasing the resulting heat flux. The correction is smallest at high altitude, where the expected carbon content near the wall is low. As surface ablation increases, the correction gets larger until reaching a maximum at peak heating. Beyond the peak heating portion of the trajectory, the correction factor persists (for both mass BCs). Two mechanisms are causing this effect: the film coefficient assumptions predict a wall state with a nonzero amount of carbon monoxide through the convective cooling phase, and the wall temperature in the material response is different than that evaluated in the CFD simulation. As mentioned previously, this persistance of an enthalpy correction in flight regimes where ablation is unlikely and where chemical non-equilibrium conditions prevail has been colloquailly termed *endgame recession*.

The dotted lines are the result of applying the blowing correction to the enthalpy corrected heat flux. Early in the trajectory, there is very little correction as no significant blowing has occurred. As the vehicle enters the atmosphere, however, the blowing correction becomes approximately 10% for this flight condition. It remains steadily at this value through the flight, appearing to increase due to the total heat flux increase. The appearance of the blowing correction diminishing during the convective cooling phase is also an artifact of plotting in the absolute scale.

The direct method surface energy balance in the material response is

$$q_{\text{direct}} - q_{\text{rerad}} + q_{\text{abl}} = q_{\text{cond}} \tag{5.29}$$

where the first term is the *direct* (or DHA) heat flux from the CFD, the second term is the reradiation from the surface to the far-field, and the third term is the solid ablation flux being calculated by interpolating in the DHA tables. The term on the RHS is the desired quantity of interest, the solid conduction flux into the vehicle.

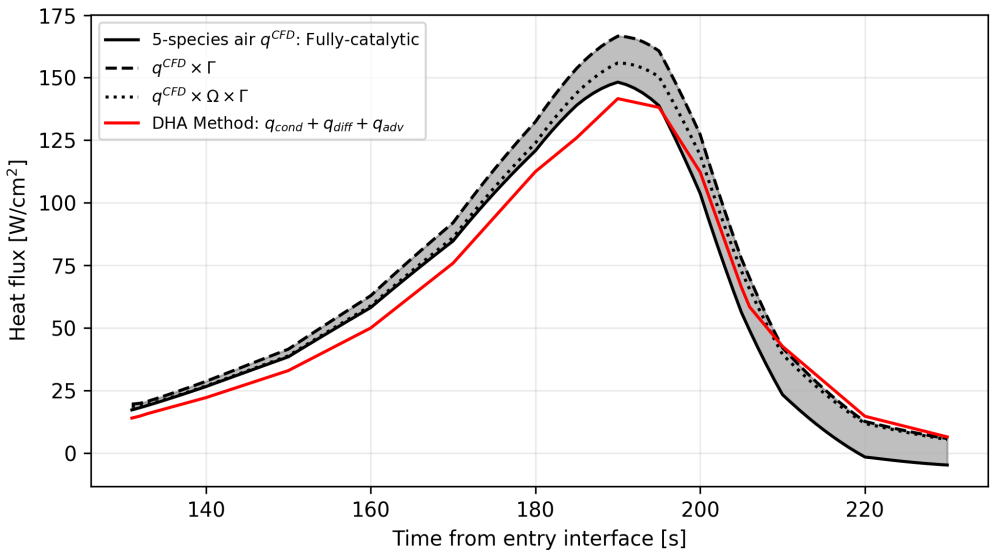

(a) Fully catalytic

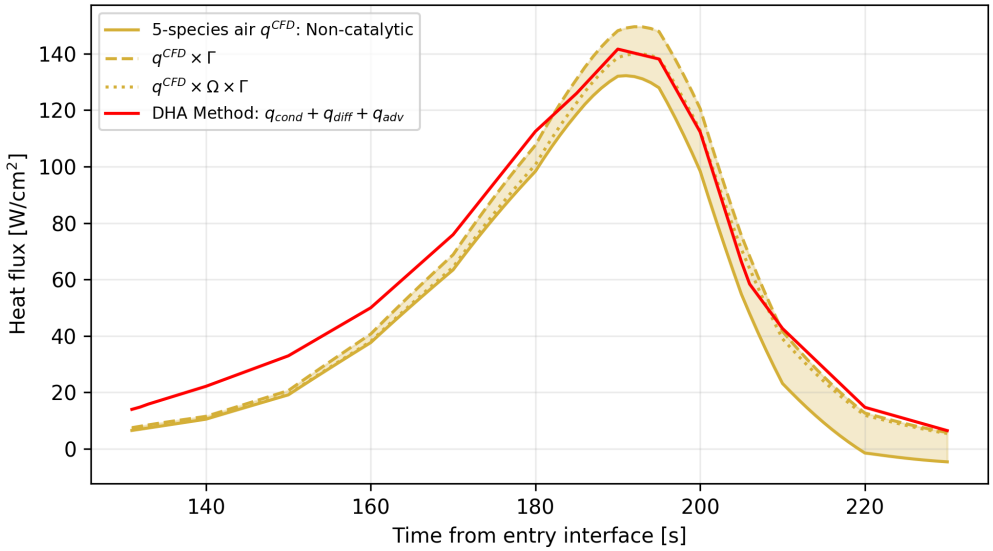

(b) Non-catalytic

Figure 5.26: Surface energy flux comparison, stagnation point

The DHA heat flux from the ablating CFD is given by

$$q_{\text{direct}} = q_{\text{cond}} + q_{\text{diff}} - q_{\text{adv}} \tag{5.30}$$

where the first term is the fluid conduction, the second term is the mass diffusion, and the third term is the advection into the fluid. These flux components are assessed for

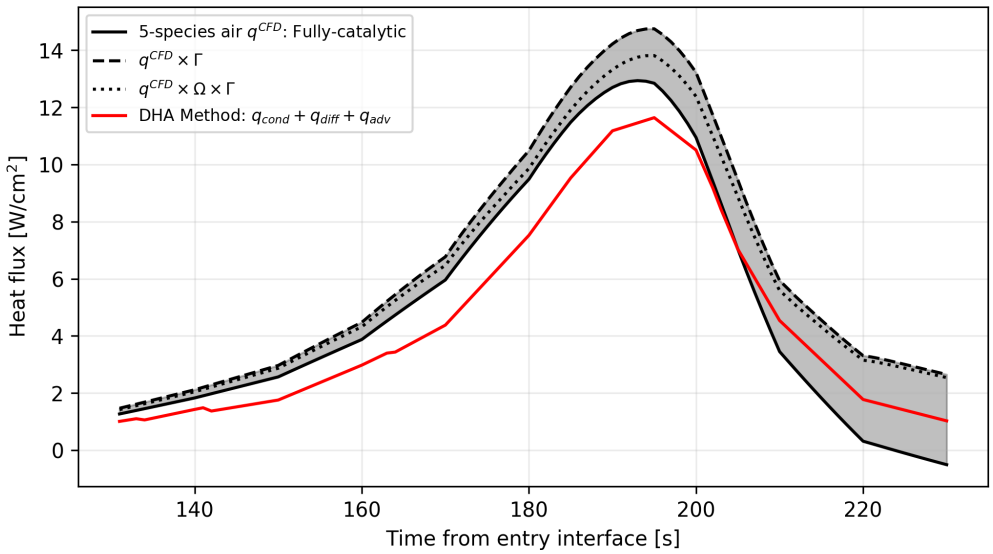

(a) Fully catalytic, shoulder

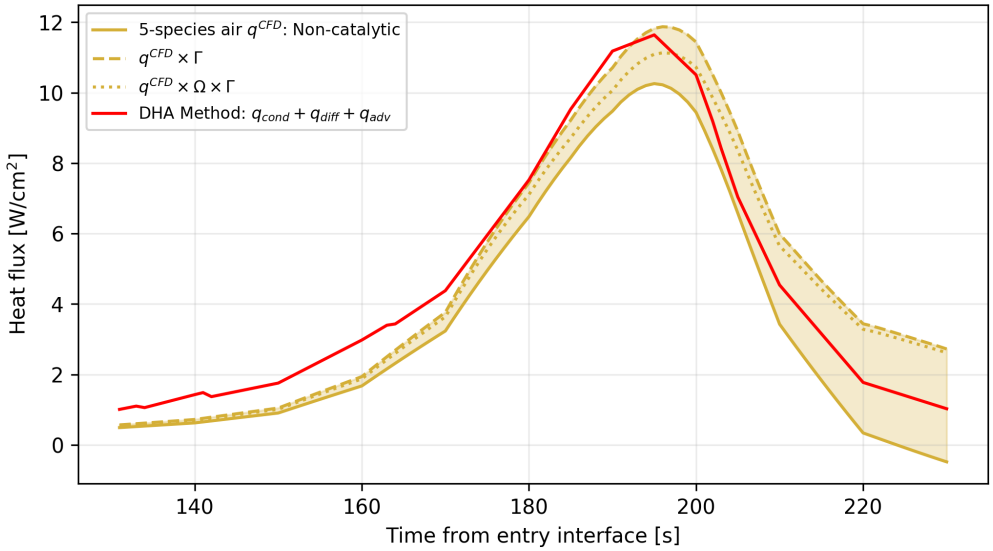

(b) Non-catalytic, shoulder

Figure 5.27: Surface energy flux comparison, shoulder

the 2.5 m vehicle in Figs. 5.26 and 5.27. The fully catalytic film coefficient heat flux predictions (with both corrections) are co-plotted in black, while the non-catalytic film coefficient is in gold. The shaded area is the largest correction possible, where the dashed line represents the enthalpy correction and the dotted line represents a reduction due to the blowing correction. The other lines comparise the components

of the DHA method, where the blue line is the fluid conduction flux, the orange line is mass diffusion flux, and the green line is the advection flux. The red line is the summation of all three component fluxes from the DHA method.

Recall that the sizing data in Table 5.12 indicated that, even with the considerable surface recession produced by the film coefficient method, that the DHA method required a larger heatshield thickness than the non-catalytic film coefficient. Through the upper atmospheric portion of the trajectory and up to peak heating, the vehicle is moving at extremely high velocity, which induces a shock wave. The shock wave creates a high temperature region behind it where dissociation of molecular particles occurs. Through the upper part of the trajectory, the dissociated atoms will reach the wall of the vehicle. For a non-ablating TPS this can cause catalytic recombination, an exothermic reaction which releases energy when the atoms recombine. For an ablating TPS, it is more reasonable to expect that the atomix oxygen will react with the exposed carbon surface, forming carbon monoxide. By modeling the catalytic process at the wall, engineers can produce a conservative (higher than required) estimate of the wall heating, but this does not represent the physics.

Figure 5.26(a) shows the stagnation point comparison between a fully catalytic FC prediction and the DHA method. The additional energy from mass diffusion contributions is higher than all of the combined DHA fluxes up until just after the peak heat pulse. On the contrary, in Fig. 5.26(b) it is seen that in the very early trajectory the DHA method predicts a higher heat flux. This higher prediction is due to permitting a mass diffusion flux. This means even if carbon reactivity is low, the atomic oxygen can still contribute to mass gradient calculations at the wall. It may be seen that the fluid conduction flux closely approximates the non-catalytic film coefficient flux, as it represents only the fluid conduction due to not having large corrections being applied. This difference in early trajectory behavior is the reason why, despite the large recession difference, the DHA method estimates a larger

heatshield sizing. It implies that the mass transfer boundary condition in the CFD is more important the effect of the recession in the material response, even when the recession is nearly 60% higher.

Figures 5.27(a) and 5.27(b) help illustrate another key finding from the previous analysis. Indeed, the DHA direct (combined) heat flux is higher than the non-catalytic FC counterpart. However, more importantly, the film coefficient corrections in the late phase of the trajectory appear as large distortions from the base CFD flux. In this case, it is now more obvious than before that the film coefficient will produce non-physical behavior during the convective cooling phase. This large difference is due to the chemical equilibrium assumption of the material response, which considers the wall in chemical equilibrium. This results in a much lower wall enthalpy which increases the difference in the numerator of the enthalpy correction. This therefore has the consequent effect of increase the heat flux prediction when applied. The base CFD heat flux from the film coefficient predicts a lower heat flux than the DHA method (for both body locations) when uncorrected. However, keep in mind that this is for non-equilibrium 5 species air wall enthalpy, as opposed to the DHA method which may have residual ablating species at the wall.

Remarks on Sphericus analysis

It was shown that for the given trajectory and flight conditions, that the DHA method produced surface temperatures between the catalytic range of the film coefficient method. At body locations where chemical equilibrium could be expected, the overall conduction and mass diffusion fluxes predicted by the DHA method strongly resembled the fully catalytic film coefficient predictions. At downstream locations, the DHA method predicted temperatures closer to the non-catalytic film coefficient. This is an indication of the DHA method's robustness to adapt to the flight condition and the body location of the vehicle. In locations where chemical equilibrium is expected,

it will perform as well as a chemical equilibrium model. In locations where the flow state is expected to be in chemical non-equilibrium it will more accurately predict the physics. This was very clearly illustrated for the shoulder in the late portion of the trajectory, where large corrections in the film coefficient lead to higher wall temperatures when the vehicle should be cooling.

5.4 Numerical case study: AS-202, Apollo Test Capsule

The complexity of the design case is now extended to the AS-202 Apollo Test Capsule, first introduced in Chapter 1.4. The main differences from the previous cases are a flight-like blunt body with a large radius of curvature on the heatshield, a lofted trajectory, and a variable angle of attack. In addition, two of the heritage surface chemistry models for carbon ablation are adopted to compare with the film coefficient methodology.

The large radius of curvature reduces the overall heating to the vehicle according to the inverse relationship with heat flux. This allows a more aggressive flight path angle to be taken for a given entry velocity and initial mass. As well, it increases the likelihood that a 1-dimensional material response analysis will be conservative (in other words it makes the semi-infinite domain assumption more realistic). The lofted trajectory reduces the peak heat flux on the first pulse. This is not necessarily a design constraint, as modern programs plan for continengencies where the ballistic trajectory drives the design. It is, however, more flight-like in the sense that programs utilize guided skip trajectories to enhance the vehicle performance to meet other design constraints, such as targetting a designated landing zone. The variable angle of attack results in a windward and leeward region of the vehicle. Consequently, the small shoulder radius of the vehicle allows for rapid expansion of the fluid creating localized hot spots along the heatshield pitch-plane on both the leeward and windward side. Unlike a ballistic trajectory whose stagnation location is fixed, the localized

augmented heating at the shoulders will vary slightly due to shifting in the angle of attack. Therefore, accurate heatshield sizing requires iterations of 1-dimensional material response analyses in the hot shoulder region to accurately capture peak heating.

In Fig. 5.28, a typical wall temperature and heat flux are presented as a function of the radial (y) coordinate. This figure shows the concept of an axisymmetrically located stagnation point and two localized regions of heating. As the flows for this analysis are always assumed laminar, this pattern of heating should remain consistent, although the physical coordinates of the peak heating will shift slightly. In turbulent flows, it is possible to see the leeward turbulent heating reach levels similar to the windside shoulder.

Trajectory

The trajectory data is extracted directly from Griffith (8) which gives the altitude, time, velocity, and angle of attack. The altitude is converted into freestream density using the Standard Atmosphere (22). The important initial condition variables have been visualized from Table IV of the cited paper in Fig. 5.29. The estimated heat flux is computed using the nose radius, freestream density, and velocity based on the Brandis-Johnston (BJ) stagnation point correlation (9). The results of this computation are given in Fig. 5.30, where the red line is the BJ correlation prediction of heat flux and the gray line linearly interpolated heat flux based upon the chosen trajectory points.

The first point, at 105 seconds, corresponds to the the 4455 second mark in the as-reported trajectory. This is the flight condition where it is arguable that the flow field will be in continuum according to the Knudsen number. The second and third trajectories are selected as peak heat flux and shortly after peak heat flux, as it was found retroactively that the point at 160 seconds did not capture peak heating.

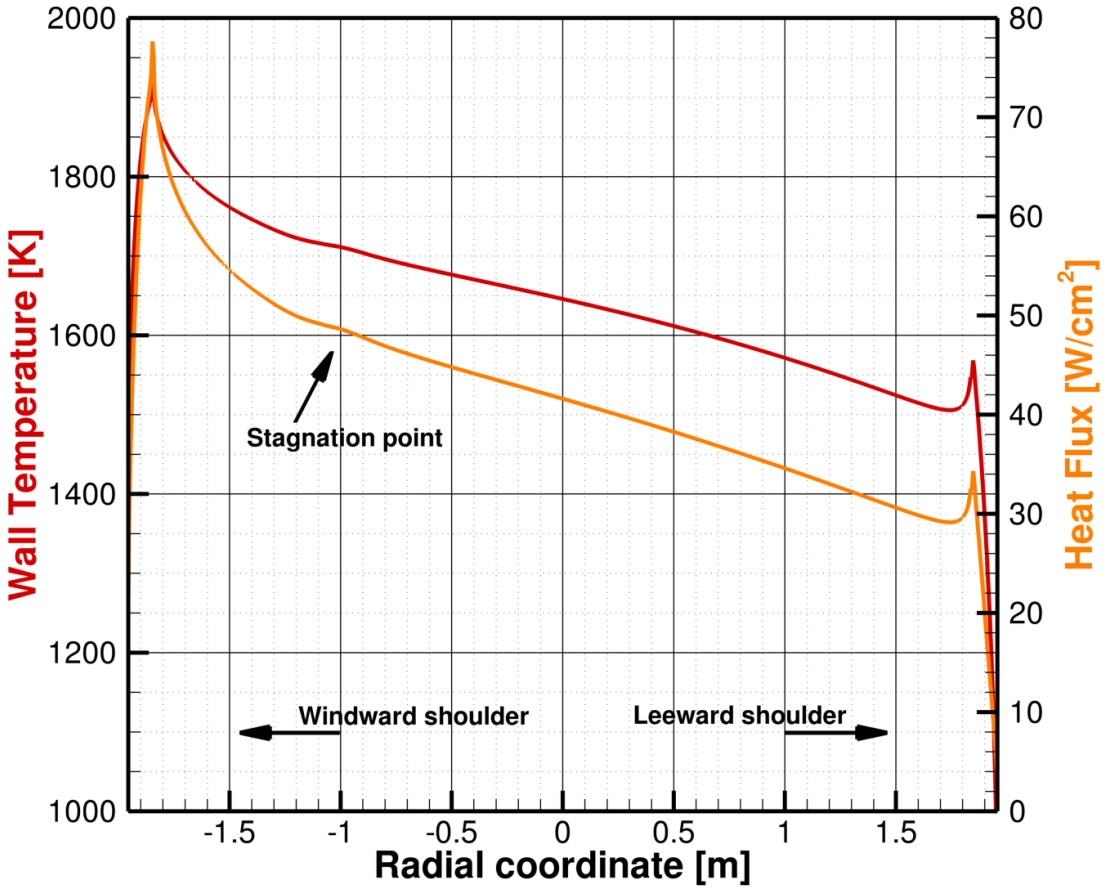

Figure 5.28: Sample thermal and heat flux wall distributions for AS-202 showing aerothermal features arising from vehicle geometry and angle of attack

The fourth point captures the *dip* in the trajectory at approximately 350 seconds. The fourth and fifth points are chosen as the peak heat flux points for the second descent into the atmosphere, while the final two trajectory points are evaluated for the convective cooling phase of the flight.

Vehicle and grid

The vehicle surface geometry is derived from Wright et al. (10) and reproduced here in Fig. 5.31. The grid is essentially over-resolved with 750 node points distributed along the vehicle surface and 750 nodes hyperbolically extruded. After initial convergence,

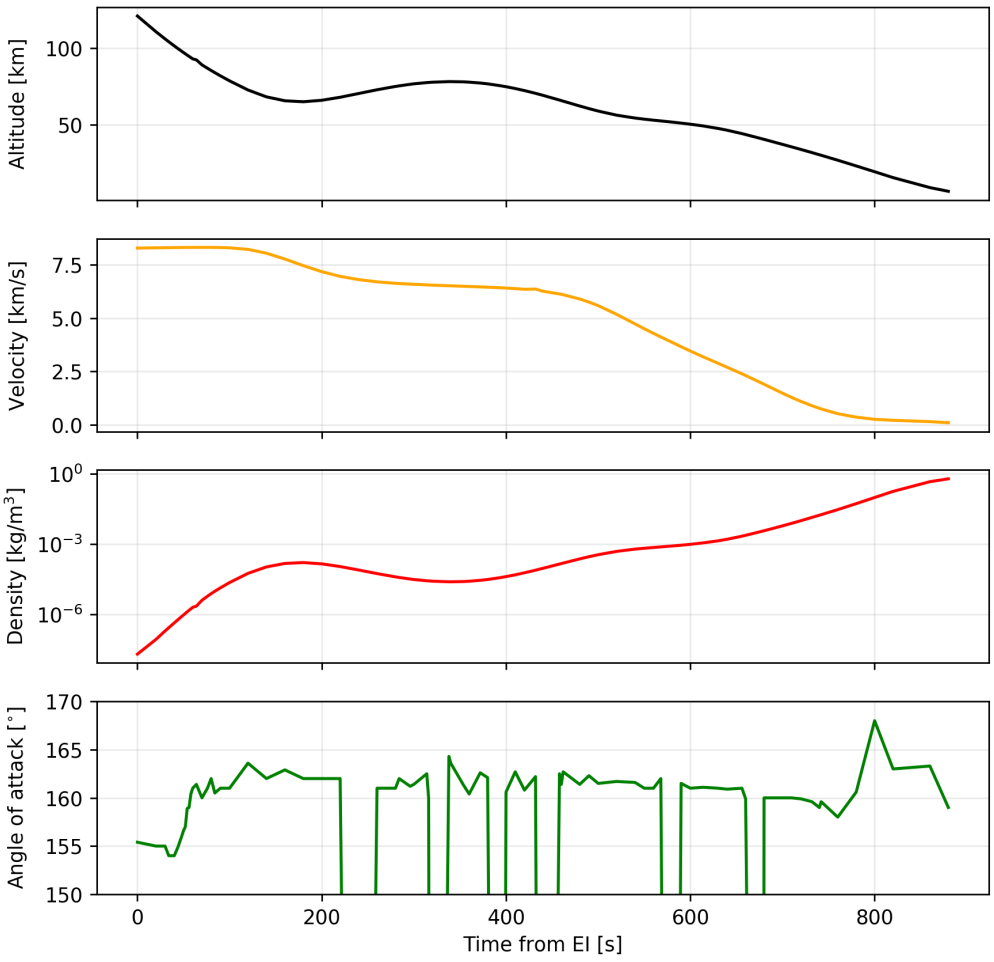

Figure 5.29: AS-202 trajectory quantities taken from Griffith (8)

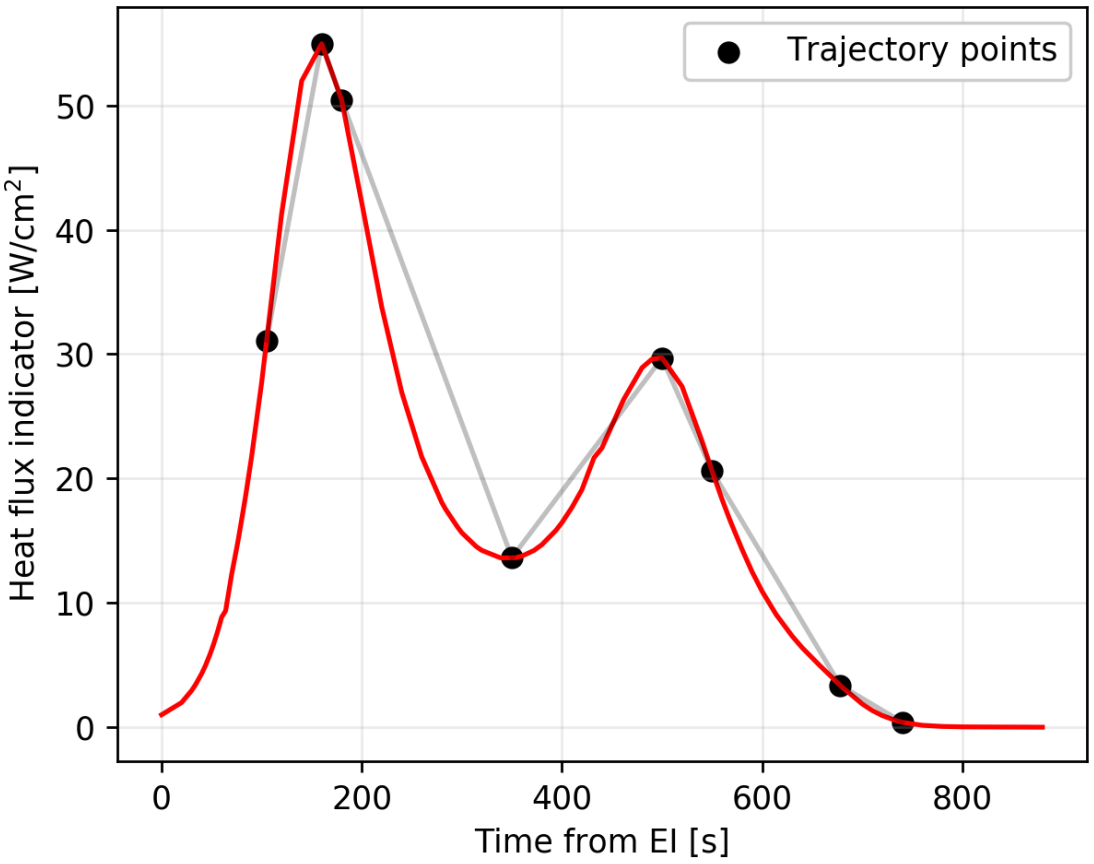

Figure 5.30: AS-202 estimated heat flux based on Brandis-Johnston stagnation point correlation (9) and selected trajectory point locations

the grid is shock-adapted and then re-converged. The pre-adapted and shock-adapted grid results in flow fields per Fig. 5.32 where the asymmetry of the angle of attack is evident.

CFD

This analysis used the Data Parallel Line Relaxation (76) (DPLR) program to compute the CFD solutions. The initial conditions are obtained from Griffith (8). The initial mass fractions are $N_2 = 0.767$ and $O_2 = 0.233$, neglecting trace elements. The viscosity and thermal conductivity are computed using the Gupta-Yos mixing model(79). The two-temperature model of Park is adopted for thermal non-equilibrium(80). Ho-

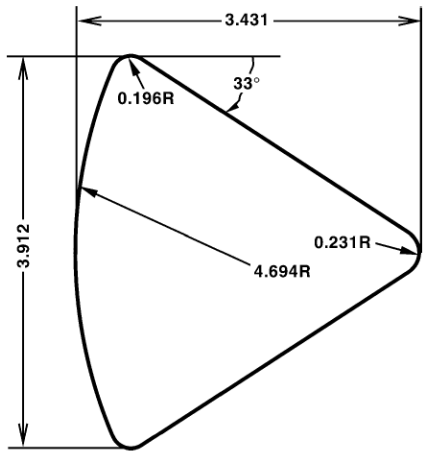

Figure 5.31: Vehicle geometry parameters extracted from Wright et al. (10)

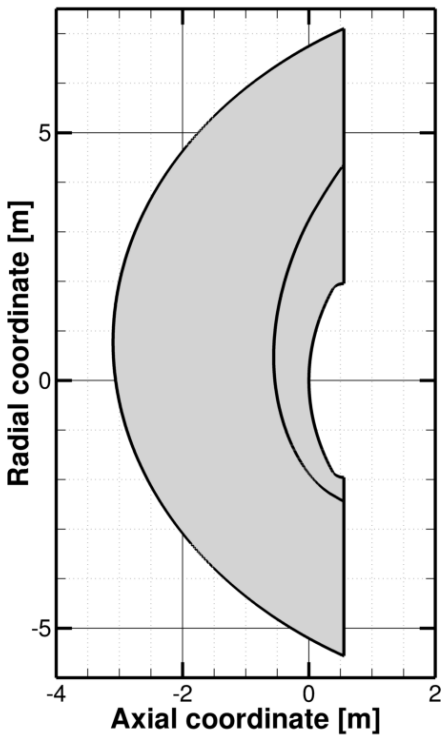

Figure 5.32: AS-202 unadapted and shock-adapted flow field

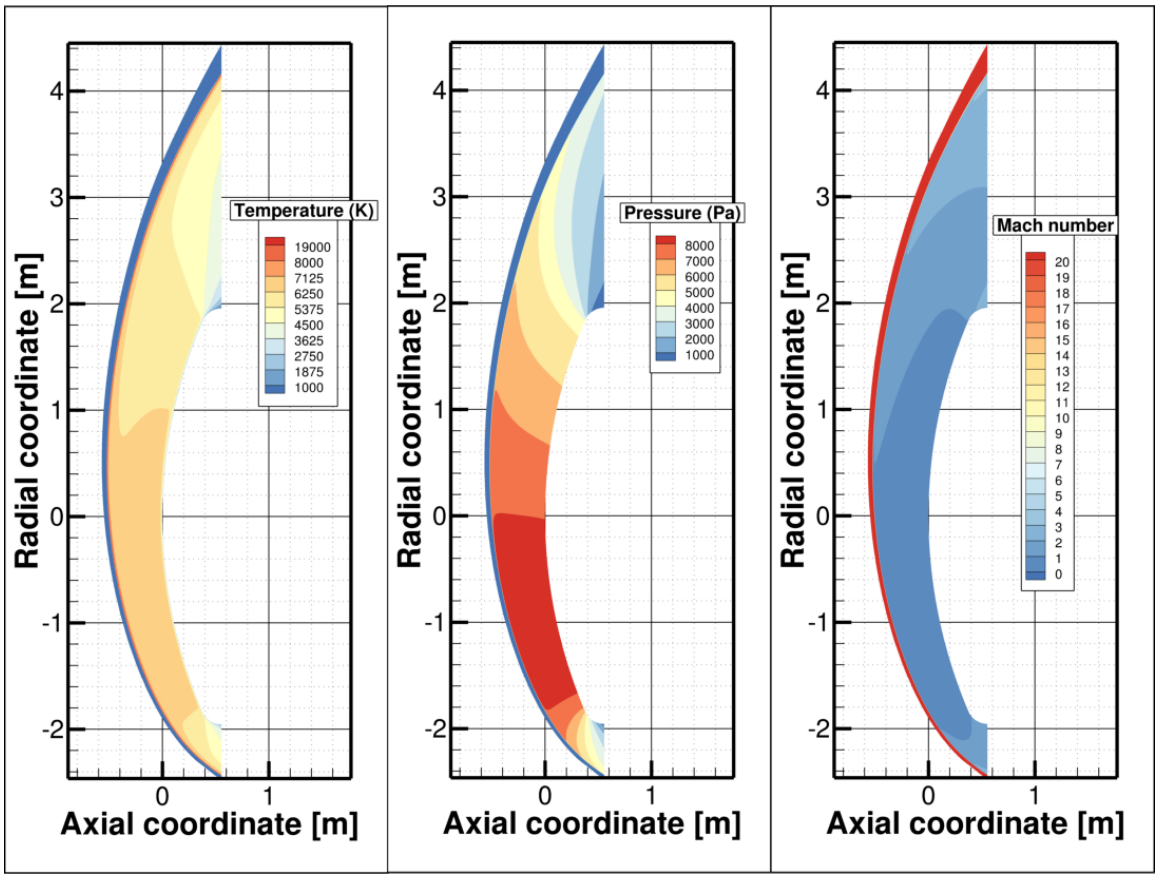

Figure 5.33: Example CFD solution for the AS-202 Apollo test vehicle

mogeneous equilibrium constants are computed from the NASA-9(78) data set. The chemistry models are described in a later section.

Each CFD solution minimizes a global density residual (as low as permitted by the solver), before and after grid adaption. Examples of the resulting temperature, pressure, and Mach fields are given in Fig. 5.33, which show the impact of flying at angle of attack. Two body points on the vehicle are analyzed, the so-called *hot* shoulder, where peak heating occurs and the lee shoulder. The hot shoulder is the location of peak heating at the time of the first heat pulse, which is located windward of the stagnation region. The lee shoulder is the point of tangency on the leeward side of the vehicle. These locations are shown in Fig. 5.34.

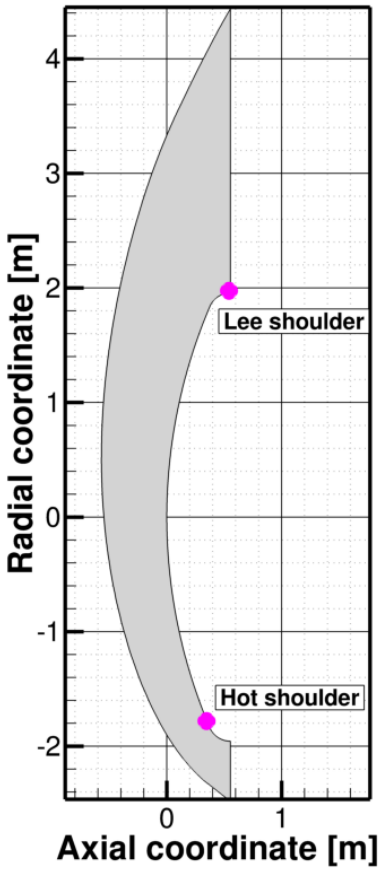

Figure 5.34: Assessed body locations for AS-202 analysis

Chemistry models

The film coefficient method uses the same chemistry models as in the previous numerical experiments, with the CFD homogeneous model being due to Park 5 species air, and the surface chemistry model also being either a non-catalytic mass transfer condition or a fully catalytic BC, also due to Park. The surface thermochemistry model is constructed for a carbon-air mixture with the TACOT 24 species and a strictly zero pyrolysis gas blowing rate. Again, refer to Fig. 4.1 for the dimensionless ablation flux and the wall enthalpy associated with this model.

The homogeneous chemistry model for the direct heating and ablation methodology is given by Park (84). The gas phase reaction set is re-stated here for clarity

Dissociation Reactions
$N_2 + M \leftrightarrow N + N + M$
$O_2 + M \leftrightarrow O + O + M$
$CO + M \leftrightarrow CO + O + M$
$CO + M \leftrightarrow C + O + M$
$C_2 + M \leftrightarrow C + C + M$
$CN + M \leftrightarrow C + N + M$
$NO + M \leftrightarrow N + O + M$
Exchange Reactions
$N_2 + O \leftrightarrow NO + N$
$NO + O \leftrightarrow O_2 + N$
$CO + C \leftrightarrow C_2 + O$
$CO + O \leftrightarrow O_2 + C$
$CO + N \leftrightarrow CN + O$
$N_2 + C \leftrightarrow CN + N$
$CN + O \leftrightarrow NO + C$
$CN + C \leftrightarrow C_2 + N$
$CO + C_2 \leftrightarrow C_3 + O$
$C_3 + N \leftrightarrow CN + C_2$
$C_3 + C \leftrightarrow C_2 + C_2$
$CO_2 + O \leftrightarrow O_2 + CO$

Table 5.14: Park 2001 homogeneous reaction set for AS-202 numerical case study

	Reaction	Type	Coefficient	T^β	E (kJ/g/mol)
1	$O + (s1) + C(b1) \leftrightarrow CO + (s1)$	E-R	0.63	0	9644
2	O_2+2(s1)+2C(b1) $\leftrightarrow 2CO + 2(s1)$	E-R	0.5	0	0.00
3	N+(s1)+C(b1) $\leftrightarrow CN + (s1)$	E-R	0.3	0	0.00
4	3(s1) + 3C(b1) $\leftrightarrow C_3 + 3(s1)$	sub.	5.19×10^{13}	0	7.7518×10^5
5	C_3 + 3(s1) $\leftrightarrow 3(s1) + 3C(b1)$	E-R	0.1	0	0.0

Table 5.15: Milos & Chen carbon-air surface thermochemistry model

in Table 5.14. Two different sets of surface reactions are used, the Milos and Chen (MC) model (73, 85) and the Zhluktov-Abe model, as taken from Ref. (73). The reactions and associated parameters are given in the same nomenclature as Marschall and MacLean in Tables 5.15 and 5.16.

The MC model contains 3 forward (irreversible) reactions of the Eley-Rideal type. Reactions 1 and 2 are carbon oxidation using both atomic and molecular oxygen.

	Reaction	Type	Coefficient	T^{β}	E (J/gmol)
1	O+E(s1) $\rightarrow$ O($s1$)	ads.	1.0	0.0	0.0
2	2O(s1) $\leftrightarrow$ $O_2 + 2E(s1)$	Arr.	3.583×10^{10}	1.0	2.5607×10^5
3	O_2+E(s1) $\leftrightarrow$ O + O($s1$)	E-R	1.0	0.0	1.1806×10^5
4	CO_2+E(s1) $\leftrightarrow$ CO + O($s1$)	E-R	0.9	0.0	0.0
5	O(s1)+C(b)$\leftrightarrow$ CO + $E(s1)$	Arr.	2.082×10^9	1.0	3.3256×10^5
6	O+O(s1)+C(b)$\leftrightarrow$ $CO_2 + E(s1)$	E-R	0.8	0.0	1.663×10^4
7	2O(s1)+C(b)$\leftrightarrow$ $CO_2 + 2E(s1)$	Arr.	3.583×10^{14}	1.0	3.3256×10^5
8	C+E(s1)$\leftrightarrow$ $E(s1)$ + C(b)	E-R	0.24	0.0	0.0
9	C_2+2E(s1)$\leftrightarrow$ $2E(s1)$ + 2C(b)	E-R	0.5	0.0	0.0
10	C_3+3E(s1)$\leftrightarrow$ $3E(s1)$ + 3C(b)	E-R	0.023	0.0	0.0
11	N+E(s1) $\rightarrow$ N($s1$)	ads.	1.0	0.0	0.0
12	N_2+E(s1) $\leftrightarrow$ N + N($s1$)	E-R	1.0	0.0	6.3685×10^5
1b	O(s1) $\rightarrow$ O + $E(s1)$	des.	1.7206×10^4	0.0	3.7413×10^5
11b	N(s1) $\rightarrow$ N + $E(s1)$	des.	1.7206×10^4	0.0	3.0429×10^5

Table 5.16: Zhluktov-Abe model surface reaction parameters

Reaction 3 is the nitridation of the carbon surface. Finally, the last reaction is a reversible sublimation reaction of C_3.

The ZA model is slightly more complex. It contains forward and backward reactions, adsorption and desorption of atomic species, and different E-R mechanisms to permit sublimation. The model also includes pathways for CO_2 production through reactions 4, 6, and 7. In working with the ZA model, the worker immediately realizes that the large coefficients in these reactions cause a dominant amount of CO_2 to form.

Material Model

The surface chemistry models proposed for this experiment were based on high density carbon ablators, such as carbon-carbon and carbon phenolic materials. Therefore, the carbon bulk density is given to be $\rho_s = 1500$ kg/m^3 for this numerical experiment. This density is also used for the heatshield material, with the charred TACOT material properties. This makes the comparison as close to one-to-one as possible.

Fixed depth analysis

In the forthcoming figures, the abcissa is the time from the first trajectory point to the last analyzed trajectory point. The ordinate is the surface temperature or the recession (both dependent properties of the interpolated DHA tables). The shaded area is the catalytic limit for the film coefficient, between the fully catalytic and non-catalytic mass transfer conditions. The orange line is the DHA method using the MC surface chemistry model, while the red line is the DHA method using the ZA model.

The surface temperature distribution for the hot shoulder of the vehicle may be seen in Fig. 5.35(a). It is apparent that the flight conditions for the AS-202 vehicle were not extremely severe, with the peak surface temperature reaching just over 1800 K. Compare this to Fig. 1.10 using only engineering correlations. In that analysis, not only did the surface temperature reach 2500 K, but the second pulse actually predicted much higher heating up to around 4000 K. This is simply confirmation that using CFD for vehicle design is a more reasonable estimation of aerothermal environments.

The DHA method employing the ZA model shows a surface temperature roughly equal to, and in some cases, higher than the fully catalytic film coefficient. This development will be explored later in the analysis, but speaks to how much of an impact certain species can affect the aerothermal heating. In this instance, the ZA model has produced CO_2 largely in place of CO which has led to energy contributions increasing from vibrational excitation and mass diffusion. Comparatively, the vibrational contribution has much less impact than the mass diffusion contribution with respect to the overall heating. This emphasizes the criticality of the correct chemistry models in assessment of the surface heating.

The DHA method employing the MC model shows a surface temperature that falls roughly between the film coefficient catalytic limits. If we accept the assumption that the ablation fluxes are not the same order of magnitude as the conduction and

mass diffusion fluxes, this means that the presence of the ablative species is less than the total energy released by the recombination of dissociated species at this flight condition. The kinetic rate processes of the MC model are very fast (actually producing more recession than the ablation model, see Fig. 5.36). Thus, the point of the DHA prediction is that, even with large amounts of CO released into the flow field from a given kinetic reaction mechanism, the effect on the energy state of the wall is much lower (through most portions of the trajectory) than the fully catalytic assumption. In this sense, the DHA method is a more practical approach because it is actually based on the physics which we expect to occur in the flow field. In fact, it is worth noting that the newer approaches from the molecular beam experiments are not only dependent upon the temperature (such as the case of the B' CO plateau), but they also depend on the amount of adsorbed atomic oxygen on the surface. This in turn allows an even more accurate recreation of the physics that occur at the surface, as opposed to bulk assumptions.

Figure 5.35(b) shows the surface temperature for the lee shoulder location. The surface temperatures are much lower at this location. The most obvious trend is the extremely high surface temperature of the fully catalytic film coefficient. The mass fraction of O_2 for this case is around 20%, while the atomic oxygen is approximately 0.01. This indicates a large amount of energy released exothermic recombination. However, the kinetic models produce a higher surface temperature during the first pulse than the non-catalytic film coefficient. This behavior continues to the second pulse, but then beyond the peak heating location, the surface temperature for both models begins to drop. The reason the DHA models have higher surface heating *cannot* be attributed to exothermic reactions at the surface. The magnitude of the ablation flux is on the order of less than 0.01 W/cm^2 or less at this body location. The catalycity is zero for the non-catalytic case. Consequently, the advective flux for minimal ablation is also insignificant. This means, that up until where the two

film coefficient temperatures split, the aeroheating flux is the enthalpy corrected conduction flux from the 5-species air CFD. Therefore the difference between the DHA and FC methods must come down to two different factors; the mass diffusion flux due to the presence of ablative species in the DHA CFD, and the difference in wall temperature between the MR and film coefficient CFD which leads to a heat flux correction. These differences will be assessed later in the analysis on an individual flux contribution level.

With a higher surface temperature, one may incorrectly assume that the DHA method employing the ZA model has a higher surface recession rate. This would lead to more recession, less thermal mass, and higher surface temperatures. Examining Fig. 5.36 quickly disproves this theory. For example, taking Fig. 5.36(a), it is seen that the surface recession due to the ZA model most closely tracks the non-catalytic film coefficient recession. This mirrors an observation made by Candler (51), which shows that at certain flight conditions the bulk recession rates between heritage approaches and kinetic models may be quite similar, while the boundary layer characteristics are completely different. Here, it is seen that the ZA model yields a similar recession rate to a non-catalytic film coefficient, but due to the creation of CO_2 in the flow field, the surface heating more closely tracks a fully catalytic film coefficient!

Looking to Fig. 5.36(b), the ZA model has the lowest recession of those evaluated. This is evidence that the DHA method employing the ZA model did not produce higher surface temperatures due to excessive, exothermic ablation. In fact, Fig. 5.36(a) and 5.36(b) both show that the largest recession is attributable to the DHA method using the Milos and Chen model. This is due to the reactions being irreversible, as well as having moderate reaction efficiencies and low activation energies. However, by combining the observations from both figures it is possible to present the following hypothesis: *The ablation rate and mass loss has less impact on the surface temperature prediction than the accurate prediction of the fluxes in the CFD.*

Thus, the juxtaposition of ablation rates and surface temperatures is warranted, as the controlling factor is the mass composition adjacent to the wall and through the boundary layer. With regards to the film coefficient method, this key component of assessing the heat flux is completely absent!

Strong comments such as these should be caveated with the idea that the kinetic mechanism may not be better at predicting the real physical scenario than the solution of the chemical equilibrium state. For example, the recent surface molecular beam data have shown that the production of CO_2 is not supported by data (66). However, the dramatic effect of including a single dominant species in the boundary layer shows how strongly the surface chemistry can affect the aerothermal heating. Furthermore, kinetic mechanisms may promote species that may not physically occur as part of a model that is meant for high surface temperatures. Noticeably, on the lee shoulder of the AS-202 vehicle, the ZA and MC models both have reaction pathways for O_2 to oxidize the surface. Equation 3 of the ZA model is an Eley-Rideal type that allows direct adsorption of an oxygen atom to the surface from molecular oxygen. Equation 2 of the Milos-Chen model permits molecular oxygen to participate in an Eley-Rideal type reaction that directly generates CO. Both of these mechanisms allow surface chemistry to occur at low temperatures when the usual nucleophilic attack from atomic oxygen is not present. While the film coefficient model had no additional energy from catalysis, the kinetic models managed to produce ablative species because of their associated reaction efficiencies and low activation energies. The film coefficient does not even attempt to compute the mass diffusion flux due to the ablative species, nor the modification to the conduction fluxes (translation/vibrational). Instead, these differences should be accounted for in the enthalpy correction. This important concept in differentiating the approaches will be analyzed in a later section.

Ablation Parameters	Zhluktov-Abe	Milos-Chen	FC fully cat.	FC non-cat.
Hot shoulder thickness [mm]	31.59	29.92	31.57	28.82
Hot shoulder recession [mm]	0.578	2.284	1.576	0.959
Lee shoulder thickness [mm]	12.478	11.41	18.22	11.64
Lee shoulder recession [mm]	1.86×10^{-6}	7.11×10^{-5}	6.05×10^{-5}	3.14×10^{-5}

Table 5.17: Recession depth and heat shield sizing for AS-202 Apollo test vehicle

Heatshield sizing analysis

Moving to the design situation where the heatshield thickness needs to be optimized based on the substructural failure temperature, the critical values are presented in Table 5.17. The trends that became evident in the fixed depth analysis also appear in this table.

For example, it was seen that the ZA model in the DHA method produced high surface temperatures. This is not due to exothermic oxidation at the surface, but rather the altered characteristics of the boundary layer due to the presence of CO_2. This directly leads to the largest heatshield thickness at the hot shoulder. Comparing to the heritage design heatshield thickness, the hot shoulder thickness is nearly identical to the fully catalytic film coefficient case. This means the mass diffusion flux from CO_2 is compensating for the energy release from recombination. However, the recession depth between the two methods at the shoulder is 63.3%. At the hot shoulder, this shows that despite an enormous discrepancy in recession depth, that the presence of ablative species can significantly alter the aerothermal heating. The data from the DHA method using the MC model (DHA-MC) shows a hot shoulder thickness that is within 4% of the DHA-ZA and fully catalytic film coefficient methods, while being approximately 5% higher than the non-catalytic film coefficient. This model has an even higher amount of recession than the fully catalytic film coefficient due to its irreversible rates. This requires that there is no backward rate computed in the overall production rates, leading to ablation rates that can exceed chemical

equilibrium. Again, this is an excellent example that illustrates that the aerothermal heating depends not only on recession (which contributes through the $\dot{m}''_c h_c$ term), but also through the mass diffusion fluxes. In this case, a combination of energy from chemical reactions and CO mass diffusion make the predicted heatshield thickness higher than the non-catalytic case (no mass diffusion), but lower than the fully catalytic and DHA-ZA cases.

The relative magnitudes of the various physical contributions to the surface energy balance have shifted at the lee shoulder. At the downstream body location, where temperatures are cooler and pressures are lower, the magnitude of the recombination energy dominates the surface energy balance. This leads to a much larger heatshield thickness sizing for the fully catalytic film coefficient than any of the other models. At this body location, the ablation rates have such a small magnitude, that the ablation energy flux is not a large contributor. However, the DHA-ZA model still results in a thicker heatshield than the non-catalytic film coefficient method due to the CO_2 mass diffusion flux.

In fact, since the ablation rates are so small, the ablation energy flux and advection fluxes should be an order of magnitude smaller than the conduction and mass diffusion fluxes. Then the heatshield thicknesses in Table 5.17 reflect the following; the non-catalytic film coefficient is a 5-species air conduction flux with an enthalpy correction based almost entirely on the difference in wall temperature between the CFD and the MR, the Milos and Chen model represents an ablative conduction and mass diffusion flux that contains CO and an odd amount of C, and the Zhluktov and Abe model represents an ablative conduction and mass diffusion flux that contains CO_2.

With the above considerations, it is important to dive deeper into the specific mechanisms that cause the overall aerothermal heating.

Blowing correction assessment

The flat plate film theory blowing correction may be assessed against the CFD-computed advective flux for the AS-202 case in a similar manner as was shown previously for the spherical geometry case. In Fig. 5.37, a similar trend is seen for the percentage of the aeroheating flux predicted by the correction model. The correction plateaus at 6.5% of the aeroheating flux at the hot shoulder. Again, this is due to reaching the B' plateau for CO generation. The lee shoulder in the expansion region never gets hot enough to reach the full 6.5% plateau. Looking to Fig. 5.38, it may be seen that this is due to the surface temperature never going above 700 K in at that location. Instead, the value of the blowing correction moves up and down the transition zone of the surface thermochemistry table.

This insight leads to the behavior of the predicted advective flux via film coefficient methodology, shown in Fig. 5.38. At the hot shoulder, the advective fluxes mirror the behavior of the aeroheating flux, peaking in both heat pulse locations. At the lee shoulder, since the aeroheating flux is considerably low, the predicted advective flux is also considerably low. The value is some small percentage of 1 W/cm^2.

This behavior may be contrasted to the direct heating and ablation methodology's computed advective flux, displayed for both analyzed chemistry models in Fig. 5.39. The blue lines in this figure represent a given DHA CFD solution computed with radiative equilibrium assumption and the surface emissivity set to 0.1. The orange lines are for a unity surface emissivity. The green lines are for a high value of surface emissivity, 10 for the Milos and Chen model and 3 for the Zhluktov-Abe model. The left column of subplots is the advective flux values plotted against time. The right column is the wall temperature. In the wall temperature plots, an additional black line is shown, which gives the wall temperature of the material response with an imposed DHA boundary condition.

Looking to Fig. 5.39(a), the hot shoulder material response wall temperature rises

from the initial condition of 300 K and quickly begins to follow the $\epsilon = 1$, orange line. This means the interpolated value of the advective flux in the DHA MR simulation will start at the lowest (hold least value) predicted by the $\epsilon = 10$ line. As the wall temperature climbs during the first dive into the atmosphere, it is interpolated between the green and orange lines. This puts the value of the advective flux at a similar value as the fully catalytic film coefficient, in this region of flight. Up until the second heat pulse, the advective flux predicted by the DHA in the MR simulation should track strongly with the orange line, which places it in the catalytic limits of the FC-predicted advective flux.

At the lee shoulder (lower two subplots), the wall temperature from the MR simulation falls between the $\epsilon = 1$ and $\epsilon = 10$ lines and remains there through most of the trajectory. This behavior mimics the hot shoulder, at a much lower magnitude, with the primary difference being that the material response wall temperature falls between the higher surface emissivities through most of the trajectory.

In the instance of the Zhluktov-Abe model, the hot shoulder material response wall temperature again, strongly tracks the $\epsilon = 1$ DHA wall temperature. This means that the advective flux will closely track the orange line in the upper left subplot, which is actually negative. Unlike the large amount of CO being produced, the ZA model produces a large amount of CO_2, which leads to negative wall enthalpies. The low surface emissivity case gets to a wall temperature much higher than the unity emissivity. The resulting higher wall temperature leads to significant CO production from the ZA model, leading to an advective flux similar to that seen in Fig. 5.39(a). These observed trends imply that the mass composition (and subsequently the kinetic model) strongly affect the CFD-computed advective heat flux. A large fraction of CO_2 even at temperature in excess of 1500 K can lead to a negative advection flux.

At the lee shoulder, there is a large amount of variation in the computed advective flux, but as shown by the wall temperature subplot in the lower right corner, the wall

temperature barely gets above 500 K. Consequently, the advective flux is not of significant magnitude to affect overall heating.

Figures 5.38 and 5.39 provide another concrete example of how the gross assumption of chemical equilibrium compares to a kinetic surface reaction mechanism. It is seen that at more moderate temperatures (lower surface temperatures than the 0.5 m spherical vehicle case), the Milos-Chen model which produces largely CO produces an advective flux that is in-family with the chemical equilibrium assumption. By in-family, it is meant that it is in between the catalytic limits of the film coefficient method. This is because the primary product of the chemical equilibrium solution is CO. By removing backward reactions, these two models produce similar mass compositions at the wall, and consequently produce similar results. The Zhluktov-Abe model, however, which includes backward rates and a primary product of CO_2 greatly changes the advective flux by altering the mass composition at the wall.

Film coefficient method flux components

To begin the assessment, the Taylor series manner of examining the constituent models of the film coefficient method is adopted. Recall that this re-states the aeroheating flux of the film coefficient method as

$$q_{\text{aero}} = q^{\text{CFD}} \times \Omega \times \Gamma \tag{5.31}$$

where q^{CFD} is the wall enthalpy from the 5-species air, base CFD simulation, $\Omega = \frac{\text{C}_\text{H}}{\text{C}_{\text{H}_0}}$ is the blowing correction, and Γ is the enthalpy correction given by

$$\Gamma = \frac{h_r - h_w^{MR}(t)}{h_r - h_w^{EQ}} \tag{5.32}$$

where h_r is the recovery enthalpy, h_w^{MR} is the material response wall enthalpy (taken from the B' surface thermochemistry tables), and h_w^{EQ} is the equilibrium wall enthalpy used in the construction of the film coefficient, which is a function of the freestream mole fractions and the CFD wall state variables, T_w and P_w.

If the subset of time between trajectory points is taken, then the only dependent variable in the gamma function is the wall enthalpy computed in the material response simulation. This is reflected in the notation of Eq. 5.32. It becomes increasingly important to understand the observed trends in Chapter 5.1.

With Eq. 5.31 in mind, examine Fig. 5.40(a). The top subplot shows the base heat flux (q^{CFD}) as a function of the trajectory time. Gold is non-catalytic, and black is fully catalytic. The dashed lines are the base heat flux multiplied by the enthalpy correction term. The dotted lines are the enthalpy corrected heat flux multiplied by the blowing correction. Figure 5.40(a) is for the hot shoulder on the vehicle.

By disentangling the correction models, it is evident that the largest difference is due to the adoption of different mass transfer boundary conditions. Another feature which is common with surface ablators, is a roughly constant blowing correction model. This is due to the nature of the carbon-air B' surface thermochemistry table. As the blowing correction model is a function of B_c' and this value plateaus over a relevant temperature range, the blowing correction remains constant. It appears to shift magnitude in the plots such as Fig. 5.40(a) because it is a percentage decrease of the base heat flux.

More intriguing is the behavior of the enthalpy correction. Recall that this model accounts for the difference in wall temperature between the CFD and the MR, and also should account for the presence of ablative species. In Fig. 5.40(a), both mass transfer BCs follow the same enthalpy correction trend, starting from roughly 15% augmentation, dropping between 10 and 0% and then steadily climbing. Beyond the 400 second mark, the enthalpy correction begins a sharper increase that persists for the remainder of the trajectory.

To understand why this occurs, the enthalpies from the CFD and the MR simulations need to be compared. Figure 5.41 shows the important distinction caused by including CO and CO_2 in the material response wall enthalpy. On the abscissa

is the wall temperature and the ordinate is the wall enthalpy. The gray and orange lines are the two body locations for a 5 species air mixture, while the blue and red lines are for the same 5 species air mixture, but permitting CO and CO_2 (i.e. the dominant products). The various lines correspond to a pressure for each trajectory point that is analyzed.

It is seen that by allowing carbon to enter the wall adjacent fluid, the wall enthalpy at any given wall temperature drops considerably. In terms of the enthalpy correction, this means that if the CFD and the MR are at the same wall temperature, then the carbon wall enthalpy will be lower than the air wall enthalpy, creating a larger numerator and an augmentation (or correction) greater than 1. This is the behavior seen in Fig. 5.40(a), which tends to diverge as lower wall temperatures are reached. This is simply a point of reaching the equilibrium solution which predicts CO_2 as the dominant oxidation species which drops the wall enthalpy further.

To further prove this point, the wall temperature at the hot shoulder location in the 5 species air CFD simulation is plotted against the surface temperature predicted in the material response simulation (see Fig. 5.42(a)). Both the fully catalytic and non-catalytic film coefficients produce a similar behavior. In the upper atmosphere and upon entering the atmosphere during the first pulse, the wall temperature of the CFD is higher than the material response. The difference is quite large at the first trajectory point, and decreases significantly as the vehicle enters the first pulse. This is seen in the drastic drop in the enthalpy correction of Fig. 5.40(a). This infers that the transient heat conduction is lagging behind the instantaneous (steady state) predicted value. In other words, the CFD will be hotter than the material response going up the first heat pulse. As the vehicle lofts, the surface temperature drops. Around this time, the convective cooling and reradiation allow the surface temperatures to nearly equilibrate between the CFD and the MR. Then the process repeats for a second heat pulse. During the second cooling phase, the energy remains

stored in the TPS. This implies that during cooling the temperature lags above the CFD predicted wall temperature. To summarize, a general trend is observed such that the MR wall temperature will lag below the wall temperature predicted by the CFD during heating and the MR wall temperature will lag above the wall temperature predicted by the CFD during cooling. Furthermore, the lagging surface temperature during cooling, coupled with the wall enthalpy behavior of the carbon-air mixture, creates an enthalpy correction that is not physical along the end of the trajectory. Although this behavior is unphysical, the exponential nature of the over-correction is not entirely due to this. Figure 5.43 shows the exponential rise, is itself, due to the wall enthalpy as computed in the CFD approaching the recovery enthalpy. In the limit as the denominator in the enthalpy correction Γ approaches zero, the enthalpy correction will increase to infinity. The two modeling errors combined are the *endgame phenomena*.

The same heat flux components are considered for the lee shoulder in Fig. 5.40(b), with the same trends appearing as for the hot shoulder. Roughly constant blowing corrections around 4% (reduction) are present for both mass BC variations. The enthalpy correction increases monotonically, with an accelerated increase beyond the 400 second mark due to differences in low temperature wall enthalpies. Figure 5.42(b) shows a similar behavior as the hot shoulder, except at the downstream location the relative difference in surface temperature between simulations is larger. This is reflected as a slightly higher enthalpy correction value than the hot shoulder counterpart. Since the lee shoulder is operating in a lower temperature environment, these body locations on the vehicle will be the primary place where the endgame phenomena may be observed.

With these observations in mind, recall that it is important to the aerothermodynamicist to understand which physics are being represented. Under the film coefficient methodology, the aeroheating flux is meant to simulate the effect of ablative species

in the boundary layer, the effect of the advective flux (or blowing), and the mass diffusion processes that should be present through the blowing and enthalpy corrections. This may be directly compared to the component fluxes of the DHA method.

Direct Heating and Ablation method flux components

In the direct heating and ablation method, as the name indicates, correction models are no longer employed, but the *physics* of interest are calculated directly in the CFD solution. The heat flux obtained from the method is therefore called the direct heat flux and is defined by its constituents as

$$q_{\text{direct}} = q_{\text{cond}} + q_{\text{mass}} + q_{\text{adv}}. \tag{5.33}$$

The conduction flux itself is composed of two contributions from the two temperature model, what will be called the translational and vibrational conduction fluxes. The second term is the heat flux due to mass diffusion, which sums all of the species mass diffusion fluxes. The last term is the advection flux, or the energy adjustment due to a velocity created by the chemical reactions taking place at the surface.

Figures 5.44 and 5.45 show the interpolated fluxes from the $\epsilon = 1$ DHA CFD cases; the translational and vibrational conduction fluxes and the mass diffusion flux. Notably absent is the advection flux, which is so small that it does not make up a significant portion of the total heat flux at the wall. The important trend in these plots are the relative magnitudes according to a specific surface thermochemistry model being used. With a model that produces largely CO_2, the DHA-ZA model, there is seen to be a striking reduction of translational conduction and a large amount of mass diffusion driving the wall heating. This is the primary reason that the DHA-ZA model produces a heatshield thickness prediction close to the fully catalytic film coefficient. Conversely, the DHA-MC model, which produces largely CO, contains a roughly 60/40% split between translational conduction being higher and mass diffusion being

lower. Recall that the recession between the cases was dominated by the DHA-MC model. This implies that although large amounts of recession may occur, the boundary layer composition can dominate the heating. And of course, this was seen in the results of the fixed depth and sizing analysis. This further implies that the component fluxes that build to a macro wall heating flux are quite sensitive to the surface thermochemistry and wall adjacent chemistry. Interestingly, the vibrational conduction flux has a not insignificant contribution to the total heat flux. The O_2 produced by fully catalytic boundary condition in the film coefficient CFD must contribute largely to the first pulse high vibrational energy content. Likewise, the CO_2 must be driving the large values of vibrational conduction flux seen in the DHA-ZA model.

By comparison to what has been shown in the film coefficient correction models, it is observed that the advection flux as computed directly in the CFD, does not significantly reduce the heat flux. This is opposed to the film coefficient which accounts for 4-5% reduction in the total wall flux. This correction model, as previously noted, is based on crude film theory assumptions. Furthermore, it is nearly impossible to determine how well the enthalpy correction is modifying the original base heat flux to get to a heat flux that best resembles the actual physics. However, it is important to see the overall comparison between the aeroheating and the direct heat fluxes.

Material response flux components

In Figs. 5.46 and 5.47 the aeroheating and direct heat fluxes are plotted versus time. As well, the ablation fluxes, computed in the material response, are also included to show the magnitude of their flux contribution. Finally, the reradiation flux is shown. The summation of all three flux quantities yields the solid conduction that the vehicle experiences as the ultimate energy boundary condition.

Figure 5.46 shows the aeroheating and direct fluxes that drive the results seen in

Fig. 5.35(a). The range of catalycity covers a large range of heat flux values under the film coefficient method. As seen in the DHA-ZA components, the large mass diffusion flux contribution drives the DHA-ZA method to a direct heat flux higher than the fully catalytic film coefficient. The DHA-MC direct heat flux winds up roughly between all of the results. This is quite interesting as it is clearly seen that the recession, and subsequently the ablation flux is the largest in the Milos/Chen model. This contribution is not large enough to overcome the mass diffusion of the DHA-ZA method or the additional recombination energy of the fully catalytic film coefficient. Thus the question to the design engineer becomes, do we continue the tradition of using non-physical, but largely conservative models for ablative TPS?

Figure 5.47 also provides insight into the large amount of energy that can be released if enough dissociated atoms reach a body location. At the lee shoulder, this manifests as a large gap between the fully catalytic film coefficient and the remaining models. At this body location, regardless of the method, the ablation flux magnitude is not large enough to contribute to the overall heat flux. The endgame phenomena is also seen in the heat flux and even in the reradiation flux, as the non-equilibrium energy state of the CFD-based models predict a lower heating at the downstream location, while the film coefficient method is attempting to substantially increase these values through the enthalpy correction. Interestingly, at the body location, all of the non-equilibrium kinetic models are closer to the non-catalytic film coefficient method. This is most likely further evidence that this body point should be considered at chemical non-equilibrium.

Remarks on the AS-202 analysis

The AS-202 trajectory and vehicle data afforded a unique opportunity to look at a case with more realistic flight design attributes. The geometry of the vehicle creates special body points that deserve critical attention. This means that most of the

body points behave similar to the analysis that was conducted for the hot shoulder, a some what close approximation for a flat plate with low body curvature. This is also an ideal test bed for film coefficient theory, as it provides the advantage of a semi-infinite plane. The trajectory itself wound up being not extremely stressing for a carbon ablator. For the flight conditions tested, some critical insights may be made from the study:

1. The evaluation of the conduction and mass diffusion fluxes (through direct CFD or film correction models) was the primary driver of heatshield thickness.

2. The correct choosing of a homogeneous and heterogeneous chemistry models can lead to vastly different flux contributions within the surface energy balance. This implores the vehicle designer to carefully and critically choose each specific chemical species that may be present at the wall.

3. The advective flux correction model reduced energy at the surface on the order of 5% while computation of the advective flux in the CFD showed very little effect.

4. The enthalpy correction of the film coefficient methodology is responsible for the so-called *endgame* phenomena, which leads to excess heating during the convective cooling phase of flight. The non-equilibrium DHA method did not produce this run away effect.

5. Without more stressing environments, the ablation flux was not a large contributor of the overall heat flux the vehicle experienced. The residual effects of thermal mass loss were also not enough to act as drivers of heatshield thickness sizing.

6. The vibrational conduction fluxes were a small (but not negligible) portion of the contributing fluxes and their variation was most likely driven by mass

composition.

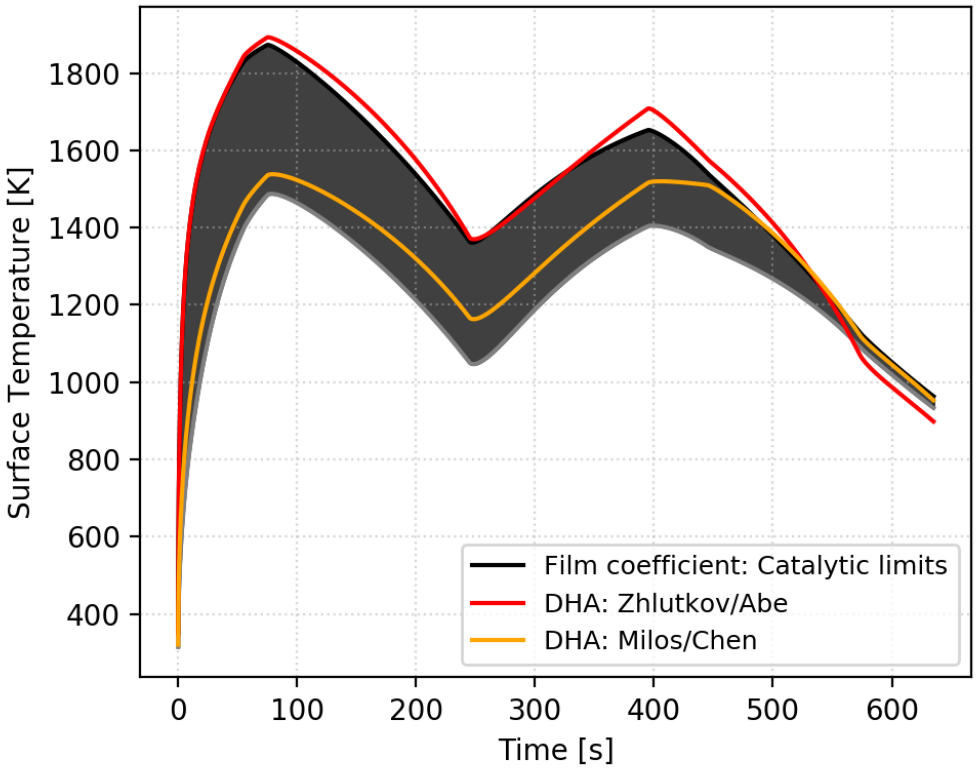

(a) *Hot* shoulder

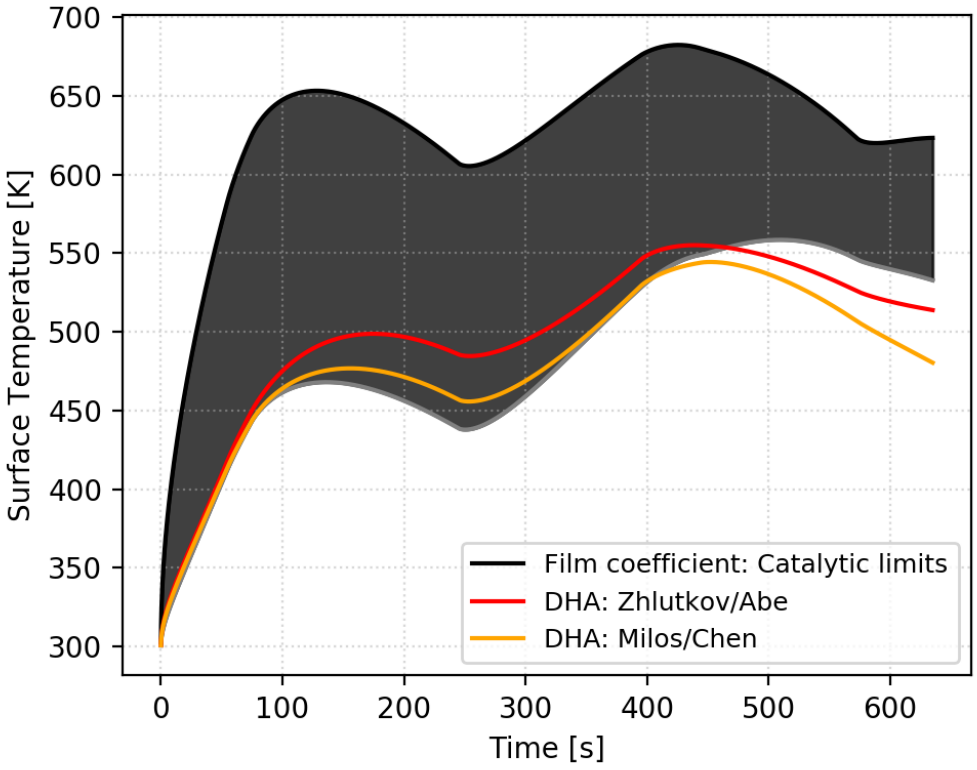

(b) Lee shoulder

Figure 5.35: AS-202 surface temperatures from material response simulation

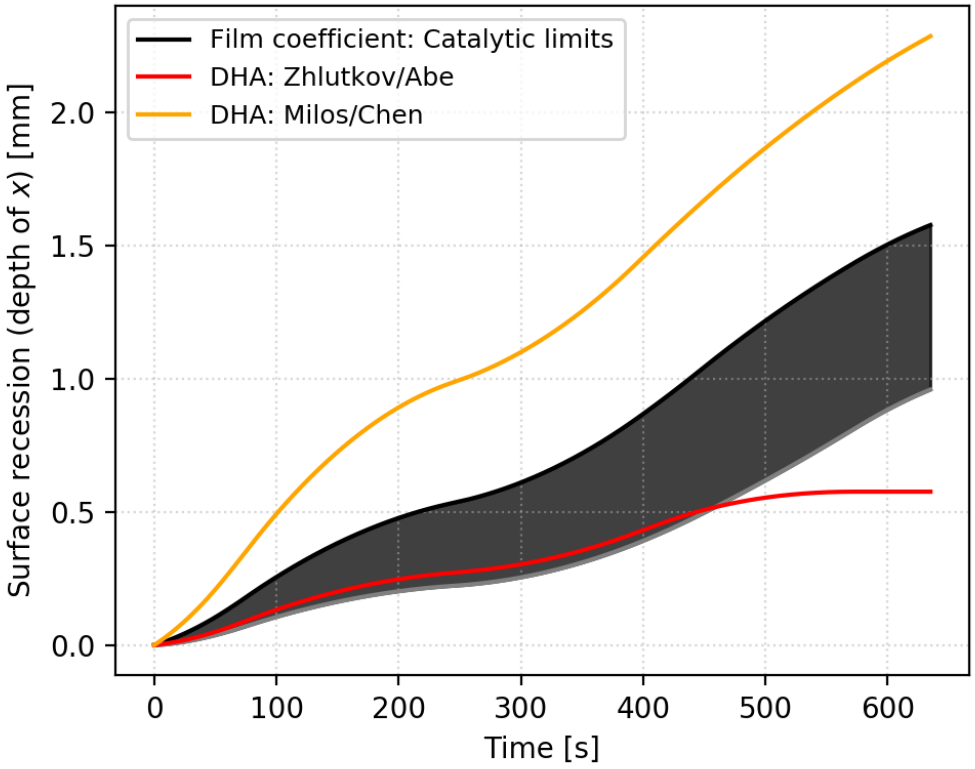

(a) *Hot* shoulder

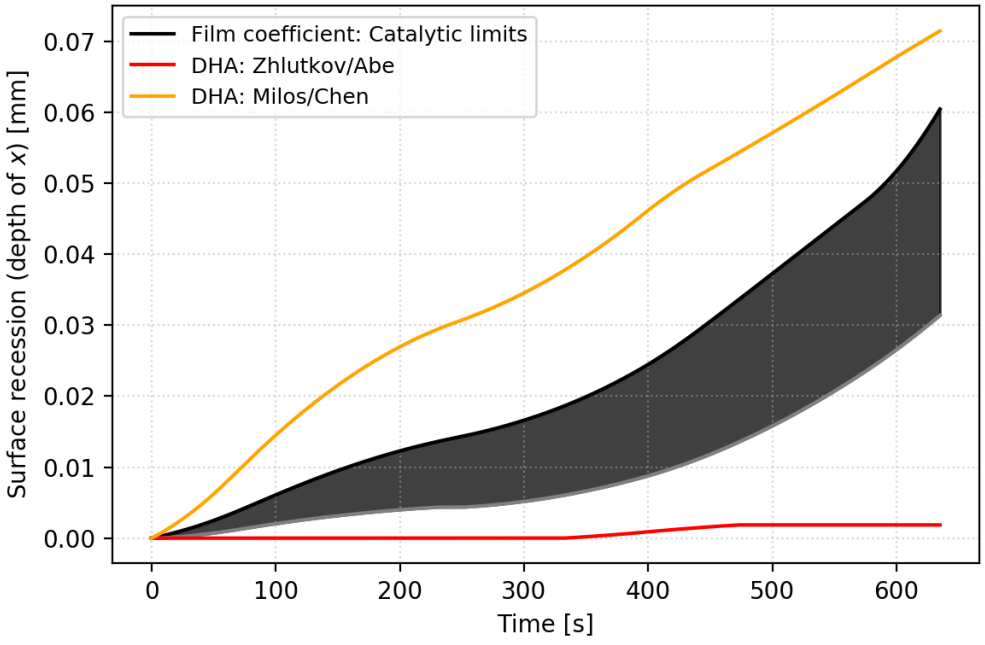

(b) Lee shoulder

Figure 5.36: AS-202 recession measurements from material response simulation

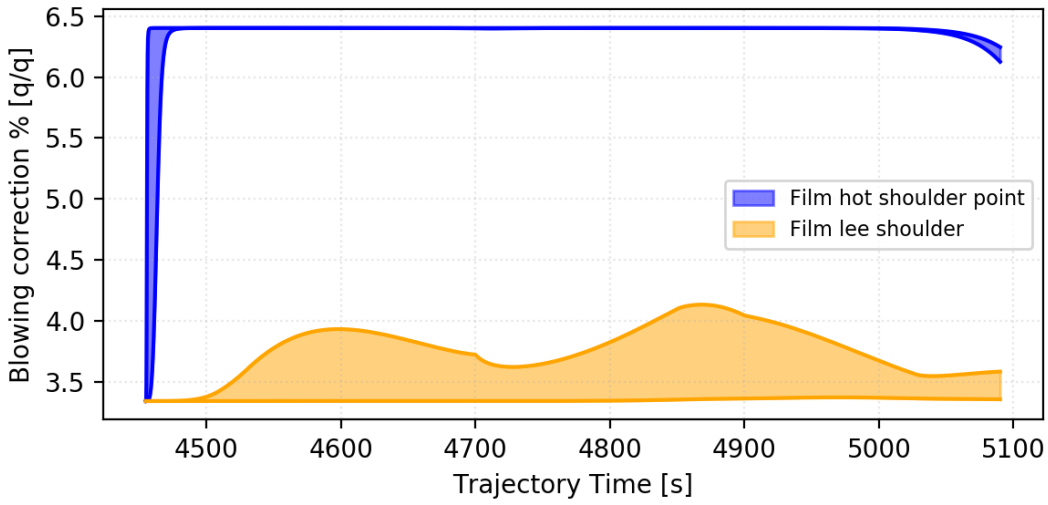

Figure 5.37: Percentage of aeroheating flux due to predicted advective flux via the film coefficient methodology

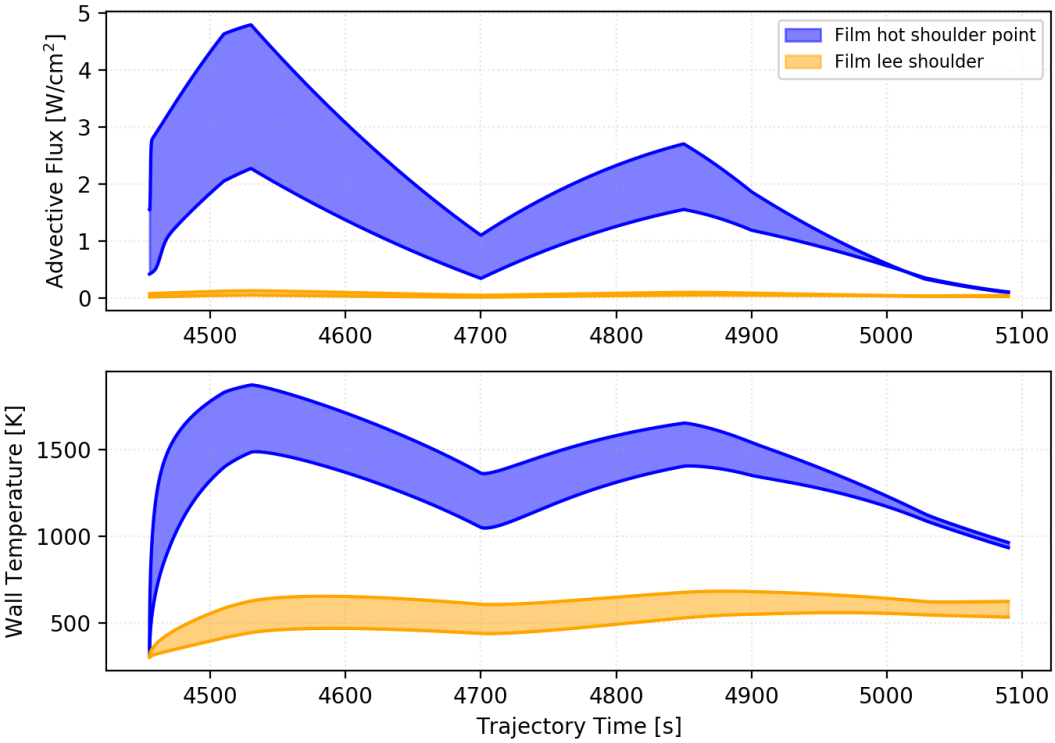

Figure 5.38: FC-predicted advective flux and wall temperatures for AS-202 vehicle

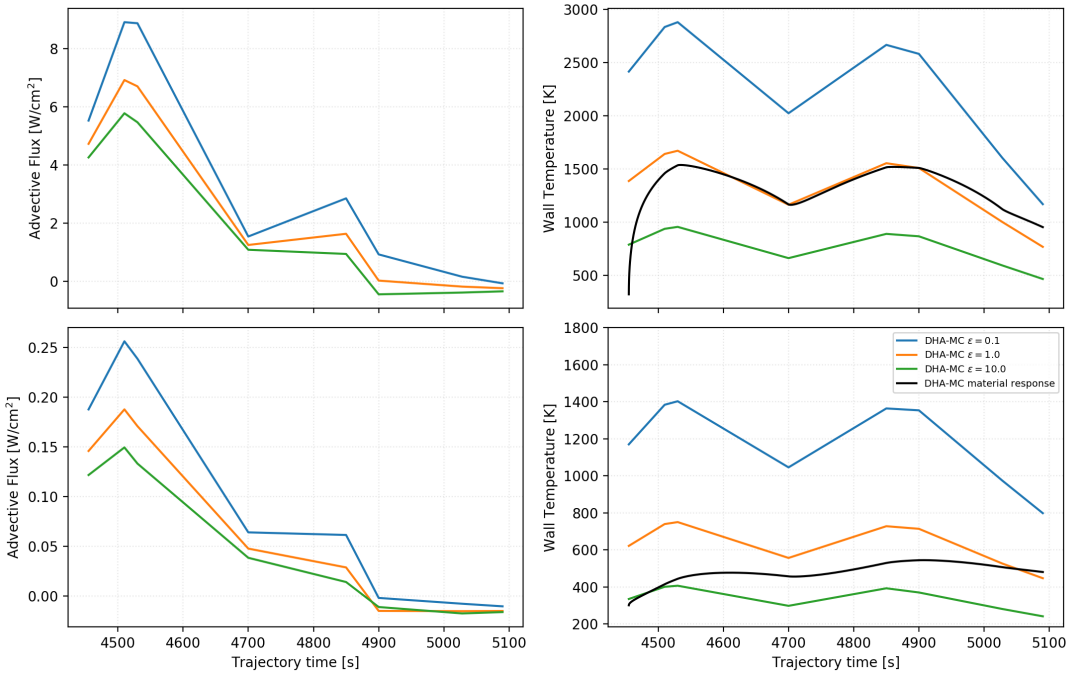

(a) DHA-MC

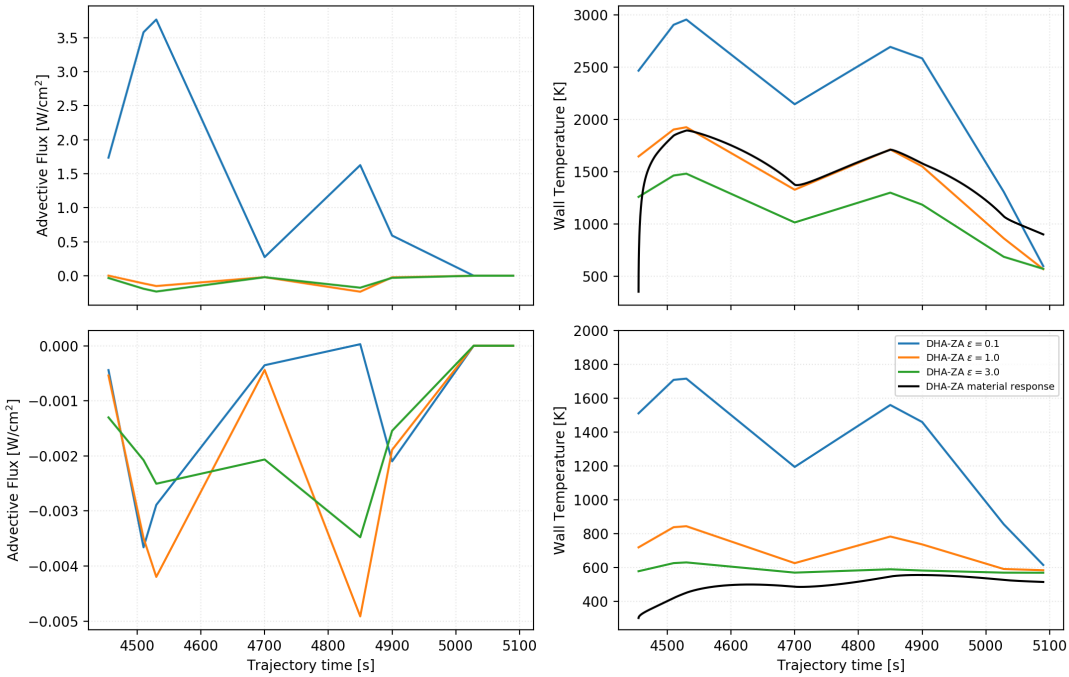

(b) DHA-ZA

Figure 5.39: DHA computed advective fluxes for AS-202 vehicle

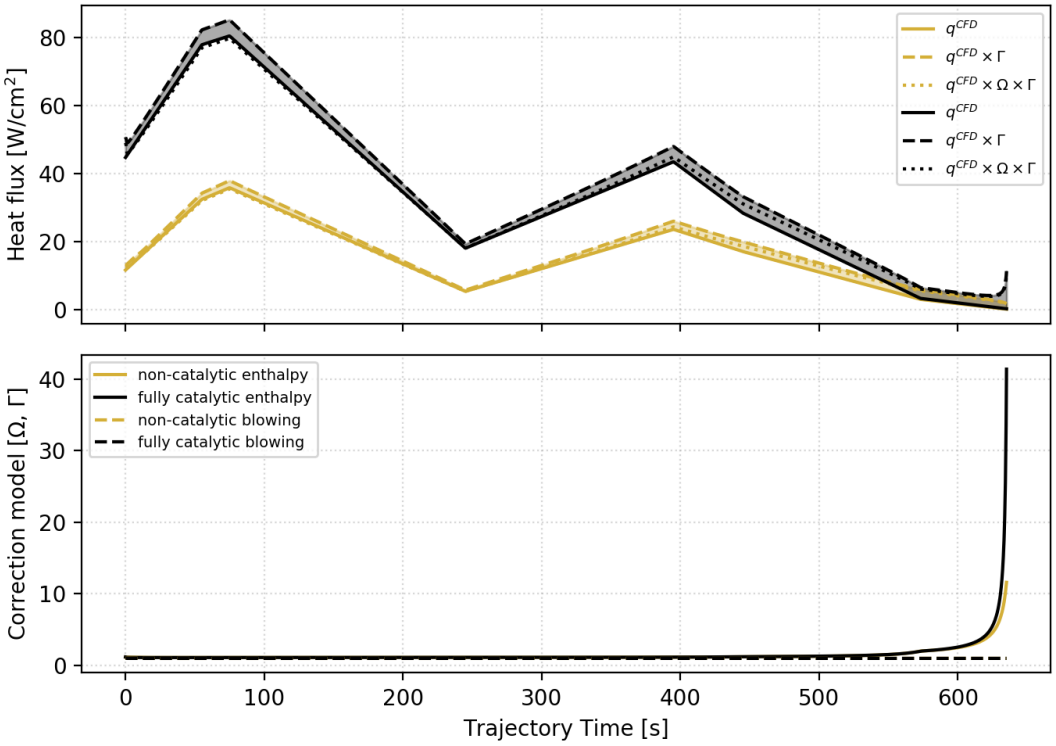

(a) Hot shoulder

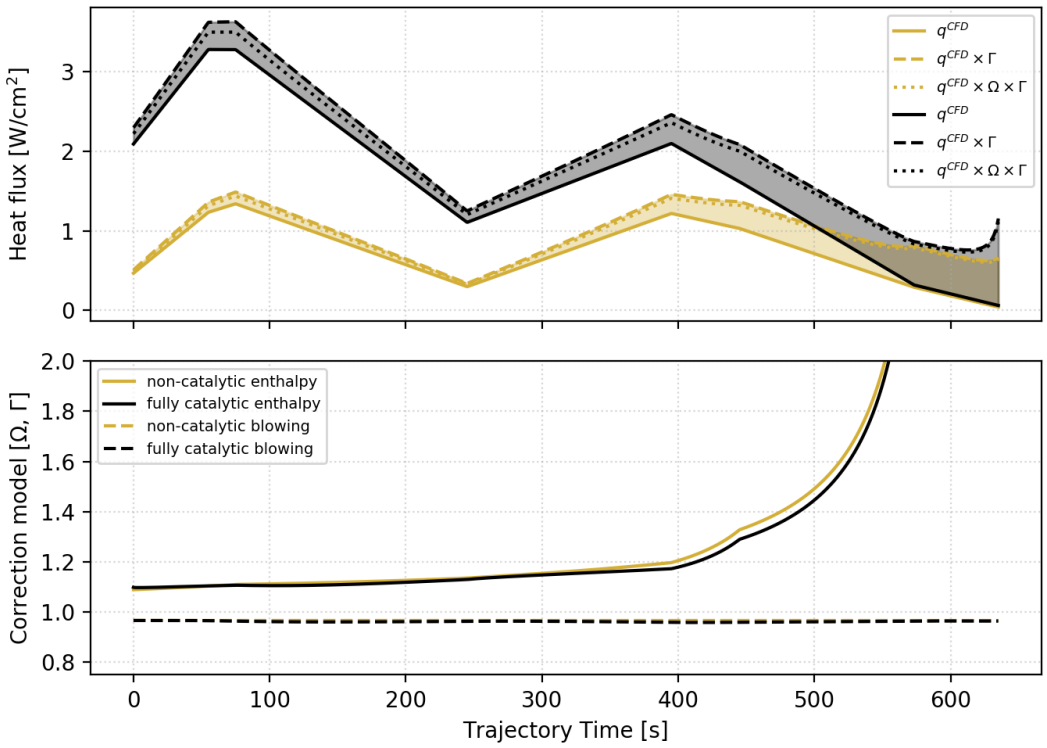

(b) Lee shoulder

Figure 5.40: Correction models of the film coefficient for AS-202 vehicle

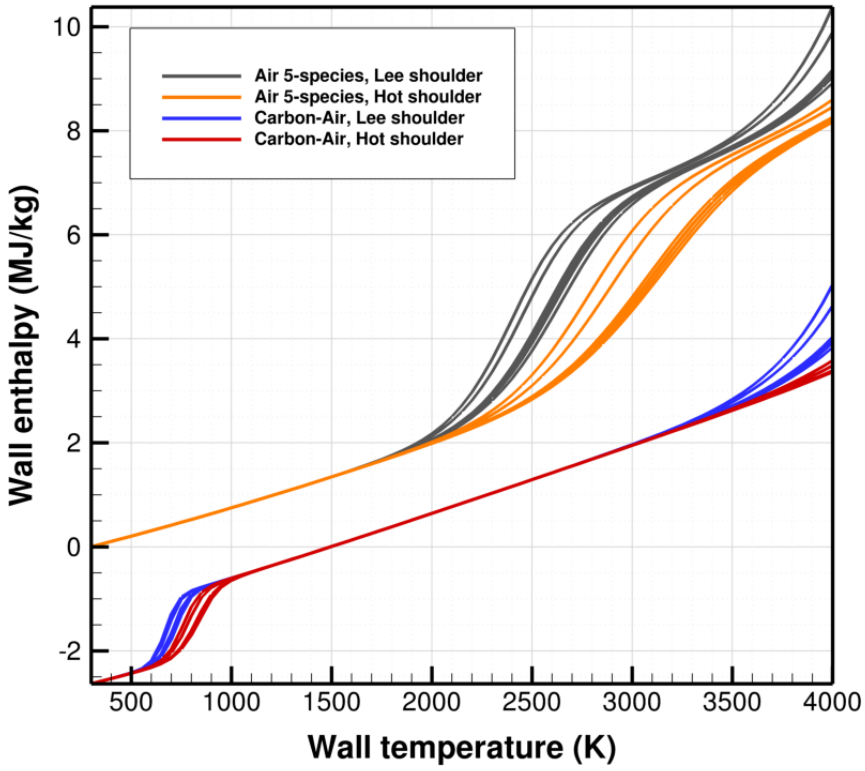

Figure 5.41: Wall enthalpy values for film coefficient evaluation of carbon-air mixture

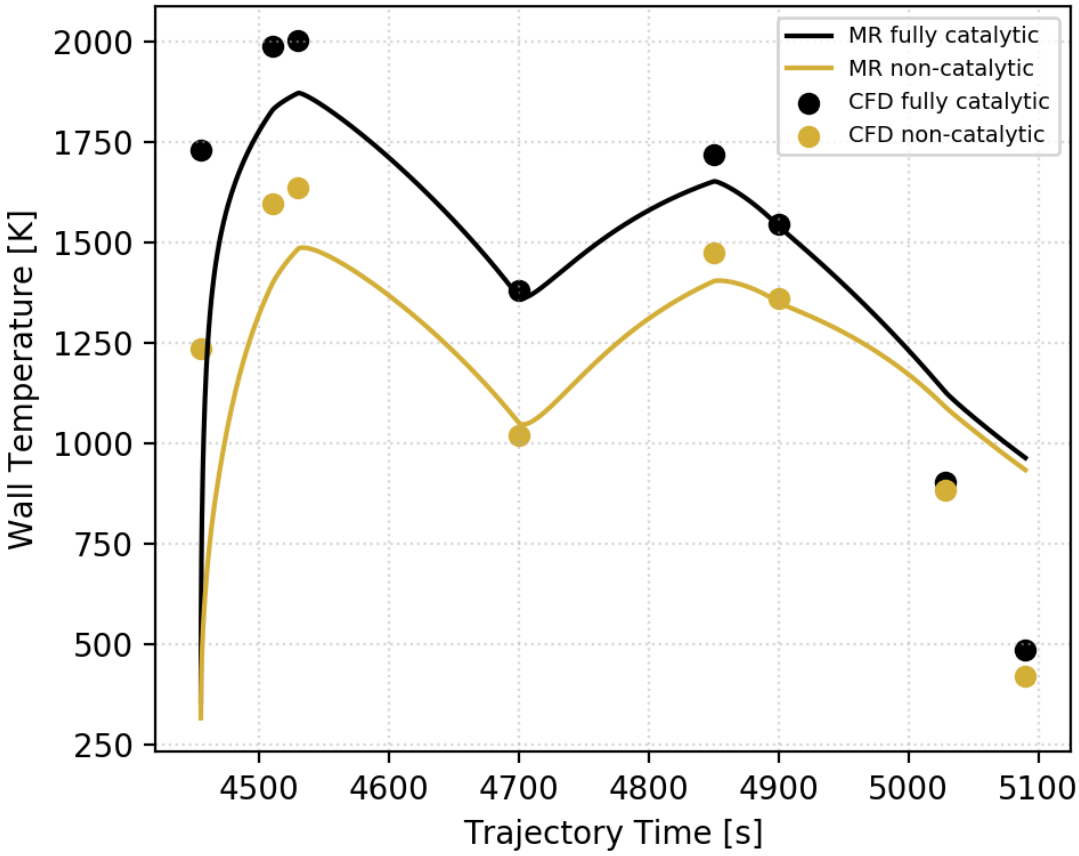

(a) Hot shoulder

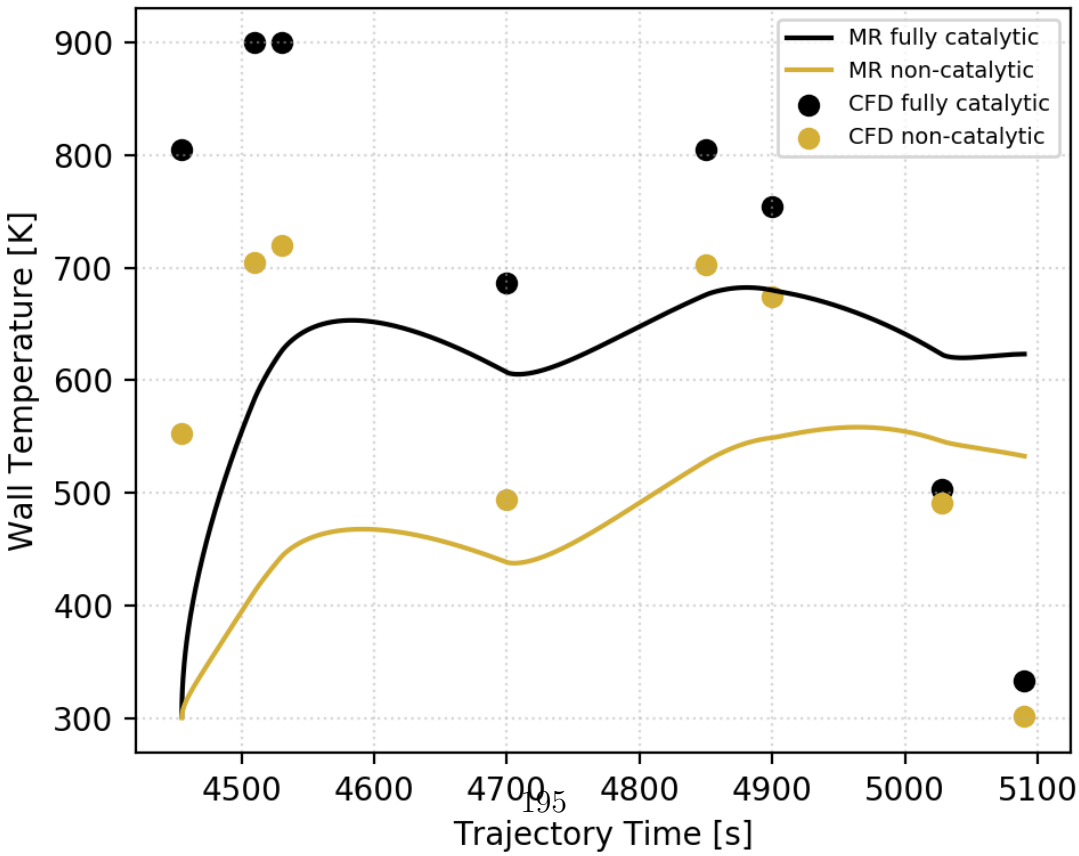

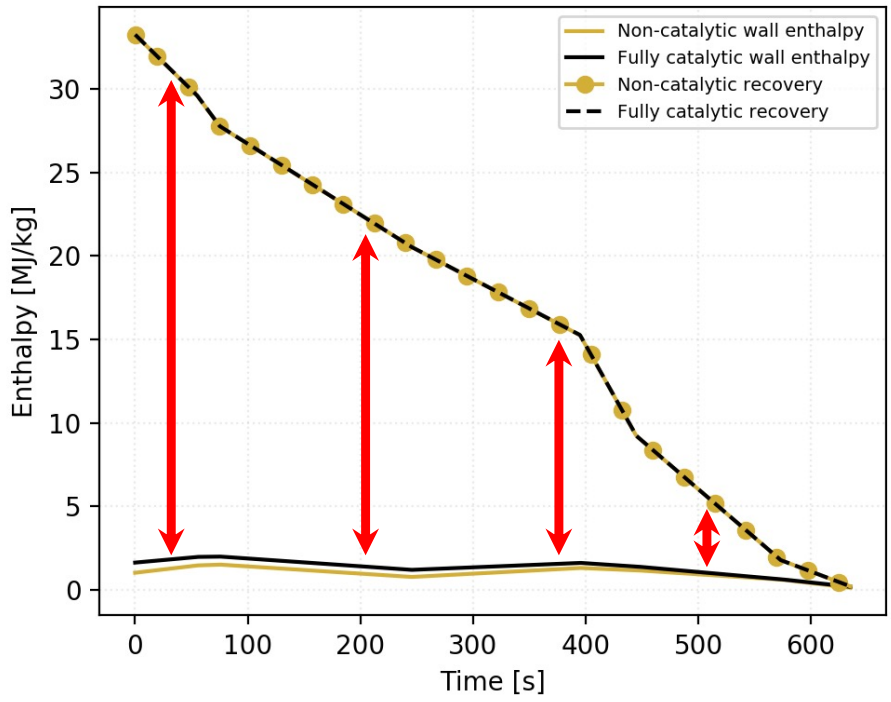

Figure 5.43: Enthalpy difference causing exponential increase in film coefficient enthalpy correction model

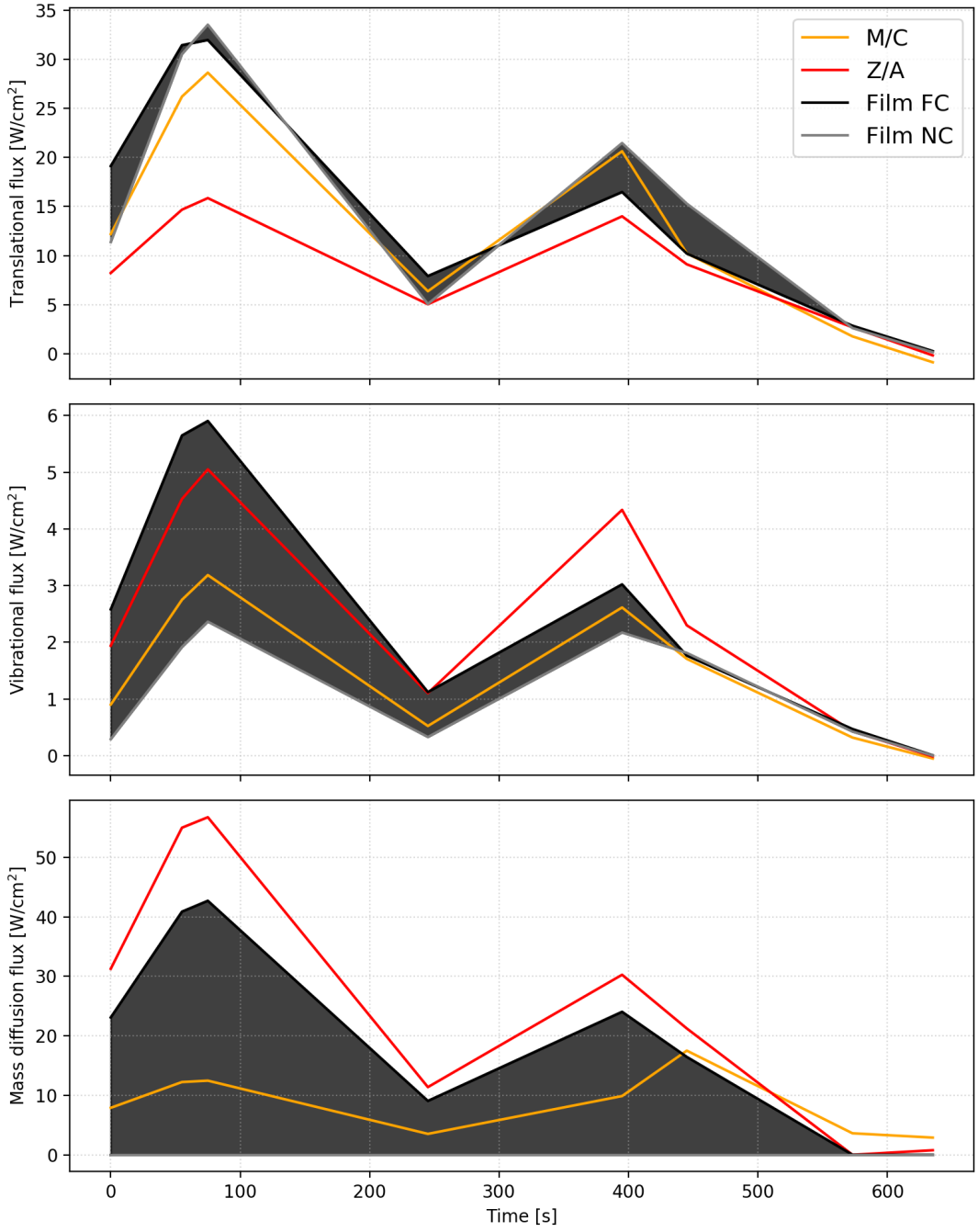

Figure 5.44: Contributing flux components of the DHA method, AS-202 hot shoulder

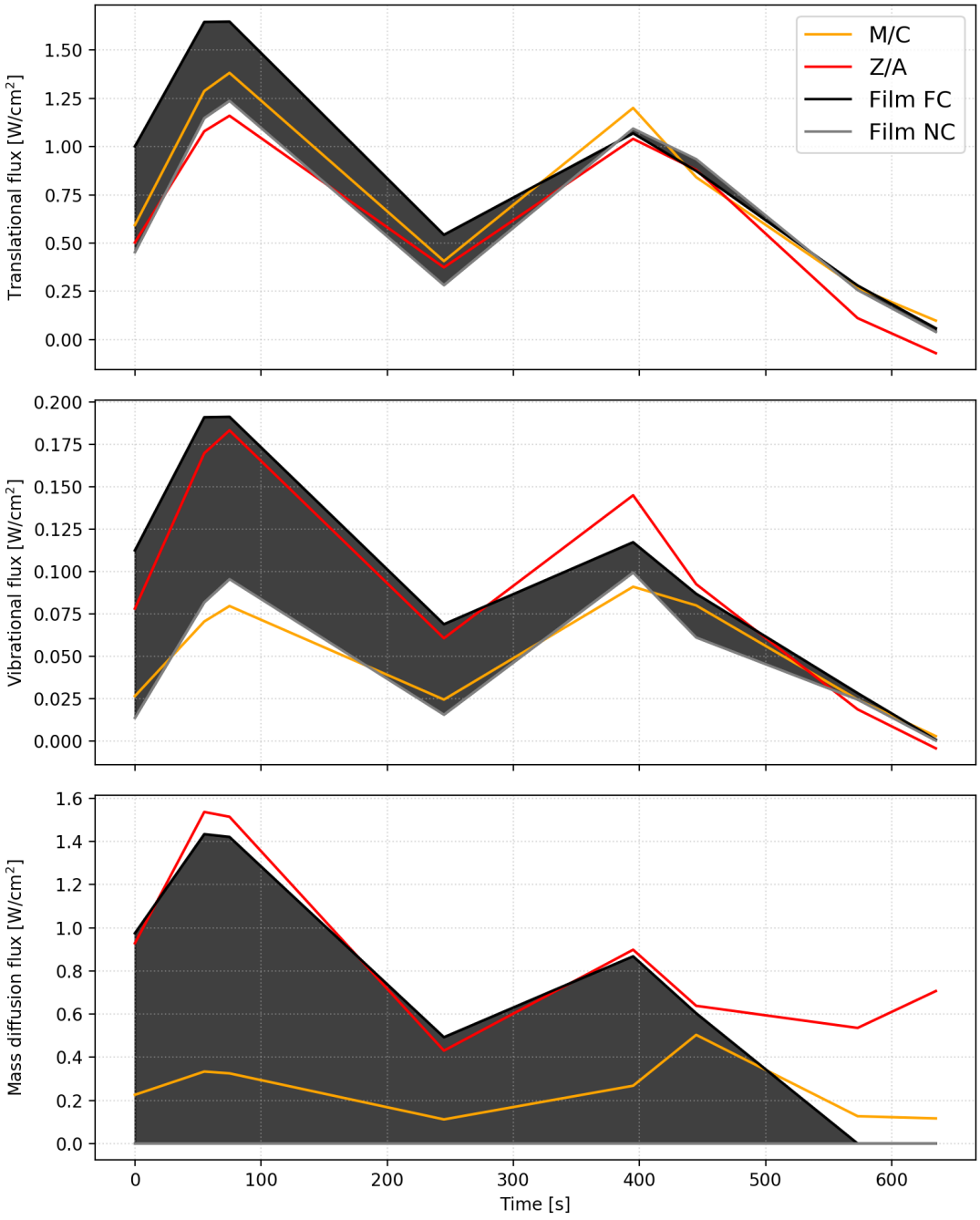

Figure 5.45: Contributing flux components of the DHA method, AS-202 lee shoulder

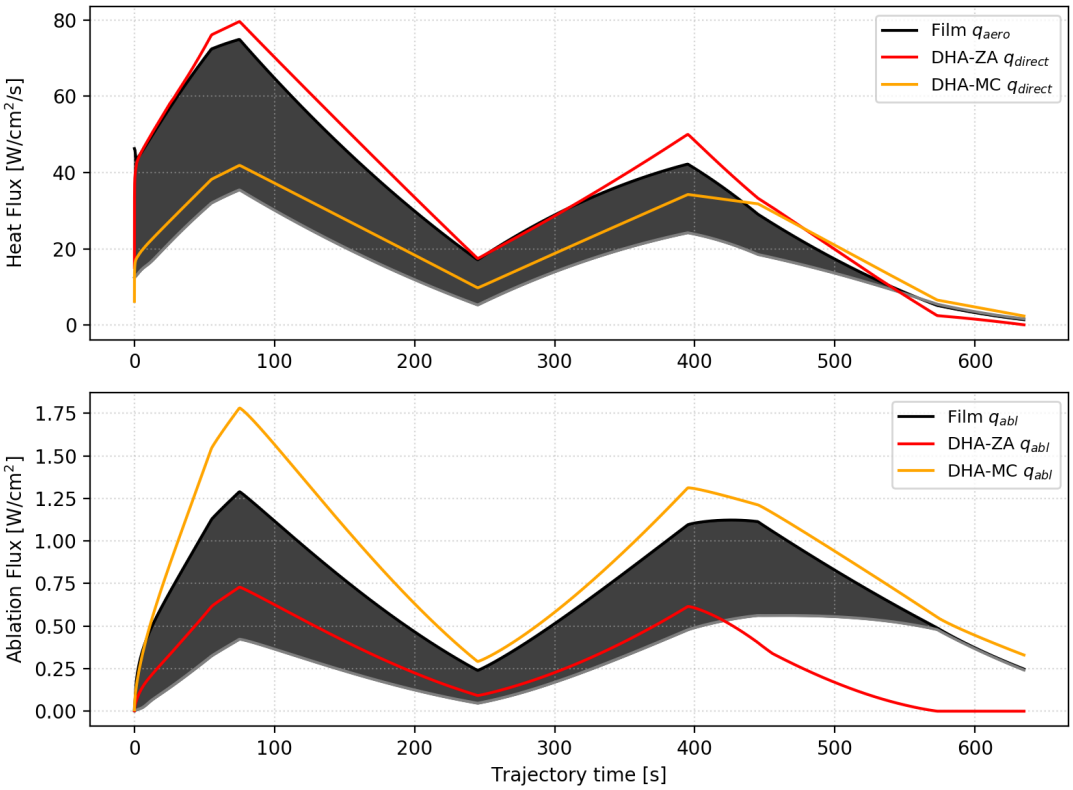

Figure 5.46: Material response flux components, AS-202 hot shoulder

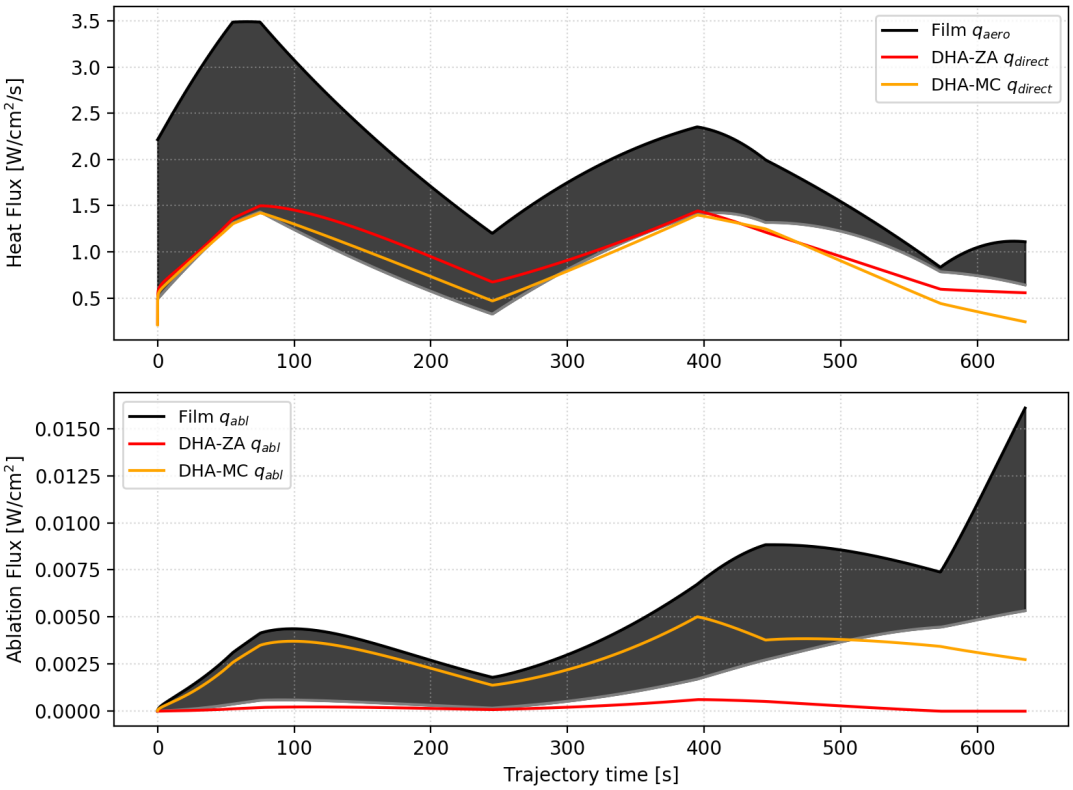

Figure 5.47: Material response flux components, AS-202 lee shoulder

Chapter 6 Extension to decomposing ablator thermal protection systems

All of the work in this research has been focused on carbon ablator systems, as they are the most well understood thermal protection system. As has been shown, the carbon ablator offers a simple test bed for the proposed methodology due to the relatively simple surface thermochemistry. However, it is hoped that the proposed methodology may be extended to the work horse of planetary entry TPS, the decomposing ablator system. What follows is a look at one such TPS and how it may be integrated into the DHA framework.

6.1 Historical context

It was well known at the time when hypersonic science was being developed that the nosetips of missiles would heat up enough to react with the surrounding atmosphere. This meant oxidation, nitridation, sublimation, melting, and spallation (86, 87) could alter the vehicle surface. These sacrificial surface phenomena are all grouped into a single term, *surface ablation*. One example of such a system is a simple graphite nose cone. Although oxidation of carbon is an exothermic process, as temperatures rise, direct sublimation occurs which is endothermic. Yet, for the most extreme peak heat fluxes, even surface ablating vehicles may not be good enough. A new type of ablator was required, the so-called *decomposing ablator*.

The Army team working on short range missiles, such as Jupiter, (down range target 1500 nautical miles) was independently developing the technology. At the same time, the Air Force long range missile, Atlas (down range target of 5500 nautical miles) was in dire need of a nose cone candidate material for its thermal protection system (TPS) technology. Both teams were required to be classified for national security, thereby isolating them from one another. Heat sinks were the dominant form of TPS,

but they were developed for V-2 spinoffs (such as the Redstone missiles) whose down range target distances were noticeably smaller. The copper heat sink was attractive due to its low mass, but the high thermal conductivity made it dangerous to attach to any substructure material. While the two military branches competed to achieve the best missile nose cone by successive material testings in the early 1950s, a young engineer by the name of George Sutton who worked at General Electric (G.E.) would be given a similar task.

According to Sutton(88), a copper heat sink had been chosen for the Atlas re-entry vehicle but engineers were concerned that the high level of ionization in the shock layer might block telemetry signals. Much like the contemporary REBR(89) vehicles, General Electric was tasked with designing a data capsule which could survive the heat of re-entry, splash-down in the ocean, and be recovered in the event of catastrophic failure. Sutton was tasked with finding the appropriate TPS for said capsule.

The idea came to him when examining jet vanes that G.E. already produced in its missile division. Jet vanes are fins placed directly inside the exhaust of a rocket engine to predictably vectorize the thrust. G.E. was currently testing plastic laminates composed of *glass cloth* and *thermosetting resins*. Production methods insisted that the "resin interlocks the fibers". Sutton's idea was to reverse this ideology so that the "fibers interlocked the resin." This meant that the fibers were now the structural support for the decomposing resin. As the resin decomposed, its gaseous product would be directly injected into the air directly adjacent to the vehicle surface. The carbonaceous matrix would still be held to the substructure until it too became oxidized. Interestingly, it would seem that von Braun had already identified these materials as potential candidates. At the time Sutton gave his first experimental results(90) (later published in 1960), von Braun was two months away from testing subscale ablative nose cones for the Jupiter program.

6.2 Prevalence and use of decomposing ablators

Table 6.1 shows a summary of planetary entry vehicle missions found in NASA/SP-2006-3401. The prevalence of decomposing ablators (20 out of 26 or 77%) as the heat shield thermal protection system highlights the importance of this special class of materials.

Mission	Heatshield Material	Decomposing Ablator	Atmospheric Entry Date
Fire II	Beryllium (heat-sink)	No	May 22, 1965
Apollo AS-201	Avco 5026-39 HC	Yes	February 22, 1966
Apollo AS-202	Avco 5026-39 HC/G	Yes	August 25, 1966
Apollo 4	Avco 5026-39 HC/G	Yes	November 9, 1967
Apollo 6	Avco 5026-39 HC/G	Yes	April 4, 1968
Re-entry F	ATJ Graphite	No	April 27, 1968
PAET	Beryllium	No	June 2, 1971
Viking Lander 1	SLA561-V	Yes	July 20, 1976
Viking Lander 2	SLA-561V	Yes	September 3, 1976
Pioneer North Probe	Carbon-phenolic	Yes	December 9, 1978
Pioneer Night Probe	Carbon-phenolic	Yes	December 9, 1978
Pioneer Day Probe	Carbon-phenolic	Yes	December 9, 1978
Pioneer Sounder	Carbon-phenolic	Yes	December 9, 1978
Orex	Reinforced CC	No	February 4, 1994
Galileo	Carbon-phenolic	Yes	December 7, 1995
Pathfinder	SLA-561V	Yes	July 4, 1997
Mirka	CFRP	Yes	October 23, 1997
ARD	Aleastrasil	No	October 21, 1998
Deep Space 2	Sirca-SPLIT	Yes	December 3, 1999
Beagle 2	Cork composite	No	December 25, 2003
Mars Rover Spirit	SLA-561V	Yes	January 3, 2004
Mars Rover Opportunity	SLA-561V	Yes	January 24, 2004
Genesis	CC/SLA-561V	Yes	September 8, 2004
Huygens	AQ60	Yes	January 14, 2005
Stardust	PICA-15	Yes	January 15, 2006
Hayabusa	Carbon-phenolic	Yes	June 13, 2010

Table 6.1: Space missions using ablative technology between 1965-2006 (Source: Planetary Mission Entry Vehicles (14) NASA/SP-2006-3401)

It is evident from Table 6.1 that more than a single type of decomposing ablator has been used in real world space missions. One specific example is the Phenolic Impregnated Carbon Ablator or PICA.

This material was first developed in the 1980's at the NASA Ames Research Center (ARC), as part of the lightweight ceramic ablator development program (91). PICA has famously been flown on the Stardust sample return mission (92), and the Mars

Figure 6.1: Stardust PICA forebody heatshield (11)

Science Laboratory (93), which safely delivered the rover Curiosity to the Red Planet on August 6th, 2012. The Stardust heatshield after entry into the Earth atmosphere and successful touchdown is shown in Fig. 6.1. The MSL tiled PICA heatshield is shown before launch in Fig. 6.2. A proprietary variant, PICA-X, still finds use today in the commercial sector (94).

The exact manufacturing and physical properties of PICA are proprietary and/or protected under International Traffic in Arms Regulations. However, an overview of the manufacturing process is described in the body of this text to clarify the relevant physics occurring in the heat shield material. This information is freely available in the public forum.

The first step for heritage PICA begins with rayon material. This initial substrate is then chopped, volatiles removed, and graphitized through a high temperature proprietary process owned by Fiber Materials Inc. (95). The resulting product is a rigid,

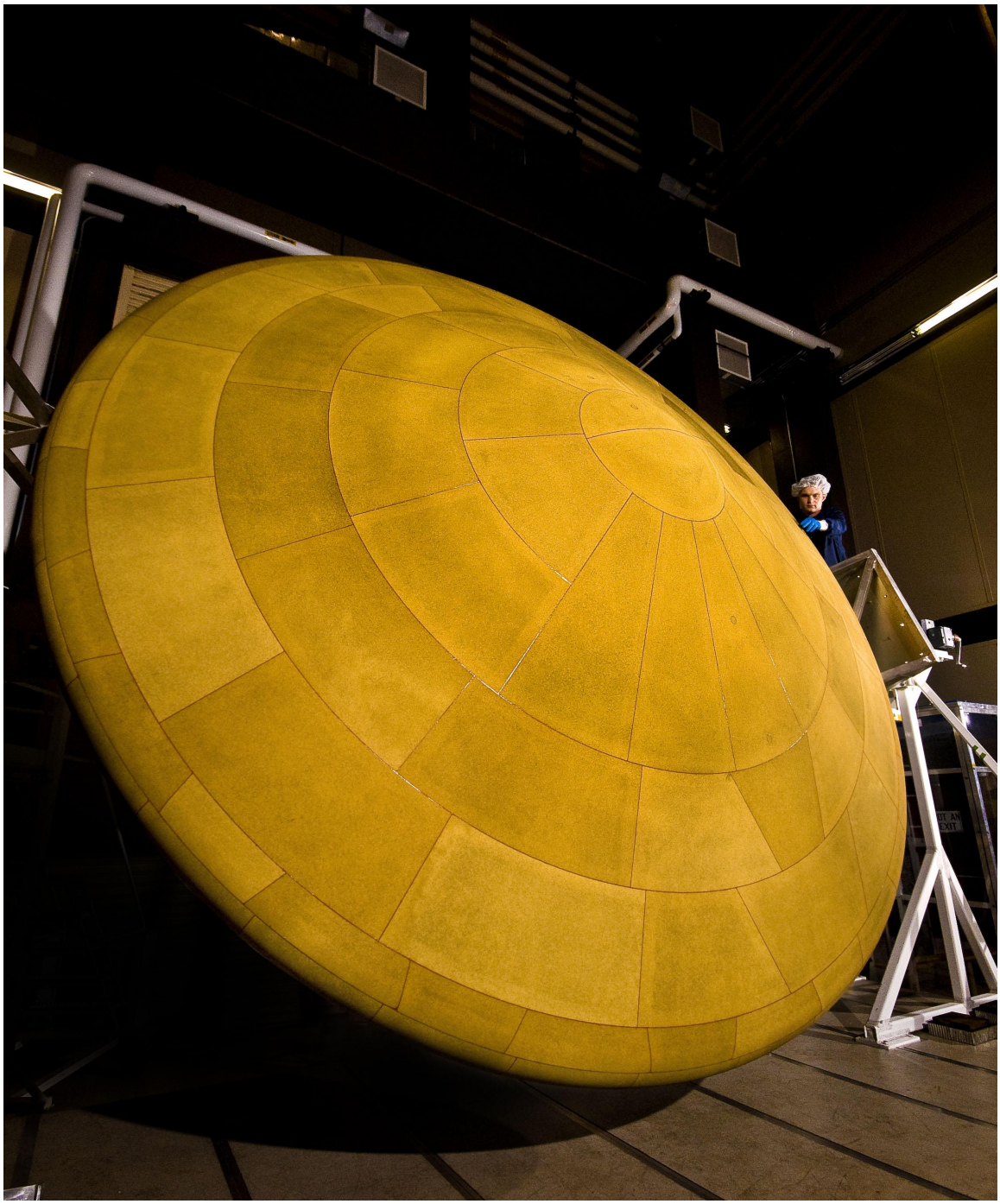

Figure 6.2: MSL tiled PICA heatshield (11)

light-weight, highly porous foam carbon, trademarked fiberform™. It is essentially rigid carbon fibers, but it's principal constituent by volume is air. Depending on downstream TPS application, this rigid material may be cast into tiles (MSL) or the entire forebody section (Stardust). The carbon substrate is then subjected to a vacuum infusion process wherein a phenolic resin is injected into the host material, coating the filaments. The final product, after curing of the resin, is designated the virgin material.

As the interaction with hypersonic air (in the case of Earth entry) heats the surface of the vehicle, the surface temperature and the internal temperature gradient begins to rise. The resin material has a much lower thermal degradation temperature than the recession temperature of the carbon matrix. Subsequently, it decomposes into what are called pyrolysis gases. At the surface, these gases are injected through momentum transfer into the boundary layer. As the isothermal front travels through the ablative material, this process repeats itself deeper and deeper beneath the surface. This in-depth decomposition continues to generate pyrolysis gases, in a narrow thermal region called the pyrolysis zone. These gases percolate through the area where the pyrolysis gas has finished evolving, i.e. the carbon skeleton which is also called the char layer. At the surface, if the temperature has increased to the correct temperature, then the carbonaceous material will begin to react with the boundary layer. This is called the char surface and the physics here can be complicated by not only reactions involving the fluid medium, but also involving the presence of pyrolysis gas.

Aside from the obvious advantage of reduced weight, the pyrolysis gases evolved generate a significant net energy savings. Not only is thermal energy absorbed through the degradation process and then transferred away from the vehicle, but the injection of gases into the boundary layer also serves to thicken the boundary layer. This is sometimes colloquially termed *mass blockage effect*. Additionally, depending on the chemical time scale of the flight condition and the composition of the atmo-

sphere, the pyrolysis gas composition can dampen the effect of surface ablation by diverting attacking atoms (such as atomic oxygen) to hydrogen atoms, which results in an exothermic release of energy but does not consume the heat shield material.

6.3 Method

While the GSI capability in the DPLR code offers a simple integrated manner of computing surface reactions within the flow field domain, it is limited in scope. In cases where a decomposing ablator is used, the surface energy balance may be computed through the so-called steady state energy balance (SSEB) which approximates the solid conduction fluxes with a linear through-the-thickness model. This requires as input a char yield parameter, which relates the expected pyrolysis gas generation to the surface charring. It also requires that the surface ablation occurs at a similar rate as the pyrolysis front moves through the material (steady state). In this research, both the steady state approximation and the use of char yield as a sensitivity parameter were found to be restrictive. In other words, parameterization cannot be achieved using what should be a constant (char yield) value.

DPLR also comes equipped with a material response coupling boundary condition which takes as input the species blowing rates (in kg/s), as well as the wall temperature (in K). One manner in which this capability may be leveraged to produce the proper surface energy balance to yield direct heating and ablation for a material response solver is now described.

Flow field

The direct heating and ablation method shifts the physics being computed in the material response into the CFD simulation. The surface energy balance for the DHA method is given by

$$q_{\text{direct}} = q_{\text{cond}} + q_{\text{diff}} - q_{\text{adv}} + q_{\text{abl}} + q_{\text{pyro}}. \tag{6.1}$$

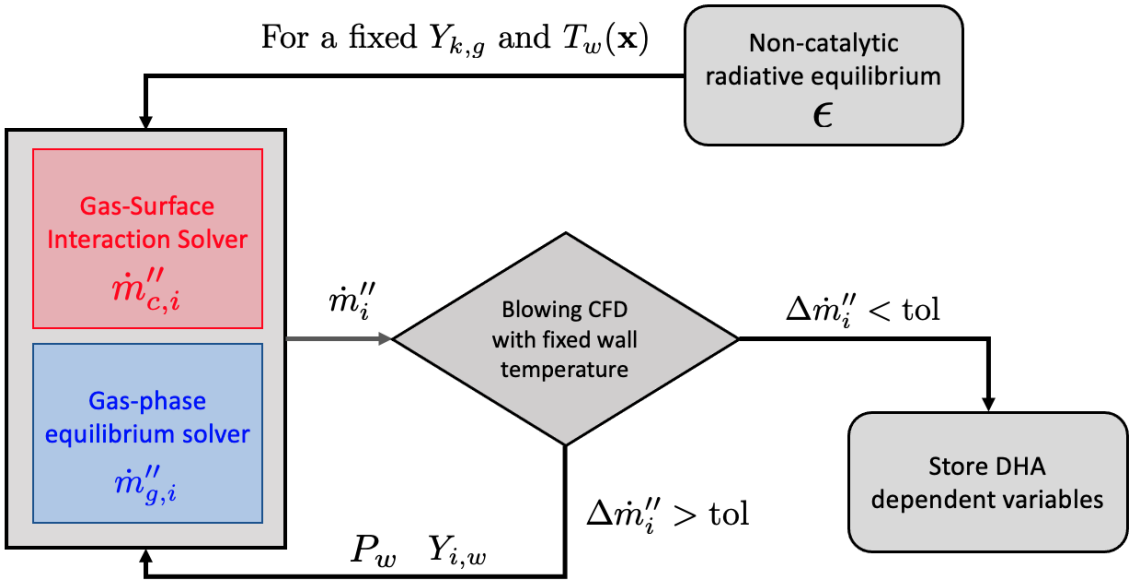

Figure 6.3: Direct Heating and Ablation (DHA) iterative CFD solution scheme

The *direct* heat flux is calculated over a range of emissivities and pyrolysis gas blowing rates, as seen in Fig. 6.3. For each trajectory body point, a radiative equilibrium solution is calculated with no injection of species. The solution is converged, grid-adapted, and then converged again. This lets the solver determine a spatially varying temperature dependence along the vehicle wall, which is due to concurrent flow physics. Based on known elemental composition, the pyrolysis gas species may be determined using the local wall temperature and pressure. Based on a user defined mass blowing flux $\dot{m}''_g$, the species blowing rates may then be defined. Combining this information with the gas-surface interaction (GSI) capability and a surface chemistry model allows the computation of ablating species $\dot{m}''_{c,i}$. Combining gives the species mass blowing rates which are passed to the CFD as a mass transpiration boundary condition with the wall temperature fixed at the radiation equilibrium temperature. The solution is allowed to converge again, where the mass fractions at the wall and the pressure will change. This is iteratively passed to the external solvers to produce updated species mass blowing rates. Upon convergence of the mass blowing rates, the surface energy balance in Eq. 6.1 is computed and the DHA dependent variables

are stored in a tabulated format according to surface emissivity and pyrolysis gas blowing rate ($(\epsilon, \dot{m}''_g)$.

This method is not ideal. Another alternative is to allow the surface energy balance to be solved as the boundary condition with the continued assumption of radiative equilibrium. The parameterization of blowing rates would be accomplished by setting them as user-specified inputs and the pyrolysis gas enthalpy would have to be evaluated during run time based on the state variables at the wall.

For each trajectory point, the necessary data have the functional relationships

$$q_{\text{direct}} = F(t, \epsilon, \dot{m}''_g, \mathbf{x}) \tag{6.2}$$

$$P_w = F(t, \epsilon, \dot{m}''_g, \mathbf{x}) \tag{6.3}$$

$$\dot{m}''_c = F(t, \epsilon, \dot{m}''_g, \mathbf{x}) \tag{6.4}$$

where the additional independent variables require E^M CFD solutions, where E is the number of emissivities and M is the number of pyrolysis gas blowing rates. This increase in parameter space requires more computational resources than the film coefficient and must be weighed against the additional physics' effect on the solution.

Material Response

The DHA surface energy balance in the material response is simply

$$q_w^{\text{MR}} = q_{\text{direct}} - q_{\text{rerad}}. \tag{6.5}$$

The ablation flux, pyrolysis gas flux, and advective fluxes have all been accounted for in the direct heat flux. The reradiation term is determined in the usual manner from the resulting wall temperature. The desired quantity, the solid conduction into the vehicle, is given by the difference of the two terms.

In this manner, the complexities of creating surface thermochemistry tables is circumvented. It is replaced by creating heterogeneous and homogeneous chemistry

models in the CFD. This greatly simplifies the application of the material response simulation for the thermal analyst.

6.4 Additional considerations for pyrolyzers

Separate from the issue of correct implementation of the DHA methodology for pyrolyzing ablators, the problem of accurate chemical mechanisms still exists. Current research is being conducted on Avcoat, the TPS for NASA's Artemis mission. A very detailed theoretical study dedicated to carbon-phenolic materials like PICA has been offered by Martin and Boyd (96) with reduced reaction sets to limit computational expense. As has been shown in this study, the altered composition of the wall adjacent fluid can drastically modify the mass diffusion flux, and subsequently the heating. The presence of hydrogen in the resin compounds means that there may exist molecules of largely varying molecular weights, which can also have an effect on the mass diffusion flux.

Chapter 7 Conclusion

7.1 Engineering Observations

The DHA methodology, just like the FC methodology, is a set of guidelines that can take many different forms of implementation. The essence of the DHA methodology is shifting the ablation physics from the material response domain to the CFD domain. Beyond this, depending on the vehicle and the TPS, careful consideration should be paid to the following areas when being applied.

1. Homogeneous models
2. Heterogeneous models
3. Surface energy balances – make sure that you do not compute fluxes twice (or not at all) between the two domains
4. Proper selection of epsilon values so that they do not break the other models you have in place
5. For extension to pyrolysis cases – proper selection of blowing values that do not break your cases

It was seen that the chemistry has a profound effect on the total aerothermal heating at the wall. In cases where chemistry becomes more complex than 5-species air, this can lead to dramatic effects as was seen in the case of CO_2.

As the DHA methodology can be implemented in any CFD and MR, it is important to understand the boundary conditions that are being applied to both the CFD and MR. If the CFD SEB *includes* the solid ablation flux and/or the pyrolysis gas flux, then these terms need to be removed from the material response SEB. Likewise,

if the fluid side of the SEB in the CFD is computed, then the material ablation terms such as the ablation flux and pyro gas flux need to be included in the SEB on the MR side. The DHA boundary condition for the MR should therefore be developed in anticipation of the CFD SEB output.

It was also found through experimentation that epsilon values needed to be considered carefully in conjunction with flight condition and body location. The typical set chosen for most of this study was $\epsilon = [0.1, 1.0, 10.0]$ which covers a large range of wall temperatures, often at a physical limit. If the reradiation term in the SEB is forced to some unphysical number, the solver may have problems converging, but also may yield an unreasonable answer. This was observed in some of the low altitude cases using the ZA surface chemistry model and an emissivity value of 10. This caused convergence problems at nearly all of the flight conditions. In complex chemistry models, these epsilon values may need to be adjusted to yield surface temperatures that reach certain activation temperatures to obtain the best resolution.

7.2 Future work

It is the author's primary wish that research continues on both homogeneous and heterogeneous reaction mechanisms. The DHA method is a framework that will need direct validation through flight experiments. The first and foremost would be to adopt the latest carbon-air model by Prata and use it in a DHA framework to validate a carbon-carbon flight experiment. NASA currently has plans to fly a spectrometer on upcoming Artemis-2+ missions which will help to characterize the species present in the shock and boundary layers. Coupled with continued molecular beam experiments in a lab setting, these data may lead to high fidelity chemistry models that have a higher confidence than the current *conservative* chemical equilibrium approach. With the properly developed PICA or Avcoat model, one day in the near future this method may be applied to a design database and rigorously compared with the heritage design

method. The additional work posed by this task is partially mitigated by the fact that the film coefficient CFD may be used as a starting point for restarting multiple DHA CFD simulations. This would be the best, and most efficient way to validate the approach for application to flight.

It would also be of interest to apply this approach to more severe regimes, such as those experienced by slender bodies. The long body promotes entropy swallowing of the boundary layer and separation. The higher temperatures ensure that the ablation flux will contribute to both ablative fluxes and advective flux calculations. The small nose radius promotes high temperatures that lead to sublimation. It would certainly be interesting from a research standpoint to see how the observed effects in this study related to this flight regime.

7.3 Final remarks

The heritage decoupled engineering methodology for the design of hypersonic vehicles under atmospheric entry was examined, both at its fundamental, boundary layer theory roots, and analytically under a plethora of various modeling assumptions. A newly proposed decoupled engineering methodology, utilizing surface reactions in the flow field was compared using three various surface chemistry models, an assortment of flight conditions, and distinct body locations.

The main result of this work is the illustration of how the novel Direct Heating and Ablation methodology removes the assumptions currently required by the heritage design paradigm while still permitting the decoupled engineering approach. The main assumptions are saturated chemical equilibrium, lewis number of unity, equal species diffusion coefficients, and the heat and mass transfer analogy.

It was shown that the scaling mechanism employed in the heat and mass transfer analogy over-predicts recession over a specific flight space. This is with a kinetic mechanism which produced carbon products in excess of a chemical equilibrium so-

lution. This points to a defiency in the heat and mass transfer analogy, which as pointed out, is not corrected by common flat plate models using the Lewis number as a correction factor.

With regard to the lewis number of unity, it is common practice to use higher fidelity multi-component diffusion models in industry and this assumption is violated in every day practice. This equates to the mass transfer condition of non-catalysis, which for aerothermal design is most likely not conservative, as shown in nearly all instances of the present study. This same practice extends to equal species diffusion coefficients, which need to be accurately calculated in the CFD to correctly predict the diffusive fluxes that drive heating (i.e. using SCEBD).

The saturated chemical equilibrium assumption was shown to yield consistent augmentation factors for the base heat flux of the CFD simulation. While this augmentation factor is meant to compensate for ablative species composition and a lagging in the wall temperature of the material response, it is more or less a monotonic augmentation factor that begins to get higher and higher toward the convective cooling phase of flight. Thus, the endgame phenomena during this period of flight should not be incorrectly assessed as owing to physical mechanisms, but rather to inefficiencies in the underlying correction model assumptions.

The DHA method removes the correction model based design method by actually computing the physics that are trying to be estimated by its predecessor. In this regard, the ablative chemical species and air species are computed through the boundary layer. This couples the ablation (creation of ablative species) with the diffusion and advective transport processes in the boundary layer. The influence of these species on the translational and vibrational conduction fluxes, and mass diffusion fluxes can be significant.

While the proposition of the DHA method is not backed by the perfect homogeneous or heterogeneous chemistry model, it was shown that despite the large difference

in underlying physical mechanisms being simulated, the overall heatshield sizing of the design method fell within the catalytic limits of the heritage model. Thus the trade off becomes, quite simply, do we stick with the heritage method whose assumptions are known to be incorrect through certain portions of flight (for example convectively cooling over-predictions and largely conservative heatshield estimates for downstream body locations due to catalycity assumptions) or do we begin to adopt a new approach that incorporates all of the fundamental non-equilibrium physics that are expected to occur during a hypersonic atmospheric entry?

Bibliography

[1] https://history.nasa.gov/monograph10/photo5.gif.

[2] https://www.nasa.gov/gateway/images.

[3] https://mars.nasa.gov/resources/22141/mars-2020s-final-four.

[4] https://solarsystem.nasa.gov/missions/viking-1/in-depth.

[5] https://apod.nasa.gov/apod/ap210615.html.

[6] https://www.nasa.gov/content/orion-spacecraft-launches-on-first-flight-test.

[7] Julien de Mûelenaere, T Magin, Jean Lachaud, and Nagi Mansour. Stagnation line approximation for ablation thermochemistry. In *42nd AIAA Thermophysics Conference*, page 3616, 2011.

[8] BJ Griffith and DE Boylan. Postflight (as-202) apollo command module aerodynamic simulation tests. Technical report, ARNOLD ENGINEERING DEVELOPMENT CENTER ARNOLD AFB TN, 1968.

[9] Aaron M Brandis and Christopher O Johnston. Characterization of stagnation-point heat flux for earth entry. In *45th AIAA Plasmadynamics and Lasers Conference*, page 2374, 2014.

[10] Michael J Wright, Dinesh K Prabhu, and Edward R Martinez. Analysis of apollo command module afterbody heating part i: As-202. *Journal of Thermophysics and heat Transfer*, 20(1):16–30, 2006.

[11] https://www.nasa.gov/centers/ames/thermal-protection-materials/tps-materials-development/low-density-ablators.html.

[12] Christopher O Johnston, Peter A Gnoffo, and Alireza Mazaheri. Study of ablation-flowfield coupling relevant to the orion heatshield. *Journal of Thermophysics and Heat Transfer*, 26(2):213–221, 2012.

[13] Chul Park. Effects of atomic oxygen on graphite ablation. *AIAA journal*, 14 (11):1640–1642, 1976.

[14] Carol Davies and Marla Arcadi. Planetary mission entry vehicles quick reference guide. version 3.0. 2006.

[15] Robert H Goddard. Rocket apparatus., July 7 1914. US Patent 1,102,653.

[16] Robert H Goddard. Rocket apparatus., July 14 1914. US Patent 1,103,503.

[17] Hsue-Shen Tsien. Similarity laws of hypersonic flows. *Journal of Mathematics and Physics*, 25(1-4):247–251, 1946.

[18] Thomas A Heppenheimer. *Facing the heat barrier: a history of hypersonics*. Courier Dover Publications, 2018.

[19] Richard Rhodes. Dark sun: the making of the hydrogen bomb, 1996.

[20] John Malik. Yields of the hiroshima and nagasaki nuclear explosions. Technical report, Los Alamos National Lab.(LANL), Los Alamos, NM (United States), 1985.

[21] Vedat S Arpaci. Conduction heat transfer. *1966, 550 &. ADDISON-WESLEY PUBLISHING CO., READING, MASS*, 1966.

[22] US Standard Atmosphere. *US standard atmosphere*. National Oceanic and Atmospheric Administration, 1976.

[23] David W Kuntz, Basil Hassan, and Donald L Potter. Predictions of ablating hypersonic vehicles using an iterative coupled fluid/thermal approach. *Journal of thermophysics and Heat Transfer*, 15(2):129–139, 2001.

[24] Alexandre Martin and Iain Boyd. Strongly coupled computation of material response and nonequilibrium flow for hypersonic ablation. In *41st AIAA Thermophysics Conference*, page 3597, 2009.

[25] Adolf Fick. Ueber diffusion. *Annalen der Physik*, 170(1):59–86, 1855.

[26] Joseph Fourier. The analytical theory of heat, 1822. *English translation: Dover*, 1955.

[27] R Bromberg. Heat transfer in boundary layers with chemical reactions due to mass addition. *Journal of Jet Propulsion*, 28(10):668–674, 1958.

[28] DB Spalding. A standard formulation of the steady convective mass transfer problem. *International Journal of Heat and Mass Transfer*, 1(2-3):192–207, 1960.

[29] Lester Lees. Convective heat transfer with mass addition and chemical reactions. In *Combustion and Propulsion, Third AGARD Colloquium*, pages 451–498. Pergamon Press Oxford, 1958.

[30] JP Hartnett and ERG Eckert. Mass transfer cooling in a laminar boundary layer with constant fluid properties. *Trans. Amer. Soc. Mech. Engrs*, 247, 1957.

[31] ERG Eckert and Robert M Drake. Heat and mass transfer, 1959. *McGraw-Hill Series in Mechanical Engineering*, 2nd edition.

[32] HS Mickley, RC Ross, AL Squyers, and WE Stewart. Heat, mass, and momentum transfer for flow over a flat plate with blowing or suction, naca techn. *Note TN*, 3208, 1954.

[33] E Eckert and O Drewitz. The heat transfer to a plate in flow at high speed. 1943.

[34] Karl Pohlhausen. Zur näherungsweisen integration der differentialgleichung der iaminaren grenzschicht. *ZAMM-Journal of Applied Mathematics and Mechanics/Zeitschrift für Angewandte Mathematik und Mechanik*, 1(4):252–290, 1921.

[35] William H Dorrance. *Viscous Hypersonic Flow: Theory of Reacting and Hypersonic Boundary Layers*. Courier Dover Publications, 2017.

[36] James A Fay. Theory of stagnation point heat transfer in dissociated air. *Journal of the Aerospace Sciences*, 25(2):73–85, 1958.

[37] Morris W Rubesin and HA Johnson. A critical review of skin-friction and heat-transfer solutions of the laminar boundary layer of a flat plate. *Trans. ASME*, 71(4):383–388, 1949.

[38] ERG Eckert. Engineering relations for friction and heat transfer to surfaces in high velocity flow, 1955.

[39] William E Meador and Michael K Smart. Reference enthalpy method developed from solutions of the boundary-layer equations. *AIAA journal*, 43(1):135–139, 2005.

[40] Carl B Moyer and Roald A Rindal. An analysis of the coupled chemically reacting boundary layer and charring ablator. part i: Summary report. 1968.

[41] Carl B Moyer and Roald A Rindal. An analysis of the coupled chemically reacting boundary layer and charring ablator. part 2-finite difference solution for the in-depth response of charring materials considering surface chemical and energy balances. 1968.

[42] Eugene P Bartlett and Robert M Kendall. An analysis of the coupled chemically reacting boundary layer and charring ablator. part 3-nonsimilar solution of the multicomponent laminar boundary layer by an integral matrix method. 1968.

[43] Eugene P Bartlett, Robert M Kendall, and Roald A Rindal. An analysis of the coupled chemically reacting boundary layer and charring ablator. part 4-a unified approximation for mixture transport properties for multicomponent boundary-layer applications. 1968.

[44] RM Kendall. A general approach to the thermochemical solution of mixed equilibrium-nonequilibrium, homogeneous or heterogeneous systems. *NASA CR-1064, June*, 1968.

[45] R. A. Rindal. An analysis of the coupled chemically reacting boundary layer and charring ablator: An approach for characterizing charring ablator response with in-depth coking reactions. *NASA CR-1065, June*, 1968.

[46] Frank S Milos and Daniel J Rasky. Review of numerical procedures for computational surface thermochemistry. *Journal of thermophysics and heat transfer*, 8(1):24–34, 1994.

[47] R Michael Evans. Jannaf boundary layer integral matrix procedure. *Aerotherm Final Report*, pages 75–152, 1975.

[48] Larry W Anderson and Howard L Morse. User's manual. volume i. boundary layer integral matrix procedure (blimp). Technical report, AEROTHERM CORP MOUNTAIN VIEW CA, 1971.

[49] Daniele Bianchi, Francesco Nasuti, Emanuele Martelli, and Marcello Onofri. A numerical approach for high-temperature flows over ablating surfaces. In *39th AIAA Thermophysics Conference*, page 4537, 2007.

[50] Peter A Gnoffo, Christopher O Johnston, and Richard A Thompson. Implementation of radiation, ablation, and free energy minimization in hypersonic simulations. *Journal of Spacecraft and Rockets*, 47(2):251–257, 2010.

[51] Graham Candler. Nonequilibrium processes in hypervelocity flows: an analysis of carbon ablation models. In *50th AIAA Aerospace Sciences Meeting including the New Horizons Forum and Aerospace Exposition*, page 724, 2012.

[52] Graham V Candler, Christopher R Alba, and Robert B Greendyke. Characterization of carbon ablation models including effects of gas-phase chemical kinetics. *Journal of Thermophysics and Heat Transfer*, 31(3):512–526, 2017.

[53] Sergey V Zhluktov and Takashi Abe. Viscous shock-layer simulation of airflow past ablating blunt body with carbon surface. *Journal of Thermophysics and Heat Transfer*, 13(1):50–59, 1999.

[54] Chul Park. Review of chemical-kinetic problems of future nasa missions. i-earth entries. *Journal of Thermophysics and Heat transfer*, 7(3):385–398, 1993.

[55] Chul Park, John T Howe, Richard L Jaffe, and Graham V Candler. Review of chemical-kinetic problems of future nasa missions. ii-mars entries. *Journal of Thermophysics and Heat transfer*, 8(1):9–23, 1994.

[56] Alexandre Martin, Ioana Cozmuta, Michael J Wright, and Iain D Boyd. Kinetic rates for gas-phase chemistry of phenolic-based carbon ablator in atmospheric air. *Journal of Thermophysics and Heat Transfer*, 29(2):222–240, 2015.

[57] David Olynick, Y-K Chen, and Michael E Tauber. Aerothermodynamics of the stardust sample return capsule. *Journal of Spacecraft and Rockets*, 36(3): 442–462, 1999.

[58] Alexandre Martin and Iain Boyd. Implicit implementation of material response and moving meshes for hypersonic re-entry ablation. In *47th AIAA Aerospace Sciences Meeting including The New Horizons Forum and Aerospace Exposition*, page 670, 2009.

[59] Ioannis Nompelis, Graham Candler, and Raul Conti. A parallel implicit cfd code for the simulation of ablating re-entry vehicles. In *47th AIAA Aerospace Sciences Meeting including The New Horizons Forum and Aerospace Exposition*, page 1562, 2009.

[60] Rochan Upadhyay, Karl Schulz, Paul Bauman, Roy Stogner, and Ofodike Ezekoye. Steady-state ablation model coupling with hypersonic flow. In *48th AIAA Aerospace Sciences Meeting Including the New Horizons Forum and Aerospace Exposition*, page 1176, 2010.

[61] Yih-Kanq Chen, Frank S Milos, and Tahir Gokcen. Loosely coupled simulation for two-dimensional ablation and shape change. *Journal of Spacecraft and Rockets*, 47(5):775–785, 2010.

[62] Haoyue Weng and Alexandre Martin. Development of a universal solver and its application to ablation problems. In *47th AIAA Thermophysics Conference*, page 3355, 2017.

[63] JW Metzger, MJ Engel, and NS Diaconis. Oxidation and sublimation of graphite in simulated re-entry environments. *AIAA Journal*, 5(3):451–460, 1967.

[64] Mark A Havstad and Robert M Ferencz. Comparison of surface chemical kinetic models for ablative reentry of graphite. *Journal of thermophysics and heat transfer*, 16(4):508–515, 2002.

[65] Ryan Gosse and Graham Candler. Evaluation of carbon-carbon ablation models using a fully coupled cfd solver. In *40th Thermophysics Conference*, page 3908, 2008.

[66] Savio Poovathingal, Thomas E Schwartzentruber, Vanessa J Murray, Timothy K Minton, and Graham V Candler. Finite-rate oxidation model for carbon

surfaces from molecular beam experiments. *AIAA journal*, 55(5):1644–1658, 2017.

[67] Krishna Sandeep Prata, Thomas E Schwartzentruber, and Timothy K Minton. Air–carbon ablation model for hypersonic flight from molecular-beam data. *AIAA Journal*, pages 1–14, 2021.

[68] John D Ramshaw. Self-consistent effective binary diffusion in multicomponent gas mixtures. *Journal of Non-Equilibrium Thermodynamics*, 1990.

[69] Chul Park. Numerical implementation of surface catalysis, reaction, and sublimation. Technical report, KOREA ADVANCED INST OF SCIENCE AND TECHNOLOGY DAEJEON (KOREA), 2007.

[70] D Stewart, J V Rakich, and M Lanfranco. Catalytic surface effects experiment on the space shuttle. In *16th Thermophysics Conference*, page 1143, 1982.

[71] William Robert Smith. Chemical reaction equilibrium analysis. *Theory and Algorithms*, 1982.

[72] Jochen Marschall and Matthew MacLean. Finite-rate surface chemistry model, i: formulation and reaction system examples. In *42nd AIAA thermophysics conference*, page 3783, 2011.

[73] Matthew MacLean, Jochen Marschall, and David Driver. Finite-rate surface chemistry model, ii: Coupling to viscous navier-stokes code. In *42nd AIAA Thermophysics Conference*, page 3784, 2011.

[74] Justin M Cooper, Joseph K Stieha, Alex M Fowler, and Alexandre Martin. Kentucky re-entry universal payload system. In *54th AIAA Aerospace Sciences Meeting*, page 2192, 2016.

[75] Kenneth Sutton and Randolph A Graves Jr. A general stagnation-point convective heating equation for arbitrary gas mixtures. 1971.

[76] Michael J Wright, Graham V Candler, and Deepak Bose. Data-parallel line relaxation method for the navier-stokes equations. *AIAA journal*, 36(9):1603–1609, 1998.

[77] BW Van Oudheusden. Compressibility effects on the extended crocco relation and the thermal recovery factor in laminar boundary layer flow. *J. Fluids Eng.*, 126(1):32–41, 2004.

[78] Sanford Gordon and Bonnie J McBride. Thermodynamic data to 20,000 k for monatomic gases. 1999.

[79] Roop N Gupta, Kam-Pui Lee, Richard A Thompson, and Jerrold M Yos. Calculations and curve fits of thermodynamic and transport properties for equilibrium air to 30000 k. 1991.

[80] Chul Park. Nonequilibrium hypersonic aerothermodynamics. 1989.

[81] David A Stewart. Surface catalysis and characterization of proposed candidate tps for access-to-space vehicles. 1997.

[82] Tom van Eekelen, Jean R Lachaud, Alexandre Martin, and Ioana Cozmuta. Ablation test-case series# 3. numerical simulation of ablative-material response: Code and model comparisons. 2012.

[83] H Julian Allen and Alfred J Eggers Jr. A study of the motion and aerodynamic heating of missiles entering the earth's atmosphere at high supersonic speeds. Technical report, NACA Ames Aeronautical Lab, 1953.

[84] Chul Park, Richard L Jaffe, and Harry Partridge. Chemical-kinetic parameters of hyperbolic earth entry. *Journal of Thermophysics and Heat transfer*, 15(1): 76–90, 2001.

[85] Yih-Kanq Chen and Frank Milos. Finite-rate ablation boundary conditions for a carbon-phenolic heat-shield. In *37th AIAA Thermophysics Conference*, page 2270, 2004.

[86] Raghava SC Davuluri, Huaibao Zhang, and Alexandre Martin. Numerical study of spallation phenomenon in an arc-jet environment. *Journal of Thermophysics and Heat Transfer*, 30(1):32–41, 2016.

[87] Alexandre Martin, Sean CC Bailey, Francesco Panerai, Raghava SC Davuluri, Huaibao Zhang, Alexander R Vazsonyi, Zachary S Lippay, Nagi N Mansour, Jennifer A Inman, Brett F Bathel, et al. Numerical and experimental analysis of spallation phenomena. *CEAS Space Journal*, 8(4):229–236, 2016.

[88] George W Sutton. The initial development of ablation heat protection, an historical perspective. *Journal of Spacecraft and Rockets*, 19(1):3–11, 1982.

[89] William Ailor, Ian Dupzyk, John Shepard, and Mark Newfield. Rebr: An innovative, cost-effective system for return of reentry data. In *AIAA SPACE 2007 Conference & Exposition*, page 6222, 2007.

[90] George W Sutton. Ablation of reinforced plastics in supersonic flow. *Journal of the Aerospace Sciences*, 27(5):377–385, 1960.

[91] Mairead Stackpoole, Steve Sepka, Ioana Cozmuta, and Dean Kontinos. Post-flight evaluation of stardust sample return capsule forebody heatshield material. In *46th AIAA Aerospace Sciences Meeting and Exhibit*, page 1202, 2008.

[92] Haoyue Weng, Ümran Düzel, Rui Fu, and Alexandre Martin. Geometric effects on charring ablator: Modeling the full-scale stardust heat shield. *Journal of Spacecraft and Rockets*, pages 1–14, 2021.

[93] Karl Edquist, Artem Dyakonov, Michael Wright, and Chun Tang. Aerothermodynamic design of the mars science laboratory heatshield. In *41st AIAA Thermophysics Conference*, page 4075, 2009.

[94] Nagi Mansour, Jean Lachaud, Thierry Magin, Julien de Mûelenaere, and Yih-Kanq Chen. High-fidelity charring ablator thermal response model. In *42nd AIAA Thermophysics Conference*, page 3124, 2011.

[95] Mairead Stackpoole, Ethiraj Venkatapathy, and Steven Violette. Sustaining pica for future nasa robotic science missions including nf-4 and discovery. In *2018 IEEE Aerospace Conference*, pages 1–7. IEEE, 2018.

[96] Alexandre Martin and Iain Boyd. Cfd implementation of a novel carbon-phenolic-in-air chemistry model for atmospheric re-entry. In *49th AIAA Aerospace Sciences Meeting including the New Horizons Forum and Aerospace Exposition*, page 143, 2011.

[97] Christopher Barrow, John F Maddox, and Alexandre Martin. Semi-empirical method for measuring thermal conductivity of fibrous insulation materials. In *AIAA Aviation 2019 Forum*, page 3472, 2019.

[98] Ludwig Prandtl. Über flussigkeitsbewegung bei sehr kleiner reibung. *Verhandl. III, Internat. Math.-Kong., Heidelberg, Teubner, Leipzig, 1904*, pages 484–491, 1904.

[99] Alexandre Martin, Huaibao Zhang, and Kaveh A Tagavi. An introduction to the derivation of surface balance equations without the excruciating pain. *International Journal of Heat and Mass Transfer*, 115:992–999, 2017.

[100] Sinclaire M Scala. Hypersonic heat transfer to catalytic surfaces. *Journal of the Aerospace Sciences*, 25(4):273–275, 1958.

[101] R0 Goulard. On catalytic recombination rates in hypersonic stagnation heat transfer. *Journal of Jet Propulsion*, 28(11):737–745, 1958.

[102] Linwood B Callis and Jane T Kemper. *A Program for Equilibrium Normal Shock and Stagnation Point Solutions for Arbitrary Gas Mixtures.* National Aeronautics and Space Administration, 1966.

[103] Nguyen X Vinh, Adolf Busemann, and Robert D Culp. Hypersonic and planetary entry flight mechanics. *NASA STI/Recon Technical Report A*, 81, 1980.

[104] John J Bertin. *Hypersonic aerothermodynamics.* AIAA, 1994.

[105] JM Picone, AE Hedin, D Pj Drob, and AC Aikin. Nrlmsise-00 empirical model of the atmosphere: Statistical comparisons and scientific issues. *Journal of Geophysical Research: Space Physics*, 107(A12):SIA–15, 2002.

Appendix A Governing Equations

The governing equations may be summarized in vector form notation as

$$\frac{\partial \mathbf{Q}}{\partial t} + \nabla \cdot (\mathcal{F}_{adv} - \mathcal{F}_{diff}) = \mathbf{S} \tag{A.1}$$

where $\mathbf{Q}$ is a vector of conserved variables under partial differentiation with respect to time, $\mathcal{F}$ is a matrix of fluxes, and $\mathbf{S}$ is a vector of source or sink terms. The quantities contained within each are determined by the domain being analyzed. For this work, the compressible, chemically reacting, variable property, laminar flow field and the porous, decomposing ablator domains are both examined.

Compressible chemically reacting laminar flow field - CFD domain

Let Ω be the fluid flow field domain. Assume a Cartesian coordinate system with $\Omega = x, y, z$ spatial coordinates and $\mathbf{U} = u, v, w$ velocity components corresponding to each corresponding spatial coordinate. The conserved variables are given by the vector

$$\mathbf{Q} = \left[\rho_{g_1}, \ldots, \rho_{g_{ngs}}, \rho_g u, \rho_g v, \rho_g w, \rho_g e\right]^T \tag{A.2}$$

where the subscript g refers to the gaseous state, the numerical subscript ngs refers to the number of the gas state chemical species, and ρ is the density of the chemical species. The components $\rho_g u$, $\rho_g v$, and $\rho_g w$ are momentum components corresponding to each velocity and e is the total energy per unit volume. The source terms are given by the vector

$$\mathbf{S} = [\dot{\omega}_1, \ldots, \dot{\omega}_{ngs}, 0, 0, 0, 0]^T \tag{A.3}$$

where $\dot{\omega}$ is the production/destruction term of the ngs gas species. The advective fluxes are those due to the bulk movement of the gas, and thus comprise a matrix of

quantities due to each velocity component. They are given by

$$\mathcal{F}_{adv} = \begin{pmatrix} \rho_{g_1} u & \rho_{g_1} v & \rho_{g_3} w \\ \vdots & \vdots & \vdots \\ \rho_{g_{ngs}} u & \rho_{g_{ngs}} v & \rho_{g_{ngs}} w \\ \rho_g u^2 + p & \rho_g vu & \rho_g wu \\ \rho_g uv & \rho_g v^2 + p & \rho_g wv \\ \rho_g uw & \rho_g vw & \rho_g w^2 + p \\ \rho_g uh & \rho_g vh & \rho_g wh \end{pmatrix} \tag{A.4}$$

where the first three rows are the components of the advection of the gaseous species. The fourth through sixth rows are the components of the advection momentum flux which includes the pressure term multipled by the identity matrix as a surface normal component. The last row contains the components of the advective energy contribution, where the property being advected due to the velocity component is $\rho_g h$, the potential energy available at the given spatial coordinate relative to some reference state.

The diffusive fluxes are those due to the random movement of the particles within the gas, each of which has an associated diffusion velocity component. They also create a matrix of quantities due to each velocity component and are given by

$$\mathcal{F}_{diff} = \begin{pmatrix} & -\mathbf{J}_1 & \\ & \vdots & \\ & -\mathbf{J}_{ngs} & \\ \tau_{xx} & \tau_{xy} & \tau_{xz} \\ \tau_{yx} & \tau_{yy} & \tau_{yz} \\ \tau_{zx} & \tau_{zy} & \tau_{zz} \\ & \tau\mathbf{u} - \dot{\mathbf{q}}'' - \sum_{i=1}^{ngs} \mathbf{J}_i h_i & \end{pmatrix} \tag{A.5}$$

where $\mathbf{J}_{ngs}$ is the mass diffusion flux for the ngs chemical species and the τ_{ij} terms are the components of the shear stress matrix. The $\tau\mathbf{u}$ term is the energy due to

viscous interactions, $\dot{q}''$ is the heat flux due to fluid conduction, and the summation term $\mathbf{J}_i h_i$ is the energy contributed by mass diffusion processes.

Porous decomposing ablator - MR domain

Let Λ be the material response domain. Assume a Cartesian coordinate system with $\Lambda = x, y, z$ and $\mathbf{U} = u_g, v_g, w_g$ velocity components corresponding to each spatial coordinate. Λ defines a porous media, composed of both a skeletal matrix and a low temperature vaporizing material, as is the case for a decomposing ablator. The conserved variables for this system are

$$\mathbf{Q} = \left[\phi\rho_{g_1}, \ldots, \phi\rho_{g_{ngs}}, \rho_{s_1}, \ldots, \rho_{s_{nss}}, \phi\rho_g u, \phi\rho_g v, \phi\rho_g w, \phi\rho_g e_g + \rho_s e_s\right]^T \tag{A.6}$$

where $\phi\rho_{ngs}$ refers to the density of the ngs pyrolysis gas chemical species multiplied by the void fraction of the porous material (i.e. the porosity ϕ). The solid density terms are given by ρ_{nss} for each nss solid species. The momentum of the pyrolysis gas through the solid medium may be tracked by computing its respective components $\phi\rho_g u$. Finally, the total energy of the system is given by the summation of the energy contributed by the pyrolysis gas $\phi\rho_g e_g$ and the total energy contributed by the solid $\rho_s e_s$.

The source terms are given by

$$\mathbf{S} = \left[\dot{\omega}_{g_1}, \ldots, \dot{\omega}_{g_{ngs}}, \dot{\omega}_{s_1}, \ldots, \dot{\omega}_{s_{nss}}, D_x, D_y, D_z, S_D\right]^T \tag{A.7}$$

where $\dot{\omega}_{ngs}$ is the chemical production term relative to the ngs gas species or nss solid species. The momentum source terms are symbolized by $\mathbf{D}_i$ to symbolize the use of the Darcy-Brinkman term which arises to viscous interaction between the pyrolysis gas and the pore walls. This also results in a modified energy source term due to the same interaction, defined by $S_D = (\nabla \cdot \mathbf{D})\,\mathbf{u}$.

The contribution due to advective fluxes is given by

$$\mathcal{F}_{adv} = \begin{pmatrix} \phi\rho_{g_1}u & \phi\rho_{g_1}v & \phi\rho_{g_3}w \\ \vdots & \vdots & \vdots \\ \phi\rho_{g_{ngs}}u & \phi\rho_{g_{ngs}}v & \phi\rho_{g_{ngs}}w \\ 0 & 0 & 0 \\ \vdots & \vdots & \vdots \\ 0 & 0 & 0 \\ \phi\rho_g u^2 + p & \phi\rho_g vu & \phi\rho_g wu \\ \phi\rho_g uv & \phi\rho_g v^2 + p & \phi\rho_g wv \\ \phi\rho_g uw & \phi\rho_g vw & \phi\rho_g w^2 + p \\ \phi\rho_g uh & \phi\rho_g vh & \phi\rho_g wh \end{pmatrix} \tag{A.8}$$

where the first three rows are the advective mass transport of the pyrolysis gas and the second three rows are exactly zero as solid mass is typically not considered transported. The next three rows are the advective momentum transport and the pressure (of the pyrolysis gas) on the pore walls, with the last row being the advective enthalpy transport of the gas.

The diffusive fluxes are succintly given by

$$\mathcal{F}_{diff} = \begin{pmatrix} -\mathbf{J}_1 \\ \vdots \\ -\mathbf{J}_{ngs} \\ \mathbf{0} \\ \mathbf{0} \\ -\dot{\mathbf{q}}'' - \sum_{i=1}^{ngs} \mathbf{J}_i h_i \end{pmatrix}. \tag{A.9}$$

where $\mathbf{J}_{ngs}$ is the mass diffusion of the ngs pyrolysis gas chemical species and the summation of $\mathbf{J}_i h_i$ refers to the diffusive enthalpy transport by the pyrolysis gas. The term $\dot{\mathbf{q}}''$ is the heat flux transfer at a boundary, which may be due to several mechanisms such as solid conduction, pyrolysis gas conduction, and surface to surface

reradiation within the pore walls. Granted reradiation is not due to diffusion, but it is often included experimentally through calculations of effective thermal conductivity (97) that is calculated (as a *model*) in this part of the equations.

Appendix B Boundary Layer Equations

From the historical perspective presented in Chapter 1, it is important to note that while it was imperative to national security that hypersonic science be developed, the numerical solutions to the full set of governing equations were beyond the available computational power. Also noting from Chapter 1.5, it is sometimes infeasible or undesirable to commit to resolving the entire set of equations under program constraints. The foundation of creating a tenable solution space for heritage methodologies began with a subtle, yet indispensable observation made by Prandtl (98) in 1904 at the Third International Mathematics Congress.

Consider a fluid flowing in an open space. Next, insert a solid, impermeable object into the flow. The fluid has no choice but to divert its path around the object. The presence of the object within the flow not only displaces the fluid in physical space, but alters the characteristics of the flow within a small space close to its surface.

The region in space where this occurs is called the *boundary layer* and the distance from the surface to where there is no effect is called the boundary layer height. Each conserved quantity is subject to its own boundary layer. The nomenclature for this text will use δ for the momentum boundary layer height, δ_c for the concentration (mass) boundary layer height, and δ_T for the thermal boundary layer height.

Prandtl observed this exact phenomena, and mathematically stated that

$$\delta(s) \ll s \tag{B.1}$$

was a direct result. Physically, this states that a given boundary layer height for a conserved quantity is much less than the running length of the surface. Note that δ is a function of s, implying that this equation pertains to a single streamwise coordinate along the surface. The boundary layer height is in the surface normal direction. Thus,

the reference frame coordinates of the boundary layer equations are in the streamwise and surface normal directions.

The second assumption of boundary layer theory, which comes from the solution of the boundary layer equations themselves, is that

$$\mathcal{O}\left(\frac{1}{\mathrm{Re}_e}\right) = \frac{\delta^2}{s}. \tag{B.2}$$

Equation B.2 uses the subscript notation e which refers to the *edge* of the boundary layer. It is defined by

$$\mathrm{Re}_e = \frac{\rho_e V_e s}{\mu_e} \tag{B.3}$$

where ρ_e is the fluid edge density, V_e is the edge total velocity (magnitude), and μ_e is the viscosity of the fluid at the boundary layer edge. It is a well known similarity parameter which measures the relative influence of kinetic to viscous forces. According to Prandtl's observation, the value on the right-hand side (RHS) of equation B.2 should be small. Thus, to satisfy the second assumption of boundary layer theory, the flow must sustain a large velocity relative to the viscous forces present.

By dimensional analysis, Eq. B.3 leads to the relationship

$$\frac{\partial P}{\partial y} = 0. \tag{B.4}$$

This equation states that the pressure gradient across the boundary layer does not change. For the two-dimensional boundary layer,

$$P(x, y) = P_w(x) = P_e(x). \tag{B.5}$$

where the pressure is constant in the surface normal direction but varies as a function of streamwise coordinate.

The governing equations of boundary layer theory may be expressed succintly in the following manner. For clarity, let the streamwise coordinate be denoted by the nomenclature x. As the equations are steady, such that no time derivatives appear

$$\mathbf{Q} = \mathbf{0}. \tag{B.6}$$

The advective fluxes are given by

$$\mathcal{F}_{adv} = \begin{pmatrix} \rho_{g_1} u & \rho_{g_1} v \\ \vdots & \vdots \\ \rho_{g_{ngs}} u & \rho_{g_{ngs}} v \\ \rho_g u^2 + P_e & \rho_g v u \\ 0 & P \\ \rho_g u h + u P_e & \rho_g v h \end{pmatrix} \tag{B.7}$$

where the continuity condition

$$\frac{\partial (\rho u)}{\partial x} + \frac{\partial (\rho v)}{\partial y} = 0 \tag{B.8}$$

is satisfied by summation of the ngs mass species equations. The diffusive fluxes are given by

$$\mathcal{F}_{diff} = \begin{pmatrix} 0 & -\mathbf{J}_1 \\ \vdots & \vdots \\ 0 & -\mathbf{J}_{ngs} \\ 0 & \tau_{xy} \\ 0 & 0 \\ 0 & \tau \mathbf{u} - \dot{\mathbf{q}}'' - \sum_{i=1}^{ngs} \mathbf{J}_i h_i \end{pmatrix} \tag{B.9}$$

where the τ_{xx} normal viscous stress is considered zero according to the fully developed assumption. The y momentum equation diffusive fluxes are now zero according to Eq. B.4. The source terms are defined just as before

$$\mathbf{S} = [\dot{\omega}_1, \ldots, \dot{\omega}_{ngs}, 0, 0, 0]^T \tag{B.10}$$

noting only the omission of the extra third dimension in the momentum equations. Equations B.7-B.10 are the components of the steady, fully-developed, compressible, chemically reacting, 2-dimensional boundary layer and are the foundation for understanding heritage boundary layer theory and convective heating estimates.

Appendix C Boundary Conditions

By integrating the governing equations (Eqs. A.1) across the volume, the Reynolds' Transport Theorem form is acquired:

$$\int_V \frac{\partial \mathbf{Q}}{\partial t} dV + \oint_A \mathcal{F} \cdot \mathbf{n} dA = \int_V \mathbf{S} dV \tag{C.1}$$

where after application of Green's Theorem, the dot product of the flux matrix and normal unit vector are integrated across the surface area of the volume element. The theorem states that the time rate of change of a conserved quantity within a volume element is equal to the net change in that quantity across the surfaces which comprise it and the creation or destruction of that quantity within the volume element itself. This powerful, yet simple concept allows a precise definition of the boundary conditions to coupled domains, as provided by Martin (99).

Suppose that a discrete volume element from domain Ω, the fluid domain, is directly adjacent to a discrete element from domain Λ. If in each volume element, the conserved quantities are defined by the governing equations, then at the interface, the two sets of equations must be equal. However, since the boundary exists as the limit in a single physical dimension, two observations must be noted. First, the time dependent storage terms do not exist at the boundary. Mathematically this is because these terms will always be equal at the overlapping interface and will cancel. Physically, this enforces uniqueness of the conserved properties rate of change at a given location in space (and time). The second observation is that the source terms do not behave this way and must be considered if they exist at the boundary. For the two domains in this work, this yields

$$\left[\int_\omega \mathcal{F} \cdot \mathbf{n} d\omega + \int_\omega \mathbf{S} d\omega\right]_{fluid} = \left[\int_\lambda \mathcal{F} \cdot \mathbf{n} d\lambda + \int_\lambda \mathbf{S} d\lambda\right]_{solid} \tag{C.2}$$

where the lower case Greek nomenclature refers to the surface area of the Ω and Λ domains, respectively. The critical boundary condition is then defined by observing the terms in Eqs. A.3 through A.9. Note that the considered surface is still the vehicle wall, but for a porous ablator, this will still contain both the gaseous/fluid phase (void fraction) and the solid phase, yielding two respective available source terms. In a coupled approach, Eq. C.2 is all that is required. In the decoupled approach, Eq. C.2 must be applied in both the CFD and the MR computation. The models comprising the surface balance equations and the details of their implementation in computational codes will be explored in much greater detail later in this text.

Appendix D Mickley Film Theory to Dimensionless Similarity Form

Mickley offers insight to the zeitgeist of conservation equation reductionism (32) existing before the modern computing era, but does not work out the algebraic details. Below is a reconstruction of his treatment of film theory, which reduces the boundary layer equations to the final dimensionless similarity form (Eq. 2.43) used in the text. An error from the 1959 text is highlighted and clarified as an instructive example of non-dimensional analysis.

Start from Eqs. 2.40-2.42 and letting the streamwise pressure gradient be zero gives the film theory set:

$$\rho v \frac{\partial u}{\partial y} = \frac{\partial}{\partial y}\left(\mu \frac{\partial u}{\partial y}\right) \tag{D.1}$$

$$\rho v c_p \frac{\partial T}{\partial y} = \frac{\partial}{\partial y}\left(k \frac{\partial T}{\partial y}\right) \tag{D.2}$$

$$\rho v \frac{\partial Y_i}{\partial y} = \frac{\partial}{\partial y}\left(\rho D_{ij} \frac{\partial Y_i}{\partial y}\right) \tag{D.3}$$

For the momentum equation, let

$$\beta_F = \frac{u}{u_e}, \tag{D.4}$$

$$\frac{d\beta_F}{dy} = \frac{1}{u_e}\frac{du}{dy}, \tag{D.5}$$

and

$$\frac{d^2\beta_F}{d^2y} = \frac{1}{u_e^2}\frac{d^2u}{dy^2}. \tag{D.6}$$

Then Eq. D.1 becomes

$$\frac{\rho v}{u_e}\frac{d\beta}{dy} = \frac{\mu}{u_e^2}\frac{d^2\beta}{dy^2}. \tag{D.7}$$

Now let

$$m_F = \frac{y}{\Delta_F} \tag{D.8}$$

and see that

$$\frac{d\beta}{dy} = \frac{d\beta}{dm_F}\frac{dm_F}{dy} = \frac{d\beta}{dm_F}\frac{1}{\Delta_F} \tag{D.9}$$

since

$$\frac{dm_F}{dy} = \frac{1}{\Delta_F}. \tag{D.10}$$

Similarly,

$$\frac{d^2\beta}{dy^2} = \frac{1}{\Delta_F^2}\frac{d^2\beta}{dm_F^2}. \tag{D.11}$$

Inserting Eqs. D.9 and D.11 into Eq. D.7 to obtain

$$\frac{\rho v}{u_e}\frac{1}{\Delta_F}\frac{d\beta}{dm_F} = \frac{\mu}{u_e^2}\frac{1}{\Delta_F^2}\frac{d^2\beta}{dm_F^2}. \tag{D.12}$$

By rearrangement and simplification of terms there is obtained

$$\frac{\rho v u_e \Delta_F}{\mu}\frac{d\beta}{dm_F} = \frac{d^2\beta}{dm_F^2}. \tag{D.13}$$

By the analogous method, for energy and mass species

$$\frac{\rho v c_p \left(T_w - T_e\right)\Delta_H}{k}\frac{d\beta}{dm_H} = \frac{d^2\beta}{dm_H^2} \tag{D.14}$$

and

$$\frac{v\left(Y_{iw} - Y_{ie}\right)\Delta_D}{D_{ij}}\frac{d\beta}{dm_D} = \frac{d^2\beta}{dm_D^2}. \tag{D.15}$$

Then the necessary transformation parameters are given by

$$\Delta_F = \frac{\Gamma_F \mu}{\rho v u_e}, \tag{D.16}$$

$$\Delta_H = \frac{\Gamma_H k}{\rho v c_p \left(T_w - T_e\right)}, \tag{D.17}$$

and

$$\Delta_D = \frac{\Gamma_D D_{ij}}{v\left(Y_{iw} - Y_{ie}\right)} \tag{D.18}$$

which vary from the classic text by the non-dimensionalization factor. The second derivative on the RHS of the equations generates an additional term which must be included in the simplification term. Inserting these parameters into their respective equations yields the final dimensionless similarity form

$$\mathbf{\Gamma}\frac{d\beta}{d\mathbf{m}} = \frac{d^2\beta}{d\mathbf{m}^2} \tag{D.19}$$

as given by Mickley, where Eq. D.19 is the abbreviated vector form of the reduced set.

Appendix E Derivation of Linear Solution to the Film-Theory Reduced, Boundary Layer Equations

If the final similarity form of the boundary layer equations, due to the film theory approximations reduced to the following:

$$\rho \mathbf{U} \cdot \nabla \Gamma - \nabla \cdot \Phi \nabla \Gamma = 0 \tag{E.1}$$

then let

$$\Gamma = (\theta_{Y_k}, \theta_h)^T \tag{E.2}$$

be solutions of Eq. E.1 where

$$\theta_{Y_k} = \frac{Y_k - Y_{k,w}}{Y_{k,e} - Y_{k,w}} \tag{E.3}$$

and

$$\theta_h = \frac{h_0 - h_w}{h_{0,e} - h_w}. \tag{E.4}$$

Since $\rho \mathbf{U}$ represent the fluid properties for each station point, and assuming that $\Phi = \Phi_{Y_k} = \Phi_h$, and given the boundary conditions that

$$\begin{aligned} &\text{At } y = 0, \text{then} \qquad \theta_{Y_k} = 0 \\ &\text{At } y = 0, \text{then} \qquad \theta_h = 0 \\ &\text{At } y = \delta, \text{then} \qquad \theta_{Y_k} = 1 \\ &\text{At } y = \delta, \text{then} \qquad \theta_h = 1 \end{aligned} \tag{E.5}$$

then the solutions θ_Y and θ_h may be equated such that

$$\frac{Y_k - Y_{k,w}}{Y_{k,e} - Y_{k,w}} = \frac{h_0 - h_w}{h_{0,e} - h_w}. \tag{E.6}$$

Appendix F Perspective on film coefficient methodology

Figure F.1 visually illustrates the two separate ways a worker may think about the application of the film coefficient methodology; the Anchor and the Taylor methods. This approach does not include additional corrections to the film coefficient, such as the blowing correction for advection, the hot wall or cold wall corrections, roughness corrections, etc.

The Anchor method is the way most thermal analysts will see the aeroheating boundary condition. In the anchor method, the recovery enthalpy approximates the adiabatic wall enthalpy and acts as an *anchor*. From this location, the negative value of the film coefficient shoots a straight line azimuth across decreasing wall enthalpy values. To obtain the heat flux at the wall, the wall enthalpy in the material response is evaluated from surface thermochemistry tables. Where the wall enthalpy intersects

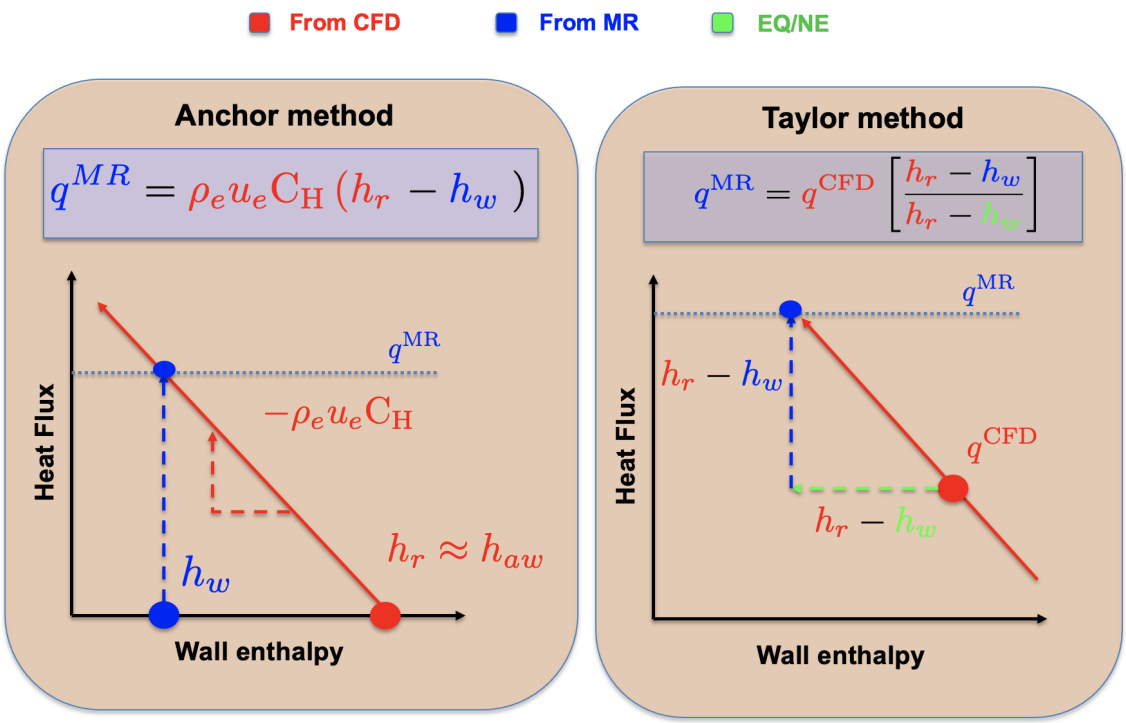

Figure F.1: Two methods of thinking about the film coefficient model

the azimuth is the heat flux value that is applied at the surface.

The Taylor method perhaps best illustrates the physics which are attempting to be modeled. In this method, the base CFD heat flux from the original CFD is obtained as a starting point. The enthalpy ratio used to construct the film coefficient is dissociated from this value, and instead forms an enthalpy ratio. This linear enthalpy ratio may be thought of as a Taylor series expansion about the base CFD heat flux. As is typically the case with a Taylor series approximation of a derivative, the larger this correction, the more likely error will be introduced. This is true in the case of heat flux as well, since it is known that the variable fluid properties at high temperatures will produce some curvature in the heat flux function. Regardless, the impact of choosing the wall enthalpy to evaluate the film coefficient (green) and how the wall enthalpy in the material response is modeled (blue) both have an impact on the overall evaluation of the heat flux at the wall.

For both ways of thinking about the film coefficient, it should be clearly understood, that the material response wall enthalpy, is acting as a correction to account for the physics that were not computed in the film coefficient CFD. This includes not only the presence of ablating and pyrolyzing species, but also the difference in wall temperature.

Appendix G Temperature dependent catalytic models and the film coefficient

Historically, researchers such as Fay and Riddell, Scala (100), and Goulard (101) investigated the effect of varying catalycity on the wall heat flux. They showed the effect on the wall heat flux between the two limiting cases of non-catalytic and chemical equilibrium (Goulard's S-curve). However, the sensitivity of the *film coefficient model* to various catalytic models was not assessed. This trend was initially observed by Giovanni Salazar after the EFT-1 mission and is reproduced here for its applicability to correctly implement the film coefficient methodology.

In the main text, it has been shown that the model used to enforce catalysis at the wall can drastically modify the surface temperature. In fact, depending on the model, it is possible to introduce non-linear effects if applied outside the intended region of applicability. An example of this is using the Park first order model for wall temperatures above 3000 K where atomic species are likely to occur at chemical equilibrium conditions. This appendix analyzes another temperature dependent model which can have an impact on the predicted heat flux from the film coefficient.

This catalytic model is for reaction-cured glass (or RCG), a surface coating intentionally applied to reduce catalysis on the space shuttle Orbiter. Stewart (81) proposed a catalytic model for this material which makes the accommodation coefficient a function of wall temperature. The model is given by

$$\gamma_{\mathrm{N}} = \begin{cases} 5.0 \times 10^{-4}, & T_w < 465K \\ 2.0 \times 10^{-5} \left(e^{1500/T_w}\right), & 465K < T_w < 905K \\ 1.0 \times 10^{1} \left(e^{-10360/T_w}\right), & 905K < T_w < 1675K \\ 6.2 \times 10^{-6} \left(e^{-12100/T_w}\right), & T_w > 1675K \end{cases} \tag{G.1}$$

and

$$\gamma_O = \begin{cases} 5.0 \times 10^{-3} \left(e^{-400/T_w}\right), & T_w < 502K \\ 1.6 \times 10^{-4} \left(e^{1326/T_w}\right), & 502K < T_w < 978K \\ 5.2 \times 10^{0} \left(e^{-8835/T_w}\right), & 978K < T_w < 1617K \\ 3.9 \times 10^{-8} \left(e^{21410/T_w}\right), & T_w > 1617K \end{cases} \tag{G.2}$$

where Eqs. G.1 and G.2 are piecewise functions given in the form of Eq. 5.20.

The same spherical vehicle as used in Chapter 5.1 is flown at higher freestream velocity (7.721 km/s) to increase the levels of dissociation in the boundary layer. The model is assessed at two body points on the vehicle, the stagnation point and the 90 shoulder. Figure G.1 shows the wall heat flux on the left y-axis and the value of the accommodation coefficients for both oxygen and nitrogen on the right y-axis. The blue lines are the accommodation coefficient values as a function of wall temperature. The red markers on the plot are CFD heat fluxes computed at various isothermal wall temperatures.

Figure G.1(a) shows the result for the stagnation point. At high heating levels the partially catalytic model has no discernable effect and the wall heating relationship is approximately linear. This is because the conduction dominates the diffusion. However, Fig. G.1(b) shows that the non-linearity in this type of catalytic model can not be captured by a constant film coefficient. The shoulder body point (90° from the stagnation point) has a smaller conduction component and thus the effect of the catalysis appears in the wall heating flux. Evaluation of the film coefficient at the incorrect wall temperature could result in under-predicting the wall heat flux. In addition, it shows how strongly the chosen model of mass boundary condition will affect the resulting predicted heat flux if the level of dissociation is high enough.

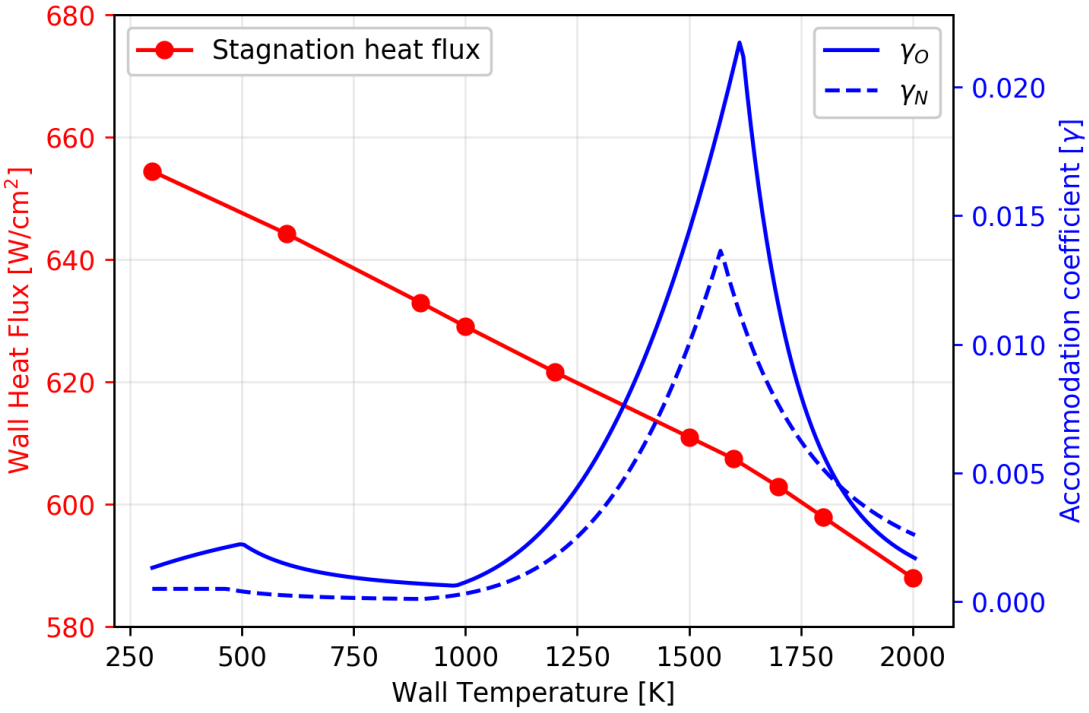

(a) Stagnation point

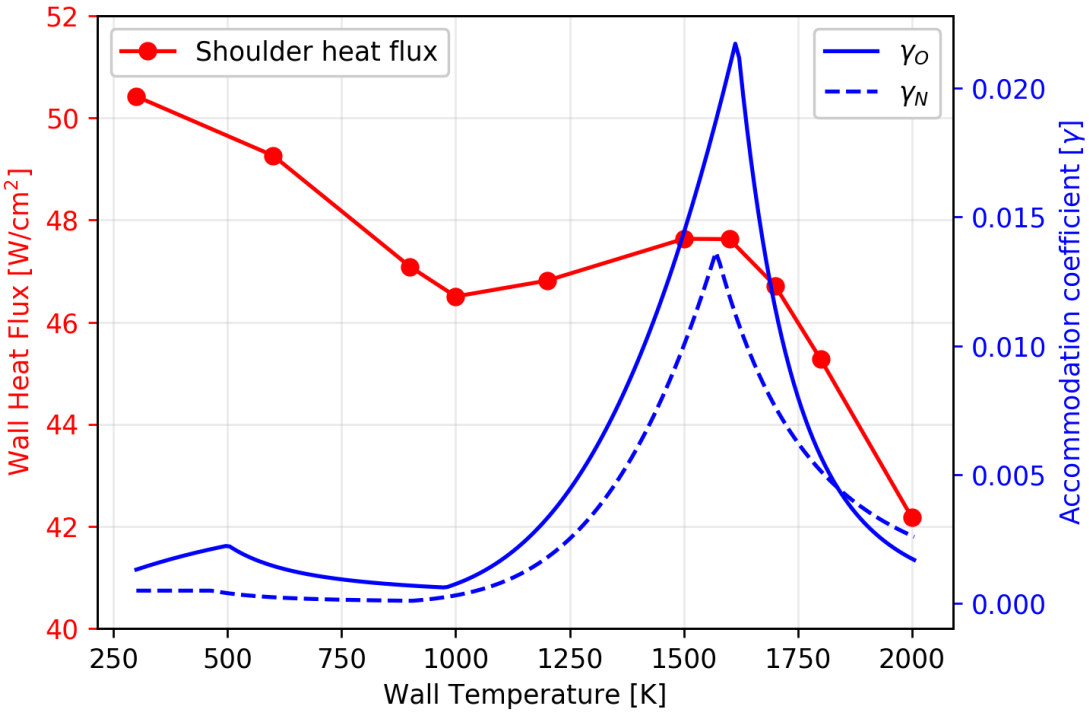

(b) Shoulder body point

Figure G.1: Catalytic effect on wall heat flux leading to non-linearity

Appendix H Fay-Riddell & Viscous, Chemically Reacting CFD

Consider the extreme limiting case of having no access to a high fidelity CFD simulation. Early stage design often requires first order estimations of heating for the initial development of spacecraft. In this instance, correlations derived from the boundary layer equations, may be useful to the design engineer.

Figure H.1 shows the Fay-Riddell (FR) correlation (36) for a binary air, chemically reacting, high speed laminar boundary layer. This correlation is meant to be applied between the following flight conditions:

- Freestream Velocity: 1767-6949 m/s
- Wall Temperature: 300-3000 K
- Altitude: 7620-38100 m

It is computed for the flight condition in Table 5.2 for each wall temperature, subject to the boundary layer assumption that the normal pressure gradient is constant such that $P_e = P_w$. The properties behind the shock are obtained by shock jump correlations, detailed in the technical note by Callis and Kemper (102). An outside program is used to compute the equilibrium conditions at the edge and the wall, as well as the dissociation enthalpy. The Prandtl number is held constant at Pr = 0.72.

From Fig. H.1, it is immediately seen that the estimated heat transfer from the FR correlation is generally lower than the CFD predictions. The closest model to the correlation is the CFD computed with a constant Lewis number based diffusion coefficient (Le = 1) and a non-catalytic wall. In the FR model, the difference in allowing catalysis (delta between red and black lines) appears to be in family with the difference obtained from the CFD solutions.

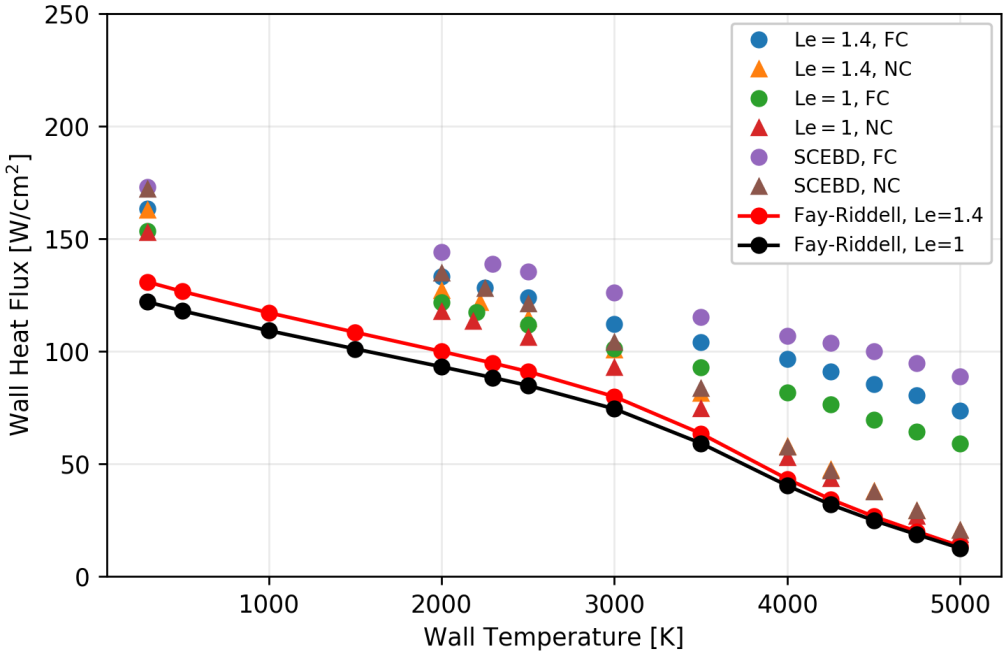

Figure H.1: Fay-Riddell heating correlation for stagnation point compared to CFD heat flux

Note that the dissociation enthalpy term is a function of edge properties and is only applied if the Lewis number does not equal 1. Since edge properties are approximately constant for a given flight condition and body location, the diffusive effect will be a constant percentage from the Le $\neq$ 1 case. This is the reason that at high wall temperatures (lower conduction fluxes) the diffusion effect seems to decrease. As well, it is implied by this figure, that at this level of dissociation the contribution from diffusive effects will be less important than correct computation of the conduction component of the convective flux. It may also be remembered that the Fay-Riddell correlation does not contain any post shock nitric oxide. Previously, it was shown that appreciable amounts of NO traveled down the streamline to the vehicle wall and increased the wall enthalpy (or more generally the energetic state at the wall).

The analysis is now extended to even higher velocities. See Fig. H.2. Figure H.2(a)

Parameter	Value	Units
Altitude	60	km
Freestream Velocity	11.0	km/s
Freestream Density	3.096×10^{-4}	kg/m^3
Freestream Temperature	247.021	K
Initial Mass Fraction [N2]	0.767	kg/kg
Initial Mass Fraction [O2]	0.233	kg/kg

Table H.1: CFD parameters for 11 species case

shows the FR correlation for the flight condition from Table 5.2 with an increased freestream velocity to approximately 7 km/s. This CFD was computed using the SCEBD diffusion model and a temperature dependent RCG catalysis model. The FR correlation reveals a similar qualitative trend as the CFD computed wall heat flux, with a considerable portion due to mass diffusion. However, it ultimately underpredicts the wall heat flux predicted by the CFD.

Figure H.2(b) shows the FR correlation for the flight condition from Table H.1. This flight condition was computed assuming ionization in the flow field with an 11-species gas phase model. The other assumptions in the CFD were a SCEBD diffusion model and a *fully catalytic* wall. Again, the FR correlation underpredicts the CFD prediction. However, this limitation is expected since the flight conditions are outside the scope of the proposed model.

While this analysis does not cover the entire range of flight conditions for which a correlation may be used, it is indicative of its behavior. Designing to a BL correlation such as Fay-Riddell must involve appropriate margins for the uncertainty in the model and the applicability of its scope. One off-hand method of obtaining rough film coefficients would be by extracting the slope of a cold wall and a moderate temperature FR solution. This is, in a sense, the same qualitative behavior as seen by the CFD, but it would need to be shifted with some amount of conservatism to reach the same levels of heating as the viscous CFD.

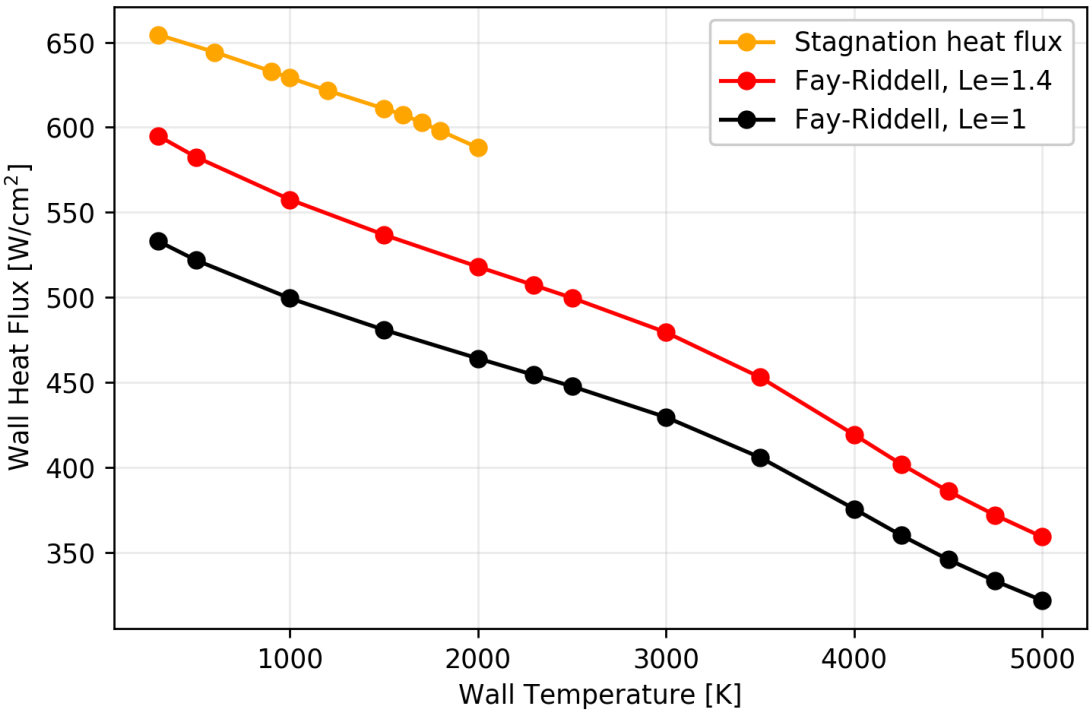

(a) Flight condition from Table 5.2 with $V_\infty = 7721$ m/s

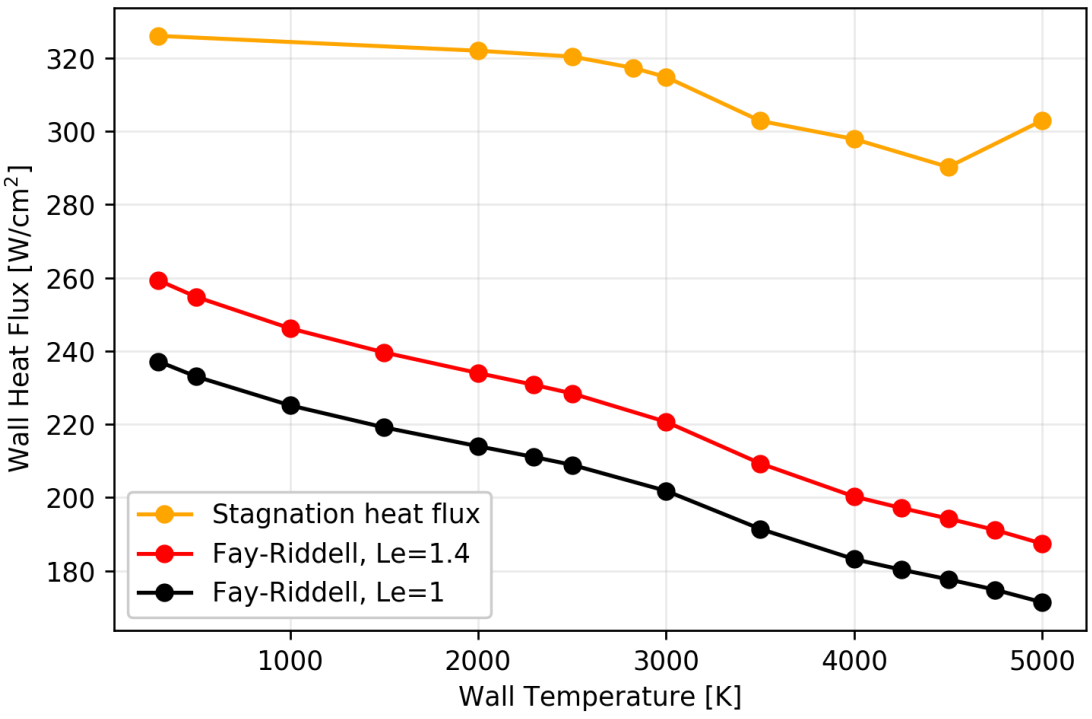

(b) Flight condition from Table H.1

Figure H.2: Fay-Riddell equilibrium correlation vs. CFD predicted heat flux

Appendix I Kentucky Trajectory Modeling Program

A simple Newton-Raphson scheme to calculate approximate ballistic trajectories and relevant flight parameters is presented. The following assumptions are required:

- Planet-centric model
- Vehicle treated as a point mass
- Fixed inertial reference frame
- Constant relative angular motion
- Origin at center of gravitational field
- Atmosphere at rest (no relative wind vector)
- No Coriolis Effect
- No thrust or lift (ballistic trajectory)

The six degree of freedom (DOF) equations follow from Vinh, Busemann, and Culp(103).

$$\begin{aligned}
\frac{dr}{dt} &= V \sin\gamma \\
\frac{d\theta}{dt} &= \left(V \cos\gamma \cos\psi\right)\left(r\cos\phi\right)^{-1} \\
\frac{d\phi}{dt} &= \left(V \cos\gamma \sin\psi\right) r^{-1} \\
\frac{dV}{dt} &= -\rho A C_d V^2 \left(2m\right)^{-1} - g\sin\gamma \\
V\frac{d\gamma}{dt} &= -\left(g - V^2/r\right)\cos\gamma \\
V\frac{d\psi}{dt} &= -V^2/r\left(\cos\gamma\cos\psi\tan\phi\right)
\end{aligned} \tag{I.1}$$

The gravitational force model is given by the familiar inverse distance formulation given a reference gravity

$$g = g_0 \left(\frac{r - h}{r} \right)^2 \tag{I.2}$$

where h is the height in meters above the planetary surface. The drag model is given by Bertin(104).

$$C_{pt2} = \begin{cases} 2.000 & \text{Newtonian Flow} \\ 1.932 & \text{Equilibrium flow} \\ 1.838 & \text{Perfect gas} \end{cases} \tag{I.3}$$

$$\Gamma = \frac{1}{4} \cos^2 \alpha \left(1 - \sin^4 \delta_c \right) + \frac{1}{8} \sin^2 \alpha \cos^4 \delta_c \tag{I.4}$$

$$\Delta = \tan \delta_c \left(\cos^2 \alpha \sin^2 \delta_c + \frac{1}{2} \sin^2 \alpha \cos^2 \delta_c \right) \tag{I.5}$$

$$\Phi = \left(\frac{r_c/r_n - \cos \delta_c}{\tan \delta_c} \cos \delta_c + \frac{\left(r_c/r_n - \cos \delta_c \right)^2}{\tan \delta_c} \right) \tag{I.6}$$

$$C_d = \left[2 C_{pt2} \left(\frac{r_n}{r_c} \right)^2 (\Gamma + \Delta \Phi) \right] \cos \alpha \tag{I.7}$$

Which satisfies C_d in the above equations given the proper vehicle parameters of nose radius, cone diameter, cone angle, etc. The choice of flow regime coefficient is left to user discrepancy.

User discrepancy also permits various ported models for density and heat flux. The density model used for this analysis is NASA's NRL-MSISE(105) which includes estiamtes for solar radio flux and geomagnetic index. The heat flux model is the Sutton-Graves model(75) for stagnation point heating in dissociated air, given as

$$q_s'' = 1.83 \times 10^{-4} \left(\frac{\rho}{r_n} \right)^{1/2} V^3. \tag{I.8}$$

The subsequent heating load may be obtained by integration of the heat flux as a function of time.

It may be noted that for ballistic cases, the additional 3 degrees of freedom separate from altitude, velocity, and flight path angle are not required. They are presented here for completeness so the reader may extend this analysis to lifting bodies or arbitrary flight vehicles if desired.

Vita

Justin M. Cooper

Education

- Bluegrass Community and Technical College, Lexington, KY
  Undergraduate pre-course work, 2005-2007

- University of Kentucky, Lexington, KY
  Organic chemistry major, 2007-2009

- University of Kentucky, Lexington, KY
  Bachelor of Science in Mechanical Engineering, Minor in Chemistry, 2013-2015
  Magna Cum Laude 3.672

- University of Kentucky, Lexington, KY
  Master of Science in Mechanical Engineering, 2015-2018
  Thesis topic: Implementation of a Surface Recession Module in a Finite Volume Ablation Solver
  CFD Graduate Certificate, 3.938

- University of Kentucky, Lexington, KY
  Pursuing Ph.D. in Mechanical Engineering, 2018-present
  Dissertation topic: A Decoupled Engineering Methodology for Accurate Prediction of Ablative Surface Boundary Conditions in Thermal Protection Systems

Academic Awards

- Oswald Research and Creativity Award, 2015

- 2022 AIAA David Weaver Thermophysics Best Student Paper Award for paper titled "Numerical Investigation of Film Coefficient Engineering Methodology for Dissociated, Chemically Reacting Boundary Layers" (AIAA-2022-1907)

Publications in Referred Journals

- Submitted: Cooper, J. M. and Martin, A., "A Novel Engineering Methodology for Decoupled Aerothermal Analysis of Hypersonic Atmospheric Entry," Journal of Spacecraft and Rockets, 2022, (Manuscript ID 2022-03-A35433)

- Submitted: Cooper, J. M., Salazar, G., and Martin, A., "Numerical Investigation of Film Coefficient Engineering Methodology for Dissociated, Chemically Reacting Boundary Layers," Journal of Thermophysics and Heat Transfer, 2022, (No Manuscript ID currently)

- Omidy, A. D., Cooper, J. M., Tagavi, K. A., and Martin, A., "VISTA, an open Avcoat material database for material response modeling," JANNAF Journal of Propulsion and Energetics, Vol. 12, No. 1, 2021, pp. 55–72

Publications in Refereed Conference Proceedings

- Cooper, J. M., Stieha, J. K., Fowler, A. M., Wright, N. A., and Martin, A., "Kentucky Re-entry Universal Payload System," 54th AIAA Aerospace Sciences Meeting, AIAA Paper 2016-2192, San Diego, CA, January 2016

- Cooper, J. M., Schroeder, O. M., Weng†, H., and Martin, A., "Implementation and Verification of a Surface Recession Module in a Finite Volume Ablation Solver," 12th AIAA/ASME Joint Thermophysics and Heat Transfer Conference, AIAA Paper 2018-3272, Atlanta, GA, June 2018

- Cooper, J. M. and Martin, A., "A Novel Engineering Methodology for Decoupled Aerothermal Analysis of Hypersonic Atmospheric Entry," AIAA Aviation, AIAA Paper 2021-3147, Virtual Event, Aug 2021.

- Cooper, J., Salazar, G., and Martin, A., "Numerical Investigation of Film Coefficient Engineering Methodology for Dissociated, Chemically Reacting Boundary Layers," AIAA SciTech Forum, AIAA Paper, Jan 2022, Accepted (Control ID 3613489).

Conference Articles/Abstracts

- Cooper, J. M., Weng, H., and Martin, A., "Numerical Implementation of 3D Adaptive Mesh Movement utilizing the Spring Analogy Method," 40th Dayton-Cincinnati Aerospace Sciences Symposium, No. 40DCASS-022, March 2015

- Cooper, J. M., Schroeder, O. M., Weng, H., and Martin, A., "Multi-Dimensional Surface Chem- istry Comparison of Iso-Q Arcjet Cases," 42nd Dayton-Cincinnati Aerospace Sciences Symposium, No. 42DCASS-076, Dayton, OH, March 2017.

- Cooper, J. M., Schroeder, O. M., Weng, H., and Martin, A., "Implicit Flux Balancing in a Finite Volume Material Response Solver," 43rd AIAA Dayton-Cincinnati Aerospace Sciences Symposium (DCASS), No. 43DCASS-119, Dayton, OH, February 2018